MODELING EXCITATIONS IN QUANTUM MAGNETS

BY

RAMESH DHAKAL

A Dissertation Submitted to the Graduate Faculty of

WAKE FOREST UNIVERSITY GRADUATE SCHOOL OF ARTS AND SCIENCES

in Partial Fulfillment of the Requirements

for the Degree of

DOCTOR OF PHILOSOPHY

Physics

May 2026

Winston-Salem, North Carolina

Approved By:

Stephen M. Winter, Ph.D., Advisor

Akbar Salam, Ph.D., Chair

Fred Salsbury, Ph.D.

Natalie Holzwarth, Ph.D.

David Carroll, Ph.D.

Acknowledgments

This thesis is the culmination of last five years of research and hard work, and I owe so much to so many incredibly thoughtful and supportive people, who provided constant encouragement and guidance throughout my time as a PhD student.

First of all, I would like to thank my advisor Prof. Steve Winter. It has been an absolute honor to learn from, and work with Steve, whose brilliant ideas and enthusiasm in science never ceases to amaze me. When I reminisce about my early days at Wake, I realize how unready and overwhelmed I truly was. Steve would always explain every small details with great patience without making me fell inadequate. I thank Steve for meeting with me any time, mentoring me, giving me life advices, and for being unfailingly tolerant and kind. You are an inspiration, and I hope to extend the same level of care and dedication to my future students.

Many people I met in graduate school became more than just colleagues. My PhD journey would have been rather isolating without them. I would like to thank Wells, Mani, and Can for being such a great companions. I've truly enjoyed our countless after-hours sports and free-food adventures. Thanks to Evan, and Katie, for being wonderful grad office mates and for the many Friday drinks we shared. In no order at all, to Tim, Areezo, Mariya, David, George, and Leda: Thank you for making my experience at Wake so memorable and enjoyable.

I would like to extend my gratitude to my Research Advisory committee members, Prof. Natalie Holzwarth, Prof. Greg Cook, and recently Prof. David Carroll for providing valuable feedback. I would also like to thank Prof. Akbar Salam and Prof. Fred Salsbury for agreeing to be in my defense committee.

In addition, I would like to thank the DEAC cluster team, especially Sean Anderson, for promptly responding to my emails and often meeting with me in person to resolve any issues.

I would like to thank my parents, and my sisters for believing in me. Somehow, you have always managed to be proud of me, even when I probably didn't deserve it. Without your support none of this would have been possible.

Thank you so much to my wife and the love of my life, Urmila, for the unconditional love. This thesis would not have been completed without your support. You have been my source of strength, hope, and comfort. My eight-month-old son's contributions were statistically negative to further this thesis, but deserves mention for bringing so much joy in my life. His giggles and babblings have given me a new perspective in life.

Finally, I want to dedicate this thesis to my brother, Rabindra, who sacrificed his higher studies and supported me, so that I can continue mine!

Contents

List of Figures **xii**

List of Tables **xiii**

List of Abbreviations **xiv**

Abstract **xvi**

Chapter 1 Magnestism **1**

1.1 Magnetism and Quantum Mechanics 1

1.2 Electron Spin and Magnetic Moment 4

1.3 Factors Determining Local Degrees of Freedom 5

1.3.1 Crystal Field Splitting 6

1.3.2 Spin-Orbit Coupling 8

1.3.3 Jahn–Teller Effect 11

1.4 Magnetic Couplings 13

1.4.1 Dipole-Dipole Interaction 13

1.4.2 Exchange Interaction 14

1.4.3 Superexchange Interactions 16

1.5 Model Spin Hamiltonians 22

1.6 Ordered Phases and Excitations in Solid 25

1.7 Quantum Spin Liquid 26

1.7.1 Kitaev's Honeycomb Model 28

1.8 Thermal Hall Effect 32

1.9 Dissertation Outline 33

Chapter 2 Methodology **35**

2.1 Review of des Cloizeaux Effective Hamiltonians 35

2.2 *Ab Initio* Phonon Calculations 40

Chapter 3 The Role of Disorder in the Magnetic Excitations of Quantum Magnets **44**

3.1 Introduction 45

3.2 Results and Discussion 46

3.3 Conclusions 53

3.4 Supplementary Information 53

3.4.1 Sample preparation and characterization 53

3.4.2 Magneto-infrared and electron spin resonance measurements 54

3.4.3 Temperature dependence of magnetic excitations 58

3.4.4 Full Details of Ab-initio Calculations 59

3.4.5 Additional Results from FIR/ESR Simulations 63

Chapter 4 Layer-Dependent Anisotropy in Quantum Magnets due to Distortions **64**

4.1 Introduction 65

4.2 Results and Discussion 66

4.3 Conclusions 78

4.4 Methods 79

4.4.1 *Ab initio* calculations 79

4.5 Supplementary Information 80

4.5.1 Ab initio calculation of exchange parameters 80

4.5.2 Density functional theory calculation of structural distortions 84

4.5.3 Compatibility of Theoretical Model with Experimental IETS Spectrum 84

Chapter 5 Hybrid Spin-Orbit Exciton-Magnon Excitations in $FePS_3$ **89**

5.1 Introduction 90

5.2 Single Site States 91

5.3 Electronic Hamiltonian . . . 92
5.4 Intersite Low-Energy Couplings . . . 94
5.5 Model Properties . . . 98
5.6 Conclusions . . . 102
5.7 Methods . . . 103
5.8 Supplemental Material . . . 104
5.8.1 Basis functions for J States . . . 104
5.8.2 Intersite Hund's Coupling Matrices . . . 108
5.8.3 Biquadratic Exchange Couplings . . . 110

Chapter 6 Spin-Phonon Coupling in Transition Metal Insulators 112

6.1 Introduction . . . 112
6.2 Spin-Phonon Couplings Theory . . . 115
6.2.1 Intuition from Perturbation Theory . . . 115
6.2.2 General Form of Spin-Phonon Operators and Inadequacy of Static Approaches . . . 122
6.2.3 Spin-Phonon Implementation Details . . . 124
6.3 Study of $MnPSe_3$ . . . 130
6.3.1 Introduction . . . 130
6.3.2 Base Magnetic Hamiltonian . . . 132
6.3.3 Phonons . . . 136
6.3.4 Spin-Phonon Couplings . . . 139
6.3.5 Modelling Raman Scattering . . . 142
6.4 Conclusions and Outlook . . . 148
6.5 Intersite Coulomb Tensors . . . 150

Chapter 7 Phonon Thermal Hall Effect in Magnetic Insulators 152

7.1 Introduction . . . 152
7.2 Results . . . 155
7.2.1 Spin-Phonon Couplings . . . 155
7.2.2 Phonon Longitudinal Thermal Conductivity . . . 160

7.2.3 Phonon Thermal Hall Conductivity 163
7.3 Supplementary Materials 165
7.3.1 Phonon Hall Viscosity as Electronic Nuclear Berry Curvature 165
7.3.2 Details of First Principles Calculations 169
7.3.3 Numerical Results for L Couplings for Acoustic Phonons 177
7.3.4 Low-q Scaling and Connection to Long-Wavelength Elastic Theory 178
7.3.5 Evaluation of Acoustic Phonon Thermal Conductivities 181

Chapter 8 Selected Co-authored Projects 189

8.1 **Characterization of Pyrochlore Compound $Ba_3Tm_2Zn_5O_{11}$** 189
8.2 **Pressure-dependent Magnetism in Li_2RhO_3** 189

Chapter 9 Conclusions and Future Outlook 190

Bibliography 193

Curriculum Vitae 225

List of Figures

1.1 Schematic illustration of crystal field splitting 6

1.2 Schematic representation of (a) low spin state in α-$RuCl_3$ due to strong crystal field splitting (b) high-spin state in $Na_2Co_2TeO_6$ due to relatively weak crystal field splitting. 7

1.3 Schematic diagram of (a) d_{z^2} orbital in octahedral environment under tetragonal elongation. Splitting of d orbitals during tetragonal (b) elongation and (c) contraction (d) $d_{x^2-y^2}$ orbital subject to tetragonal contraction. 11

1.4 Schematic illustration of orbital splitting under (a) trigonal elongation and (b) trigonal compression. 12

1.5 Representative orbitals illustrating Goodenough–Kanamori rules of superexchange interactions. 17

1.6 Energy spectrum for two site Hubbard model. 19

1.7 Spin canting in an otherwise antiferromagnet due to Dzyaloshinskii–Moriya interaction 24

1.8 A triangular lattice demonstrating geometric frustration for antiferromagnetically interacting Ising spin. Red lines denotes energetically unfavorable (unhappy) bonds, while green lines indicates energetically favorable (happy) bonds. 27

1.9 Valence bond and resonating valence bond states 28

1.10 Kitaev interactions in a honeycomb lattice 29

1.11 Thermal Hall Effect 33

2.1 Figure illustrating des Cloizeaux Effective Hamiltonians scheme 36

2.2 Visualization of the lowest order terms in the cluster expansion for the nearest- neighbor honeycomb lattice 39
2.3 Schematic illustration of finite displacement method 41

3.1 Unpolarized optical magneto-spectroscopy measurements on $Na_2Co_2TeO_6$. 47
3.2 Polarized magneto-optical response of single-crystal $Na_2Co_2TeO_6$ 48
3.3 Model simulations of INS and FIR magneto-absorption spectra 50
3.4 Normalized far-IR magneto-transmission spectra of $Na_2Co_2TeO_6$ 54
3.5 ESR spectroscopy results of $Na_2Co_2TeO_6$. 56
3.6 Comparison of ESR spectra with normalized FIR magneto-transmission spectra of $Na_2Co_2TeO_6$. 56
3.7 Comparison of ESR spectrum with normalized FIR magneto-transmission spectra of $Na_2Co_2TeO_6$. 57
3.8 Temperature-dependent magneto-IR spectroscopy results of $Na_2Co_2TeO_6$. . 58
3.9 Different structures employed for modeling Na disorder 59
3.10 Model simulations of polarized FIR/ESR spectra 63

4.1 Three-dimensional electron diffraction and demonstration of IETS measurements on 1L α-$RuCl_3$ 68
4.2 Temperature-dependent IETS of few-layer α-$RuCl_3$ 70
4.3 Magnetic-field-dependent IETS on few-layer α-$RuCl_3$ 72
4.4 Lateral magnetotransport measurement on 1L α-$RuCl_3$ with dual gates . . 74
4.5 Three primary distortions of 1L α-$RuCl_3$ and magnetic phase diagram . . . 76
4.6 Computed structural variation of the magnetic couplings with no buckling ($\Delta\zeta_{\mathrm{Ru}} = 0$) 83
4.7 Computed structural variation of the magnetic couplings with finite buckling ($\Delta\zeta_{\mathrm{Ru}} = 0.3$ Å) 85
4.8 Local dynamical spin structure factor for bulk model computed via exact diagonalization. 87

5.1 Structure of $FePS_3$ showing honeycomb motif 91

5.2 Splitting of local single-ion multiplets with spin-orbit coupling (SOC) and trigonal distortion 92

5.3 Evolution of lowest energy eigenvalues for two site Z_1-bond cluster. (b,c) Evolution of bilinear couplings in $J_{\text{eff}} = 1$ model for large U_{t2g} for first and third neighbors, respectively 95

5.4 Intersite interactions for Z_1 bond and $U_{t2g} = 4.2$ eV for full $J_{\text{eff}} = 1, 2$, and 3 model. 99

5.5 Results from LFWT. 100

5.6 Intersite biquadratic interactions for Z_1 bond as a function of U_{t2g}. 110

6.1 Schematic definition of two-orbital model 116

6.2 Structure of $MnPSe_3$ monolayer viewed (a) along c-axis, with two-site honeycomb unit cell highlighted, and (b) from the side. (c) Definition of first, second, and third neighbor interactions between Mn sites. 131

6.3 Computed one-magnon dispersion for $MnPSe_3$ at the level of linear spin-wave theory. 137

6.4 View of the displacements of the Mn and Se atoms for the lowest energy Raman-active optical $q = 0$ phonons 138

6.5 (a) Computed 2-magnon Raman scattering intensity in the VV polarization as a function of temperature (b) Computed phonon Raman lineshapes . . . 144

6.6 (a-d) Computed $q = 0$ phonon self-energy as a function of temperature (e) Computed phonon lifetime τ_ν. (f) computed center frequency $\tilde{\omega}_\nu$. 146

7.1 **Momentum dependence of the computed spin-phonon couplings.** $\mathbb{A}_{ij}^{q\nu}$ is depicted for the nearest-neighbor Z-bond along the high symmetry K-Γ-M path. (a): Frobenius norm $||\mathbb{A}||$. (b)-(g): Magnitude of different components of $\mathbb{A}$ in cubic coordinates. (h): Four unit cells of α-$RuCl_3$ showing definition of nearest-neighbor X-, Y-, and Z-bonds. (i): Unit cell showing definition of cubic x, y, z coordinates. (j)-(m): Primary displacements associated with $q = 0$ optical phonons. 156

7.2 **Low-momentum angle dependence of acoustic-mode spin-phonon couplings.** Computed $\mathbb{A}_{ij}^{\theta\nu}$ for the nearest-neighbor Z-bond are shown as a function of the momentum angle θ. (a)-(c): diagonal $\mathbb{A}_{xx}$, $\mathbb{A}_{yy}$, and $\mathbb{A}_{zz}$ components. (d)-(e): off-diagonal $\mathbb{A}_{xy}$, $\mathbb{A}_{xz}$, and $\mathbb{A}_{yz}$ components. The acoustic modes ZA, TA, and LA are labelled in the upper right of each panel. (g): Z-bond in real space showing definition of the unit cell a, b axes and cubic (x, y, z) coordinates. (h): first Brillouin zone showing definition of the a^*, b^* axes, and θ (measured from the a^* axis). (i): orientation, in q-space, of the relevant symmetry operations for the Z-bond. 1 rlu $= 4\pi/(\sqrt{3}a)$. 159

7.3 **Longitudinal phonon thermal conductivity.** Shown for (a): magnetic field $\mathbf{B} \,||\, a$ and (b): $\mathbf{B} \,||\, b^*$. Inset in (a) shows zigzag ($B < B_c$) and polarized ($B > B_c$) magnetic states. Inset in (b) shows 24 site cluster used in ED. . . 161

7.4 **Phonon thermal Hall conductivity.** (a): Evolution of phonon thermal Hall conductivity $\kappa_{xy}^{\mathrm{ph}}$ as a function of field for $\mathbf{B} \,||\, a$ computed using ED bond correlations. (b-d): Phonon Berry curvature Ω_ν^θ as a function of field and momentum direction for three acoustic phonon bands; $1\,\mathrm{rlu} = 4\pi/(\sqrt{3}a)$. (e): Field angle dependence of $\kappa_{xy}^{\mathrm{ph}}$ at $|\mathbf{B}| = 12\,\mathrm{T}$. Inset: Sign of $\kappa_{xy}^{\mathrm{ph}}$ as a function of in-plane field direction, with definition of field angle ϕ. 162

7.5 Relaxed high-symmetry crystal structure of α-$RuCl_3$ with the $P\bar{3}1m$ symmetry (a): view along c-axis showing honeycomb planes. (b): side view showing AA stacking. Ru and Cl atoms are shown in blue and green colors respectively. 170

7.6 Evolution of the real and imaginary parts of the phonon eigenvectors $e_{\alpha n}^{q\nu}$ for ZA, TA, and LA modes in the chosen gauge. Arrows indicate the dominant direction of atomic displacement corresponding to eigenvectors at different q-points in the Brillouin zone. Transforming the ZA eigenvectors to be purely real and the TA and LA eigenvectors to be purely imaginary in the limit $q \to 0$ ensures smooth spin-phonon couplings in the same limit. 172

7.7 Momentum angle dependence of the computed $\mathbf{L}_i^{\theta\nu;\nu'}$ spin-phonon couplings. (a)-(c): (x, y, z) components of $\mathbf{L}_i^{\theta\nu;\nu'}$. The pairs of acoustic modes $\nu;\nu' =$ ZA, TA, and LA are labelled in the upper right of each panel. (d): first Brillouin zone showing the definition of a^* and b^* axes and θ (measured from the a^* axis). (e): orientation, in q-space, of the relevant symmetry operations for the single-site couplings. (f) Single Ru site showing definition of cubic axes. 1 rlu $= 4\pi/(\sqrt{3}a)$, reciprocal lattice unit. 177

7.8 Evolution of different components of the long-wavelength Hall viscosity tensor obtained by fitting computed $\overline{\eta}_\theta^{\nu;\nu'}$ to approximate long-wavelength forms for (a): $\mathbf{B} \parallel a$ and (b): $\mathbf{B} \parallel b^*$. Results based on zero-temperature bond correlations computed using exact diagonalization of the spin model discussed in the main text. 184

7.9 Comparison of computed longitudinal phonon thermal conductivity as a function of Lorentzian broadening (γ in meV) of the poles of the dynamical bond correlation functions obtained from exact diagonalization. $\kappa_{xx}^{\rm ph}(B)/\kappa_{xx}(0)$ is relatively insensitive to choice of broadening. $\gamma = 0.5\,$meV is employed in the main text. 187

List of Tables

3.1 Computed J-values for different disordered structures of $Na_2Co_2TeO_6$ with the exact diagonalization of full d-orbital model 61

3.1 Computed J-values for different disordered structures of $Na_2Co_2TeO_6$ with the exact diagonalization of full d-orbital model 62

4.1 Summary of the estimated exchange couplings (meV) for 1L and bulk α-$RuCl_3$ 77

4.2 Comparison of average structural parameters obtained from experiment with theoretical structural relaxation for monolayer α-$RuCl_3$ 86

6.1 Summary of lowest energy Raman active phonons and their computed $q = 0$ spin-phonon couplings. For the doubly degenerate E_g modes, the phonons have been symmetrized into horizontal (H) and vertical (V) polarizations. See Fig. 6.4(g) for definition of bonds. 139

List of Abbreviations

AFM	Antiferromagnetic
CEF	Crystalline Electric Field
CFS	Crystal Field Splitting
dCEHs	des Cloizeaux effective Hamiltonians
DFT	Density Functional Theory
DOS	Density of States
EPW	Electron-phonon Wannier
ESR	Electron Spin Resonance
FIR	Far-infared
FM	Ferromagnetic
FPLO	Full-potential local-orbital
FTIR	Fourier-Transform Infrared
GGA	Generalized Gradient Approximation
gHK	generalized-Heisenberg–Kitaev
GHz	Gigahertz
hBN	Hexagonal Boron Nitride
IETS	Inelastic Electron Tunnelling Spectroscopy
INS	Inelastic Neutron Scattering
IR	Infra-red
LL	Landau-Lifshitz
LSWT	Linear Spin Wave Theory
NN	Nearest Neighbor

PAW	Projector Augmented Wave
PBE	Perdew–Burke–Ernzerhof
PBEsol	Revised PBE for solids
QSL	Quantum spin liquid
RMM-DIIS	Residual Minimization Method with Direct Inversion in the Iterative Subspace
SCF	Self-Consistent Cycle
SIA	Single Ion Anisotropy
SOC	Spin Orbit Coupling
SPC	Spin-Phonon Coupling
THE	Thermal Hall Effect
THz	Terahertz
TNN	Third Nearest Neighbor
VASP	Vienna Ab Initio Simulation Package
vdW	van der Waals
XRD	X-ray Diffraction
ZZ	Zigzag

Abstract

The interactions and dynamics of different quasi-particles in magnetic materials have risen to the forefront of both fundamental and applied quantum materials research. Especially in quantum magnets, these many-body effects are complex and enriched due to strong spin-orbit interactions. This thesis reviews the theory of spin-phonon interaction and their consequences for experiments such as the thermal Hall effect in magnetic insulators from the first principles point of view. We first develop the generic approach to compute spin-phonon couplings for a material of interest and apply it to study a strongly correlated magnetic insulator. We demonstrate that strong spin-orbit coupling can give rise to finite phonon thermal Hall effect in magnetic insulator by introducing chirality into phonons through spin-phonon interactions. Alongside, the effects of structural distortions and disorder on the magnetic response are studied in the context of magnetic insulators. With honeycomb structure, we find that the spin Hamiltonian is sensitive to the details of structural perturbations and can significantly enhance and modify magnetic response. The importance of spin-orbit coupling on the ground state and excitations of $3d$ transition-metal-based compound with unquenched orbital moments is also discussed.

Chapter 1

Magnestism

1.1 Magnetism and Quantum Mechanics

In this section, we will attempt to give a brief account of the key historical developments and understanding of the modern theory of magnetism. There are several excellent textbooks [1–3] and lecture notes [4–6] that discuss this subject in great detail. We will extensively use these resources as a reference for this thesis. For the sake of completeness, we will introduce some important concepts here and refer readers to textbooks for the exhaustive discussion of this topic.

The series of development in the early twentieth century (1911-1930) set the foundation for the modern theory of magnetism. Following the Rutherford's scattering experiment (1911), Bohr had proposed the quantized atomic model (1913), and the structure of atom was emerging with greater clarity. In 1922, Stern and Gerlach performed their famous experiment of passing silver atoms through inhomogeneous magnetic field and presented an irrefutable evidence of the quantization of angular momentum [7]. A few years later, Goudsmit and Uhlenbeck (1925) demonstrated that electron must have an intrinsic spin angular momentum of $\frac{\hbar}{2}$, in addition to it's orbital angular momentum [8]. The associated magnetic moment was, however, twice the expected value for a charge particle with a given angular momentum. This discrepancy was later resolved by Dirac (1928) by introducing relativistic quantum theory for spin $\frac{1}{2}$ particle [9]. In this framework, solutions to the Dirac equation are four component spinor matrices that are built from Pauli matrices.

By the time of sixth Solvay conference (October, 1930), Le magnétisme, a coherent theoretical picture of magnetism had largely emerged. At this point, the statistics to understand bosons (1924-25) [10] and fermions (1926) [11, 12] had already been developed. With the Schrodinger wave equation and Pauli's exclusion principle (1925) [13] already in picture, Slater had constructed single determinant (1929) to describe wavefunction of multi-fermionic system that obeys proper symmetry of electron wavefunction [14]. Alongside, Heisenberg and Dirac (1928-29) were able to explain ferromagnetism in terms of exchange interactions [15, 16] by exploiting the concept of overlap of the electronic wavefunction and Pauli's exclusion principle, an idea that was initially proposed by Heitler and London (1927) to describe a chemical bonding in hydrogen molecule [17]. Not long afterwards, Bloch (1930) proposed spin waves (magnons) as the elementary excitations in ferromagnetic materials [18].

The theory of magnetism associated with the free electrons gas was also relatively well established by 1930. The Pauli's paramagnetism [19], which is accounts for the weak interaction of intrinsic spin of electrons to external magnetic field, and Landau diamagnetism [20], which is due to the quantization of orbital motion of electrons under an external magnetic field (Landau levels) were able to resolve the puzzling experimental observation in metals at the time. The free electrons in metals were supposed to follow Curie's law but susceptibility of free electrons in metals was almost temperature independent. Pauli showed that because of the Fermi-Dirac statistics, only electrons near the Fermi level response to the external field making susceptibility independent of temperature in these materials. Landau demonstrated that quantization and degeneracy of orbits spontaneously led to non-zero, negative susceptibility in metals, in contrast to the prediction of classical theory. The same year, it was observed experimentally that strong magnetic field at low temperatures leads to oscillation in magnetic susceptibility of metal due to the passing of Landau levels through Fermi surface, now known as De Haas–Van Alphen effect [21].

Despite these advances, there were still no existing theories to explain why Iron, Cobalt, Nickel were ferromagnetic and has non-integer spin moments. Though Heisenberg theory of ferromagnetism was good for localized spin, it could not explain the non-integer magnetic moments of these metals. The problem was attacked by John Slater and Edmund Stoner in 1930s, which led to the development of band theory for ferromagnetic metals [22–26].

The band theory, however, hit the wall when two Dutch scientist de Boer and Verwey reported a puzzling observation that many metal oxides [27] with incompletely filled $3d$ bands were found to be insulators. Using NiO as a model, the importance of the role of electron interactions was established by Mott [28], and theoretical explanation was later given by Hubbard [29]. The mechanism through which these type of materials can exhibit magnetism, widely known as superexchange interaction, was first pointed out by Kramers [30] and was refined by Anderson [31]. Later, Goodenough and Kanamori systematically studied this mechanism [32–34] and laid out the set of semi-empirical rules to determine the sign and strength of superexchange interaction based on the symmetry, and geometry of ligand-metal ion orbitals, now known as Goodenough-Kanamori rules.

In 1932, when Néel proposed antiferromagnetism to describe the temperature independent paramagnetic susceptibility of Chromium and Manganese [35], the idea was widely contested because such alternating spin order was thought to violate quantum mechanics [36]. In fact, Hans Bethe had already calculated the exact energy eigenstate of 1 D Heisenberg antiferromagnetic chain [37] and later Hulthén had shown that the the groundstate of such arrangement is the chain of spin singlet not the up-down order as proposed by Néel [38]. However, neutron scattering measurements on different metallic oxides presented a conclusive evidence that Néel type antiferromagnetic groundstate with finite long range order is possible [39]. The next year (1952), Anderson presented a theoretical explanation on why antiferromagnetic order can survive in two or higher dimensions [40]. In 1973, his work on antiferromagnetism led him to suggest that ground state of spin $\frac{1}{2}$ Heisenberg antiferromagnet on a triangular lattice could realize a resonating valence bond state [41], which, although later shown to be incorrect, laid the groundwork for frustration and quantum spin liquid. This new state of matter is a highly entangled quantum superposition of different spin configuration and is of particular interest to us, of which we will have more to say in the following chapters.

While it is tempting to list the individual contribution and attempt to recount the historical developments, a comprehensive review would take us too far afield. Hence, we shall refrain ourself from such digression and return back to our original agenda of introducing important concepts that is required to understand our research.

In the next sections, we introduce the Hamiltonians describing magnetic degrees of freedom and their interactions.

1.2 Electron Spin and Magnetic Moment

Let us consider an electron of mass m with charge e is rotating in a circular orbit. Then from classical mechanics, the magnetic moment of electron due to this orbital motion takes the form

$$\boldsymbol{\mu}_L = -\frac{e}{2m}\boldsymbol{L} \tag{1.1}$$

Where $\boldsymbol{\mu}_L$ is the magnetic moment due to orbital angular momentum $\boldsymbol{L}$. This is true for quantum mechanical system as well. It turns out that magnetic moment due to intrinsic spin, which has no classical analogue, is twice the value of orbital magnetic moment

$$\boldsymbol{\mu}_S = -\frac{e}{m}\boldsymbol{S} \tag{1.2}$$

The total angular momentum and its associated magnetic moment in an atom is due to the combined effect of spin and orbital contribution of several electrons, and is determined by quantum mechanics. Expressing this in terms of Landé g-factor, we get,

$$\boldsymbol{\mu} = -\mathrm{g}\left(\frac{e}{2m}\right)\boldsymbol{J} \tag{1.3}$$

We note that the direction of magnetic moment is opposite to the direction of angular momentum. The Landé g-factor takes the value of 1 for pure orbital moment and 2 for pure spin moment (from Dirac equation) giving back equation 1.1 and 1.2 respectively. It can be shown that

$$\mathrm{g} = 1 + \frac{J(J+1) + S(S+1) - L(L+1)}{2J(J+1)} \tag{1.4}$$

This is appropriate for free ions in space, but in the crystal, g-factor becomes a tensor quantity. The spin orbit coupling and local crystal symmetry give rise to anisotropy in the

g-factor, and it becomes a second rank tensor

$$\mathbf{g} = \begin{pmatrix} g_{xx} & g_{xy} & g_{xz} \\ g_{yx} & g_{yy} & g_{yz} \\ g_{zx} & g_{zy} & g_{zz} \end{pmatrix} \tag{1.5}$$

Let us express equation 1.3 in the terms of Bohr magneton,

$$\boldsymbol{\mu} = -\,\mathbf{g}\,\mu_B\,\frac{\boldsymbol{J}}{\hbar} \tag{1.6}$$

where $\mu_B = \frac{e\hbar}{2m}$ is a physical constant called Bohr magneton.

When an atom with a magnetic moment $\boldsymbol{\mu}$ is placed in an external magnetic field $\boldsymbol{B}$, the interaction energy can be written as

$$\hat{\mathcal{H}}_{\text{zeeman}} = -\boldsymbol{\mu} \cdot \boldsymbol{B} \tag{1.7}$$

If the magnetic field is along z-direction, then using equation 1.6, we have

$$\hat{\mathcal{H}}_{\text{zeeman}} = \mathbf{g}\,\mu_B\,B\,\frac{\hat{J}_z}{\hbar} \tag{1.8}$$

It is evident that when an atom is placed in an external magnetic field, the the energy of the atom is modified and is proportional to the field and $\langle \hat{J}_z \rangle$. According to quantum mechanics, $\frac{\langle \hat{J}_z \rangle}{\hbar}$ can take values from j, $(j-1)$, $(j-2)$, $\ldots$, $(-j+1)$, $-j$. This phenomena of splitting of energy of an atomic system into $2j+1$ levels, under a magnetic field is called Zeeman effect.

1.3 Factors Determining Local Degrees of Freedom

In this section, we will briefly discuss the effect of crystal environment on magnetic ions. When an isolated ion is placed in a crystal environment, the spherical symmetry is broken and new local symmetry emerge, which strongly modifies the spatial motion of electrons. Typically, energy levels of an atom in transition-metal compounds is heavily influenced by lattice environment due to strong hybridization of outer-shell d orbitals with the surround-

ings. We discuss the scenario in which all electrons are localized on the transition metal ion, as is the case in strongly correlated magnetic insulators.

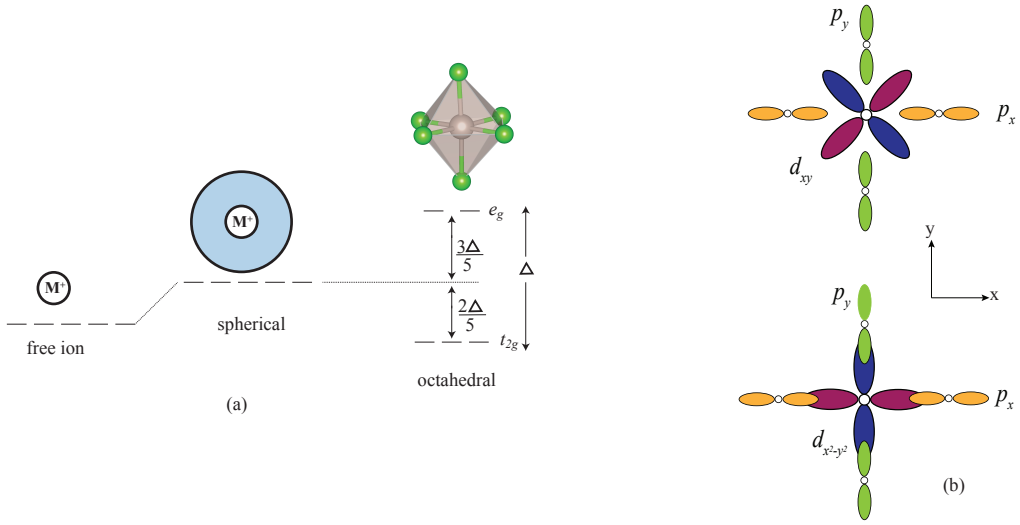

Figure 1.1: Schematic illustration of crystal field splitting. (a) When a free ion is placed in a uniform distribution of negative charge, the energy of d orbitals rises, but when it is placed in an octahedral environment, the degeneracy of d orbitals is lifted as shown in figure. Δ is the crystal field splitting. (b) Figure showing $d_{x^2-y^2}$ orbitals hybridizing strongly to p orbitals compared to d_{xy} orbitals.

1.3.1 Crystal Field Splitting

In transition metal compounds, the crystal field splitting is a consequence of electrostatic repulsion between electrons in d orbitals of metal ion and the surrounding ligands. The nature of splitting is determined by the symmetry of the crystal and surrounding ligand field. In octahedral crystal environment, this results in the splitting of five degenerate d orbitals into lower-lying t_{2g} states (d_{xy}, d_{yz}, d_{xz} orbitals) and higher-lying e_g states ($d_{x^2-y^2}$, d_{z^2} orbitals). This is because depending on the spatial orientation and geometry of the d orbitals and ligands, electrostatic repulsion and hybridization can be stronger or weaker. For example, d_{xy} orbitals hybridize weakly to p orbitals of the ligands compared to $d_{x^2-y^2}$ orbitals. As a consequence, d_{xy} orbital has lower energy compared to $d_{x^2-y^2}$ orbital.

At this point, the electronic wavefunction is largely governed by Hund's coupling. The competition between the energy cost of placing an electron in already singly occupied d orbitals and crystal field energy determines whether the system prefers high-spin or low-

spin state. We will discuss both scenarios by giving example of two compounds that we have studied and will be discussed in detail in later chapters.

In α-$RuCl_3$, each Ruthenium ion sits in an octahedral cage of six Chlorine atoms. With Ru^{3+} state, the electronic configuration is d^5 with five electrons in d orbitals. Due to strong crystal field splitting, the energy gap between e_g and t_{2g} orbitals is large ($\approx$ 2 eV). Therefore, it is energetically preferable to populate electrons in t_{2g} states first before filling the e_g states resulting in $S = \frac{1}{2}$ state. This is an example of low-spin state.

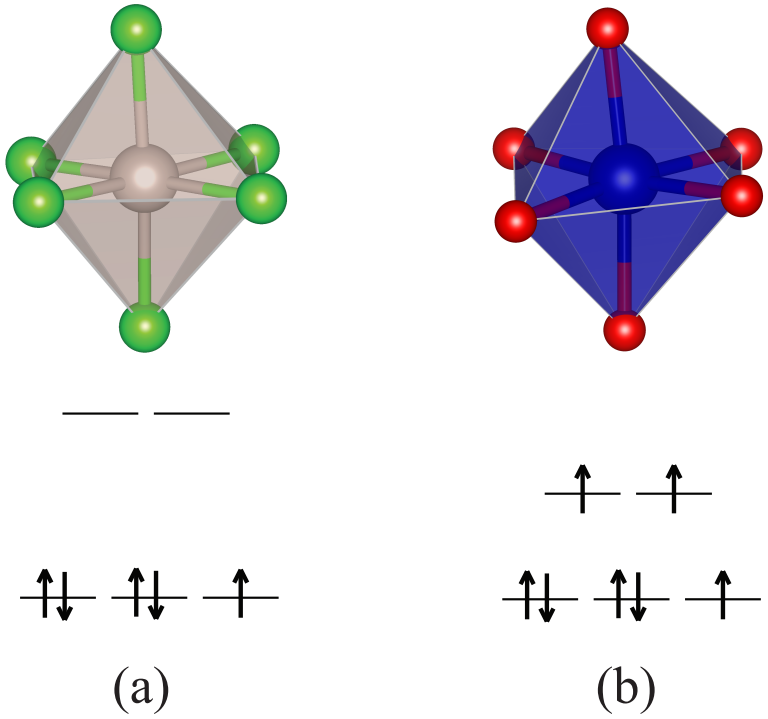

Figure 1.2: Schematic representation of (a) low spin state in α-$RuCl_3$ due to strong crystal field splitting (b) high-spin state in $Na_2Co_2TeO_6$ due to relatively weak crystal field splitting.

$Na_2Co_2TeO_6$ is an example of a compound, where the high-spin state is preferred. In this case, each Cobalt ion is surrounded by six oxygen atoms forming an octahedral geometry. In the Co^{2+} state, it has d^7 configuration with seven electrons. Due to the weak ligand-field of oxygen atoms, the energy gap is small, and hence it is favorable to fill higher-lying e_g states before we doubly populate the electrons in the t_{2g} states. The results for both cases are illustrated in Fig. 1.2.

Single-ion Anisotropy and Kramer's Theorem

In the presence of spin-orbit coupling, a spin in the crystalline system can interact with the crystal field, favoring spin alignment along specific crystalline direction. The Hamiltonian that describe such anisotropy can be written as [3]

$$\begin{aligned}\hat{\mathcal{H}}_{\text{SIA}} &= D\hat{S}_z^2 + E(\hat{S}_x^2 - \hat{S}_y^2) \\ &= D\hat{S}_z^2 + \frac{E}{2}(\hat{S_+^2} - \hat{S_-^2})\end{aligned} \tag{1.9}$$

where D and E define uniaxial and biaxial anisotropies. Here, $D < 0$ favors easy axis anisotropy while $D > 0$ favors easy plane anisotropy. The $(2S{+}1)$ fold degeneracy can be lifted by the anisotropy Hamiltonian. For integer and half odd-integer spin, we have

$$S_z\,(\text{Integer}) = \pm S,\, \pm(S-1),\, \cdots \pm 1,\, 0 \tag{1.10}$$

$$S_z\,(\text{half odd integer}) = \pm S,\, \pm(S-1),\, \cdots \pm \frac{1}{2} \tag{1.11}$$

The second term in equation 1.9 acts as a perturbation and connects states with $\Delta S_z = \pm 2$. For half-odd integer spin, $\Delta S_z = \pm\,\text{odd integer}$, and therefore E term can not completely lift the degeneracy of these states. This is known as Kramer's theorem, which states that in systems with an odd number of fermions and time reversal invariant Hamiltonian, the degeneracy can not be completely lifted for any state. The states are known as Kramer's doublet. For integer spin, the doubly degenerate states produced by first term are split by second term.

1.3.2 Spin-Orbit Coupling

Spin-orbit coupling (SOC) can be defined as the relativistic quantum mechanical interaction between intrinsic spin **S** and orbital **L** part of electron's wavefunction. In many cases, this effect can be treated as a perturbation on well defined **L** and **S** states. In this regime, **L** and **S** are no longer a good quantum numbers. However, total angular momentum, $\mathbf{J} = \mathbf{L} + \mathbf{S}$, is a conserved quantity. Also, $\mathbf{L}^2 = L(L+1)$ and $\mathbf{S}^2 = S(S+1)$ are separately conserved.

The Hamiltonian takes the form

$$\mathcal{H}_{soc} = \lambda \mathbf{L} \cdot \mathbf{S} \tag{1.12}$$

Expanding $\mathbf{J}^2 = (\mathbf{L} + \mathbf{S})^2$, and expressing in terms of $\mathbf{L} \cdot \mathbf{S}$, equation 1.12 can be written as,

$$\mathcal{H}_{soc} = \frac{\lambda}{2} \left[\mathbf{J}^2 - \mathbf{L}^2 - \mathbf{S}^2\right] \tag{1.13}$$

$$= \frac{\lambda}{2} \left[J(J+1) - L(L+1) - S(S+1)\right] \tag{1.14}$$

Here, J can take the value from $|L - S|$ to $L + S$. The initial $(2S + 1)(2L + 1)$ degeneracy is lifted due to spin-orbit coupling and sorted according to J value. Each J has $(2J + 1)$ degeneracy, which can be lifted by the application of magnetic field.

Let us make it concrete by taking an example of α-$RuCl_3$ and $Na_2Co_2TeO_6$. From Fig. 1.2, we see that α-$RuCl_3$ has d^5 configuration with $S = \frac{1}{2}$ and $L_{\text{eff}} = 1$. Without SOC, this configuration has $(2S + 1)(2L + 1) = 6$ degenerate multiplets. In the presence of SOC, J_{eff} (now onward written as J) takes the value from $|L - S| = \frac{1}{2}$ to $L + S = \frac{3}{2}$. The degeneracy is lifted, and we have the $J = \frac{3}{2}$ states with $(2J + 1) = 4$ degenerate states and $J = \frac{1}{2}$ states with 2 degenerate states. Similar arguments follow for d^7 electronic configuration of $Na_2Co_2TeO_6$. With $S = \frac{3}{2}$ and $L_{\text{eff}} = 1$, J can take values from $|L - S| = \frac{1}{2}$ to $L + S = \frac{5}{2}$ with the degeneracy of $(2J + 1)$ for each J. Here, we expand states in $|J, m_J\rangle$ basis into $|S, m_S; L_{\text{eff}}, m_L\rangle$ basis.

For α-$RuCl_3$, the $J = \frac{3}{2}$ state are:

$$\begin{aligned}
\left|J = \frac{3}{2}, m_J = \frac{3}{2}\right\rangle &= \left|\frac{1}{2}, \frac{1}{2}; 1, 1\right\rangle \\
\left|J = \frac{3}{2}, m_J = \frac{1}{2}\right\rangle &= \sqrt{\frac{2}{3}}\left|\frac{1}{2}, \frac{1}{2}; 1, 0\right\rangle + \frac{1}{\sqrt{3}}\left|\frac{1}{2}, -\frac{1}{2}; 1, 1\right\rangle \\
\left|J = \frac{3}{2}, m_J = -\frac{1}{2}\right\rangle &= \frac{1}{\sqrt{3}}\left|\frac{1}{2}, \frac{1}{2}; 1, -1\right\rangle + \sqrt{\frac{2}{3}}\left|\frac{1}{2}, -\frac{1}{2}; 1, 0\right\rangle \\
\left|J = \frac{3}{2}, m_J = -\frac{3}{2}\right\rangle &= \left|\frac{1}{2}, -\frac{1}{2}; 1, -1\right\rangle
\end{aligned} \tag{1.15}$$

The $J = \frac{1}{2}$ state are:

$$\begin{aligned}\left|J = \frac{1}{2}, m_J = \frac{1}{2}\right\rangle &= -\frac{1}{\sqrt{3}}\left|\frac{1}{2}, \frac{1}{2}; 1, 0\right\rangle + \sqrt{\frac{2}{3}}\left|\frac{1}{2}, -\frac{1}{2}; 1, 1\right\rangle \\ \left|J = \frac{1}{2}, m_J = -\frac{1}{2}\right\rangle &= -\sqrt{\frac{2}{3}}\left|\frac{1}{2}, \frac{1}{2}; 1, -1\right\rangle + \frac{1}{\sqrt{3}}\left|\frac{1}{2}, -\frac{1}{2}; 1, 0\right\rangle\end{aligned} \tag{1.16}$$

Similarly, for $Na_2Co_2TeO_6$, the $J = \frac{5}{2}$ states are:

$$\begin{aligned}\left|J = \frac{5}{2}, m_J = \frac{5}{2}\right\rangle &= \left|\frac{3}{2}, \frac{3}{2}; 1, 1\right\rangle \\ \left|J = \frac{5}{2}, m_J = \frac{3}{2}\right\rangle &= \sqrt{\frac{2}{5}}\left|\frac{3}{2}, \frac{3}{2}; 1, 0\right\rangle + \sqrt{\frac{3}{5}}\left|\frac{3}{2}, \frac{1}{2}; 1, 1\right\rangle \\ \left|J = \frac{5}{2}, m_J = \frac{1}{2}\right\rangle &= \frac{1}{\sqrt{10}}\left|\frac{3}{2}, \frac{3}{2}; 1, -1\right\rangle + \sqrt{\frac{3}{5}}\left|\frac{3}{2}, \frac{1}{2}; 1, 0\right\rangle + \sqrt{\frac{3}{10}}\left|\frac{3}{2}, -\frac{1}{2}; 1, 1\right\rangle \\ \left|J = \frac{5}{2}, m_J = -\frac{1}{2}\right\rangle &= \sqrt{\frac{3}{10}}\left|\frac{3}{2}, \frac{1}{2}; 1, -1\right\rangle + \sqrt{\frac{3}{5}}\left|\frac{3}{2}, -\frac{1}{2}; 1, 0\right\rangle + \frac{1}{\sqrt{10}}\left|\frac{3}{2}, -\frac{3}{2}; 1, 1\right\rangle \\ \left|J = \frac{5}{2}, m_J = -\frac{3}{2}\right\rangle &= \sqrt{\frac{3}{5}}\left|\frac{3}{2}, -\frac{1}{2}; 1, -1\right\rangle + \sqrt{\frac{2}{5}}\left|\frac{3}{2}, -\frac{3}{2}; 1, 0\right\rangle \\ \left|J = \frac{5}{2}, m_J = -\frac{5}{2}\right\rangle &= \left|\frac{3}{2}, -\frac{3}{2}; 1, -1\right\rangle\end{aligned} \tag{1.17}$$

The $J = \frac{3}{2}$ states are:

$$\begin{aligned}\left|J = \frac{3}{2}, m_J = \frac{3}{2}\right\rangle &= -\sqrt{\frac{3}{5}}\left|\frac{3}{2}, \frac{3}{2}; 1, 0\right\rangle + \sqrt{\frac{2}{5}}\left|\frac{3}{2}, \frac{1}{2}; 1, 1\right\rangle \\ \left|J = \frac{3}{2}, m_J = \frac{1}{2}\right\rangle &= -\sqrt{\frac{2}{5}}\left|\frac{3}{2}, \frac{3}{2}; 1, -1\right\rangle - \frac{1}{\sqrt{15}}\left|\frac{3}{2}, \frac{1}{2}; 1, 0\right\rangle + 2\sqrt{\frac{2}{15}}\left|\frac{3}{2}, -\frac{1}{2}; 1, 1\right\rangle \\ \left|J = \frac{3}{2}, m_J = -\frac{1}{2}\right\rangle &= -2\sqrt{\frac{2}{15}}\left|\frac{3}{2}, \frac{1}{2}; 1, -1\right\rangle + \frac{1}{\sqrt{15}}\left|\frac{3}{2}, -\frac{1}{2}; 1, 0\right\rangle + \sqrt{\frac{2}{5}}\left|\frac{3}{2}, -\frac{3}{2}; 1, 1\right\rangle \\ \left|J = \frac{3}{2}, m_J = -\frac{3}{2}\right\rangle &= -\sqrt{\frac{2}{5}}\left|\frac{3}{2}, -\frac{1}{2}; 1, -1\right\rangle + \sqrt{\frac{3}{5}}\left|\frac{3}{2}, -\frac{3}{2}; 1, 0\right\rangle\end{aligned} \tag{1.18}$$

The $J = \frac{1}{2}$ states are:

$$\begin{aligned}\left|J = \frac{1}{2}, m_J = \frac{1}{2}\right\rangle &= \frac{1}{\sqrt{2}}\left|\frac{3}{2}, \frac{3}{2}; 1, -1\right\rangle - \frac{1}{\sqrt{3}}\left|\frac{3}{2}, \frac{1}{2}; 1, 0\right\rangle + \frac{1}{\sqrt{6}}\left|\frac{3}{2}, -\frac{1}{2}; 1, 1\right\rangle \\ \left|J = \frac{1}{2}, m_J = -\frac{1}{2}\right\rangle &= \frac{1}{\sqrt{6}}\left|\frac{3}{2}, \frac{1}{2}; 1, -1\right\rangle - \frac{1}{\sqrt{3}}\left|\frac{3}{2}, -\frac{1}{2}; 1, 0\right\rangle + \frac{1}{\sqrt{2}}\left|\frac{3}{2}, -\frac{3}{2}; 1, 1\right\rangle\end{aligned} \tag{1.19}$$

In each case, it is nominally the $J = \frac{1}{2}$ states that span the low energy magnetic degrees of

freedom, with their specific spin-orbital composition affecting the coupling between them and their g-tensor. In general, SOC is in competition with symmetry lowering distortions.

1.3.3 Jahn–Teller Effect

In a real system, spin orbit coupling effects can be suppressed by a crystal field distortions that spontaneously break the symmetry of the crystal, which further lifts the degeneracy of the energy states. This is very common in the octahedral complexes, and the phenomenon is known as Jahn–Teller effect. This happens because very often such distortion reduces the overall energy of the system. The nature of splitting depends on the type of distortion and whether the ligands move away (elongation) or towards (compression) the metal center. Following Ref [42], we present the case of trigonal and tetragonal distortion of octahedral geometry.

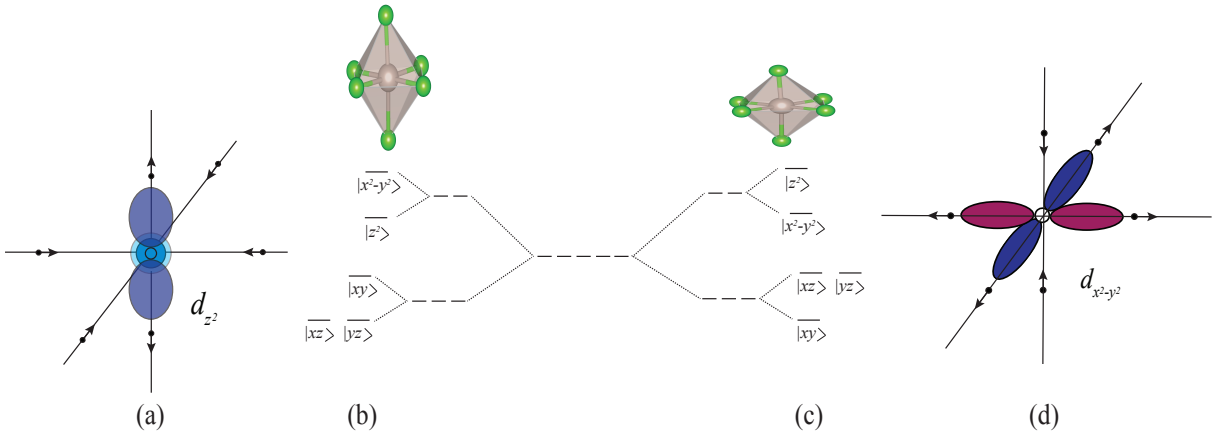

Figure 1.3: Schematic diagram of (a) d_{z^2} orbital in octahedral environment under tetragonal elongation. Splitting of d orbitals during tetragonal (b) elongation and (c) contraction (d) $d_{x^2-y^2}$ orbital subject to tetragonal contraction.

Let us consider the case of tetrahedral elongation of octahedral geometry as shown in Fig. 1.3 (a) and (b). Due to the elongation in z direction, ligands along this axis moves further away from the metal ion, while the ligands in the x and y direction comes closer. This results in lifting the degeneracy of e_g states, where d_{z^2} orbital is stabilized and $d_{x^2-y^2}$ is destabilized relative to the original energy level. The same reasoning can be extended to tetragonal compression, which leads to the opposite conclusion. The ligands in the x and y axes move away from the metal ion reducing the energy of $d_{x^2-y^2}$ compared to d_{z^2}. In

other words, the ligands p orbitals along the z axis hybridize strongly with d_{z^2} and raise its energy compared to weakly hybridizing in-plane $d_{x^2-y^2}$ orbitals. The splitting of t_{2g} orbitals can be understood with similar arguments. It is insightful to note that t_{2g} and e_g splitting follow the same basic rules. For example, when $d_{x^2-y^2}$ is higher in energy in e_g states, d_{xy} would be higher in t_{2g} states. If d_{z^2} is higher in energy in e_g states, the orbitals with z-component, d_{xz} and d_{yz} in t_{2g} states would be destabilized.

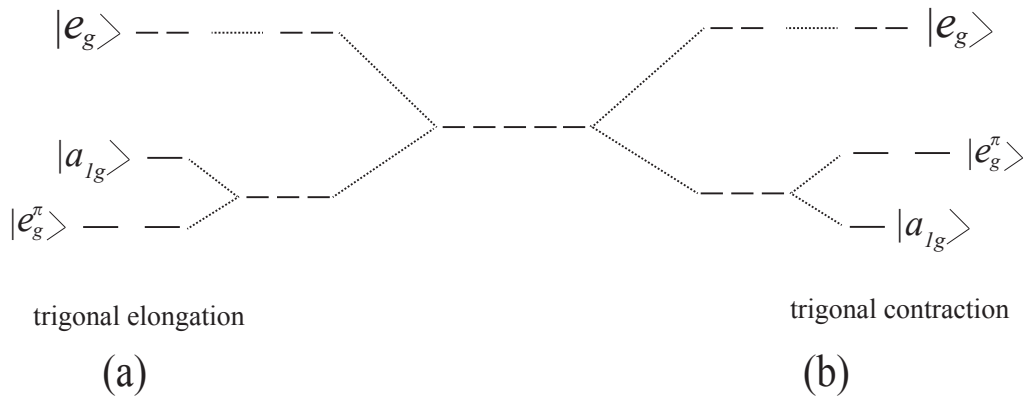

Figure 1.4: Schematic illustration of orbital splitting under (a) trigonal elongation and (b) trigonal compression.

Another type of distortion that is very common in octahedral geometry is trigonal distortion. In this case, the distortion is along one of the [111] axes. It leads to rather complicated mixing of different orbitals forming e_g^π and a_{1g} states at t_{2g} level, while leaving the e_g states unchanged (see Fig. 1.4). The a_{1g} state is essential analogous to d_{z^2} in the local coordinate system with the lobes pointing along z' direction, where z' represents the axis along the trigonal distortion. The expression for e_g^π and a_{1g} states can be written as,

$$|a_{1g}\rangle = \frac{1}{\sqrt{3}}\left(|xy\rangle + |yz\rangle + |xz\rangle\right) \tag{1.20}$$

$$|e^\pi_{1g\pm}\rangle = \pm\frac{1}{\sqrt{3}}\left(|xy\rangle + e^{\pm\frac{i2\pi}{3}}|xz\rangle + e^{\mp\frac{i2\pi}{3}}|yz\rangle\right) \tag{1.21}$$

To model such effect, we write crystal field Hamiltonian in the second quantization formal-

ism [43],

$$\mathcal{H}_{\mathrm{CFS}} = \sum_{\sigma} \mathbf{c}^{\dagger}_{i,\sigma}\, \mathbb{D}\, \mathbf{c}_{i,\sigma} \tag{1.22}$$

where σ can take the value $\uparrow$ or $\downarrow$. Here, $\mathbf{c}^{\dagger}_{i,\sigma}$ creates an electron in a particular d orbitals at site i, and can be expanded as,

$$\mathbf{c}^{\dagger}_{i,\sigma} = \left(c^{\dagger}_{i,yz,\sigma},\ c^{\dagger}_{i,xz,\sigma},\ c^{\dagger}_{i,xy,\sigma},\ c^{\dagger}_{i,z^2,\sigma}\ c^{\dagger}_{i,x^2-y^2,\sigma} \right) \tag{1.23}$$

For a given local coordinate system, $\mathbb{D}$ can take the form,

$$\begin{pmatrix} 0 & \Delta_2 & \Delta_2 & 0 & 0 \\ \Delta_2 & 0 & \Delta_2 & 0 & 0 \\ \Delta_2 & \Delta_2 & 0 & 0 & 0 \\ 0 & 0 & 0 & \Delta_1 & 0 \\ 0 & 0 & 0 & 0 & \Delta_1 \end{pmatrix} \tag{1.24}$$

where Δ_1 and Δ_2 represent e_g-t_{2g} splitting and trigonal distortion respectively. The details of crystal field environment, Coulomb interactions and nature of distortion (elongation or compression) ultimately determine the sign of Δ_2.

As a consequence, the specific composition of the local moments are affected by the details of spin, orbital, charge and lattice degrees of freedom.

1.4 Magnetic Couplings

1.4.1 Dipole-Dipole Interaction

We have demonstrated that electrons in the solids have an intrinsic magnetic moments. These dipoles can interact with each other through the dipolar interaction. Now we want to ask a question, "Is this interaction sufficient to explain the observed magnetic ordering in magnets?" The field generated by dipole-dipole interaction has the form

$$E_{\mathrm{dd}} = \frac{\mu_0}{4\pi r^3}\Big[\boldsymbol{\mu}_1 \cdot \boldsymbol{\mu}_2 - \frac{3(\boldsymbol{\mu}_1 \cdot \mathbf{r})(\boldsymbol{\mu}_2 \cdot \mathbf{r})}{r^2}\Big] \tag{1.25}$$

where $\boldsymbol{\mu}_1$ and $\boldsymbol{\mu}_2$ are two dipoles with separation $\boldsymbol{r}$. To get the sense of magnitude of dipole-dipole interaction, let us consider two dipoles, each of magnitude $1\,\mu_B$ that are separated by 1 Å, and estimate the energy

$$E_{\rm dd} \sim \frac{\mu_0}{4\pi r^3}\,\mu^2 = \frac{4\pi \times 10^{-7}}{4\pi\,(1\times 10^{-10})^3}\,(9.274\times 10^{-24})^2 \tag{1.26}$$

$$\approx 8.6\times 10^{-24}\ \text{J} \tag{1.27}$$

$$T \sim \frac{E_{\rm dd}}{k_B} = \frac{8.6\times 10^{-24}}{1.380649\times 10^{-23}} \approx 0.62\ \text{K} \tag{1.28}$$

However, it is a common knowledge that many magnetic materials order at much higher temperature. For example, Iron can be ferromagnetic at ≈ 1043 K. Hence we conclude that dipolar interaction is too weak to explain the magnetic ordering in solids, except in some specific cases, and hence we must look elsewhere if we are to understand this phenomenon.

1.4.2 Exchange Interaction

The exchange interaction is a consequence of electrostatic repulsion of electrons and Pauli's exclusion principle. This interaction can influence the intra-atomic as well as inter-atomic spin alignment in solids. The intra-atomic contribution is responsible for the spin alignment in the unfilled atomic shells, and forms the basis of Hund's rules whereas the inter-atomic interactions are responsible for the relative spin alignment in neighboring atoms and determine the nature of magnetic order in materials. An extensive second quantization formalism of this topic can be found in Ref. [2], while an introductory discussion is given in Ref. [1].

Let us consider a simple case of two electrons in space with states $\phi_a(\boldsymbol{r}_1)$ and $\phi_b(\boldsymbol{r}_2)$ respectively. We now want to construct a wavefunction obeying exchange symmetry when the electrons swap their position. We note that the combined electronic wavefunction in space and spin should be anti-symmetric. Then, the singlet and triplet state can be written as

$$\psi_S = \frac{1}{\sqrt{2}}\left[\phi_a(\boldsymbol{r}_1)\phi_b(\boldsymbol{r}_2) + \phi_a(\boldsymbol{r}_2)\phi_b(\boldsymbol{r}_1)\right]\chi_S \tag{1.29}$$

$$\psi_T = \frac{1}{\sqrt{2}} \left[\phi_a(\boldsymbol{r}_1)\phi_b(\boldsymbol{r}_2) - \phi_a(\boldsymbol{r}_2)\phi_b(\boldsymbol{r}_1)\right] \chi_T \tag{1.30}$$

where χ_S and χ_T are the spin part of singlet and triplet state respectively. For the singlet state, the spatial part is symmetric and the spin part is antisymmetric thereby ensuring the total wavefunction is antisymmetric. A similar argument follows for the triplet state, where the spin and spatial part are symmetric and antisymmetric respectively. The experession for the energies of these two states are,

$$E_S = \int \psi_S^* \, \mathcal{H} \, \psi_S \, d\boldsymbol{r}_1 \, d\boldsymbol{r}_2 \tag{1.31}$$

$$E_T = \int \psi_T^* \, \mathcal{H} \, \psi_T \, d\boldsymbol{r}_1 \, d\boldsymbol{r}_2 \tag{1.32}$$

The exchange energy is evaluated by taking the difference of energies between singlet and triplet states.

$$E_S - E_T = 2 \int \phi_a^*(\boldsymbol{r}_1) \, \phi_b^*(\boldsymbol{r}_2) \mathcal{H} \, \phi_a(\boldsymbol{r}_2) \, \phi_b(\boldsymbol{r}_1) \, d\boldsymbol{r}_1 \, d\boldsymbol{r}_2 \tag{1.33}$$

For spin $\frac{1}{2}$ particles, following Ref [1], the Hamiltonian can be written in terms of effective Hamiltonian as,

$$\mathcal{H} = \frac{1}{4}(E_S + 3E_T) - (E_S - E_T) \, \mathbf{S_1} \cdot \mathbf{S_2} \tag{1.34}$$

The first term in equation 1.34 is constant, however, the spin dependent second term is of our interest. Let us define the effective spin Hamiltonian in terms of this spin dependent term.

$$\mathcal{H}_{\text{spin}} = -J \, \mathbf{S}_1 \cdot \mathbf{S}_2 \tag{1.35}$$

where

$$J = E_S - E_T \tag{1.36}$$

is a scalar exchange constant. Equation 1.35 can be generalized to many body system as

$$\mathcal{H} = \sum_{\langle i,j \rangle} J_{ij}\, \mathbf{S}_i \cdot \mathbf{S}_j \tag{1.37}$$

Here, we have absorbed the negative sign in J. The sign of J determines whether the spin energetically prefer to align in the same or opposite direction. When J is positive, the spins favor antiparallel alignment, whereas negative J favors parallel spin. The scale of exchange interaction in strong ferromagnet can be on the order of 10^3 K, and is responsible for magnetic ordering. The Hamiltonian described by equation 1.37 is famously known as Heisenberg model. Now, we will briefly discuss two exchange mechanism that are relevant for our study.

1.4.3 Superexchange Interactions

In magnetic insulators, it turns out that very often the direct exchange interaction, which is due to the direct overlap of electronic wavefunctions between neighboring ions, is unlikely to be the dominant mechanism in determining the magnetic properties. In these compounds, in many cases, the metal ions are separated by large non-magnetic anions such as the O and Cl atoms forming the $RuCl_6$ and CoO_6 octahedra, as discussed in the previous section. Since the d orbitals of transition metal (TM) ions are strongly localized, the direct hopping between metal sites is very weak. Thus, the primary mechanism in such case is superexchange interaction, where electrons hopping between magnetic ions is mediated by non-magnetic ions (ligands) as shown in figure. In general, this type of interaction results in anti-ferromagnetic groundstate because such configuration allows electrons to delocalize over the extended space, thus reducing the kinetic energy. In special circumstances, superexchange interaction can lead to weak ferromagnetic exchange interaction. The sign and strength of this interaction is set by Goodenough–Kanamori rules [32–34], a semi-empirical rules proposed by John B. Goodenough and Junjiro Kanamori. For our purpose, we adapt them from Ref [42].

- If two partially filled d orbitals of two metal sites overlap with the same ligand p orbitals, this results in strong antiferromagnetic exchange interaction.

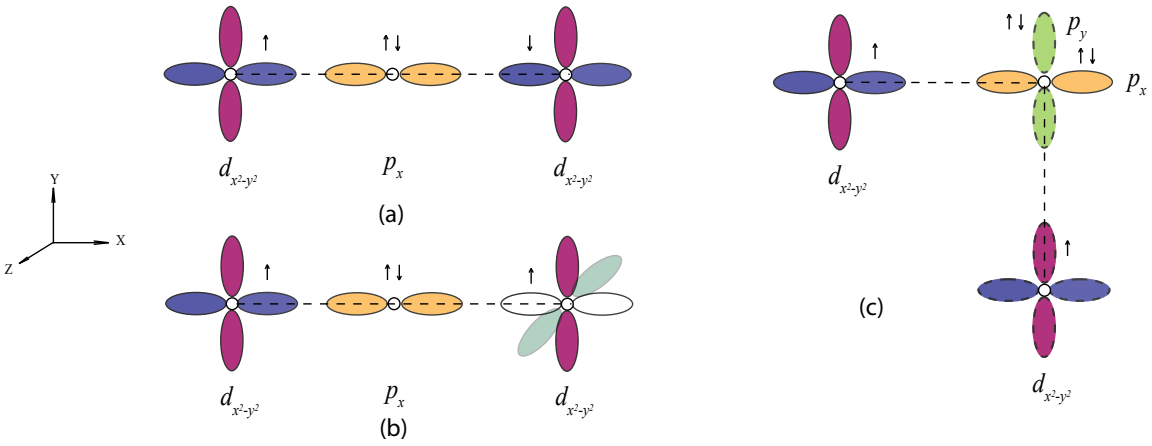

Figure 1.5: Representative orbitals illustrating Goodenough–Kanamori rules of superexchange interactions.

- If one empty and one partially filled d orbital of two metal sites overlap with the same ligand p orbitals, this leads to weak ferromagnetic exchange interaction.
- If the angle between TM - ligand - TM bonds is 90°, and if the partially filled d orbitals overlap with different orthogonal p orbitals of ligand, then the interaction is weakly ferromagnetic.

The origin of antiferromagnetic contribution to superexchange can be demonstrated with the Hubbard model. In the limit, where the onsite Coulomb repulsion is much larger than the intersite electrons hopping ($U >> t$), the model assumes antiferromagnetic ground state.

Hubbard Model

In magnetic insulators and related compounds, electrons are not allowed to move freely due to strong on-site Coulomb repulsion, and are therefore highly correlated. A minimal model where the electronic hopping and Coulomb repulsion compete with each other is the Hubbard model. This competition ultimately controls the transition between the metallic and insulating phases.

For simplicity, let us consider the half-filled two-site Hubbard model with one orbital per site. There are six possible ways to put two electrons in two sites abiding Pauli's exclusion principle.

$$
\begin{aligned}
|A\rangle &= c^{\dagger}_{1\uparrow}, c^{\dagger}_{1\downarrow}|0\rangle \\
|B\rangle &= c^{\dagger}_{2\uparrow}, c^{\dagger}_{2\downarrow}|0\rangle \\
|C\rangle &= \frac{1}{\sqrt{2}}\left(c^{\dagger}_{1,\uparrow}c^{\dagger}_{2,\downarrow} - c^{\dagger}_{1,\downarrow}c^{\dagger}_{2,\uparrow}\right)|0\rangle \\
|D\rangle &= c^{\dagger}_{1\uparrow}, c^{\dagger}_{2\uparrow}|0\rangle \\
|E\rangle &= c^{\dagger}_{1\downarrow}, c^{\dagger}_{2\downarrow}|0\rangle \\
|F\rangle &= \frac{1}{\sqrt{2}}\left(c^{\dagger}_{1,\uparrow}c^{\dagger}_{2,\downarrow} + c^{\dagger}_{1,\downarrow}c^{\dagger}_{2,\uparrow}\right)|0\rangle
\end{aligned}
\tag{1.38}
$$

Equation 1.38 represents the six states, where the first three are the singlet states, whereas the other three are the triplet states. $c^{\dagger}_{1\uparrow}$ creates a spin $\uparrow$ electron at site 1. We note that the states $|A\rangle$ and $|B\rangle$ correspond to configurations where two electrons occupy the same site, whereas in other states, each site has one electron. The associated Hamiltonian can be written as,

$$
H = -t \sum_{\sigma=\uparrow,\downarrow} \left(c^{\dagger}_{1\sigma}c_{2\sigma} + c^{\dagger}_{2\sigma}c_{1\sigma}\right) + U\sum_{i=1}^{2} n_{i\uparrow}n_{i\downarrow} \tag{1.39}
$$

where

$$
n_{i\sigma} = c^{\dagger}_{i\sigma}c_{i\sigma}.
$$

In equation 1.39, the first term represents the kinetic energy and the second term represents the Coulomb energy. Here, $c^{\dagger}_{1\sigma}$ and $c_{2\sigma}$ creates and destroys an electron of spin σ at site 1 and 2 respectively. These fermionic operators follow the following commutation relations.

$$
\begin{aligned}
\{c_{l\sigma},\, c_{l'\sigma'}\} &= 0 \\
\{c^{\dagger}_{l\sigma},\, c^{\dagger}_{l'\sigma'}\} &= 0 \\
\{c_{l\sigma},\, c^{\dagger}_{l'\sigma'}\} &= \delta_{ll'}\,\delta_{\sigma\sigma'}
\end{aligned}
\tag{1.40}
$$

Consequently the Hamiltonian takes the form of a 6×6 matrix, where the singlet and triplet blocks are given by

$$H_{singlet} = \begin{array}{c|ccc} & |A\rangle & |B\rangle & |C\rangle \\ \hline \langle A| & H_{AA} & H_{AB} & H_{AC} \\ \langle B| & H_{BA} & H_{BB} & H_{BC} \\ \langle C| & H_{CA} & H_{CB} & H_{CC} \end{array} = \begin{pmatrix} U & 0 & -\sqrt{2}t \\ 0 & U & -\sqrt{2}t \\ -\sqrt{2}t & -\sqrt{2}t & 0 \end{pmatrix} \tag{1.41}$$

$$H_{triplet} = \begin{array}{c|ccc} & |D\rangle & |E\rangle & |F\rangle \\ \hline \langle D| & H_{DD} & H_{DE} & H_{DF} \\ \langle E| & H_{ED} & H_{EE} & H_{EF} \\ \langle F| & H_{FD} & H_{FE} & H_{FF} \end{array} = \begin{pmatrix} 0 & 0 & 0 \\ 0 & 0 & 0 \\ 0 & 0 & 0 \end{pmatrix} \tag{1.42}$$

Diagonalizing matrices 1.41 and 1.42 gives us energies for the singlet and triplet states

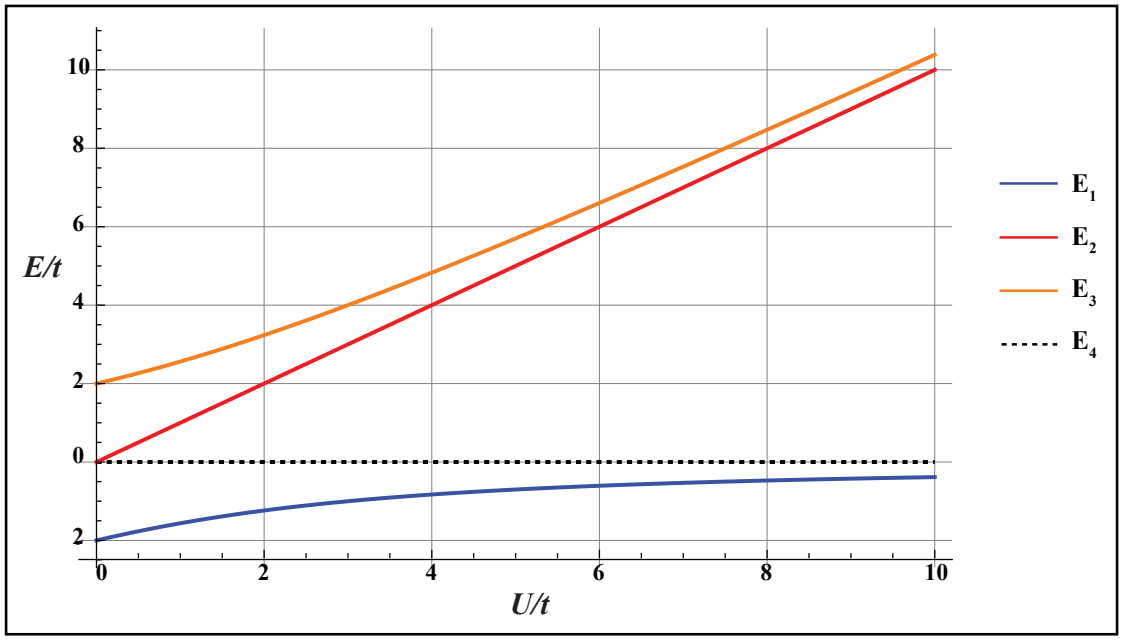

Figure 1.6: Energy spectrum for two site Hubbard model.

respectively.

$$\left.\begin{aligned} E_1 &= \frac{1}{2}\left(U - \sqrt{U^2 + 16t^2}\right) \\ E_2 &= U \\ E_3 &= \frac{1}{2}\left(U + \sqrt{U^2 + 16t^2}\right) \end{aligned}\right\} \quad \text{singlet} \tag{1.43}$$

$$\left.\begin{aligned} E_{4-6} &= 0, 0, 0 \end{aligned}\right\} \quad \text{triplet} \tag{1.44}$$

where E_1 is the ground state spin singlet. The other two spin singlets are higher in energy and are denoted by E_2 and E_3 (see fig 1.6) . Right next to the ground state spin singlet E_1, there are higher lying three fold degenerate triplet states E_4. Hence, we find that the total energy of the system is lower with an antiferromagnetic alignment between spins on neighboring sites. For parallel spins, the hopping is not allowed due to Pauli's exclusion principle, which ultimately increase the overall energy of the system. This mechanism is also called kinetic exchange.

In the limit $U \gg t$, the square root term in equation 1.43 can be expanded using binomial series. Taking the lowest order term in the expansion, the ground state energy takes the form

$$E_1 \approx -\frac{4t^2}{U} \tag{1.45}$$

with the corresponding eigenstate being $\frac{1}{\sqrt{2}}\left(c^\dagger_{1,\uparrow}c^\dagger_{2,\downarrow} - c^\dagger_{1,\downarrow}c^\dagger_{2,\uparrow}\right)|0\rangle$.

Let us compare this result with the effective spin model describing two interacting spin $\frac{1}{2}$ particles.

$$\mathcal{H}_{\text{eff}} = J\,\mathbf{S}_1 \cdot \mathbf{S}_2 \tag{1.46}$$

We know,

$$\mathbf{S_{Tot}} = \mathbf{S}_1 + \mathbf{S}_2 \tag{1.47}$$

$$\mathbf{S^2_{Tot}} = \mathbf{S}_1^2 + \mathbf{S}_2^2 + 2\,\mathbf{S}_1 \cdot \mathbf{S}_2 \tag{1.48}$$

Substituting the value of $\mathbf{S}_1 \cdot \mathbf{S}_2$ from equation 1.48 to 1.46, we get

$$\mathcal{H}_{\text{eff}} = \frac{J}{2}\left[\mathbf{S}^{\mathbf{2}}_{\mathbf{Tot}} - \mathbf{S}_1^2 - \mathbf{S}_2^2\right] \tag{1.49}$$

$$= \frac{J}{2}\left[\mathbf{S}_{\mathbf{Tot}}(\mathbf{S}_{\mathbf{Tot}}+1) - \frac{3}{4} - \frac{3}{4}\right] \tag{1.50}$$

$$= \frac{J}{2}\left[\mathbf{S}_{\mathbf{Tot}}(\mathbf{S}_{\mathbf{Tot}}+1) - \text{const}\right] \tag{1.51}$$

$$= \begin{cases} 0 - \text{const}, & \mathbf{S}_{\mathbf{Tot}} = 0\,(\text{singlet}) \\ J - \text{const}, & \mathbf{S}_{\mathbf{Tot}} = 1\,(\text{triplet}) \end{cases} \tag{1.52}$$

Comparing equations 1.41, 1.45 and 1.52, we have,

$$J \approx \frac{4t^2}{U} \tag{1.53}$$

We note that this results only considers the lowest order term in an expansion of $\frac{t}{U}$ in equation 1.45 for $\mathbf{S} = \frac{1}{2}$ local degree of freedom and two sites. For local degrees of freedom with $\mathbf{S} > \frac{1}{2}$ or more sites important higher-order contributions can arise, such as the biquadratic exchange term (appearing at order $\frac{t^4}{U^3}$) or ring-exchange terms $(\mathbf{S}.\mathbf{S})^2$ in square or cubic lattices.

$$J = \frac{4t^2}{U} + \text{higher-order terms} \tag{1.54}$$

From Figure 1.6, we see that as Coulomb repulsion becomes higher, some energy states are well separated from the low-lying triplet and ground state singlet. At this limit, the system can be well described by the effective Hamiltonian that is spanned just by these low energy states. This low-energy effective Hamiltonian framework is routinely exploited to compute exchange interactions in our research. The extensive discussion on this topic is presented in the next chapter.

1.5 Model Spin Hamiltonians

We have established that the interaction between spins is predominantly due to exchange interaction, which is ultimately responsible for magnetic order in many magnetic materials. In previous section, we define Heisenberg Hamiltonian as,

$$\mathcal{H} = \sum_{\langle i,j \rangle} J_{ij}\, \mathbf{S}_i \cdot \mathbf{S}_j \tag{1.55}$$

Here, we should be careful about the nature of $\mathbf{S}_i$ and $\mathbf{S}_j$ operators. Equation 1.55 does not give us the information about whether the operator here is a pure spin operator or total angular momentum operator (combination of $\mathbf{L} + \mathbf{S}$ operator). In materials with strong spin–orbit interaction, $\mathbf{S}$ often represents the total angular momentum operator. The notation $\mathbf{J}$ is typically avoided to prevent confusion with the exchange constant.

We express this Hamiltonian in generic bilinear form as:

$$\mathcal{H} = \sum_{\langle i,j \rangle} \mathbf{S}_i\, \mathbb{J}_{ij}\, \mathbf{S}_j \tag{1.56}$$

Here $\mathbb{J}$ is a second rank tensor. When SOC is considered in magnetic couplings, various additional interactions can appear. Let us discuss some general cases of this model.

- The relatively general form, which introduce uniaxial magnetic anisotropy, is called XXZ model and can be written as

$$\mathcal{H} = \sum_{\langle i,j \rangle} J_{ij} \left(S_i^x S_j^x + S_i^y S_j^y + \Delta\, S_i^z S_j^z \right) \tag{1.57}$$

  Here, the parameter Δ determines the nature of anisotropy. If $\Delta > 1$, the system is in axial regime (easy axis) while $\Delta < 1$ gives the planar regime, where spin prefers to point in the xy plane. With $\Delta = 0$, we will have XX model. If $\Delta \to \infty$, equation 1.57 can be written as

$$\mathcal{H}_{\text{Ising}} = \sum_{\langle i,j \rangle} J_{ij}\, S_i^z S_j^z \tag{1.58}$$

  which is the Hamiltonian for Ising spin model. Here, we emphasize the need to

distinguish between the spin-space and lattice-space dimensions. The restrictions here is for spin-space. For example, we can have an Ising model, where spin can only take two values (up and down), in 1D, 2D, or 3D systems.

- The more general Hamiltonian with different component of exchange tensor can be written as

$$\mathcal{H} = \sum_{\langle i,j \rangle} \left(J_x \, S_i^x S_j^x + J_y \, S_i^y S_j^y + J_z \, S_i^z S_j^z \right) \tag{1.59}$$

This model is known as XYZ model. This give rise to anisotropy in the nearest neighbor interaction. If the third term in equation 1.59 is zero, the model is called XY model. Apart from these symmetric anisotropies, the system can have anti-symmetric anisotropic interaction (DM interaction).

Dzyaloshinskii–Moriya Interaction

Dzyaloshinskii–Moriya (DM) interaction is an antisymmetric exchange interaction present between the sites that are not related by inversion symmetry. This interaction is responsible for the weak ferromagnetism in antiferromagnet, thus favoring the spin canting in neighboring spins. Since the ferromagnetic component responds much more strongly to external magnetic field than antiferromagnetic component, DM interactions can have strong effects even with a weak ferromagnetic contribution. This interaction was first identified by Dzyaloshinskii on the basis of symmetry arguments of crystal structure in antiferromagnetic sublattices [44], and later derived by Moriya [45] by including spin-orbit coupling in Anderson's theory of superexchange [46]. For neighboring spins $\mathbf{S}_i$ and $\mathbf{S}_j$, the Hamiltonian for DM interaction takes the form

$$\mathcal{H}_{\mathrm{DM}} = \sum_{\langle i,j \rangle} \mathbf{D}_{ij} \cdot (\mathbf{S}_i \times \mathbf{S}_j) \tag{1.60}$$

$$= \sum_{\langle i,j \rangle} \left[D_x \left(S_i^y S_j^z - S_i^z S_j^y \right) + D_y \left(S_i^z S_j^x - S_i^x S_j^z \right) + D_z \left(S_i^x S_j^y - S_i^y S_j^x \right) \right] \tag{1.61}$$

where $\mathbf{D}_{ij}$ is the Dzyaloshinskii–Moriya vector for the given bond (ij), with $\mathbf{D}_{ij} = -\mathbf{D}_{ji}$. When allowed by symmetry, this interaction is generally comparable in strength to single-ion anisotropy and is stronger than symmetric exchange anisotropy [42].

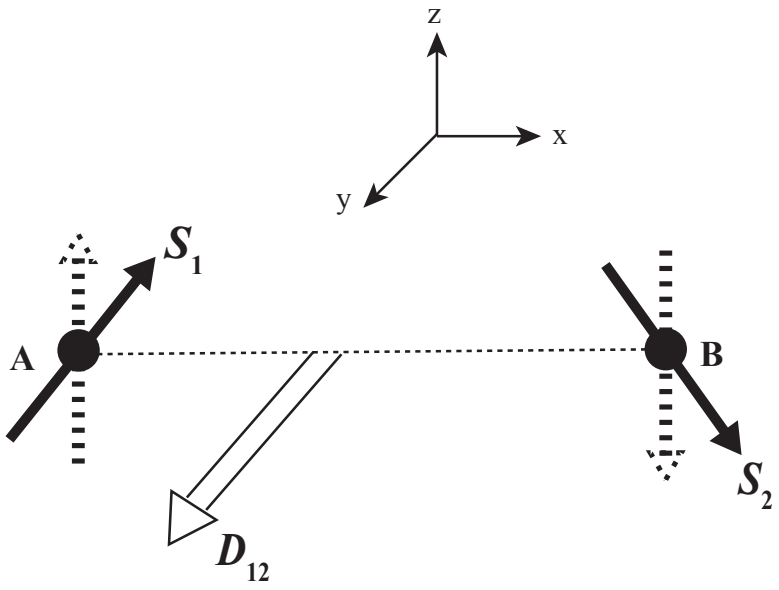

Figure 1.7: Spin canting in an otherwise antiferromagnet due to Dzyaloshinskii–Moriya interaction

We note that the existence DM vector $\mathbf{D}_{ij}$ for a given pair of spins does not always results in net ferromagnetic moment in the crystal. In many cases, different DM vectors on different layers might point in opposite directions and cancel out in the absence of external magnetic field. But it is also possible to have situation where this interaction can lead to net magnetization in the ground state of antiferromagnetic materials. One of the important consequences of these type of anisotropic interactions is that they may lead to a opening of a gap in magnetic excitations.

At this point, we separate the generic bilinear Hamiltonian into symmetric and anti-symmetric terms.

$$\mathcal{H} = \sum_{\langle i,j \rangle} \mathbf{S}_i \, \mathbb{J}_{ij} \, \mathbf{S}_j \tag{1.62}$$

where

$$\mathbb{J}_{ij} = \mathbb{J}_{ij}^{\text{sym}} + \mathbb{J}_{ij}^{\text{asym}} \tag{1.63}$$

$$= \begin{pmatrix} J^x & \Gamma^{xy} & \Gamma^{xz} \\ \Gamma^{xy} & J^y & \Gamma^{yz} \\ \Gamma^{xz} & \Gamma^{yz} & J^z \end{pmatrix} + \begin{pmatrix} 0 & D_z & -D_y \\ -D_z & 0 & D_x \\ D_y & -D_x & 0 \end{pmatrix} \tag{1.64}$$

We note that $\mathbb{J}_{ij}^{\text{sym}} = \mathbb{J}_{ji}^{\text{sym}}$ whereas $\mathbb{J}_{ij}^{\text{asym}} = -\mathbb{J}_{ji}^{\text{asym}}$. More complex anisotropic interactions, such as the Kitaev interaction, can give rise to a richer exchange tensor. For example, the exchange matrix in α-$RuCl_3$ considering the extended Kitaev interactions for Z-bond can be written as

$$\mathbb{J}_{ij} = \begin{pmatrix} J & \Gamma & \Gamma' \\ \Gamma & J & \Gamma' \\ \Gamma' & \Gamma' & J+K \end{pmatrix} \tag{1.65}$$

where K is the Kitaev term. The form of interactions for X and Y bonds are related by rotational symmetry. The first principles method to derive these kind of spin Hamiltonians is discussed in chapter 2.

1.6 Ordered Phases and Excitations in Solid

One of the fundamental properties of condensed matter systems is the emergence of spontaneous order at low temperature. For example, in magnetic materials, the spin can align in specific configuration to give ferromagnetic or anti-ferromagnetic order. The another example is the transition from disordered liquid to ordered solid. The appearance of spontaneous order is often associated with critical temperature T_c and the order parameter. Below the critical temperature ($T < T_c$), the order parameter has finite value. For ($T > T_c$) it is zero. For ferromagnetic-paramagnetic transition, the order parameter is magnetization.

The formation of long range order is often associated with the spontaneous breaking of underlying symmetry. This can lead to phenomena such as phase transition as discussed above. Another important consequence of spontaneous symmetry breaking is the excita-

tions in solids. At absolute zero temperature, there are no excitations and everything is ordered perfectly. Thermal fluctuation weaken the order at finite temperature through the population of these excitations. Some examples of these excitations are lattice waves (phonons) and spin waves (magnons).

1.7 Quantum Spin Liquid

The concept of associating distinct phases of matter with order parameter and symmetry-breaking, as discussed above, was challenged by the discovery of fractional quantum Hall states [47]. It was realized that these distinct quantum Hall states can host quantum fluid ground states with fractional excitations [48]. It is now well understood that this new state of matter is distinguished by topological order and it's groundstate wavefunctions has long range quantum entanglement. These topologically ordered states has gap between ground states and excited states in the bulk since the local excitations cost finite energy. One may then ask whether similar phenomena can be realized in spin systems.

The concept of quantum spin liquid (QSL) was first proposed by Anderson by introducing the concept of resonating valence bond state [41]. The key idea is that the frustration can emerge form the inability of all bonds to simultaneously satisfy a particular type of interaction. For example, in a triangular lattice, the Ising like spin can not satisfy antiferromagnetic configuration for all the three bonds (see Fig.1.8). For a given Hamiltonian $\mathcal{H} = -\sum_{\langle i,j \rangle} J_{ij}\, S_i^z \cdot S_j^z$, the frustration in triangular lattice give rise to six degenerate ground states ($E = -J$) and two excited state ($E = 3J$). If we consider unfrustrated triangular lattice with ferromagnetic configuration, we have only two ground state configuration ($\uparrow\uparrow\uparrow$ and $\downarrow\downarrow\downarrow$) with $E = -3J$. Thus, we noted that frustration induce degeneracy in the system.

This idea of frustration can be extended to resonating valence bond (see Fig. 1.9) by considering the quantum nature of the spin. We know that the ground state of the antiferromagnetic interaction between two nearest neighbor sites is spin singlet. By considering different configuration of degenerate singlets and taking their superposition, we get the wavefunctions for the resonating valence bond states for the infinite two dimensional trian-

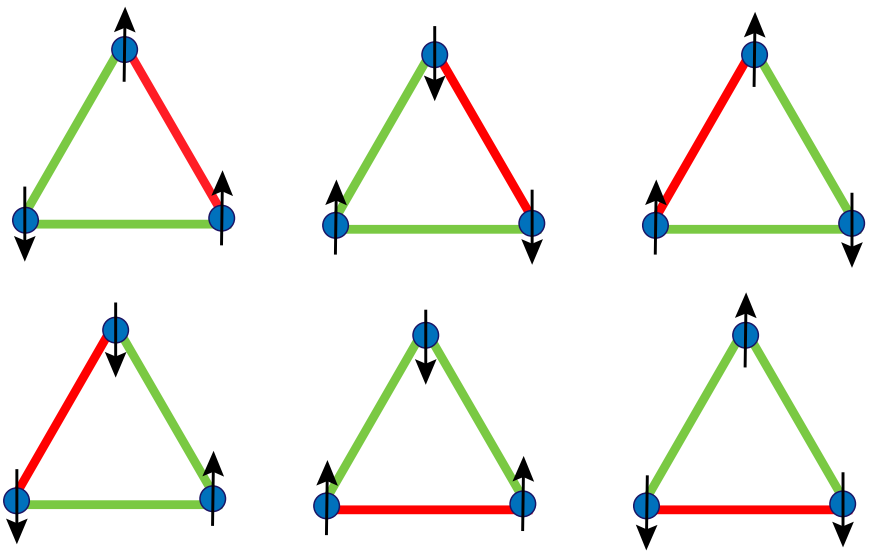

Figure 1.8: A triangular lattice demonstrating geometric frustration for antiferromagnetically interacting Ising spin. Red lines denotes energetically unfavorable (unhappy) bonds, while green lines indicates energetically favorable (happy) bonds.

gular lattice. Such states can be highly entangled and do not break rotational symmetry. There are several excellent reviews in this topic [49–53]. Here we will discuss some key features of quantum spin liquid and focus on a particular type of QSL, Kitaev quantum spin liquid [54–58].

Quantum spin liquids are characterized by the absence of long-range magnetic order even at absolute zero temperature. The geometric frustration or competing magnetic exchange interactions contribute to this apparent spin disorder and can lead to strong quantum fluctuations. As discussed above, this collective quantum spin state does not break rotational symmetry since each bond can be represented as entangled spin singlet state.

One can make a phenomenological classification of quantum spin liquid as gapped and gapless QSL. Similar to the fractional quantum Hall effect, topological order can be present in the gapped quantum spin liquid. This often leads to robust degeneracy of the ground state as they are stable against the local perturbations. The gapped QSLs thus have well defined non-local quasiparticle excitations. These quasiparticles are highly entangled and follow non-trivial mutual statistics. In two dimensional system, such excitations manifest as anyons and acquire a non-trivial phase (Berry phase) upon exchange. A well-known example

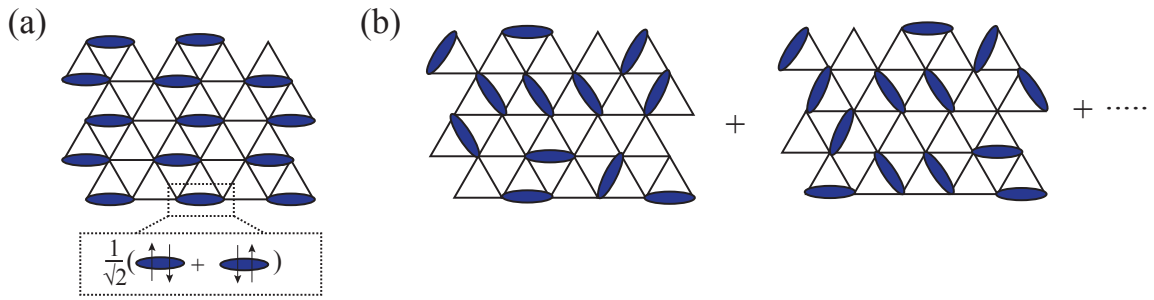

Figure 1.9: **Valence bond and resonating valence bond state** (a) A frustration-induced valence bond state in an antiferromagnet showing specific pattern of entangled singlets state. (b) Resonating valence bond states illustrating the superposition of different patterns.

of such quasiparticle is a spinon, which carries spin $\frac{1}{2}$, but no charge. In the gapless QSLs, however, there may arise a situation where quasiparticle description fails completely [59]. Unlike gapped spin liquids, where the correlations of physical observables have exponential decay as a function of distance, gapless spin liquid follow power law decay.

There are several proposed models that can host quantum spin liquid state such as Toric Code [60], Kitaev Honeycomb [54], frustrated anisotropic Heisenberg Kagome [61], and triangular lattice quantum dimer model [62]. Here, we will focus on Kitaev's honeycomb model.

1.7.1 Kitaev's Honeycomb Model

Kitaev's honeycomb model is an exactly solvable model for spin $\frac{1}{2}$ in 2D honeycomb lattice. It is characterized by bond-dependent Ising like interactions, and can host topological quantum spin liquid ground state with Majorana fermions emerging as fractionalized excitations. Originally proposed by Alexei Kitaev [54], and extended to realistic systems by Jackeli and Khaliullin [63, 64], several Mott-insulators have since been studied to realize this physics [65–69]. In this thesis, we study α-$RuCl_3$ in various contexts, which is the prime Kitaev candidate.

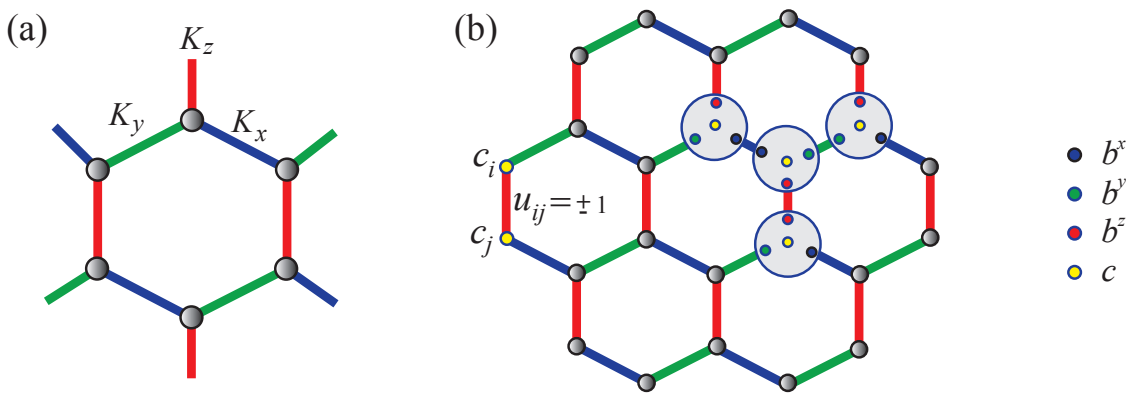

Figure 1.10: **Kitaev interactions in a honeycomb lattice** (a) Figure illustrating bond-dependent K_x, K_y, and K_z interactions. Blue, green, and red lines denotes x, y, and z bonds respectively. (b) A spin $\frac{1}{2}$ degree of freedom can be fractionalized into four flavors of Majorana fermions as shown. The three localized Majorana fermions (blue, green and red) can recombine to form static Z_2 gauge field (u_{ij}) leaving free itinerant Majorana fermion (yellow).

The Hamiltonian for the Kitaev model can be written as

$$\begin{aligned} H &= -\sum_{\langle ij\rangle_\gamma} K_\gamma S_i^\gamma S_j^\gamma \\ &= -K_x \sum_{\langle ij\rangle_x} S_i^x S_j^x - K_y \sum_{\langle ij\rangle_y} S_i^y S_j^y - K_z \sum_{\langle ij\rangle_z} S_i^z S_j^z \end{aligned} \tag{1.66}$$

Here, K_x, K_y and K_z are Kitaev exchange interactions along nearest neighbor bonds x, y and z. S_i^x,S_i^y and S_i^z are spin operators for spin $\frac{1}{2}$ at site i . A spin sitting at site i is frustrated because it can not simultaneously align along mutually incompatible directions x, y and z. In real materials, such magnetic couplings are possible due to strong spin-orbit coupling which entangles spatial anisotropy to spin anisotropy.

Equation 1.66 can be solved by introducing four flavors of Majorana fermions for the spin operators. We express the Pauli operators in terms of these Majorana operators,

$$\sigma_i^\gamma = i\, b_i^\gamma c_i \tag{1.67}$$

which satisfy the following commutation relations:

$$\{c_i\, c_j\} = 2\,\delta_{ij} \tag{1.68}$$

$$\{b_i^{\gamma}\, b_j^{\beta}\} = 2\,\delta_{ij}\delta_{\gamma\beta} \tag{1.69}$$

Majorana operators defined in such way can be expressed in terms of regular creation-annihilation fermionic operators as,

$$c_1 = f + f^{\dagger} \tag{1.70}$$

$$c_2 = i(f - f^{\dagger}) \tag{1.71}$$

Here, we note that we have introduced four flavors of Majorana fermions per site to represent a spin $\frac{1}{2}$ system. As a consequence, we have a fermionic Fock space that is double in size. Compared to the physical spin Hilbert space, this additional degree of freedom introduces redundancy, making it essential to find a way to project onto the physical space. The physical Hilbert space is the subspace where:

$$\sigma^x\,\sigma^y\,\sigma^z = i\,\mathbb{I}_{2\times 2} \tag{1.72}$$

$$(i\,b_i^x c_i)\,(i\,b_i^y c_i)\,(i\,b_i^z c_i) = i \tag{1.73}$$

$$\hat{D}_i \equiv b_i^x\, b_i^y\, b_i^z\, c_i = 1 \tag{1.74}$$

where $\hat{D}_i$ is the gauge operator with $[\hat{D}, \sigma^{\gamma}] = 0\,\text{for all}\,\gamma$. Now, we can define the projection operator

$$\mathbb{P} = \prod_i \frac{1}{2}\left(1 + \hat{D}_i\right) \tag{1.75}$$

This operator removes the unphysical states. The spin Hamiltonian can be rewritten in terms of the Majorana fermions,

$$\mathcal{H} = -\frac{1}{4}\sum_{\langle ij\rangle_\gamma} K_\gamma \,(i\, b_i^\gamma c_i)\,(i\, b_j^\gamma c_j) \tag{1.76}$$

$$= -\frac{1}{4}\sum_{\langle ij\rangle_\gamma} K_\gamma \, b_i^\gamma b_j^\gamma c_i c_j \tag{1.77}$$

$$= \frac{i}{4}\sum_{\langle ij\rangle_\gamma} K_\gamma \, \hat{u}_{ij}\, c_i c_j \tag{1.78}$$

where $\hat{u}_{ij} = i\, b_i^\gamma b_j^\gamma$. Since the operator $\hat{u}_{ij}$ commutes with the Hamiltonian, $\langle \hat{u}_{ij} \rangle$ is constant in time. As a result, $\langle \hat{u}_{ij} \rangle$ can be replaced by u_{ij}. It is straight forward to show that $\hat{u}_{ij}^2 = 1$ giving $u_{ij} = \pm 1$. This means the Hilbert space splits into two sectors, reducing the Hamiltonian to a free Majorana problem in the background of a static $\mathbb{Z}_2$ gauge field.

The Hamiltonian described by equation 1.78 is gauge invariant under local $\mathbb{Z}_2$ gauge transformation, however, $\hat{u}_{ij}$ is not. For this reason, $\hat{u}_{ij}$ itself is not physically observable quantity. We recall that any physical operator in the spin Hilbert space is gauge invariant. We begin by evaluating the product of spin bond operator around a hexagon,

$$\hat{W}_p = \sigma_1^y \, \sigma_2^x \, \sigma_3^z \, \sigma_4^y \, \sigma_5^x \, \sigma_6^z = \pm 1 \tag{1.79}$$

$$= (\sigma_1^z \sigma_2^z)(\sigma_2^y \sigma_3^y)(\sigma_3^x \sigma_4^x)(\sigma_4^z \sigma_5^z)(\sigma_5^y \sigma_6^y)(\sigma_6^x \sigma_1^x) \tag{1.80}$$

$$= -u_{12}\, u_{23}\, u_{34}\, u_{45}\, u_{56}\, u_{61} \tag{1.81}$$

This gauge-invariant operator is called a Wilson loop. In this picture, u_{ij} acts as a $\mathbb{Z}_2$ gauge field defined on the bond, and $\hat{W}_p$ is the magnetic flux through a plaquette. If $w_p = 1$ for all hexagons, it corresponds to a ground state. The $\mathbb{Z}_2$ magnetic flux excitation (vison excitation) would be $w_p = -1$, which corresponds to $\mathbb{Z}_2$ vortex, and a Majorana fermion upon encircling this hexagonal plaquette acquires a phase -1.

This model has been of interest for realization in real materials due to the particular statistics of the flux and fermionic excitations, which allow for topological quantum computing applications. As a consequence, there has been significant interest in defining precise experimental signatures to test for the Kitaev spin liquid ground state. One such experi-

ment, suggested in Kitaev's original paper, is measurement of the thermal Hall conductivity in magnetic field.

1.8 Thermal Hall Effect

The thermal Hall effect (THE), often referred to as the Righi-Leduc effect, is a well-known phenomenon for metals and semiconductors with a large concentration of high-mobility carriers[70–72]. When a temperature gradient is applied longitudinally across the sample in the presence of a magnetic field, a transverse temperature gradient emerges in the material. Since a magnetic field can not exert electromagnetic Lorentz force on chargeless phonon, one would not expect such effect to be present in insulators. However, THE can also arise from topological magnetic excitations [73]. Kitaev model in the presence of magnetic field predicts gapped bulk and gapless edge states like in the quantum Hall effect. The gapless edge modes provide $\frac{\kappa_{xy}}{T} = \frac{1}{2}K_Q$, which is a strong potential benchmark for the presence of this state. However, other heat carriers exist such as phonons, and magnons.

In 2005, the phononic thermal hall effect (PHE) was reported for the first time in paramagnetic insulator $Tb_3Ga_5O_{12}$ [74] instigating the search for this phenomenon in a variety of insulators[75–81]. Alongside, numerous theoretical attempts have been made to understand the underlying physics of these heat-carrying phonons[82–91]. The above-mentioned studies focus on both intrinsic and extrinsic contributions to the origin of thermal hall conductivity κ_{xy}.

A significant κ_{xy} has been measured in a variety of quantum magnets [92–98] and the pertinent question to ask is what contributes substantially to the observed κ_{xy}? While numerous theoretical approaches are focused on spinon or magnon contributions [99–105], the indication of phonon contributions to κ_{xy} has been reported in the literature[77–79, 98]. Very recently, Léo Mangeolle and collaborators have proposed a mechanism of skew scattering of phonons by collective modes [87, 88] to explain the observed phononic contribution by invoking the higher-order correlation function of the fluctuating field.

In magnetic insulators, heat can be carried by both spin excitations and phonons i.e. $\kappa = \kappa_{\mathbf{s}} + \kappa_{\mathbf{ph}}$. The thermal conductivity 'κ' is related to heat flux '$\mathbf{j}$' and temperature

gradient '∇T' by the following relation

$$\mathbf{j} = -\kappa.\nabla T$$

where κ can be defined as

$$\kappa = \begin{pmatrix} \kappa_{xx} & \kappa_{xy} & \kappa_{xz} \\ \kappa_{yx} & \kappa_{yy} & \kappa_{yz} \\ \kappa_{zx} & \kappa_{zy} & \kappa_{zz} \end{pmatrix} \tag{1.82}$$

The diagonal components give the longitudinal conductivity which at most temperatures is dominated by phonons [106, 107] whereas the contribution of phonons to the Hall conductivity is not fully understood yet[80, 98]. Our primary goal is to address how phonons interact with spin and help contribute to thermal Hall conductivity in real materials.

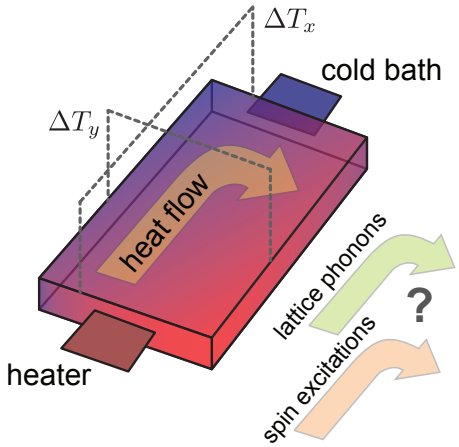

Figure 1.11: Thermal Hall Effect

1.9 Dissertation Outline

This dissertation is organized as follows. In chapter 2, we give a detailed introduction to des Cloizeaux Effective Hamiltonians approach. We have exploited this method to derive magnetic exchange interactions, crystalline electric field excitations, g-tensors, and spin-

phonon couplings for the material of interest. Following this, we outline the theoretical framework of the finite difference supercell scheme used to compute phonons for the related materials.

During my PhD, I have extensively studied the effect of disorder and distortion in the magnetic response of honeycomb structure magnetic insulators. In chapter 3, the impact of structural disorder on the magnetic excitation of Heisenberg-Kitaev quantum magnet, $Na_2Co_2TeO_6$, is presented. This chapter includes experimental data as well as theoretical modeling of magnetic excitations due to such disorder. Chapter 4 provides the theoretical insights into the structural dependence of magnetic response in α-$RuCl_3$. Here, we discuss how the distortion in the monolayer form of α-$RuCl_3$ cause the reversal in magnetic anisotropy compared to its bulk structure.

In Chapter 5, we study the ground state and excitations of another layered van der Waals magnet, $FePS_3$. We demonstrate the complex spin-orbital phenomena and its role in the mixing and spectral overlap of different spin-orbital single-ion states in this compound.

In chapter 6, we present a comprehensive theoretical formalism to derive spin-phonon coupling in transition metal insulators. We subsequently apply this method to estimate the temperature-dependent optical phonon lineshapes in $MnPSe_3$ to benchmark and validate our approach. In chapter 7, we adopt the formalism developed in Chapter 6 to estimate the magnitude and sign of planar thermal Hall effect in α-$RuCl_3$, a layered van der Waals material with a strong spin-orbit interaction. Chapter 8 provides a brief summary of selected projects to which I have contributed as a coauthor. The conclusions and perspectives are summarized in chapter 9.

Chapter 2

Methodology

Section 2.1 of this chapter is adapted from the arXiv:2407.00659 preprint titled "Spin-Phonon Coupling in Transition Metal Insulators: General Computational Approach and Application to $MnPSe_3$".

In this chapter, we discuss two important first principles methods that we exploit to compute spin-phonon coupling (SPC) in the material of interest. The computational framework of SPC is built on accurate prediction of spin-exchange interaction and phonon eigenvectors. We derive spin-exchange interaction matrix by employing des Cloizeaux Effective Hamiltonians (dCEH) scheme [108]. The phonon energies and eigenvectors are obtained using phonopy[109, 110]. The spin-phonon coupling can be evaluated in the dCEH framework by explicitly introducing the phonon degree of freedom.

2.1 Review of des Cloizeaux Effective Hamiltonians

In general, low-energy models constitute (i) an effective Hamiltonian in a reduced Hilbert space that replicates the low-energy spectrum of the full Hamiltonian, and (ii) a mapping between the degrees of freedom of the low-energy space and the full Hilbert space. In the context of magnetic couplings, the full Hilbert space is spanned by the electronic degrees of freedom, while the low-energy magnetic Hamiltonian is written in terms of spin operators. When using perturbation theory, the mapping between spin and electronic variables is well-defined, and the magnetic couplings are directly obtained in terms of the hopping and

Coulomb parameters of the electronic model. However, use of perturbation theory becomes increasingly fraught as the electronic model becomes more complicated, and a convenient separation of the Hamiltonian into a zeroth order and perturbing term cannot be found. In such cases, it is advantageous simply to diagonalize the electronic Hamiltonian exactly (at least on a small number of sites), and identify the "exact" low-energy states directly. However, this only produces the local spectrum and low-energy states in terms of electronic degrees of freedom; a mapping to spin-variables is still necessary in order to obtain a low-energy Hamiltonian.

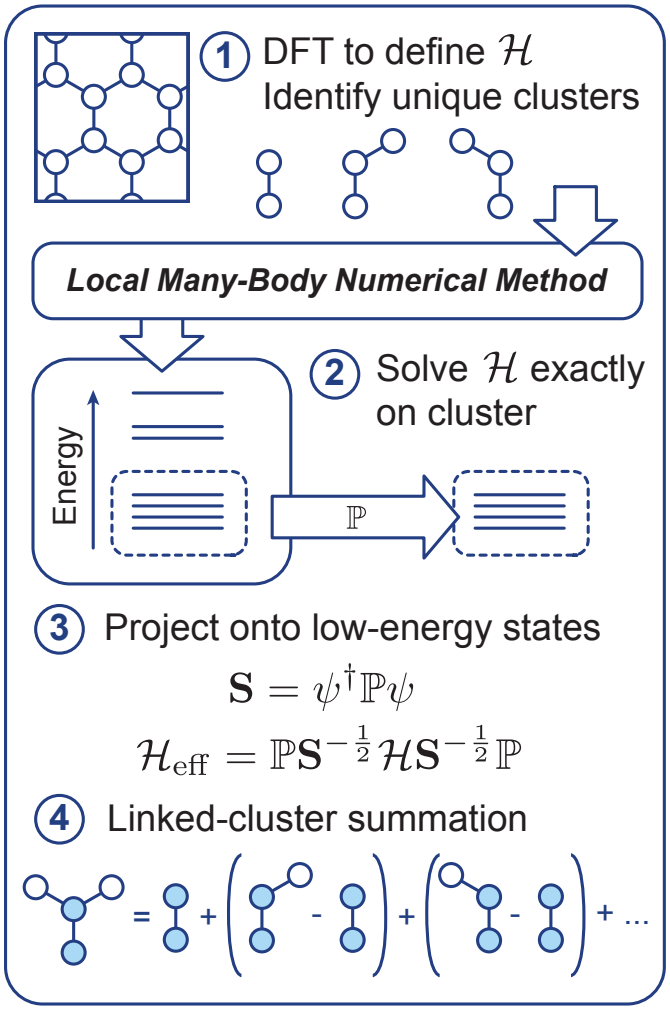

Figure 2.1: Figure illustrating des Cloizeaux Effective Hamiltonians scheme

There are various schemes to construct this mapping. For example, a popular method of estimating magnetic couplings from *ab-initio* calculations is total energy mapping us-

ing density functional theory (DFT) [111]. In this approach, DFT calculations are performed with magnetic moments at each site suitably constrained to realize various different static magnetic patterns. The resulting energies are interpreted as corresponding to classical spin wavefunctions (i.e. single electronic Slater determinant states, as required by the Kohn-Sham construction). While this is very successful in simple cases, more complex spin-orbital moments can sometimes lead to ambiguity in the mapping, because their local multi-determinant structure may not be precisely captured in the Kohn-Sham wavefunction. As an alternative, one can use explicit multi-determinant wavefunction-based methods (sometimes referred to as "Quantum Chemistry" approaches), in which case the mapping can be made on symmetry grounds[112–116], or by projection onto idealized low-energy states[117, 118]. Here we describe the latter approach, suggested originally by des Cloizeaux[108], and implemented in a wide variety of contexts[119]. Notable contributions to the calculation of magnetic Hamiltonians in this context have been made by Malrieu [120–124] and Maurice [125–130].

The essential idea of des Cloizeaux Effective Hamiltonians (dCEHs) is to construct the mapping by requiring the true low-energy states to have maximal overlap with an idealized low-energy basis. For the purpose of computing magnetic couplings, we apply this approach to the results of exactly diagonalizing the electronic Hamiltonian on small clusters of sites, which are ultimately combined via a linked cluster expansion[131]. *Ab-initio* dCEHs have recently been utilized by the authors to study quantum magnets with strongly anisotropic spin interactions [43, 117, 132], multi-spin ring-exchange [133, 134], and complicated admixture of different J_{eff} states[135]. The steps are as follows.

1. Define the electronic Hamiltonian using appropriate *ab-initio* methods and/or input from experiments. This may include estimation of the hopping and crystal field terms via Wannier fitting of DFT calculations, fitting of experimental spectra, etc.

2. Exactly diagonalize the electronic Hamiltonian on a finite number of sites to obtain the low-energy eigenstates $|\phi_n\rangle$ and energies E_n in terms of the electronic degrees of

freedom. The low-energy Hamiltonian is therefore:

$$\mathcal{H}_{\text{low}} = \sum_n E_n |\phi_n\rangle\langle\phi_n| \tag{2.1}$$

3. Define an idealized low-energy space of spin-orbital states in terms of the electronic degrees of freedom, $|\psi_n\rangle$. The projection operator onto the low-energy space is therefore $\mathbb{P} = \sum_n |\psi_n\rangle\langle\psi_n|$. This is essentially the same as the projection operator appearing in equation (6.13). For example, it's role is to project out double occupancies to arrive at a pure spin or spin-orbital state.

4. Rotate/project the low energy Hamiltonian into the idealized basis. Formally, this is accomplished via:

$$\mathcal{H}_{\text{eff}} = \mathbb{P}\mathbf{S}^{-1/2}\mathcal{H}_{\text{low}}\mathbf{S}^{-1/2}\mathbb{P} \tag{2.2}$$

where $\mathbf{S}$ is the overlap matrix of the projected low-energy states, with matrix elements:

$$[\mathbf{S}]_{nm} = \langle\phi_n|\mathbb{P}|\phi_m\rangle \tag{2.3}$$

The meaning of this expression is as follows. An intermediate basis can be constructed from the projection of the electronic states, $|\phi'_n\rangle \equiv \mathbb{P}|\phi_n\rangle$. However, these $|\phi'_n\rangle$ are not orthonormal. In order to orthonormalize them, we apply the symmetric (Löwden) approach, $|\phi''_n\rangle = \mathbf{S}^{-1/2}|\phi'_n\rangle$, where $[\mathbf{S}]_{nm} = \langle\phi'_n|\phi'_m\rangle$. By noting that $\mathbb{P}^2 = \mathbb{P}$, one arrives at equation (2.3). The symmetric orthogonalization procedure has the feature that it preserves all symmetries, and maximizes $\sum_n \langle\phi''_n|\phi'_n\rangle$. Once $\mathcal{H}_{\text{eff}}$ is obtained numerically, the different matrix elements can then be analyzed to write the couplings in conventional forms in terms of multipole operators.

It may be noted that $\mathbf{S}^{-1/2}\mathbb{P}$ defines a unitary transformation that preserves the eigenvalues of $\mathcal{H}_{\text{low}}$, so the resulting effective Hamiltonian is guaranteed to preserve the low-energy spectrum of the electronic model on the chosen cluster of sites, while being explicitly written in terms of low-energy operators.

With the above procedure defined, the remaining question is how to combine dCEHs from different clusters of sites? Here, the insight is that the dCEHs for different clusters include different subsets of terms in a hypothetical perturbation theory expansion. For example, a two-site cluster will include all terms up to t^2/U, plus a subset of additional higher order contributions (where t is the intersite hopping). A three-site cluster will include all terms up to t^3/U^2 plus a different subset of higher order contributions. By considering which terms are included on each cluster, it can be seen that the couplings in the low-energy Hamiltonians satisfy a convergent linked cluster expansion provided the standard perturbation theory in t/U converges. In this expansion, the *essential* contributions of each cluster are summed, which are defined as the value of the coupling measured on that cluster, minus the essential contributions of all subclusters. For the smallest cluster on which that coupling may be defined (i.e. when there are no subclusters), the essential contribution is equal to the value of the coupling on that cluster. If the cluster expansion is carried out to sufficiently large clusters, then it is possible to mitigate any spurious symmetry breaking induced by truncation of the clusters to a small number of sites.

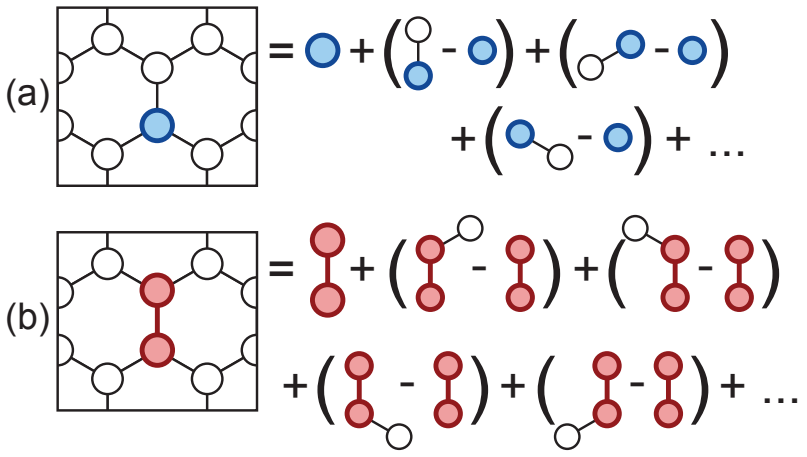

Figure 2.2: Visualization of the lowest order terms in the cluster expansion for the nearest-neighbor honeycomb lattice for (a) one-site couplings and (b) two-site couplings.

Fig. 2.3 shows the pictorial representation of the lowest order contributions in the cluster expansions for one-site and two-site couplings. For example, consider a coupling defined on one site, such as a single-ion anisotropy term. The cluster expansion up to three-site

clusters is:

$$D_i = D_{i()} + \sum_j \left(D_{i(j)} - D_{i()}\right) + \sum_{jk} \left(D_{i(jk)} - D_{i(j)} - D_{i(k)} + D_{i()}\right) + ... \tag{2.4}$$

where the notation $D_{i(j)}$ denotes the value of D_i obtained in the dCEH for a two site cluster with sites i and j. Similarly, the cluster expansion for a bond interaction term can be written:

$$J_{ij} = J_{ij()} + \sum_k \left(J_{ij(k)} - J_{ij()}\right) + \sum_{kl} \left(J_{ij(kl)} - J_{ij(k)} - J_{ij(l)} + J_{ij()}\right) + ... \tag{2.5}$$

In practice, however, it may not be necessary to consider clusters of more than two sites in each case. The point is that $J_{ij()} \propto t^2/U$, while the essential contribution from a three-site cluster is $(J_{ij(k)} - J_{ij()}) \propto t^3/U^2$ at most. Provided the perturbation theory is well converging, the cluster expansion may converge rapidly with cluster size. It is always prudent to check larger clusters when computational resources allow, in order to confirm convergence.

2.2 *Ab Initio* Phonon Calculations

The *ab initio* phonon calculations of crystalline solids require accurate prediction of force constants, which is the derivatives of crystal potential energy with respect to the displacement of atoms. Most of the available *ab initio* codes utilize first principles Density Functional Theory (DFT) [136, 137] to compute phonon dispersion. In this framework, linear response approach [138, 139] and finite difference supercell approach [140–142] are the two standard choices for the first principles phonon calculations. For our purpose, we employ the finite difference supercell approach as available in phonopy [109, 110].

In this framework, single or multiple atoms in the supercell are displaced in different

configurations, and forces on all atoms in the supercell due to these displacements are calculated. Crystal symmetry is utilized to reduce the degrees of freedom of the supercell force constants, which heavily reduces the computational cost. The dynamical matrices are then derived by performing mass normalized Fourier transform of the interatomic force constants. The diagonalization of these dynamical matrices gives phonon frequencies and polarization modes. It is important to note that the dynamical matrices constructed in this manner are exact only at certain **q**-points that are allowed by the supercell periodic boundary conditions. At other points, one has to perform a Fourier interpolation. This approximation works well for the sizable supercell because atomic interactions are expected to decay rapidly with respect to atomic distance.

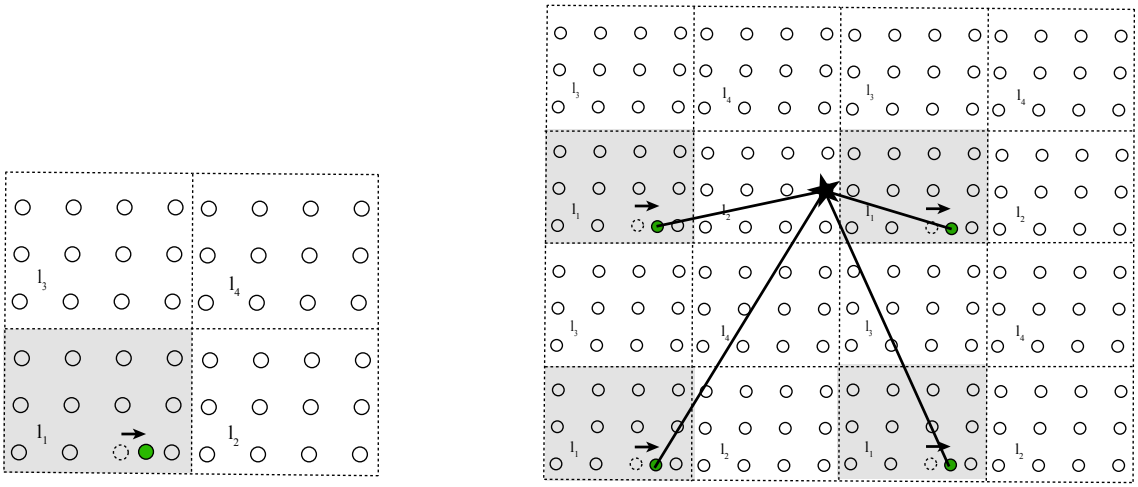

Figure 2.3: Schematic illustration of finite displacement method (a) Figure showing the supercell with a single displacement of an atom in the primitive cell l_1. Periodicity of the lattice is broken by this displacement (b) An atom (shown by star) feels the forces due to this displacements from all the periodic replicas of the supercell. Figure is adapted from [110]

Let us consider the atoms in the unitcell l are vibrating about the equilibrium positions with displacements u along direction α. The crystal potential can be expanded using Taylor series,

$$V = V_0 + \sum_{\alpha ln} \left.\frac{\partial V}{\partial u_{\alpha ln}}\right|_0 u_{\alpha ln} + \frac{1}{2}\sum_{\alpha ln}\sum_{\beta l'n'} \left.\frac{\partial^2 V}{\partial u_{\alpha ln}\,\partial u_{\beta l'n'}}\right|_0 u_{\alpha ln}\,u_{\beta l'n'} + \frac{1}{3!}\sum_{\alpha ln}\sum_{\beta l'n'}\sum_{\gamma l''n''} \left.\frac{\partial^3 V}{\partial u_{\alpha ln}\,\partial u_{\beta l'n'}\,\partial u_{\gamma l''n''}}\right|_0 \times u_{\alpha ln}\,u_{\beta l'n'}\,u_{\gamma l''n''} + \cdots \tag{2.6}$$

The force on the atoms due to the displacement u (first- order force constant) is given by,

$$F_{\alpha ln} = -\frac{\partial V}{\partial u_{\alpha ln}} \tag{2.7}$$

Since the forces on the atoms at the equilibrium position is zero, the first order force constant is zero. The second order force constants can be written as,

$$\Phi_{\alpha ln,\,\beta l'n'} = \frac{\partial^2 V}{\partial u_{\alpha ln}\,\partial u_{\beta l'n'}} \tag{2.8}$$

In the harmonic approximation, the higher terms can be neglected. Thus, one can write,

$$V_{\text{harm}} = V_0 + \frac{1}{2}\sum_{\alpha ln}\sum_{\beta l'n'} \Phi_{\alpha ln,\,\beta l'n'}\,u_{\alpha ln}\,u_{\beta l'n'} \tag{2.9}$$

Setting $V_0 = 0$, the energy of the of the vibrating atoms of mass M_n can be written as ,

$$H = \frac{1}{2}\sum_{\alpha ln} M_n \left(\frac{du_{\alpha ln}}{dt}\right)^2 + \frac{1}{2}\sum_{\alpha ln}\sum_{\beta l'n'} \Phi_{\alpha ln,\,\beta l'n'}\,u_{\alpha ln}\,u_{\beta l'n'} \tag{2.10}$$

In the mass normalized coordinates,

$$H = \frac{1}{2}\sum_{\alpha ln} \left(\frac{d\tilde{u}_{\alpha ln}}{dt}\right)^2 + \frac{1}{2}\sum_{\alpha ln}\sum_{\beta l'n'} \tilde{u}_{\alpha ln}\;\tilde{\Phi}_{\alpha ln,\,\beta l'n'}\;\tilde{u}_{\beta l'n'} \tag{2.11}$$

where,

$$\tilde{\Phi}_{\alpha ln,\,\beta l'n'} = \frac{\Phi_{\alpha ln,\,\beta l'n'}}{\sqrt{M_n M_{n'}}} \tag{2.12}$$

is the reduced force constants. To find phonon frequencies and eigenvectors, we have to solve the eigenvalue problem of the Dynamical matrices D(**q**),

$$\sum_{\beta n'} D_{\alpha n,\beta n'}(\mathbf{q})\, e_{\beta n'}(\mathbf{q}j) = \omega^2(\mathbf{q}j)\, e_{\alpha n}(\mathbf{q}j) \tag{2.13}$$

where

$$D_{\alpha n,\beta n'}(\mathbf{q}) = \sum_{l'} \tilde{\Phi}_{\alpha 0n,\,\beta l'n'}\, e^{\,i\mathbf{q}\cdot(\mathbf{R}_{l'n'}-\mathbf{R}_{0n})} \tag{2.14}$$

We note that D(**q**) is a Hermitian matrix, so its eigenvalues, $\omega^2(\mathbf{q}j)$, must be real. Here, $\omega(\mathbf{q}j)$ and $e_{\alpha n}(\mathbf{q}j)$ denote the phonon frequency and eigenvector of the phonon mode $(\mathbf{q}j)$. At this point, we can write the displacement operator $\hat{u}$ in terms of creation-annihilation operators.

$$\hat{u}_{\alpha ln} = \sqrt{\frac{\hbar}{2M_n N}} \sum_{\mathbf{q}j} \left[\frac{a_{\mathbf{q}j} + a^{\dagger}_{-\mathbf{q}j}}{\sqrt{\omega(\mathbf{q}j)}}\right] e_{\alpha n}(\mathbf{q}j)\, e^{\,i\mathbf{q}\cdot\mathbf{R}_{ln}} \tag{2.15}$$

Here, $a^{\dagger}_{qj}$ creates a phonon of band-index j at a phonon wavevector $\mathbf{q}$, whereas a_{qj} destroys it.

Chapter 3

The Role of Disorder in the Magnetic Excitations of Quantum Magnets

This chapter is adapted from the paper published as "Disorder-enriched magnetic excitations in a Heisenberg-Kitaev quantum magnet $Na_2Co_2TeO_6$ in Physical Review Letters, ***131****, 076701, (2023) [143].*

In this chapter, we present a co-authored project, where I analyzed how structural disorder caused the anomalous magnetic excitations in Far- infrared (FIR) magnetoabsorption spectra of $Na_2Co_2TeO_6$ (NCTO). I demonstrated that the couplings are strongly affected by the disorder in this compound owing to its relatively weak spin-orbit interaction. I also simulate the inelastic neutron scattering (INS) spectra of NCTO in order to compare it with experimental INS spectra. To estimate the range of disorder, I carry out *ab initio* calculations and find the theoretical spread of magnetic couplings for different possible Na occupancies within the nominally $P6_322$ unit cell. Five unique Na distributions are identified and for each structure, couplings are estimated by exact diagonalization of the full d-orbital model on two-site clusters and projection onto ideal $j_{1/2}$ states, according to the standard des Cloizeaux approach as discussed in chapter 2.

We find that the couplings are strongly affected by the disorder for the first neighbor

Co atoms. We also notice that the local g tensors depend strongly on the random relative locations of the Na atoms around each Co atom. I implement this disorder-induced variation to solve the model at the level of linear spin wave theory using spinW code. On the experimental front, our colleagues used optical magneto-spectroscopy to investigate the magnetic excitations of $Na_2Co_2TeO_6$ in a broad magnetic field range ($0\ \mathrm{T} \leq \mathrm{B} \leq 17.5\ \mathrm{T}$) at low temperature. Our conclusion is that the disorder is important in the spin environment in the search for Kitaev quantum spin liquid states in practicable materials.

These results highlight how strongly structure-dependent magnetic Hamiltonians can be, which is a consistent theme of this thesis.

3.1 Introduction

Quantum spin liquids (QSLs) represent an intriguing phase of matter that can be formed by interacting quantum spins in certain magnetic materials where quantum fluctuations impede the formation of long-range magnetic order even at the lowest temperatures [144–148]. Kitaev's spin-1/2 honeycomb model [145] has attracted considerable attention as it predicts an exotic QSL state with fractionalization of quantum spins into Majorana fermions in a potentially realizable context for real materials. Among Kitaev candidate materials, α-$RuCl_3$ is the most studied due to strong Kitaev interactions and signatures of a QSL state [149–158]. To describe the system, a generalized Heisenberg–Kitaev (gHK) model is frequently employed. Although the precise interactions remain debated [159, 160], analysis of α-$RuCl_3$ within the gHK model indicates significant departures from the ideal Kitaev model, prompting the search for new candidate materials.

Recently, with theoretical studies proposing that the $3d$ electrons with a high-spin d^7 configuration can provide pseudospin $J_{\mathrm{eff}} = 1/2$ with Kitaev interactions [161–164], a Co-based honeycomb structure compound $Na_2Co_2TeO_6$ has been investigated extensively as another candidate to realize Kitaev physics [165–169], together with other Co honeycomb compounds [170–178]. Compared with α-$RuCl_3$, $Na_2Co_2TeO_6$ does not have observable stacking disorder between layers, but does have disorder in the interlayer Na positions [165, 168]. It exhibits a similar zigzag antiferromagnetic (AFM) order with $T_N \approx 27$ K. An

in-plane magnetic field suppresses the magnetic ordering and was suggested to induce a QSL-like spin disordered state followed by a spin-polarized (SP) state above $B_c \approx 10$ T [169, 179]. However, recent elastic neutron scattering revealed that the zigzag Bragg peaks persist up to B_c [180], thus questioning the intermediate QSL scenario. Early powder inelastic neutron scattering (INS) measurements were shown to be compatible with the gHK model, but reported parameters of competing Kitaev- and non-Kitaev interactions vary in a large range [181–184], the majority of which fail to reproduce the relative simplicity of the later-reported single-crystal INS data [184–186]. These discrepancies have led to debate over the correct model, and even the magnetic ground state of $Na_2Co_2TeO_6$ [180, 185, 187, 188]. The robustness of Kitaev-dominant interactions has also been recently questioned [43, 174, 189].

3.2 Results and Discussion

Here, we report on a systematic optical magneto-spectroscopy study of single-crystal NCTO to probe the magnetic excitations in a broad magnetic field range at low temperatures. Our experiment reveals a rich set of in-plane excitation modes across the AFM to SP magnetic phases. Especially we observe a surprisingly large number of excitation modes in the SP state, which is in contrast to the case of α-$RuCl_3$ and cannot be explained by any theoretical models proposed to date. Ab-initio calculations of the magnetic couplings and g-tensors together with polarized optical measurements reveal that the previously unconsidered Na-occupation disorder plays a crucial role in $Na_2Co_2TeO_6$. Theoretical results are further compared with literature-reported INS data and optical magneto-spectroscopy of this work to extract the interaction energies. With a comprehensive picture of the magnetic excitations as well as the non-trivial role of disorder, our work provides new insights and initiates re-thinking of the competing interactions in Kitaev QSL candidate materials.

Millimeter-size $Na_2Co_2TeO_6$ single crystals used in this study were grown by flux method [179]. The crystal structure, following Ref. [168], is illustrated in Fig. 3.1(a). The reported $P6_322$ unit cell contains two formula units; each of the six Na sites is disordered with 2/3 occupied on average. A representative local realization of the Na disorder is shown in Fig. 3.1(b). Far-infared (FIR) transmission spectroscopy was performed on single crystals.

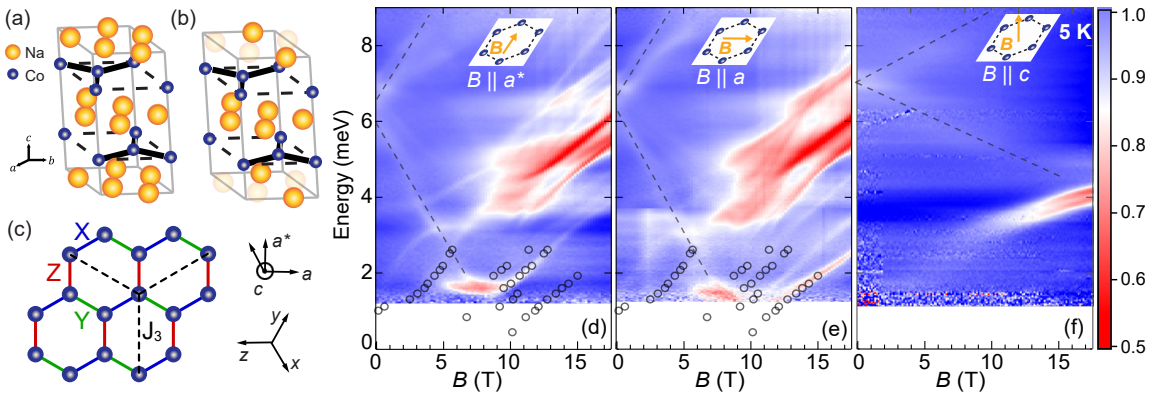

Figure 3.1: (color online) **Unpolarized optical magneto-spectroscopy measurements on $Na_2Co_2TeO_6$.** (a) Average crystal structure with each Na site 2/3 occupied; Te and O atoms are omitted for clarity. (b) Representative structure showing Na-occupation disorder. See section 3.4 for further details. (c) Honeycomb lattice of Co^{2+} ions with nearest neighbor X, Y, Z and third neighbor J_3 bonds indicated. Crystallographic (a, a^*, c) and cubic (x, y, z) coordinates are shown. (d-f) Normalized magneto-transmission measured on single-crystal $Na_2Co_2TeO_6$ at $T = 5$ K with $B \parallel a^*$ (d), $B \parallel a$ (e), and $B \parallel c$ (f). Black circles are excitation modes extracted from the ESR spectra measured on powdered $Na_2Co_2TeO_6$ samples at $T = 5$ K. Dashed lines are guides to the weak excitation modes at ~ 6.5 meV. The normalization procedure and raw ESR spectra can be found in section 3.4.

To probe the lower-energy excitations, electron spin resonance (ESR) spectroscopy was also carried out on powdered samples. More experimental details can be found in section 3.4.

Figures 3.1(d-f) show the color map plots of the normalized FIR transmission intensity measured at $T = 5$ K as a function of excitation energy and magnetic field applied $B \parallel a^*$, $B \parallel a$, and $B \parallel c$. The red color represents strong absorption. The excitation modes below 2.6 meV, extracted from the ESR spectra of powdered $Na_2Co_2TeO_6$ samples, are plotted as black circles in Figs. 3.1(d,e). The magnetic excitations revealed in ESR are well consistent with those observed in the FIR spectra measured on single-crystal samples with the magnetic field applied in-plane (See section 3.4 for detailed comparison of ESR and FIR results). Although the magneto-optical response of $Na_2Co_2TeO_6$ summarized in Figs. 3.1(d-f) displays a quite complex behavior, it is possible to identify three distinct spectral regions with respect to the suggested (T–B) phase diagram [179, 188]: (I) Low-field region ($B < 6$ T) with relatively weak excitations observed. Specifically, for in-plane magnetic fields, a zero-field gap of ~ 1 meV is revealed, which is attributed to magnons according to the reported INS data [186]. In addition, excitations at ~ 6.5 meV, which split into two

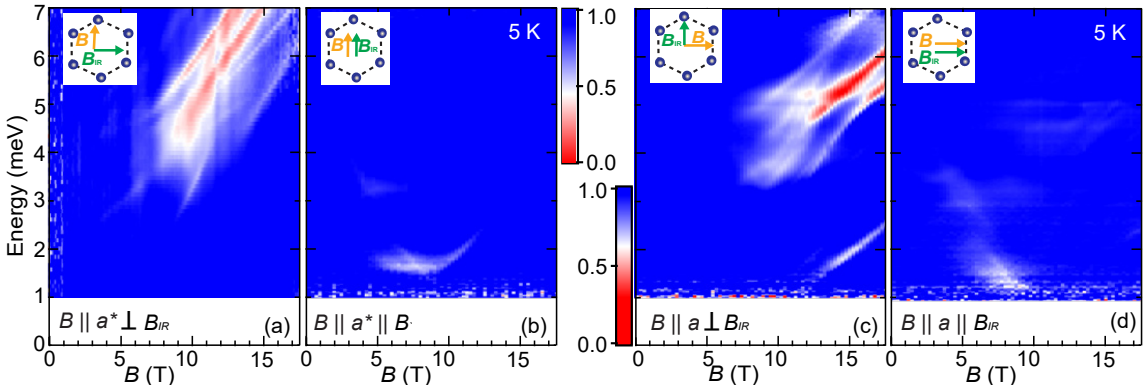

Figure 3.2: (color online) **Polarized magneto-optical response of single-crystal $Na_2Co_2TeO_6$.** Color map plots show normalized FIR transmission intensity measured at $T = 5$ K and with $B \parallel a^* \perp B_{IR}$ (a), $B \parallel a^* \parallel B_{IR}$ (b), $B \parallel a \perp B_{IR}$ (c), and $B \parallel a \parallel B_{IR}$ (d). Top and bottom color bars are for plots in (a,b) and (c,d), respectively.

branches under applied magnetic field with different slopes between in- and out-of-plane (dashed lines in Figs. 3.1(d-f)), are resolved for all field directions. (II) Intermediate-field region (6–9 T) with dispersionless modes at ~ 1.7 meV and in-plane field only, consistent with the proposed spin disordered phase region [179]. (III) High-field ($B > 10$ T) SP state featuring strong magnon-like modes detected for all three field orientations. While two parallel excitation branches with slopes corresponding to $g_c \sim 3.7$ are detected for $B \parallel c$, the spectra of magnetic excitations with in-plane magnetic fields are much richer, indicating a strong anisotropy between in- and out-of-plane interactions. Furthermore, some subtle differences between $B \parallel a^*$ and $B \parallel a$ spectra at low-energy (< 3 meV) are observed. For instance, the visible lowest-energy excitation in the $B \parallel a$ direction (starting from $\sim$10 T and reaching $\sim$2 meV at 17 T) is absent in the $B \parallel a^*$ direction. The exact reason for such difference is uncertain for now, it could be due to in-plane anisotropic exchange interaction, or inhomogeneous magnetic domain structure that still survives in the high-field SP state. The temperature dependence of the FIR magneto-transmission up to 40 K is reported in section 3.4.

The most striking feature of the FIR spectra is the richness of excitations in the high-field in-plane SP state, which are dominated by several strong absorption modes. This is in sharp contrast to the expectation for a pristine sample; the four Co atoms in the unit cell support a maximum of four magnon branches in the SP state. In practice, only

one dominant absorption is expected, as two branches have weak intensity at $k = 0$, and the other two would overlap energetically due to weak interplane coupling. Furthermore, the number of one-magnon modes would be expected to dramatically reduce below B_c, given that the low-field zigzag state is composed of multiple domains, each with a magnetic unit cell twice the volume of the crystallographic cell. These expectations are satisfied for α-$RuCl_3$ [155, 157, 158, 190, 191], but not for $Na_2Co_2TeO_6$.

In principle, the spectra of $Na_2Co_2TeO_6$ may be enriched by multi-magnon and/or fractional excitations, as observed in α-$RuCl_3$ [155, 157, 158, 190–192]. To investigate this possibility, polarized FIR spectroscopy measurements were carried out (Fig. 3.2). Specifically, for both in-plane field directions, $B \parallel a^*$ (Figs. 3.2(a,b)) and $B \parallel a$ (Figs. 3.2(c,d)), the magnetic component of IR light B_{IR} is polarized in the transverse $B \perp B_{IR}$ and longitudinal $B \parallel B_{IR}$ directions, which capture the dominant one-magnon and two-magnon channels, respectively, in the asymptotic high-field limit. The high-field in-plane magnetic excitations are pronounced only in the transverse $B \perp B_{IR}$ channel for both $B \parallel a^*$ and $B \parallel a$ directions. Moreover, all relatively strong excitations exhibit a similar $\mathrm{d}E/\mathrm{d}B$ slope with in-plane g-factor $g_{ab} \sim 4.6$. These results, in concert, suggest that the high-field in-plane magnetic excitations are one-magnon in nature. These findings are compatible with the reported magnetization data, which shows that $Na_2Co_2TeO_6$ is nearly fully polarized at B_c [188, 193]; fluctuations that would be associated with strongly anisotropic couplings are weak, which calls into question the gHK model.

The experimental findings raise several questions: (i) what is the correct model for $Na_2Co_2TeO_6$, and (ii) what is the role of Na disorder? To address these, we investigated, with ab-initio calculations, the theoretical spread of magnetic couplings and g-tensors for different possible Na occupancies within the nominally $P6_322$ unit cell. Five unique Na distributions are identified, one of which is depicted in Fig. 3.1(b) (see section 3.4 for full details). For each structure, couplings were estimated by exact diagonalization of the full d-orbital model on two-site clusters and projection onto ideal $j_{1/2}$ states, according to the standard des Cloizeaux approach [108, 118]. This approach captures all bond-dependent anisotropic couplings [43], but does not include additional ligand exchange processes. It is thus sufficient to demonstrate a strong effect of Na disorder on the couplings, but the

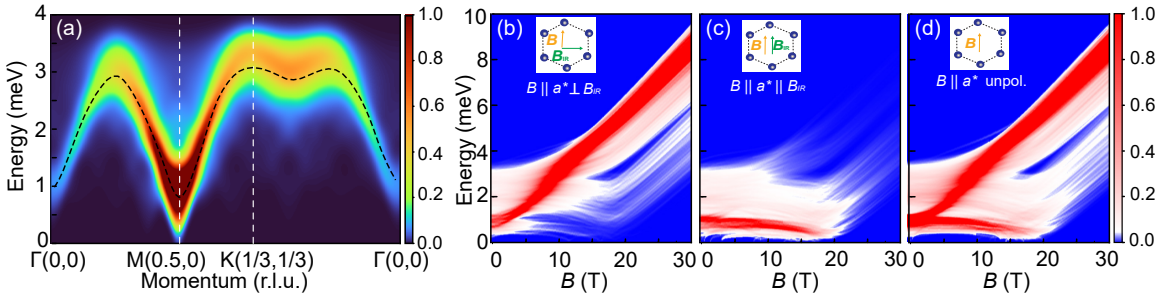

Figure 3.3: (color online) **Model simulations of INS and FIR magneto-absorption spectra** for random J^1 defined by the average values $\overline{J^1_x}, \overline{J^1_y} = -0.13$ meV, $\overline{J^1_z} = -0.24$ meV, $\overline{\Gamma^1_{xy}}, \overline{\Gamma^1_{yx}} = -0.05$ meV, $\overline{\Gamma^1_{xz}}, \overline{\Gamma^1_{zx}}, \overline{\Gamma^1_{yz}}, \overline{\Gamma^1_{zy}} = -0.08$ meV, and a range of values of width 0.8 meV for each. J_3 is Heisenberg matrix with $\overline{J_3} = 1.8$ meV and a range of values of width 0.4 meV. (a) Simulated INS spectra (color plot) as compared with the experimental INS spectra from Ref. [186] (dashed line). (b-d) Simulated optical magneto-spectroscopy spectra with the measurement geometry of $B(\| a^*) \perp B_{IR}$ (b), $B(\| a^*) \| B_{IR}$ (c), and $B \| a^*$ unpolarized (d).

ultimate model will be determined by fitting to experiment. Full calculation results are presented in section 3.4.

The g-tensors reflect the specific spin-orbital composition of the local moments, as determined by competing spin-orbit coupling (SOC) and crystal field splitting of the t_{2g} orbitals of Co. At first consideration, one might expect disorder in the interlayer Na atoms to have little impact on the Co crystal fields. Despite the computed variation of the inter-t_{2g} crystal field across different Co sites in the Na-disordered structures being only 2 to 18 meV, it is significant when compared to the small SOC strength in $3d$ Co, $\lambda_{\mathrm{Co}} \approx 60$ meV. As a consequence, the local g-tensors depend strongly on the random relative locations of the Na atoms around each Co; we find values in the range $g_a, g_b \sim 4.0$ to 5.8, and $g_c \sim 1.1$ to 2.9. The average computed in-plane value of $\overline{g_{ab}} \sim 4.9$ agrees well with the measured slope of the high-field excitations.

The magnetic couplings are $\mathcal{H} = \sum_{ij} \mathbf{S}_i \cdot \mathbb{J}_{ij} \cdot \mathbf{S}_j$, with $\mathbb{J}_Z = [(J_x, \Gamma_{xy}, \Gamma_{xz}), (\Gamma_{yx}, J_y, \Gamma_{yz}), (\Gamma_{zx}, \Gamma_{zy}, J_z)]$ for the Z-bonds, where J (Γ) are the on-diagonal (off-diagonal) exchange constants. The global (x, y, z) coordinate system is defined in Fig. 3.1(c). The corresponding interactions for the X- and Y-bonds can be obtained by C_3 rotation along the c-axis. In the presence of Na disorder, the symmetry of each bond is reduced, such that it is convenient to describe the computed ranges of each coupling constant, denoted $R(...)$. For first neighbors,

we estimate $R(J^1_x, J^1_y) = -0.6$ to 0.2 meV, $R(J^1_z) = 0.1$ to 0.5 meV, $R(\Gamma^1_{xy}, \Gamma^1_{yx}) = 0.2$ to 0.9 meV, and $R(\Gamma^1_{xz}, \Gamma^1_{zx}, \Gamma^1_{yz}, \Gamma^1_{zy}) = -0.3$ to 0.0 meV. Thus, we find that the nearest neighbor interactions are considerably weaker than previous estimates from fitting the powder INS data [180–184], and moreover they vary with Na disorder on a scale similar to their overall magnitude. In contrast, for the third neighbor couplings, we find $R(J^3_\mu) = 2.3$ to 3.5 meV and $R(\Gamma^3_{\mu\nu}) = -0.9$ to -1.3 meV. This corresponds to an AFM XXZ coupling. The employed method tends to overestimate the third neighbor couplings due to underlocalization of the DFT Wannier functions, but the finding of dominant third neighbor interactions is robust. See section 3.4 for full results.

Before addressing the FIR/ESR spectra, given uncertainties in the model and structure of $Na_2Co_2TeO_6$, we first optimize the couplings to better fit reported single-crystal INS spectra [186]. To this end, we consider a simpler model ignoring anisotropy in the third neighbor couplings. The nearest neighbor couplings are taken to be completely random for each bond (any spatial correlations associated with particular Na distributions are ignored), and are selected from a uniform distribution between prescribed limits. The g-tensors are also taken to be completely random symmetric tensors, with fixed ranges, in the global (x, y, z) coordinates, following from the ab-initio results: $R(g_{\mu\nu}) = 3.0$ to 4.8 for $\mu = \nu$ and -1.3 to -0.6 for $\mu \neq \nu$. The model is solved at the level of linear spin wave theory (LSWT) for $8 \times 8 \times 1$ supercells and the resulting spectra are averaged over the three different zigzag domains and 20 different random choices of interactions. Results and details for the final model are shown in Fig. 3.3. Despite having random interactions, the model has a zigzag ground state as a result of the dominant antiferromagnetic J_3 and nearest neighbor couplings that are ferromagnetic on average. The low-energy INS data is perfectly reproduced at the level of LSWT (Fig. 3.3(a)). The smallness of the excitation gap at $k = 0$ results from the overall weakness of the bond-dependent couplings, which is also compatible with the aforementioned immediate saturation of the magnetization at B_c [188, 193]. The existence of a single dominant magnon branch at zero field, despite overlapping response from three zigzag domains, can also be explained by the large J_3 model. With only J_3, the lattice is decoupled into three separate honeycomb sublattices. Different zigzag domains are related by global spin rotations on the decoupled sublattices, which cannot alter the

magnon dispersions. Thus, in the J_3-only model, the zigzag domains have precisely identical magnon dispersions. A similar model was suggested in Ref. [186].

Finally, we address the polarized FIR spectra. LSWT results for the disordered model are shown in Figs. 3.3(b-d). At zero field, the random couplings lead to a significant distribution of the excitation energies over the range of 1–4 meV, which is compatible with the experimental range. Since the disorder breaks all lattice symmetries, the number of observable modes is unchanged at B_c. As expected, the one-magnon modes rapidly lose intensity in the longitudinal channel ($B||B_{\mathrm{IR}}$) with increasing B above B_c. While further elaboration of the model to include spatially correlated disorder may improve agreement with experiment in terms of the precise value of B_c and number of distinct modes, it is already clear that the known Na disorder in $Na_2Co_2TeO_6$ has a sufficient impact to explain the anomalously rich FIR/ESR spectra of Figs. 3.1 and 3.2.

Our finding provides insight into several recent studies. In Ref. [186], the nearly dispersionless (i.e., local) excitations observed at ~ 6 meV are difficult to reconcile with one-magnon excitations without fine tuning. Our FIR data (Figs. 3.1(d-f) dashed lines) provides a possible identification. For all field orientations, this mode splits into two branches at finite B, with energies that follow roughly $dE/dB = \pm 2g$. For in-plane field, the lower branch appears to reach zero energy precisely at B_c. This is suggestive of local $\Delta S \approx \pm 2$ bound states in the zigzag phase, which are not captured by LSWT shown in Fig. 3.3, but may gain intensity from disorder-induced non-collinearity of the spins.

Regarding various complex $Na_2Co_2TeO_6$ phase diagrams, a first-order transition is observed at low temperatures for $B \parallel a^*$ at ~ 6 T with significant hysteresis in the magnetization [168, 179, 193–195]. While initially interpreted as a possible QSL state [179], it is now revealed that well-defined zigzag Bragg peaks survive up to $B_c \approx 10$ T [180]. Interestingly, the populations of the different zigzag domains in $Na_2Co_2TeO_6$ are weakly field-dependent in comparison to α-$RuCl_3$ [196, 197], which has contributed to speculation about an alternative single-domain triple-Q order [185, 195]. Our model favors zigzag order, as does an extensive recent experimental investigation [188]. The dominant interaction (J_3) does not have bond-orientation dependence, which leads to weaker energetic preference for moment orientation within a given zigzag domain, reducing the effectiveness of a field for se-

lecting a particular domain. Furthermore, disordered couplings may locally select domains and pin domain walls, leading to hysteretic magnetization processes that do not constitute transitions out of zigzag order.

3.3 Conclusions

In conclusion, we have reported on the combined experimental magneto-IR/ESR spectroscopy and theoretical study of low-energy magnetic excitations in $Na_2Co_2TeO_6$. To explain the rich anisotropic spectrum of excitations observed in the experiment, we have developed a microscopic model that takes into account all unique possible Na occupancies. Complemented by the modeling of recent INS data, we thus propose a comprehensive picture of magnetic excitations in $Na_2Co_2TeO_6$ that reveals a key role of Na-occupation disorder. The findings highlight the fragility of spin-orbital moments in $3d$ compounds, where weak SOC enhances effects of disorder and distortions. In a more general context, our results further emphasize the necessity to consider disorder in the spin environment in the search for practicable materials potentially hosting Kitaev quantum spin liquid states.

3.4 Supplementary Information

3.4.1 Sample preparation and characterization

Polycrystalline $Na_2Co_2TeO_6$ samples were prepared by a solid-state reaction method. First, fully ground Na_2CO_3 (Alfa, 99.997%), Co_3O_4 (Alfa, 99.7%), and TeO_2 (Alfa, 99.99%) powders were mixed in a stoichiometric molar ratio with 5% excess Na_2CO_3. Next, the mixture was loaded in an alumina crucible and sintered at 850 °C in the air for 40 h. Then, the flux method was used for single-crystal growth. Specifically, polycrystalline $Na_2Co_2TeO_6$ powders were mixed with the flux of Na_2O and TeO_2 in a molar ratio of 1:0.5:2 and gradually heated up to 900 °C at the rate of 3 °C/min in the air. The mixture was retained at 900 °C for 30 h and cooled to 500 °C at 3 °C/h. After it, the furnace was shut down for faster cooling to room temperature.

To confirm the structure and purity of the samples, powder X-ray diffraction (XRD)

measurement was performed with a HUBER imaging-plate Guinier camera 670, using Cu $K_{\alpha 1}$ radiation ($\lambda = 1.54051$ Å). The magnetization and heat capacity characterizations of single-crystalline $Na_2Co_2TeO_6$ samples can be found in Ref. [179].

3.4.2 Magneto-infrared and electron spin resonance measurements

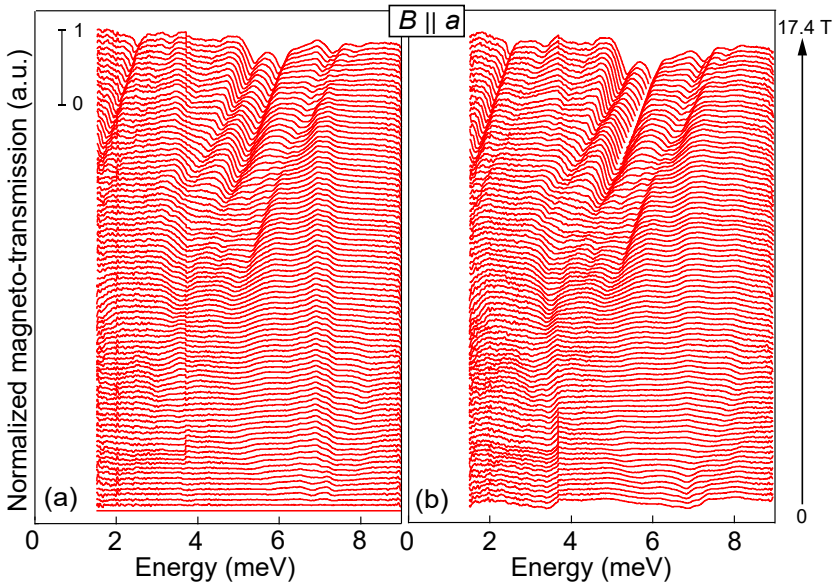

Figure 3.4: (color online) **Normalized far-IR magneto-transmission spectra of $Na_2Co_2TeO_6$.** Comparison of unpolarized relative magneto-transmission spectra, $T(B)/T_{ref}$, of $Na_2Co_2TeO_6$ measured at $T = 5$ K with magnetic field $B \parallel a$. The raw transmission spectra $T(B)$ are normalized by the zero-field (a) or (0-2) T averaged (b) reference. Spectra are shifted vertically for clarity.

Magneto-infrared measurements were performed on oriented $Na_2Co_2TeO_6$ single crystals using the infrared (IR) spectroscopy facility at the National High Magnetic Field Laboratory. The magneto-spectroscopy setup employs a 17.5 T vertical-bore superconducting magnet coupled to a Fourier-transform infrared (FTIR) spectrometer Bruker Vertex 80v. Broadband IR light provided by the FTIR spectrometer is guided via evacuated brass light pipes to the sample space situated at the center of the magnet. The transmitted IR light is delivered to a composite Si-bolometer (IR Labs, Inc.) mounted in the same cryogenic environment cooled by low-pressure helium gas to a temperature of about 5 K. For increased sensitivity in the far-IR (FIR) spectral region of interest, a low-pass THz filter (QMC Instr.) with a cut-off frequency of about 120 cm^{-1} was placed in front of the sample. We used

both Faraday and Voigt experiment geometries with the wave vector of the incoming IR light parallel or perpendicular to the magnetic field direction to measure the $Na_2Co_2TeO_6$ transmission spectra with an out-of-plane ($B \parallel c$) or in-plane ($B \parallel a, a^*$) magnetic field. The polarized FIR measurements were carried out in Voigt geometry only with one linear FIR polarizer (QMC Instr.) placed in front of the sample. The polarization extinction ratio of the actual IR setup was measured as a ratio of the IR transmission intensity through two parallel- or crossed-oriented polarizers placed at the nominal sample position. For the FIR spectral region of interest below 120 cm^{-1}, the measured amount of unwanted polarization leak, α, is about 30%. The experimental data shown Figs. 1 and 2 show relative magneto-transmission corrected for the low-field average spectral function of the instrument as described below.

The color-map plots in Figures 1 and 2 in the main text show field-induced changes in relative magneto-transmission, $T = T(B)/T_{ref}$, where the raw spectra taken at each magnetic field, $T(B)$, are normalized by the low-field, (0-2) T averaged reference spectrum T_{ref}. In Figure 3.4, we compare magneto-transmission spectra normalized by the zero-field reference and the (0-2) T averaged spectra. While both normalization methods reveal the same field-dependent features (i.e., magnetic excitations in this case), the averaged referencing provides a better picture effectively improving the S/N ratio and reducing unphysical features appearing as vertical lines in the $T(B)/T_0$ spectra. For the measurements with polarized IR light, the experimentally measured magneto-transmission includes about 30% contribution of the unwanted polarization-leak component. To account for the polarization leak, this amount of the unwanted component was subtracted from the spectra for target polarization.

High-field electron spin resonance (ESR) spectroscopy measurements were performed at the EMR Facility of the National High Magnetic Field Laboratory. The ESR spectra from powdered $Na_2Co_2TeO_6$ samples were collected by a custom ESR spectrometer equipped with a 15/17T superconducting magnet [198]. Sub-THz wave radiation in the 50–640 GHz frequency range (Virginia Diodes Inc.) is delivered to the sample via oversized cylindrical waveguides. The transmission signal is detected by a wide-band, low-noise, liquid helium cooled InSb bolometer (QMC Inc.)

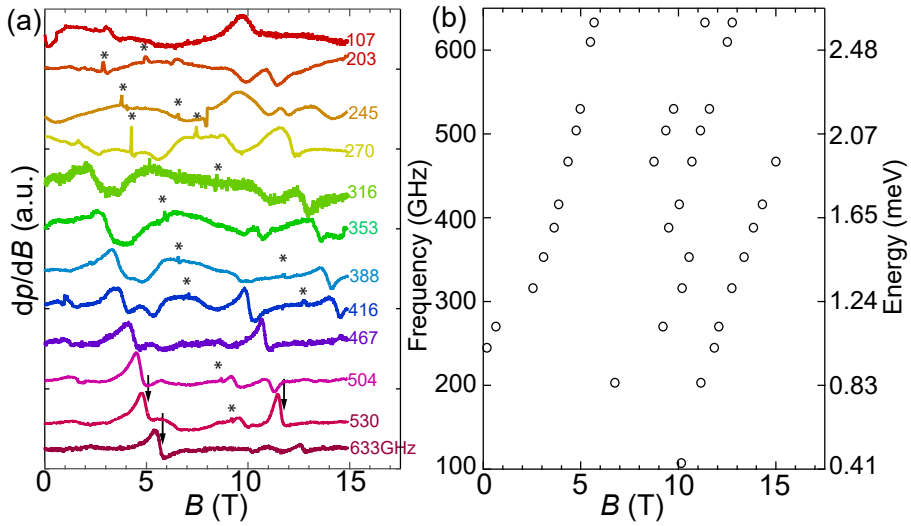

Figure 3.5: (color online) **ESR spectroscopy results of $Na_2Co_2TeO_6$.** (a) The ESR spectra recorded at different frequencies from 107 GHz to 633 GHz, measured on powdered $Na_2Co_2TeO_6$ at $T = 5$ K with applied magnetic field up to 15 T. Step-like features are magnetic excitations of $Na_2Co_2TeO_6$, the positions of which are marked by representative black arrows. Asterisks (*) mark sharp peaks which are excitations from oxygen. Spectra are shifted vertically for clarity. (b) Magnetic excitations as a function of frequency (left axis) or energy (right axis) and magnetic field as extracted from the ESR spectra of (a).

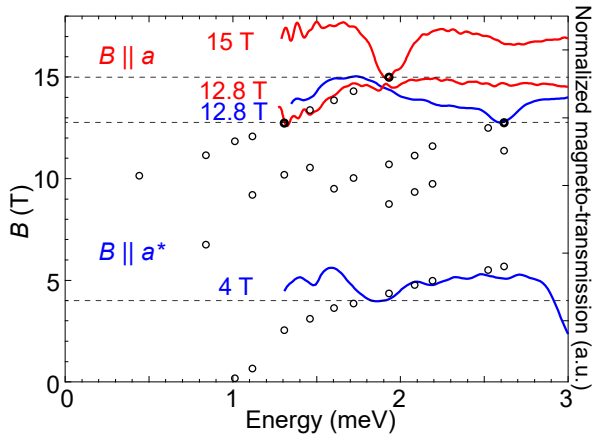

Figure 3.6: (color online) **Comparison of ESR spectra with normalized FIR magneto-transmission spectra of $Na_2Co_2TeO_6$.** Black circles: Magnetic excitations as a function of energy (bottom axis) and magnetic field (left axis) as extracted from the ESR spectra measured on powdered $Na_2Co_2TeO_6$. Color lines: Examples of normalized FIR magneto-transmission spectra (right axis) at fixed magnetic fields measured on single-crystal $Na_2Co_2TeO_6$ with the field direction of $B \parallel a^*$ (blue) and $B \parallel a$ (red). Dip-like features in IR spectra are identified as magnetic excitations of $Na_2Co_2TeO_6$, which is also seen in the ESR spectra at the corresponding magnetic field and energy positions (indicated by dashed lines and thick black circles).

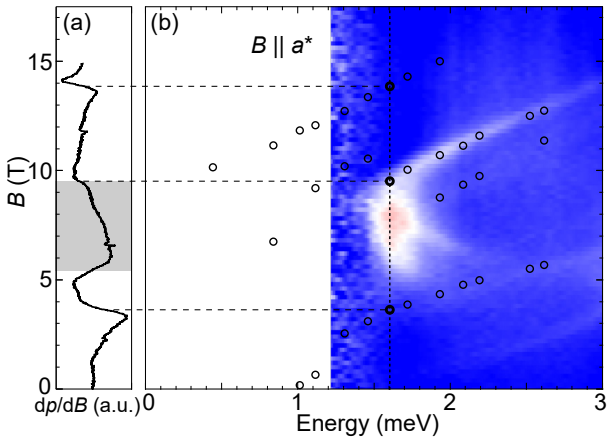

Figure 3.7: (color online) **Comparison of ESR spectrum with normalized FIR magneto-transmission spectra of $Na_2Co_2TeO_6$.** (a) The ESR spectrum recorded at 388 GHz (1.6 meV) measured on powdered sample. (b) Normalized magneto-transmission measured on single-crystal $Na_2Co_2TeO_6$ with $B \parallel a^*$, plotted as color map. Black circles are magnetic excitations as extracted from the ESR spectra. Vertical horizontal line marks the energy where ESR spectrum are recorded for comparison. Step-like features (marked by horizontal dashed lines) in ESR spectra are identified as magnetic excitations. Grey color indicates the broad excitation region of ESR spectrum, where dispersionless excitation is also observed in FIR results.

Figure 3.5(a) presents the ESR spectra at different frequencies from 107 GHz to 633 GHz, measured on powdered $Na_2Co_2TeO_6$ at $T = 5$ K with applied magnetic field up to 15 T. The sharp peaks marked by asterisks are due to a common ESR artifact, the ESR signal from oxygen trapped in the power sample. The extracted $Na_2Co_2TeO_6$ ESR frequencies/energies are plotted in Figure 3.5(b) and in Fig. 2 in the main text.

Figure 3.6 presents a comparison of the ESR results measured on powdered $Na_2Co_2TeO_6$ and normalized FIR magneto-transmission spectra measured on single-crystal $Na_2Co_2TeO_6$ at the field of 12.8 T and 15 T for $B \parallel a$, and 4 T and 12.8 T for $B \parallel a^*$. The magnetic excitations are revealed as dip-like features in the normalized IR spectra. As shown in the figure, in the overlapping field-region, the magnetic excitations revealed from ESR spectra and IR spectra are consistent with each other. Furthermore, ESR spectra measured on powdered $Na_2Co_2TeO_6$ could reveal excitations from both in-plane $B \parallel a$, a^* magnetic-field directions that are only revealed in the $B \parallel a$ direction (the excitation at 12.8 T, $\sim$1.3 meV) or in the $B \parallel a^*$ direction (the excitation at 12.8 T, $\sim$2.6 meV). Figure3.7 presents a comparison of an exemplary ESR spectrum recorded at 1.6 meV and the FIR results. The

magnetic excitations are revealed as step-like features in the ESR spectrum. In addition, a broad excitation region in the ESR spectrum is observed between around 6 – 9T, where dispersionless excitation is also observed in FIR results.

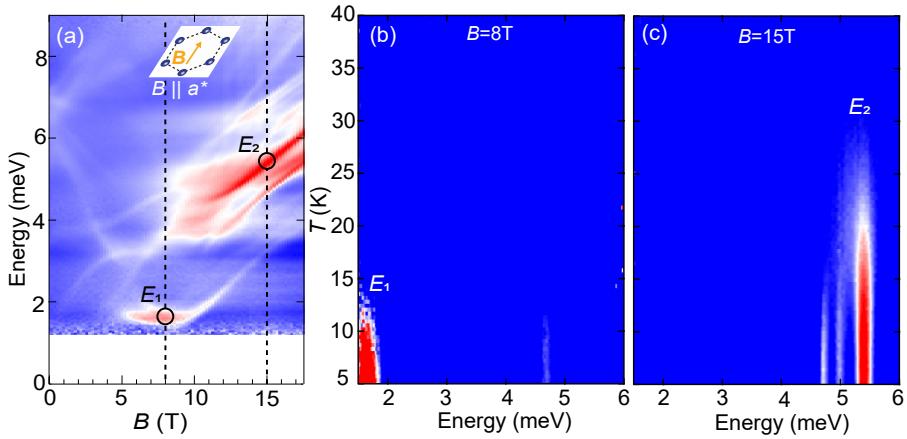

Figure 3.8: (color online) **Temperature-dependent magneto-IR spectroscopy results of $Na_2Co_2TeO_6$.** (a) Color contour plot of the normalized FIR absorption intensity measured on single-crystal $Na_2Co_2TeO_6$ at $T = 5$ K as a function of excitation energy and magnetic field with the field direction of $B \parallel a^*$ (same plot as in Fig. 2(a) in the main text). Dashed lines mark the fixed magnetic fields, 8 T and 15 T, where temperature-dependent magneto-IR spectroscopy measurements were taken. Circles mark the most pronounced magnetic excitations, E_1 and E_2 at 8 T and 15 T, respectively. (b,c) Color contour plot of the normalized (by 40 K spectrum) FIR absorption intensity at fixed magnetic field $B = 8$ T (b) and $B = 15$ T (c) as a function of excitation energy and temperature with $B \parallel a^*$.

3.4.3 Temperature dependence of magnetic excitations

Figures 3.8 presents the temperature-dependent magneto-IR spectroscopy results of NCTO, measured at fixed magnetic fields $B = 8$ T and 15 T with the field direction of $B \parallel a^*$. For temperatures well above the reported antiferromagnetic transition temperature $T_N \sim 27$ K, the spectra are featureless. With cooling, strong absorptions, i.e., excitation modes, develop. Specifically, at $T = 5$ K and below 6 meV, one magnetic excitation (at energy 1.7 meV) is observed for the intermediate magnetic phase region $B = 8$ T, and three magnetic excitations (at energies 4.7 meV, 5.0 meV and 5.4meV, respectively) are revealed for the spin polarized state $B = 15$ T. Focusing on the most pronounced excitations E_1 and E_2, it is further noticed that different excitations have different temperature evolution. While E_1 becomes hardly resolvable above 15 K, E_2 is well recognized for temperature up to ~ 25 K.

3.4.4 Full Details of Ab-initio Calculations

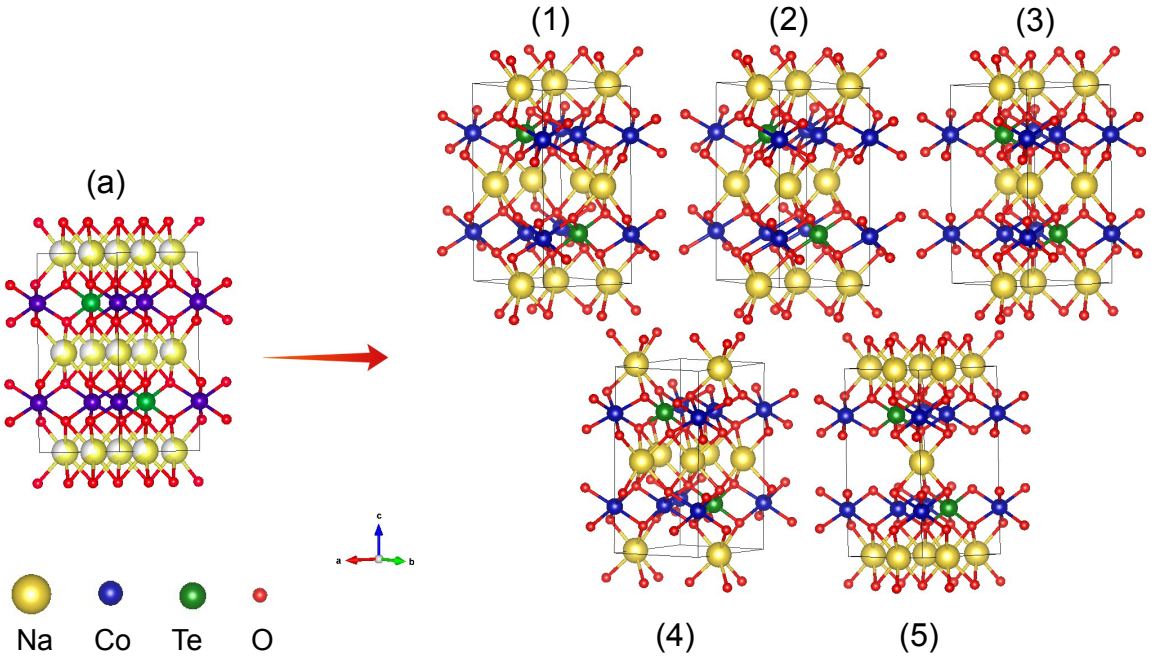

Figure 3.9: (color online) **Different structures employed for modeling Na disorder.** (a) Pristine average structure of $Na_2Co_2TeO_6$ showing fractional occupancy of Na positions. (1–5) Symmetrically inequivalent structures with fixed Na positions employing the same unit cell as the average structure.

In order to understand the effect of Na disorder on the magnetic Hamiltonian, we considered five different cases for the occupancy of the partially occupied Na sites (see Figure 3.9). For structure *1*, *2* and *3*, Na atoms are evenly distributed on Z = 0.0 and 0.5 planes but on different sites (3 sites are available for 2 atoms, 2/3 sites are occupied). For structure *4* three sodium atoms are at located at Z = 0.5 and one is at Z = 0.0. For structure *5* three sodium atoms are at Z = 0.0 and one is at Z = 0.5. On each structure, we first carried non spin-polarized DFT calculations as implemented in the FPLO [199, 200]. The exchange and correlation effect is approximated by Perdew-Burke-Ernzerhof Generalized Gradient Approximation (PBE-GGA) [201]. The spin-orbit coupling is accounted by considering fully relativistic approach. The self-consistent field calculation was carried out by taking dense Monkhorst-Pack grid of $12 \times 12 \times 12$. From these calculations, we computed hopping integrals $\mathcal{H}_{\text{hop}}$, CEF terms $\mathcal{H}_{\text{CFS}}$, and SOC terms $\mathcal{H}_{\text{SOC}}$ via projected Wannier

functions in the d-only basis. In this basis, the total Hamiltonian is given by

$$\mathcal{H} = \mathcal{H}_{\text{hop}} + \sum_i \mathcal{H}_i, \tag{3.1}$$

where $\mathcal{H}_{\text{hop}}$ denotes the hopping between Co sites. $\mathcal{H}_i$ is the local Hamiltonian at each Co site i, which is a sum, respectively, of Coulomb interactions, CEF splitting, and spin-orbit coupling

$$\mathcal{H}_i = \mathcal{H}_U + \mathcal{H}_{\text{CFS}} + \mathcal{H}_{\text{SOC}}. \tag{3.2}$$

The Coulomb interactions are most generally written as

$$\mathcal{H}_U = \sum_{\alpha,\beta,\delta,\gamma} \sum_{\sigma,\sigma'} U_{\alpha\beta\gamma\delta}\ c^\dagger_{i,\alpha,\sigma} c^\dagger_{i,\beta,\sigma'} c_{i,\gamma,\sigma'} c_{i,\delta,\sigma}, \tag{3.3}$$

where $\alpha, \beta, \gamma, \delta$ label different d-orbitals. In the spherically symmetric approximation [202], the coefficients $U_{\alpha\beta\gamma\delta}$ are parameterized by three Slater parameters F_0, F_2, F_4, from which the t_{2g} Kanamori parameters are

$$U_{t2g} = F_0 + \frac{4}{49}\left(F_2 + F_4\right), \tag{3.4}$$

$$J_{t2g} = \frac{3}{49}F_2 + \frac{20}{441}F_4. \tag{3.5}$$

We use $U_{t2g} = 4.25$ eV, and $J_{t2g} = 0.85$ eV. We also take the approximate ratio $F_4/F_2 = 5/8$, which is appropriate for $3d$ elements [203].

The exchange couplings for nearest neighbor (NN) and third nearest neighbor (TNN) Co atoms were then computed for the five different cases by exactly diagonalizing the full d-orbital model on two Co sites, and extracting the couplings via projection. A summary of the actual computed J-values can be found in Table 3.1. We note that these couplings are strongly affected by the disorder for the first neighboring Co atoms whereas for the TNN Co atoms disorder effect is relatively smaller. Further, we may note that interactions between edge-sharing Co(II) atoms are highly sensitive to various details of the local crystal environment, which makes fully ab-initio calculation of precise couplings difficult. We therefore

take seriously the computed signs and disorder-induced variations in the computed couplings, but search for an optimized model to fit the experimental data, as discussed in the main text. We also note that this method tends to overestimate third neighbor interactions, most likely due to underlocalization of the d-orbital Wannier functions at the GGA level.

Table 3.1: Computed J-values for different disordered structures of $Na_2Co_2TeO_6$ with the exact diagonalization of full d-orbital model. U_{t2g} = 4.25 eV and J_{t2g} = 0.85 eV is used for the calculation.

2*Bond-direction	J-matrix elements (meV)								
	J_{xx}	J_{xy}	J_{xz}	J_{yx}	J_{yy}	J_{yz}	J_{zx}	J_{zy}	J_{zz}
Structure-*1* (First neighbor)									
Z-bond	-0.62	0.61	-0.08	0.61	-0.61	-0.08	-0.08	-0.08	0.08
Y-bond	-0.10	-0.15	0.52	-0.14	0.28	-0.15	0.52	-0.15	-0.24
X- bond	0.28	-0.13	-0.15	-0.15	-0.10	0.52	-0.16	0.52	-0.23
Structure-*1* (Third neighbor)									
Z-bond	2.26	-0.98	-1.07	-0.98	2.26	-1.08	-1.08	-1.08	3.19
Y-bond	2.46	-1.09	-1.20	-1.09	2.43	-1.21	-1.20	-1.21	3.53
X-bond	2.43	-1.09	-1.20	-1.09	2.46	-1.20	-1.20	-1.21	3.53
Structure-*2* (First neighbor)									
Z-bond	-0.57	0.87	-0.17	0.36	-0.40	0.03	0.00	-0.28	0.11
Y-bond	-0.18	-0.26	0.51	-0.02	0.20	-0.02	0.51	-0.26	-0.18
X-bond	0.11	-0.28	-0.00	0.03	-0.41	0.36	-0.17	0.87	-0.56
Structure-*2* (Third neighbor)									
Z-bond	2.77	-1.20	-1.08	-0.91	2.29	-0.91	-1.09	-1.19	2.74
Y-bond	2.87	-1.25	-1.14	-0.95	2.35	-0.96	-1.14	-1.25	2.87
X-bond	2.74	-1.19	-1.09	-0.91	2.29	-0.92	-1.08	-1.20	2.78
Structrue-*3* (First neighbor)									
Z-bond	-0.41	0.87	-0.30	0.36	-0.55	-0.01	0.03	-0.17	0.11

Table 3.1: Computed J-values for different disordered structures of $Na_2Co_2TeO_6$ with the exact diagonalization of full d-orbital model. U_{t2g} = 4.25 eV and J_{t2g} = 0.85 eV is used for the calculation.

2*Bond-direction	J-matrix elements (meV)								
	J_{xx}	J_{xy}	J_{xz}	J_{yx}	J_{yy}	J_{yz}	J_{zx}	J_{zy}	J_{zz}
Y-bond	-0.41	-0.30	0.87	0.03	0.11	-0.17	0.36	-0.00	-0.55
X-bond	0.18	-0.24	-0.24	-0.03	-0.22	0.52	-0.03	0.52	-0.22
Structure-*3* (Third neighbor)									
Z- bond	2.32	-1.19	-1.19	-0.91	2.75	-1.09	-0.91	-1.09	2.72
Y-bond	2.32	-1.19	-1.19	-0.91	2.72	-1.09	-0.91	-1.09	2.75
X-bond	2.39	-1.26	-1.26	-0.96	2.87	-1.15	-0.96	-1.15	2.87
Structure-*4* (First neighbor)									
Z-bond	0.21	0.25	-0.18	0.45	0.21	-0.29	-0.27	-0.17	0.46
Y-bond	-0.23	-0.04	0.33	-0.30	0.28	-0.10	0.59	-0.18	-0.19
X-bond	0.29	-0.03	-0.18	-0.30	-0.22	0.59	-0.11	0.32	-0.17
Structure-*4* (Third neighbor)									
Z-bond	2.96	-1.17	-1.14	-1.34	2.97	-1.23	-1.23	-1.13	2.45
Y-bond	2.91	-1.15	-1.12	-1.29	2.88	-1.20	-1.20	-1.10	2.44
X-bond	2.87	-1.15	-1.10	-1.28	2.91	-1.19	-1.20	-1.12	2.43
Structrue-*5* (First neighbor)									
Z-bond	0.21	0.45	-0.29	0.25	0.21	-0.18	-0.17	-0.27	0.46
Y-bond	-0.22	-0.31	0.59	-0.04	0.29	-0.18	0.32	-0.10	-0.17
X-bond	0.28	-0.29	-0.09	-0.04	-0.24	0.34	-0.19	0.59	-0.19
Structure-*5* (Third neighbor)									
Z-bond	2.97	-1.34	-1.23	-1.17	2.96	-1.14	-1.13	-1.23	2.45
Y-bond	2.91	-1.28	-1.19	-1.15	2.87	-1.10	-1.12	-1.20	2.43
X-bond	2.88	-1.29	-1.21	-1.15	2.92	-1.12	-1.10	-1.20	2.44

3.4.5 Additional Results from FIR/ESR Simulations

For comparison with the FIR and ESR measurements presented in the main text, we show in Figure 3.10 full results of simulations using the model of disordered interactions discussed in the main text. It may be emphasized that these simulations employ linear spin wave theory, which only captures one-magnon excitations. Some panels are repeated from the main text for ease of comparison. The different slopes for $B||a$ and $B||c$ are related to the differences of the g-values.

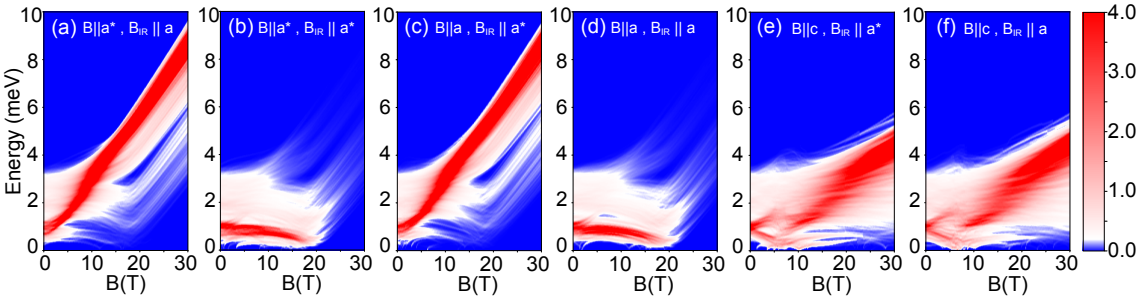

Figure 3.10: (color online) **Model simulations of polarized FIR/ESR spectra** for random nearest neighbor couplings defined by the average values $\overline{J_x^1}, \overline{J_y^1} = -0.13$, $\overline{J_z^1} = -0.24$, $\overline{\Gamma_{xy}^1}, \overline{\Gamma_{yx}^1} = -0.05$, $\overline{\Gamma_{xz}^1}, \overline{\Gamma_{zx}^1}, \overline{\Gamma_{yz}^1}, \overline{\Gamma_{zy}^1} = -0.14$, and a range of values of width 0.8 meV for each. $\overline{J_3}$ =+1.8 with a range of values of width 0.4. (a) $B(\parallel a^*) \perp B_{IR}$, (b) $B(\parallel a^*) \parallel B_{IR}$, (c) $B(\parallel a) \perp B_{IR}$, (d) $B(\parallel a) \parallel B_{IR}$, (e) $B(\parallel c) \perp B_{IR}||a^*$, and (f) $B(\parallel c) \perp B_{IR}||a$.

Chapter 4

Layer-Dependent Anisotropy in Quantum Magnets due to Distortions

*This chapter is lightly edited version of the paper "Magnetic anisotropy reversal driven by structural symmetry-breaking in monolayer α-$RuCl_3$" as published in Nature Materials **22**,50 (2023) [132].*

In this chapter, we present the collaborative project that reports the reversal of magnetic anisotropy in monolayer α-$RuCl_3$ due to structural symmetry breaking. α-$RuCl_3$ is a layered van der Waals material that is extensively studied for its possibility to host Kitaev physics. We address this material again in later chapter. In bulk α-$RuCl_3$, the in-plane magnetic field of $\sim$7-8 T can suppress zigzag anti-ferromagnetic ground state whereas the critical field of $\sim$ 30 T or higher is required for the out-of-plane field to drive the ground state to a spin-disordered state. However, for the monolayer α-$RuCl_3$, the evolution of magnons with magnetic field indicates a clear change in the magnetic anisotropy from easy plane to easy axis. This experimental peculiarity is associated with the deviation of the monolayer structure from its bulk crystal.

In order to rationalize the structural dependence of the magnetic response, I investigate the trends in the magnetic couplings via ab-initio calculations for different distorted

structures. We notice that the reversal of magnetic anisotropy for monolayer α-$RuCl_3$ because of the modification of the spin Hamiltonian $\mathcal{H} = \sum_{i,j} \mathbf{S}_i.\mathbf{M}_{ij}.\mathbf{S}_j$ due to the observed distortion. For experimental measurement, our colleagues use a combination of tunnelling spectroscopy, magnetotransport, electron diffraction to study the layer-dependent magnons, magnetic anisotropy, structure and exchange coupling in atomically thin samples. Our work opens the door to the possible exploration of Kitaev physics in the true two-dimensional limit.

4.1 Introduction

The Kitaev model is a celebrated spin-$\frac{1}{2}$ model on a two-dimensional honeycomb lattice with bond-dependent Ising interactions [145], that features a highly entangled quantum spin liquid (QSL) ground state, fractionalized Majorana excitations and a series of magnetic-field-induced quantum phase transitions [145, 204–206]. The search for materials realizing the Kitaev model has been an ongoing challenge for over a decade and may potentially lead to applications in fault-tolerant topological quantum computing [207]. Yet the unavoidable presence of non-Kitaev interactions (Heisenberg, off-diagonal, next nearest neighbour and so on) almost always drives the ground state away from the QSL phase, and a careful tuning of the exchange parameters is needed [56, 117, 208, 209].

The layered van der Waals material, α-$RuCl_3$, is a particularly promising candidate to realize Kitaev physics [58, 210]. Although the ground state is zigzag (ZZ) antiferromagnetic (AFM), this ordering can be suppressed with the application of an $\sim$ 6–8 T in-plane magnetic field. The presence of a half-integer thermal quantum Hall effect has been reported in this intermediate phase at low temperature [211, 212], while an unusual continuum of magnetic excitations can be seen even without a magnetic field, that persists far above the Néel temperature ($T_N \approx$ 7–8 K) [66, 213]. Both observations hint at α-$RuCl_3$ being in proximity to a QSL, making it a current subject of intense scrutiny. Yet from a theoretical point of view, a QSL induced by an in-plane field generally cannot be accounted for, as most calculations for α-$RuCl_3$ show Kitaev phases more broadly emerging from an out-of-plane field [114, 206, 214–216]. Due to the strong 'easy-plane' magnetic anisotropy of bulk

crystals, however, prohibitively high fields above 30 T are required to access such states [217–219].

4.2 Results and Discussion

The strong coupling between the spin, charge and lattice degrees of freedom in α-$RuCl_3$ presents an exciting opportunity to tune its magnetic interactions via changing dimensionality, the aim of the present study. Moreover, pure monolayer systems are in principle expected to more closely realize the Kitaev model compared with their bulk counterparts [220]. To this end, we start by exfoliating α-$RuCl_3$ crystals on oxidized silicon wafers within a nitrogen-filled glove box and identifying their thickness by optical reflection contrast. To confirm that the thinnest flakes are indeed monolayers, we pick up these samples, encapsulate them with monolayer graphene, and transfer them to 10-nm-thick silicon nitride membranes for three-dimensional electron diffraction measurements. Fig. 4.1**a** shows an electron diffraction pattern of such a structure. Some of the fundamental Bragg peaks of α-$RuCl_3$ used for determining the monolayer structure are circled, although the graphene peaks (along the thick grey circle) can be seen as well. Measuring relative to the graphene peaks, the in-plane lattice constant of our exfoliated α-$RuCl_3$ is determined to be 5.9981–6.0088 Å, which is consistent with the value for the bulk crystal and thus indicates negligible overall strain [221, 222]. By tilting the sample, we can measure the diffraction spots as a function of out-of-plane crystal momentum (k_z). A side-view schematic of the Bragg rod structure for several of the monolayer (1L) α-$RuCl_3$ peaks is shown in Fig. 4.1**b**, and the experimental Bragg rod intensities are shown in Fig. 1c as discrete points together with their expected values in solid lines. In particular, the $(1\bar{2}10)$ and $(\bar{1}2\bar{1}0)$ peaks exhibit a reduction of symmetry from the ideal crystal. As the k_z dependence for bilayer (2L) and trilayer (3L) crystals are markedly different, we can confirm our ability to exfoliate and encapsulate α-$RuCl_3$ crystals down to monolayer thickness.

It has been previously demonstrated that inelastic electron tunnelling spectroscopy (IETS) is a powerful tool to probe for spin waves in ultrathin insulating magnets in the $\sim$ 1–10 meV range [223, 224], the same energy window where various magnetic excitations have

been observed in bulk α-$RuCl_3$ [66, 149, 151, 153, 155, 157, 158, 190, 213, 222, 225, 226]. We thus fabricate a series of metal/α-$RuCl_3$ /metal tunnel junctions in inert atmosphere to carry out temperature- and magnetic-field-dependent IETS on 1L, 2L and 3L α-$RuCl_3$ samples. To maximize inelastic electron tunnelling, the metal should possess a sizeable Fermi surface with a substantial density of states [227]. We mostly use ultrathin ($< 10nm$) T_d-$MoTe_2$ as our metal electrode, although graphene shows qualitatively similar behaviour. A side-view illustration of our device and measurement geometry is shown in Fig. 4.1**d**, and a colourized optical image of a representative device is shown in Fig. 4.1**e**. Hexagonal boron nitride (hBN) flakes are used as encapsulation layers for protection.

The upper panel of Fig. 4.1**f** shows the measured a.c. conductance ($\frac{dI}{dV}$; I, current; V, voltage) of a 1L tunnel junction at 2 K as a function of the d.c. voltage. Subtle steps in the curve can be seen centred at $\sim \pm$ 1 mV, which can be interpreted as increases in the tunnelling conductance when the potential difference across the electrodes reaches the energy of a particular inelastic excitation in α-$RuCl_3$ [223, 224, 228]. These can be seen more clearly as peaks in the numerical derivative ($\frac{d^2I}{dV^2}$) shown in the lower panel of Fig. 4.1**f**. To extract the position and shape of the peaks, we fit them to a pair of Lorentzians (blue) on top of a background (grey). The resultant fitting is shown in red, and closely traces the experimental result. We next investigate the dependence of these excitation peaks on temperature across samples of different thicknesses to understand whether they are of magnetic or phononic nature.

Figure 4.2**a** shows the normalized and background-subtracted $\frac{d^2I}{dV^2}$ spectrum for 1L, 2L and 3L devices from 2 K to 10 K in a two-dimensional false-colour plot for positive bias. The trace at the base temperature is overlaid in blue as a reference. The mode at $\sim$1 meV appears in all three devices at low temperature and disappears above $\sim$8 K. This is near the T_N measured for the bulk crystal [222, 225] which suggests a magnetic origin. Indeed, phonon features have been observed in this energy range [229], but they persist up to room temperature. Linear spin wave and exact diagonalization calculations based on ab initio studies show a large magnon scattering intensity near 1 meV at the Y and M points [192], while several experiments have reported bulk magnons near this energy [149, 151, 157]. We have further integrated the previous bulk magnon intensity calculations across the Brillouin

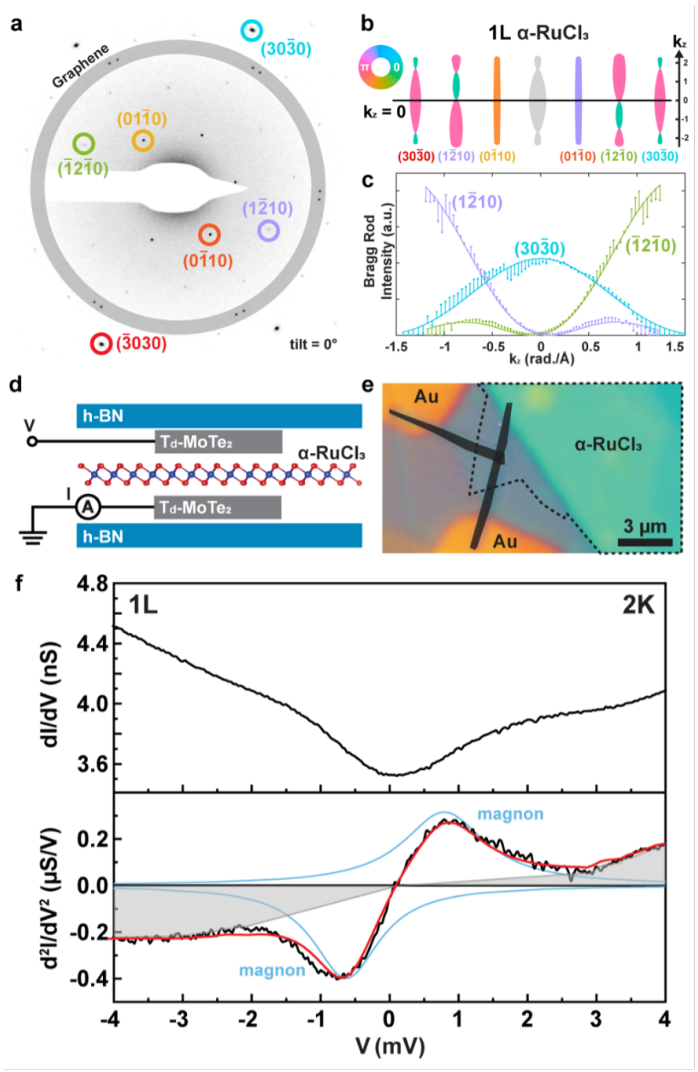

Figure 4.1: Three-dimensional electron diffraction and demonstration of IETS measurements on 1L α-$RuCl_3$. **a**, Electron diffraction pattern for graphene- encapsulated 1L α-$RuCl_3$ at 0° tilt. Bragg peaks for graphene layers are marked by a thick grey circle. Several α-$RuCl_3$ Bragg peaks selected for analysis are circled. **b**, Schematic of calculated out-of-plane momentum (k_z) dependence for the various Bragg rods of 1L α-$RuCl_3$ chosen in **a**. The thickness and colour indicate the complex magnitude and phase of the structure factor, respectively. **c**, Experimental Bragg intensities (scatter points) for (1$\bar{2}$10), ($\bar{1}$2$\bar{1}$0) and (30$\bar{3}$0) peaks, plotted as a function of k_z, show great agreement with a fitted kinematic model (lines) of 1L α-$RuCl_3$. Vertical lines are the residuals from fitting the kinematic model (solid lines) to experimental data (scatter points). **d**, Side-view schematic of an IETS device with vertical T_d-$MoTe_2$ contacts to few-layer α-$RuCl_3$. **e**, Colorized optical image of a 1L α-$RuCl_3$ device. Black shaded areas represent T_d-$MoTe_2$, and dashed lines outline a α-$RuCl_3$ flake. **f**, Representative IETS results for 1L α-$RuCl_3$ taken at 2 K. The upper panel shows the a.c. tunnelling conductance $\frac{dI}{dV}$ as a function of applied d.c. voltage, showing subtle steps due to magnon excitations at both positive and negative voltages. The lower panel shows the numerical derivative (black trace) of the experimental $\frac{dI}{dV}$ curve, $\frac{d^2I}{dV^2}$, together with results from the fitting (grey, background; blue lines, Lorentzian fits to magnon peaks; red, overall fit).

zone (see 4.5.3), and the resultant spectrum indeed exhibits a peak at ∼1 meV. Our observed mode can thus be attributed to the lowest-energy excitation of the ZZ AFM order.

The smaller overall conductance of the thicker 3L device allows us to probe with IETS at higher voltages. Between 5–10 meV, a broad excitation spectrum is observed that persists up to the highest temperature measured with no apparent discontinuity at T_N. This is consistent with the continuum excitations identified in bulk crystals by Raman and neutron scattering, which have been discussed to be connected to fractionalized and/or incoherent excitations [66, 157, 158, 213]. Our results thus show that such unconventional magnetic signatures persist down to at least 3L samples.

To determine T_N more precisely for different thicknesses, we start by fitting Lorentzians to the low-energy mode in the manner described above. This function is known to be a convolution of the intrinsic spectral weight with a temperature-dependent thermal broadening function

$$\chi(V) = \frac{1}{kT} e^x \frac{(x-2)(e^x + x + 2)}{(e^x - 1)^3} \tag{4.1}$$

where $x = \frac{eV}{kT}$ (e, electron charge; k, Boltzmann constant; T, temperature), and a temperature-independent instrument broadening function [228]. The latter is negligible for our measurement conditions. We thus extract the intrinsic peak by deconvolving the fitted experimental curve with χ and integrating the resultant intensity. These values are plotted as a function of temperature in the main panels of Fig. 4.2**b** for the three samples. The intercept of a linear fit applied to the data at low temperature yields T_N, values for which are explicitly shown in the inset as a function of sample thickness. The range of T_N measured for high-quality bulk crystals is marked by the grey band. Unlike Heisenberg(-like) magnets obeying the Mermin–Wagner theorem [230], the critical temperature for α-$RuCl_3$ remains essentially unchanged down to a monolayer.

In bulk α-$RuCl_3$, magnons can evolve nonmonotonically with the application of an in-plane magnetic field [155, 157, 158, 226]. For example, the magnons at the Γ point first shift down to lower energies with increasing field, reaching a minimum at 6–8 T before shifting up. This critical field has been suggested to host an intermediate QSL region (between the ZZ ground state and high-field paramagnetic state) [157, 211, 212], an idea that remains

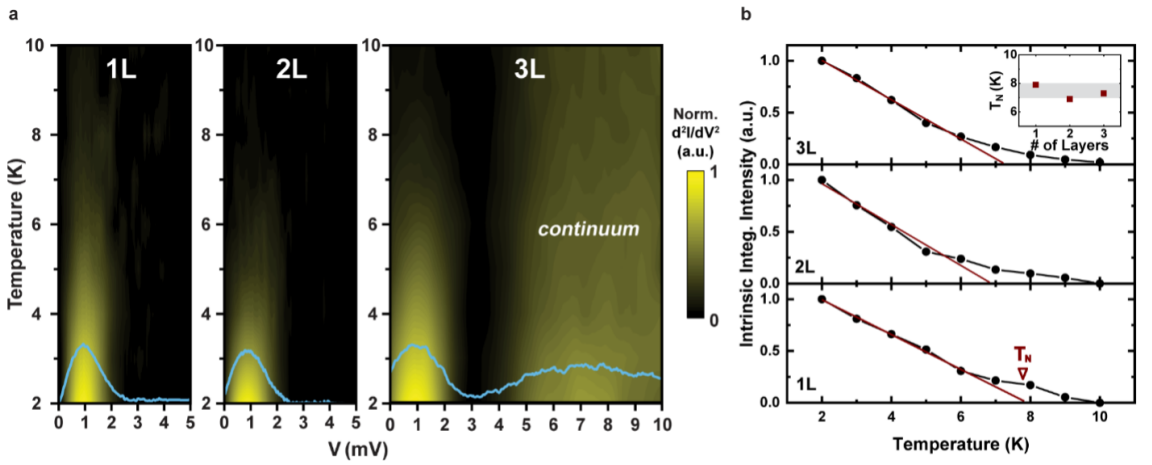

Figure 4.2: Temperature-dependent IETS of few-layer α-$RuCl_3$. **a**, False colour plot of normalized and background-subtracted $\frac{d^2I}{dV^2}$ spectra for 1L, 2L and 3L α-$RuCl_3$ from 2 K to 10 K at positive d.c. bias. The trace at 2 K for each thickness is overlaid in blue. A broad excitation between ∼5 meV to ∼10 meV is observed for 3L and attributed to the magnon continuum. **b**, Intrinsic integrated intensity of ∼1 meV magnon for 1L, 2L and 3L α-$RuCl_3$ at each temperature. The data points from 2 K to 6 K are utilized for linear fittings (red lines), whose x intercepts yield T_N. The inset shows the thickness-dependent T_N for 1L, 2L and 3L α-$RuCl_3$, all of which fall in the range of 7–8 K (grey band), which corresponds to the range reported for high-quality bulk crystals.

controversial, in part because theoretical studies have only identified models with QSL phases induced by out-of-plane fields [114, 206, 214–216]. Due to the easy-plane anisotropy of bulk crystals, however, an out-of-plane field of $\gtrsim$ 30 T is needed to change the magnetic state, rendering such predicted QSLs largely inaccessible [114, 192, 217–219]. We thus proceed to measure the low-energy magnon for all three sample thicknesses with changing magnetic field. In Fig. 4.3**a**, we show 1L, 2L and 3L IETS spectra taken at 2 K for in-plane magnetic field ($B_{\parallel}$) between 0 and 14 T (in 1 T increments), with the traces background subtracted and offset for clarity. To determine the magnon energies more quantitatively, we performed a Lorentzian fit for each trace, and the extracted peak positions are marked by the inverted grey triangle in Fig. 4.3**a** and plotted explicitly in Fig. 4.3**b** with changing $B_{\parallel}$. The 2L and 3L samples show qualitatively similar characteristics—with increasing field, the magnon energy first decreases and then increases, although the field at which the minimum energy occurs appears to be slightly larger for 2L. These results can be compared with calculations for the momentum-integrated bulk magnon intensity with changing in-plane

magnetic field (see 4.5.3). In addition, we observe that the high-energy continuum feature for 3L also changes with in-plane field, which is consistent with its magnetic origin.

By contrast, the magnon for 1L is essentially unchanged with a magnetic field up to 14 T, which suggests that the critical in-plane field necessary to drive the monolayer out of the ZZ state is pushed to a substantially higher value. This trend is captured by the thick blue line in Fig. 4.3**b**. We further note that the observed magnon stiffening for 1L appears to be independent of whether the field is directed along either of the two in-plane crystalline axes.

Figure 4.3**c** shows the out-of-plane field dependence ($B_\perp$) of the IETS spectra. Here, an opposite trend is observed with changing thickness. The 3L has the stiffest response, consistent with the result for bulk crystals [225], while the low-energy peak position for both 2L and 1L exhibit more curvature with field. Interestingly, a secondary peak at higher energy also develops for the latter samples at finite fields. We have fit all the observed peaks to Lorentzians, and the positions are marked in Fig. 4.3**c** by grey and magenta inverted triangles and plotted explicitly in Fig. 4.3**d** as a function of $B_\perp$. At high fields, the secondary peaks appear to shift with field at roughly twice the rate compared with the low-energy magnon, suggesting that they may originate from two-magnon excitation [155, 157, 158, 192] . The larger curvature exhibited by this higher-energy mode also allows us to clearly identify the critical field for which the energy is minimum—it shifts to higher values with increasing thickness. This trend is captured by the thick orange line in Fig. 4.3**d** and is consistent with the extremely large out-of-plane critical field expected for the bulk crystal. Taken together, the results of Fig. 4.3 suggest that the magnetic anisotropy is reversed from easy-plane anisotropy for bulk crystals to easy-axis (out-of-plane) anisotropy for 1L α-$RuCl_3$. Such a change is striking; however, we must ascertain whether it is intrinsic to monolayer samples or a result of proximity to the T_d-$MoTe_2$, a system with strong spin–orbit coupling.

To address this issue, we have fabricated an ultrashort two-terminal device for 1L α-$RuCl_3$ with both few-layer graphene electrodes and top and bottom gates to investigate the field dependence of lateral transport. A colorized scanning electron microscope image and side-view schematic of the device are shown in Fig. 4.4**a**. The sample is only in contact with

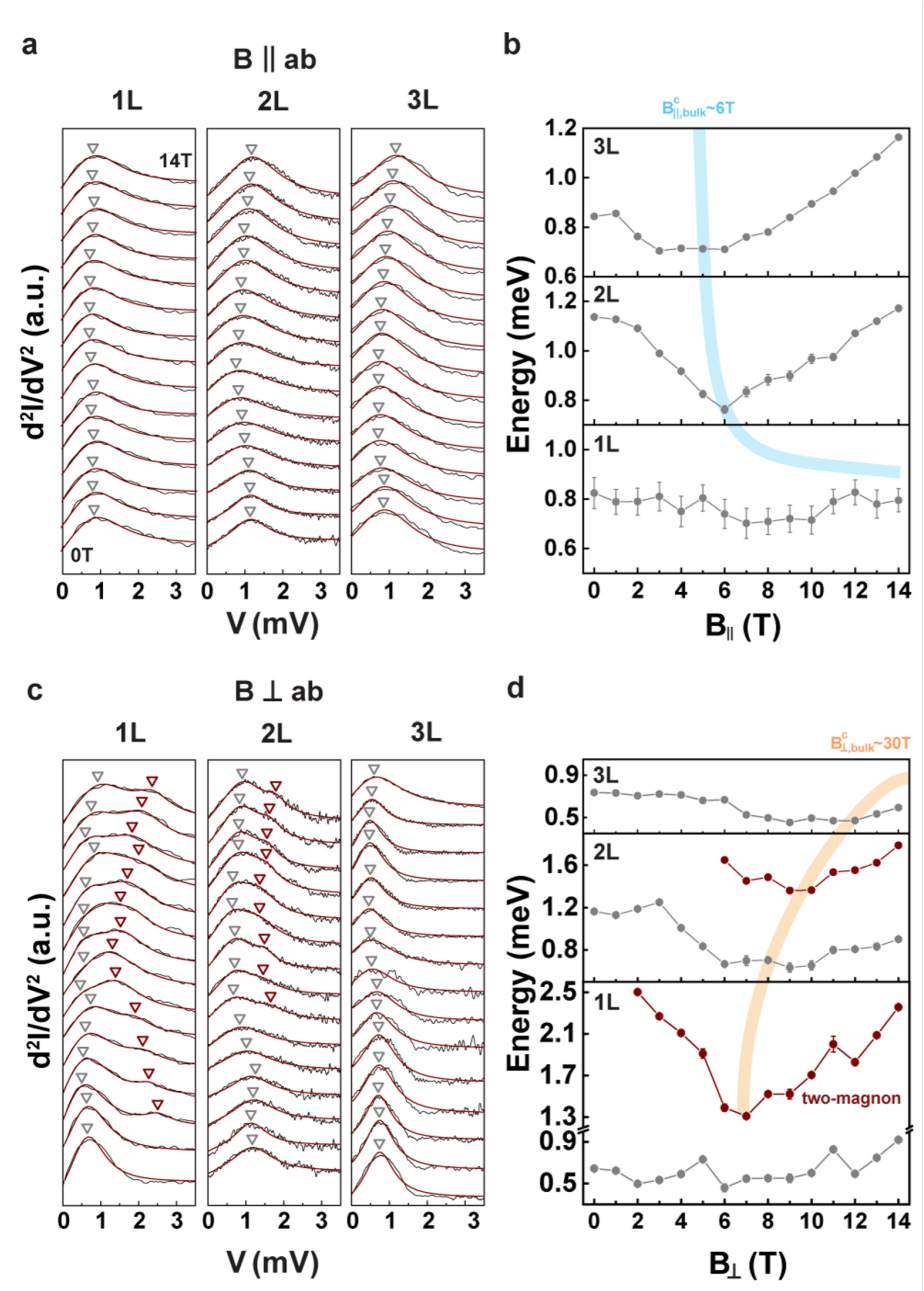

Figure 4.3: Magnetic-field-dependent IETS on few-layer α-$RuCl_3$. a–d, The 1L, 2L and 3L α-$RuCl_3$ spectra (black lines) with changing $B_\parallel$ (**a**) and $B_\perp$ (**c**) from 0 T to 14 T in 1 T increments and offset for clarity. Lorentzian fitting and background subtraction is performed for each $\frac{d^2I}{dV^2}$ trace (red lines). The extracted peak positions are marked by the inverted grey and magenta triangles and plotted explicitly as a function of $B_\parallel$ (**b**) and $B_\perp$ (**d**). Grey points are results for low-energy magnons, and magenta points are secondary peaks at higher energy, which correspond to two-magnon scattering at high fields. The thick blue and orange lines capture trends in the changing critical field with thickness, for $B_\parallel$ and $B_\perp$, respectively. Error bars represent standard errors of the peak position obtained from Lorentzian fitting of the IETS spectra. In most cases, the size of the data point is larger than the error bars.

hBN across the channel (length, $\sim$ 300 nm). Figure 4.4**b** shows the d.c. current–voltage dependence at base temperature for different gate values. Due to the insulating nature of α-$RuCl_3$, the sample shows a measurable current only at low bias when large positive gate voltages are applied (electron doping). In the most conductive state (top gate voltage V_{TG} = 9 V, bottom gate voltage V_{BG} = 6 V), we have measured the a.c. conductance upon sweeping the magnetic field (both in plane and out of plane) continuously, and the results are plotted in Fig. 4.4**c** for several different temperatures. Overall, there is very little change with the in-plane field, consistent with this field direction being along the hard axis. By contrast, there is a larger change when the field is applied along the easy axis, out of plane. Moreover, a marked kink can be seen in the magneto-conductance at $B_\perp \approx 6.5$ T at low temperatures. This coincides with the critical field for the two-magnon feature measured by IETS. Upon raising the temperature, the kink gradually disappears above T_N. These results indicate that the magnetic anisotropy reversal in monolayer α-$RuCl_3$ is likely of intrinsic origin as opposed to proximal contact with T_d-$MoTe_2$.

It is well understood that spin moments in α-$RuCl_3$ are strongly coupled to the charge and lattice degrees of freedom [56, 114, 159, 231, 232]. In particular, electron transfer effects have been previously observed in various two-dimensional heterostructures incorporating α-$RuCl_3$ [233]. Theoretical analysis shows that the magnetic anisotropy is unlikely to be affected by doping, however [220]. Thus, a more probable cause is that the structure of 1L α-$RuCl_3$ deviates from that of the bulk crystal. To investigate whether this is the case, we again turn to electron diffraction measurements performed on the monolayer sample. By carefully fitting the k_z dependence for the various Bragg peaks, we observe three primary distortions of the honeycomb lattice of edge-sharing $RuCl_6$ octahedra, which are illustrated in Fig. 4.5**a**. First, there is an out-of-plane buckling of the Ru atoms, $\Delta\zeta_{\mathrm{Ru}}$, discernable from the asymmetric $(01\bar{1}0)$ and $(0\bar{1}10)$ Bragg rods shown in Fig. 4.5**b**. Due to negligible overall strain in the lattice (as described in the discussion of Fig. 4.1**a**), the in-plane distortion of Ru should not be substantial. Second, there is a change in the c-axis position Cl atoms relative to the Ru atoms, λ_{Cl}, as well as a third in-plane distortion of the Cl atoms that are opposite for the top and bottom sublayers, $\mathbf{\Delta r}_{\mathrm{Cl}}$. A table summarizing the experimentally bounded values for these three distortions is shown in Fig. 4.5**a**. Similar

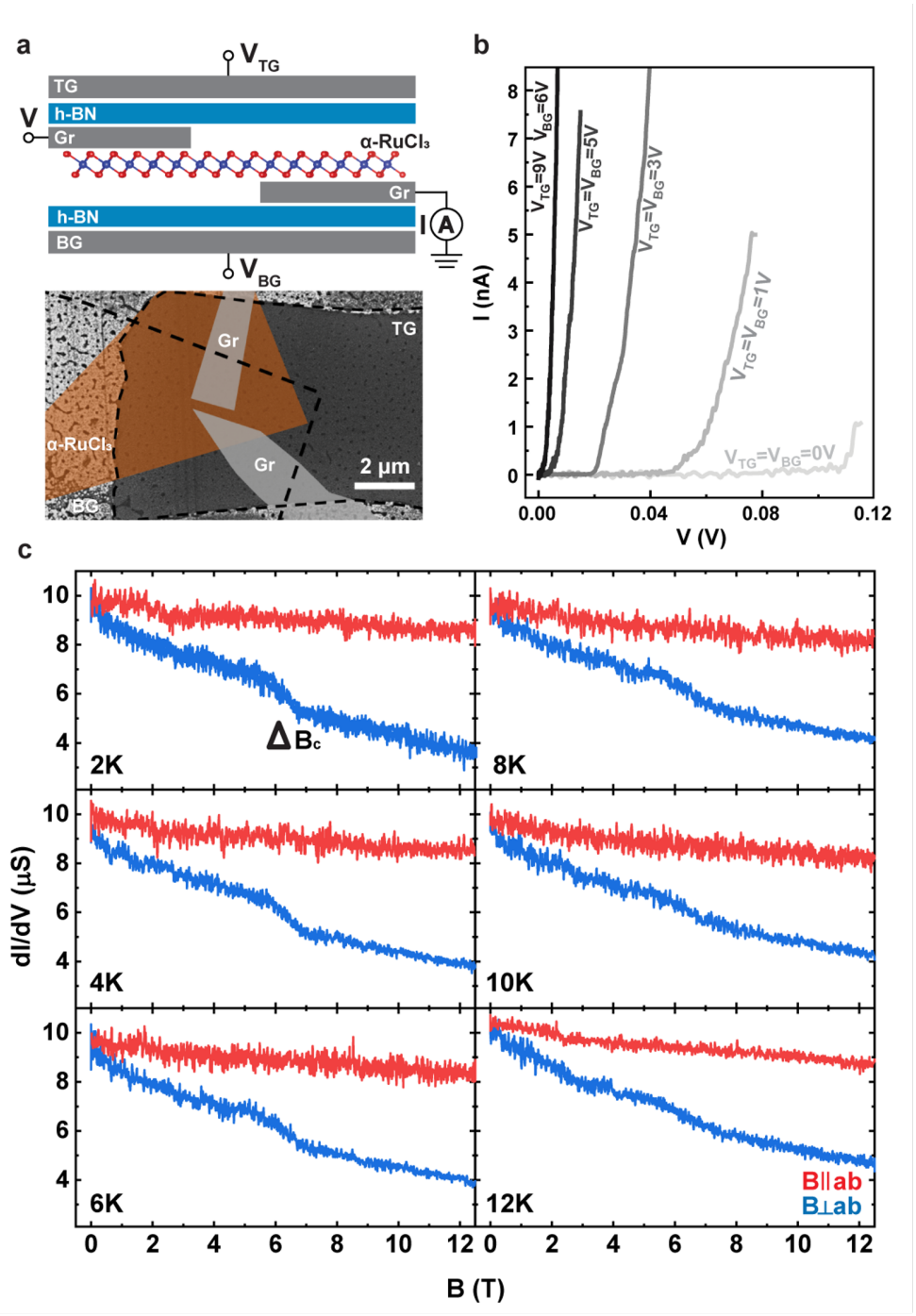

Figure 4.4: Lateral magnetotransport measurement on 1L α-$RuCl_3$ with dual gates. **a**, Side-view schematic (top) and colorized scanning electron microscopy image (bottom) of device with channel length of $\sim$ 300 nm (TG, top gate; BG, bottom gate; Gr, graphene). Dashed lines outline the top and bottom gates. **b**, Curves of the d.c. current–voltage characteristics at 2 K taken with various gate voltages. **c**, The a.c. conductance at 20 mV d.c. bias, 9 V top gate and 6 V bottom gate with changing $B_{\parallel}$ (red) and $B_{\perp}$ (blue) from 2 K to 12 K. The magnetoconductance has a larger change overall with $B_{\perp}$ and a marked kink at $B_{\perp} \approx 6.5$ T (marked with a black arrow) that gradually disappears above $T_N \approx$ 8K.

distortions have been previously observed on the surfaces of exfoliated α-$RuCl_3$ flakes and have been attributed to Cl vacancies despite preparation in an inert atmosphere [234]. Our results suggest that they may instead be intrinsic to the monolayer when interlayer coupling is absent; although, diffraction provides a precise measure of the average crystal structure and distortions, but is much less sensitive to real-space fluctuations. The reversal of magnetic anisotropy for 1L α-$RuCl_3$ signifies a modification of the spin Hamiltonian

$$\mathcal{H} = \sum_{\langle i,j \rangle} \mathbf{S}_i \, \mathbf{M}_{ij} \, \mathbf{S}_j \tag{4.2}$$

due to the observed distortions, where $\mathbf{S}_{i(j)}$ is the spin of Ru site i(j). For coplanar Ru, the matrix $\mathbf{M}$ (for the z bond) can be expressed as

$$\mathbf{M} = \begin{pmatrix} J & \Gamma & \Gamma' \\ \Gamma & J & \Gamma' \\ \Gamma' & \Gamma' & J+K \end{pmatrix} \tag{4.3}$$

for nearest-neighbour interactions, where J, K and Γ (Γ') refer to the Heisenberg, Kitaev and off-diagonal coupling terms, respectively, although a third neighbour Heisenberg term J_3 is expected to contribute as well. With Ru buckling, the symmetry of $\mathbf{M}$ is lowered to

$$\mathbf{M} = \begin{pmatrix} J_x & \Gamma_{xy} & \Gamma_{xz} \\ \Gamma_{xy} & J_y & \Gamma_{yz} \\ \Gamma_{xz} & \Gamma_{yz} & J_z \end{pmatrix} \tag{4.4}$$

where the Kitaev coupling is now defined by

$$K = J_z - \frac{J_x + J_y}{2} \tag{4.5}$$

The sense of the exchange anisotropy is determined by the sum of the off-diagonal couplings

$$\sum \Gamma = \Gamma_{xy} + \Gamma_{xz} + \Gamma_{yz} \tag{4.6}$$

with positive (negative) values indicative of easy-plane (easy-axis) anisotropy. In the bulk,

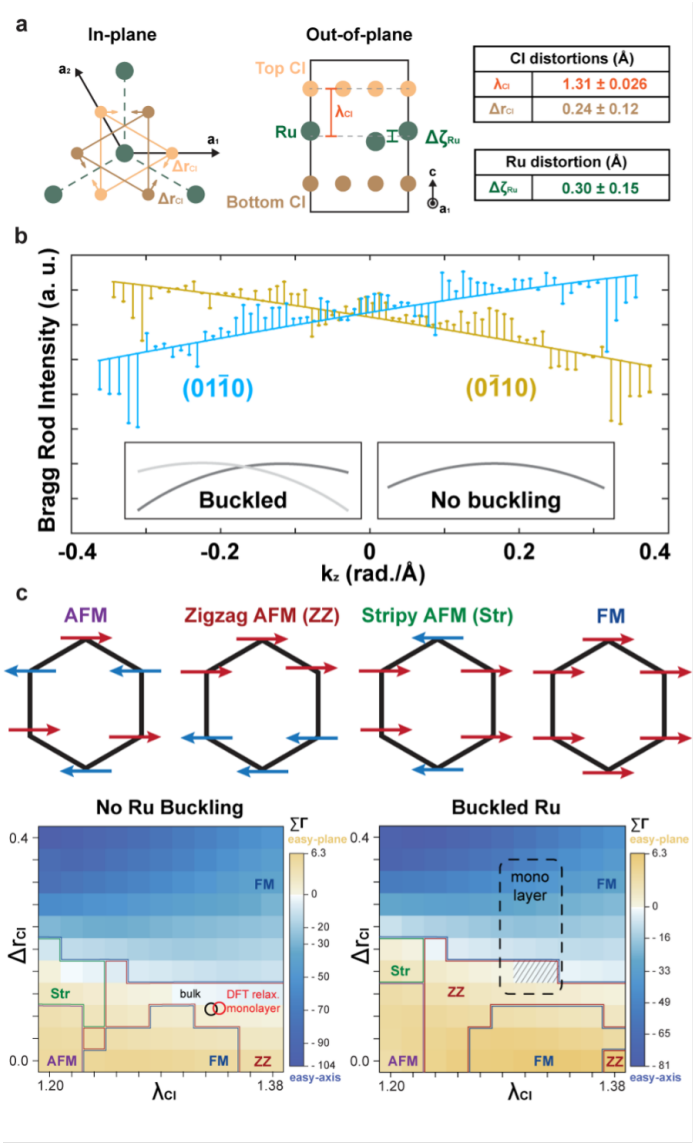

Figure 4.5: Three primary distortions of 1L α-$RuCl_3$ and magnetic phase diagram. **a**, Schematic illustration of three distortions ($\Delta\zeta_{Ru}$, λ_{Cl} and $\boldsymbol{\Delta}r_{Cl}$; left) and summary of the values determined by three-dimensional electron diffraction measurements (right). $\vec{a}_1 = a(1,0)$ and $\vec{a_2} = a(-\frac{1}{2}, \frac{\sqrt{3}}{2})$ are the lattice vectors of α-$RuCl_3$, where a = 5.979Åis the lattice constant. **b**, Asymmetric $(01\bar{1}0)$ and $(0\bar{1}10)$ Bragg rod intensities versus k_z indicate out-of-plane Ru buckling. The inset shows a schematic for the two Bragg rods with and without Ru buckling. Vertical lines are residuals of fit. **c**, The lower panel shows a magnetic phase diagram determined by ab initio calculations of $\sum\Gamma$ as a function of the Cl distortions without Ru buckling ($\Delta\zeta_{Ru} = 0$ Å, left) and with Ru buckling ($\Delta\zeta_{Ru} = 0.3$ Å, right). Yellow (blue) regions correspond to easy-plane (easy-axis) magnetic anisotropy. Positions for the experimental bulk structure and density functional theory (DFT)-relaxed monolayer are circled in the case of no buckling. The dashed rectangle in the right panel outlines our 1L α-$RuCl_3$ within the error limits of electron diffraction. The hashed area marks a region, within the rectangle, where the ZZ magnetic anisotropy has flipped to out of plane (easy axis). The upper panel shows schematics of the various classical magnetic orders in the phase diagram.

the large out-of-plane critical field stems primarily from the large off-diagonal $\Gamma > 0$ term, which is the main competitor to the Kitaev interaction.

To correlate the distortions with microscopic interactions, we performed ab initio calculations of the spin Hamiltonian for a range of distortions and evaluated the classical ground state magnetic order, schematics of which are shown in the upper part of Fig. 4.5**c** (see 4.5.1 as well). The results are shown in the lower panels of Fig. 4.5**c** as two sets of false-colour plots for $\sum \Gamma$ as a function of the Cl distortions. The left (right) panel is calculated without (with) Ru buckling. The plots also map out a phase diagram for the magnetic ordering. Regions where classical striped (Str), ZZ and ferromagnetic (FM) phases compete have been theorized to realize a QSL state in the bulk [114, 209]. The position of bulk α-$RuCl_3$ is marked by the black circle in the left panel of Fig. 4.5**c** [221, 222], while the dashed rectangle in the right panel outlines our 1L α-$RuCl_3$ within the error limits of electron diffraction. We have also used density functional theory to calculate the relaxed structure of the free-standing monolayer (see 4.5.2), which appears near that of the experimental bulk structure and does not exhibit Ru buckling (red circle, left panel). While the precise microscopic origin of the observed buckling is left as an open question, we can effectively rule out the effect of the substrate as well as a high density of Cl vacancies (see 4.5.2). The distortions collectively increase (decrease) the cation–cation (cation–anion) distance, creating more-favourable Coulomb interactions.

Table 4.1: Summary of the estimated exchange couplings (meV) for 1L and bulk α-$RuCl_3$. The Heisenberg (J), Kitaev (K) and off-diagonal (Γ, Γ') coupling terms for bulk α-$RuCl_3$ with no buckling are listed in the upper rows of the table. The elements of the matrix of exchange coupling terms ($\mathbf{M}$) are listed in the lower rows for 1L α-$RuCl_3$ with Ru buckling

	J		K		Γ	Γ'
No Buckling Bulk α-$RuCl_3$	-3.3		-6.4		3.6	-0.7
	J_x	J_y	J_z	Γ_{xy}	Γ_{yz}	Γ_{xz}
Ru buckling (1L α-$RuCl_3$)	-3.1	-4.0	-11.8	2.3	-4.5	1.4

The hashed area in the phase diagram on the right of Fig. 4.5**c** marks a region within the ZZ state (that is also within the dashed rectangle) where the magnetic anisotropy has

flipped to be out of plane, which lies on the border of FM order. To narrow the 1L phase boundary further, we performed magnetic circular dichroism measurements on 1L α-$RuCl_3$ to measure the out-of-plane magnetization, and the results are inconsistent with a FM phase with easy-axis anisotropy, indicating that our monolayers most likely retain the ZZ configuration and possess a value of $\sum\Gamma$ that is small and negative (and hence reside in the hashed region). The various exchange terms estimated for this region as well as for the bulk structure are summarized in Table 4.1. We thus see that the anisotropy reversal in monolayer samples is largely driven by the in-plane Cl distortion, which suppresses and reverses the off-diagonal exchange. Similar analysis of the g-factor supports this conclusion (see 4.5.1). The 1L α-$RuCl_3$ appears to be near a transition to out-of-plane FM ordering as a result. Proximity to this phase boundary necessarily leads to greater spin frustration and an enhanced Kitaev interaction. Specifically, we calculate

$$K = J_z - \frac{J_x + J_y}{2} = -8.25\text{meV} \tag{4.7}$$

for the hashed region, larger than that for the bulk. Due to out-of-plane Cl compression relative to the bulk structure, 1L α-$RuCl_3$ also lies closer to the region where Str, ZZ and out-of-plane FM phases compete.

4.3 Conclusions

In conclusion, our tunnelling measurements on two-dimensional α-$RuCl_3$ reveal the presence of single-magnon and/or two-magnon modes down to the monolayer limit, and a magnon continuum in 3L α-$RuCl_3$. The evolution of magnons with magnetic field indicates a clear change in the magnetic anisotropy from easy plane to easy axis in monolayer form that is supported by magnetotransport measurements in a gated lateral geometry. Three-dimensional electron diffraction shows that 1L α-$RuCl_3$ possesses several structural distortions, among which an in-plane Cl distortion predominantly drives the anisotropy reversal. This is supported by ab initio calculations, which are also used to extract a microscopic spin Hamiltonian and distortion-dependent magnetic phase diagram. Relative to the bulk,

the ground state of 1L α-$RuCl_3$ has a larger Kitaev interaction and lies in closer proximity to the intersection of several competing spin orders. Furthermore, while a field-induced QSL for in-plane fields in bulk α-$RuCl_3$ remains a subject of intense debate, a variety of theoretical works have predicted QSL phases for out-of-plane fields that have hitherto been inaccessible due to the large easy-plane anisotropy [114, 206, 214–216]. Such states may now be potentially realized for monolayer samples. Our results demonstrate the importance of dimensionality in tuning magnetism in strongly correlated spin systems and pave the way for versatile experimental knobs used for two-dimensional materials (electric field, doping, strain and so on) to further modify the magnetic order in atomically thin α-$RuCl_3$.

4.4 Methods

4.4.1 *Ab initio* calculations

Magnetic Couplings

In order to estimate the magnetic couplings, we employed the exact diagonalization method outlined in refs. [117, 118]. Hopping integrals, crystal field tensors and spin–orbit coupling in the basis of the five Ru $4d$ orbitals were first computed for each structure using the density functional theory package FPLO [235] at the fully relativistic generalized gradient approximated (Perdew–Burke–Ernzerhof) level. For structures without Ru buckling, we employed an idealized monolayer structure with P312/m symmetry and a large vacuum gap between monolayers. The in-plane lattice constant was set to 5.979 Å, which is consistent with the results of electron diffraction. To simulate the Ru buckling, we repeated the calculations with $\Delta\zeta_{\mathrm{Ru}} = 0.3$ Å, representing the best fit from electron diffraction (formally lowering the symmetry to P3). For each structure, the computed one-particle terms, H_{1-p}, were used to define a two-site model with a Hamiltonian given by $H = H_{1-p} + H_U$ where the Coulomb interactions, H_U, were defined in the spherically symmetric approximation according to the Slater parameters F_0, F_2 and F_4 [202]. For this purpose, we use the Hubbard repulsion $U_{t_{2g}} = 2.58$ and Hund's coupling $J_{t_{2g}} = 0.29$ eV following ref. [236], and approximate $\frac{F_4}{F_2} = \frac{5}{8}$ [203]. This corresponds to $F_0 = 2.15$ eV, $F_2 = 3.24$ eV and $F_4 = 2.02$

eV. After exactly diagonalizing the two-site model, we extract the magnetic couplings by projecting onto pure $J_{eff} = \frac{1}{2}$ doublets of the ideal d^5 ground state.

The g-tensors

In order to estimate the magnetic g-tensors, we employed the method outlined in ref. [237]. From the structures employed in the calculation of the magnetic interactions, we extracted the coordinates of a single $[RuCl_6]^{3-}$ octahedron. For each, we computed the g-tensors using ORCA (ref. [238]) at the def2-SVP/PBEO/CAS-SCF(3,5) level. This approach has proved reliable in previous studies of $RuCl_3$ and other materials, and is consistent with expected trends.

Density functional theory structural relaxation

Our structural relaxation calculation of monolayer α-$RuCl_3$ was based on spin-polarized density functional theory as implemented in Vienna Ab-initio Simulation Package code [239] with a generalized gradient approximated exchange–correlation functional. The interaction between ion cores and valence electrons was described by a pseudopotential of projector augmented-wave type. A correction due to van der Waals forces was included through the DFT-D2 scheme of Grimme [240]. A plane-wave cut-off of 600 eV was used for the 2×2 supercell in the slab geometry with $3 \times 3 \times 1$ k-point sampling. The in-plane lattice parameters ($a = b = 12.00$ Å for 2×2 supercell) were chosen based on the electron diffraction results. A minimum distance of 9 Å was kept between two periodic images along the c direction.

4.5 Supplementary Information

4.5.1 Ab initio calculation of exchange parameters

In order to rationalize the structural dependence of the magnetic response, we investigate the trends in the magnetic couplings via ab-initio calculations. As noted in the main text, nearest neighbor (edge-sharing) bonds in the undistorted layers of α-$RuCl_3$ have

approximate C_{2v} symmetry, which restricts the form of the magnetic interactions to be $\mathcal{H} = \sum_{\langle i,j \rangle} \mathbf{S}_i \, \mathbf{M}_{ij} \, \mathbf{S}_j$ with

$$\mathbf{M}_{ij} = \begin{pmatrix} J & \Gamma & \Gamma' \\ \Gamma & J & \Gamma' \\ \Gamma' & \Gamma' & J+K \end{pmatrix} \tag{4.8}$$

for the Z-bonds. The related interactions for the X- and Y-bonds can be obtained by rotation $(x, y, z) \rightarrow (y, z, x) \rightarrow (z, x, y)$. With Ru buckling, the bonds are reduced to C_i symmetry, which restricts $\mathbf{M} = \mathbf{M}^T$, which leaves six independently defined terms. For this reason, we discuss:

$$\mathbf{M}_{ij} = \begin{pmatrix} J_x & \Gamma_{xy} & \Gamma_{xz} \\ \Gamma_{xy} & J_y & \Gamma_{yz} \\ \Gamma_{xz} & \Gamma_{yz} & J_z \end{pmatrix} \tag{4.9}$$

For the bulk material, there has been extensive discussion of the magnetic couplings [56, 117, 204, 207–210] . While precise parameterization remains unsettled, it is generally agreed that $J < 0$, $K < 0$, and $\Gamma > 0$, with $|K| > |\Gamma| > |J|$. These couplings arise from a subtle competition between different exchange processes, and are thus strongly dependent on the local bonding geometry. In addition, the antiferromagnetic zigzag order observed in the bulk is thought to be stabilized by a third neighbor $J_3 \sim +0.5$ meV (or greater) that should be weakly dependent on structure.

In Fig. 4.6(b-e), we first show the computed structure dependence of J, K, Γ and Γ' as a function of $\mathbf{\Delta} r_{\mathrm{Cl}}$ and λ_{Cl} in the absence of buckling ($\Delta\zeta_{\mathrm{Ru}} = 0$). The couplings are computed as described in Methods. To estimate the classical ground state of each point, we supplement the computed nearest neighbor couplings with $J_3 \sim +0.5$ meV, and consider commensurate classical phases known for this model [58, 211]. The results are shown in Fig. 4.6(a). The bulk structure falls in the region of $(\mathbf{\Delta} r_{\mathrm{Cl}}\ ,\ \lambda_{\mathrm{Cl}}\ ,\ \Delta\zeta_{\mathrm{Ru}}) = (0.09, 1.33, 0)$ Å , which corresponds to a narrow strip of zigzag order bordered by regions of ferromagnetic ground state. The experimental electron diffraction measurements indicate that the monolayers have larger $\mathbf{\Delta r}_{\mathrm{Cl}}$ values compared to the bulk. As a general trend, we find that all couplings

tend to become more negative with increasing $\mathbf{\Delta}r_{\mathrm{Cl}}$. This has the effect of suppressing the subdominant $\Gamma > 0$ couplings, while effectively enhancing the small $J < 0$ and $\Gamma' < 0$. As noted in the main text, the anisotropy of the critical field (signifying the field-induced transition from zigzag order to the asymptotically polarized state) is determined entirely by the off-diagonal couplings. While increasing $\mathbf{\Delta}r_{\mathrm{Cl}}$ ultimately leads to a phase transition from zigzag order to a ferromagnetic ground state at zero field, there exists a narrow strip of zigzag order near the phase boundary where we estimate the critical fields satisfy H_c (ab) $> H_c$ (c) due to the average of the off-diagonal couplings becoming negative ($\Gamma + 2\Gamma' < 0$).

In Fig. 4.6(f,g) we show the estimated variation of the g-tensor components without buckling. The anisotropy of the g-tensor is generally determined by the sign of the local trigonal crystal field splitting [212], which is a function of the relative Cl positions. The bulk satisfies $g_{\mathrm{ab}} > g_{\mathrm{c}}$, which enhances the discrepancy between in-plane and out-of-plane critical fields. As a general trend, we find the g-anisotropy is reversed with increasing $\mathbf{\Delta}r_{\mathrm{Cl}}$. The enhanced trigonal crystal field terms modify the local $j_{\mathrm{eff}} = 1/2$ spin-orbital moments to become strongly axial, which may even completely suppress g_{ab} in the extreme limit. This causes H_c (ab) to be significantly enhanced, as the moments decouple from in-plane fields. For this reason, we conclude that the expected trends in the g-anisotropy also support the notion that increasing $\mathbf{\Delta}r_{\mathrm{Cl}}$ in monolayer samples leads to a reversal of the critical field anisotropy.

In order to evaluate these trends for buckled structures, we repeat the calculations for $\Delta\zeta_{\mathrm{Ru}} = 0.3$ Å, which is consistent with the experimental structures (see Fig. 4.7). With buckling, the symmetry is lowered such that $J_x \neq J_y$ and $\Gamma_{xz} \neq \Gamma_{yz}$. While the diagonal couplings are only weakly modified (Fig. 4.7(a,b)), the off-diagonal couplings are strongly enhanced with $\Gamma_{yz} < 0$ and $\Gamma_{xz} > 0$ (Fig. 4.7(e,f)). Nonetheless, the overall trends are similar to the unbuckled structures: all terms tend to become more negative with increasing $\mathbf{\Delta}r_{\mathrm{Cl}}$ and there exists a narrow region of zigzag order where we estimate that the critical field anisotropy is reversed compared to the bulk. While we do not completely rule out a more complex magnetic ground state with large unit cell, ferromagnetic order appears as the main competitor to zigzag order. The experimental confidence region for the monolayer structures from electron diffraction falls largely within the ferromagnetic region; however,

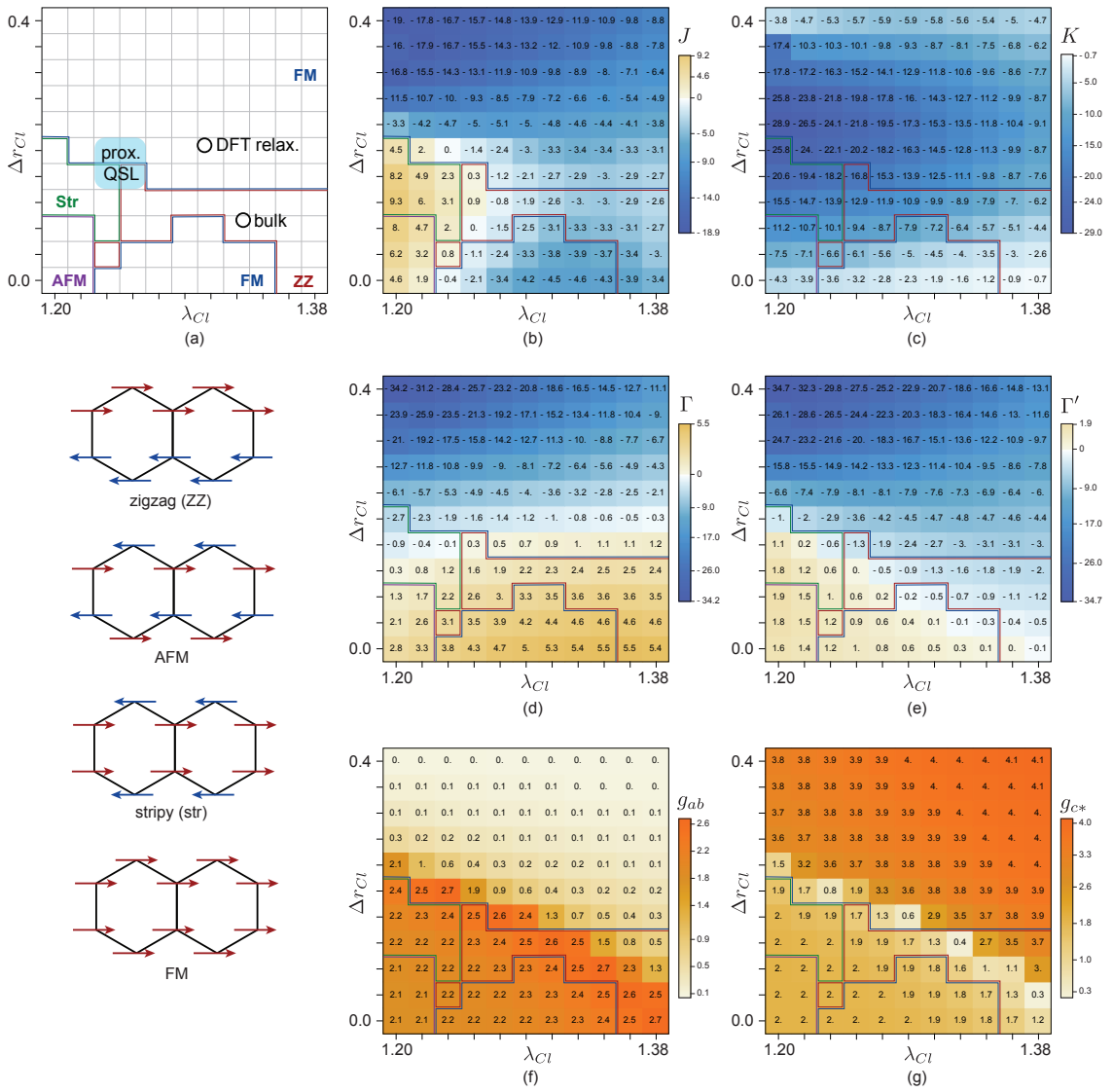

Figure 4.6: Computed structural variation of the magnetic couplings with no buckling ($\Delta\zeta_{\mathrm{Ru}} = 0$). (a): Schematic phase diagram showing various ordered regions: FM = ferromagnetic, ZZ = zigzag, Str = stripy, and AFM = Neel antiferromagnetic. The approximate locations of the bulk structure and theoretical monolayer structure obtained by DFT relaxation are shown. (b-e): Magnetic exchange interactions. (f,g): g-tensor components.

magnetic circular dichroism measurements appear to rule out ferromagnetic order. In this regard, we note that while *ab-initio* reproduces expected trends in the couplings, the strong sensitivity of the interactions to various contributions make precise prediction challenging. For example, it has been suggested that $J_3 > 2$ meV [207], which would significantly extend the stability region of zigzag ground state. Overall, we speculate that an appropriate starting point for describing the monolayers may be $g_{\mathrm{ab}} \sim 1$, $g_{\mathrm{c}} \sim 3$, $J_x \approx J_y \sim -3$ meV, $J_z \sim -10$ meV, $\Gamma_{yz} \sim -5$ meV, Γ_{xz} , $\Gamma_{xy} \sim 0$, and $J_3 > 0$ of sufficient magnitude to ensure a zigzag ground state. Refinement of this model is an important subject of future work.

4.5.2 Density functional theory calculation of structural distortions

In order to obtain insight into the observed structural changes in the monolayer samples, we investigated the minimum energy theoretical structures (see Methods). We considered an isolated monolayer of α-$RuCl_3$. The chosen cell corresponded to 2×2 supercell with total in-plane lattice parameter (a = b = 12.00 Å). We also considered monolayer α-$RuCl_3$ sandwiched between two layers of h-BN (in AA stacking). The chosen cell corresponded to 2×2 supercell of α-$RuCl_3$ and 5×5 supercell of h-BN, with total in-plane lattice parameter (a = b = 12.52 Å). This leads to a small 4% in-plane strain (expansion) of the α-$RuCl_3$ monolayer compared to the bulk. Finally, we performed structural relaxations in the presence of both Cl vacancies and h-BN encapsulating layers (with same cell parameters as above). The average values of the structural parameters are shown in Table 4.2 and are compared with the experimental bulk and monolayer structure. While the modulation of the Ru heights can be induced by Cl vacancies on average, the distortion rapidly decays away from the Cl vacancy location and a very high density of vacancies ($> 10\%$, on the scale of one vacancy per unit cell) would be required to yield the experimentally observed degree of buckling, which is inconsistent with our electron diffraction measurements.

4.5.3 Compatibility of Theoretical Model with Experimental IETS Spectrum

While a complete description of the inelastic magnetic scattering function is beyond the scope of this work, we now demonstrate that the experimental IETS is compatible with

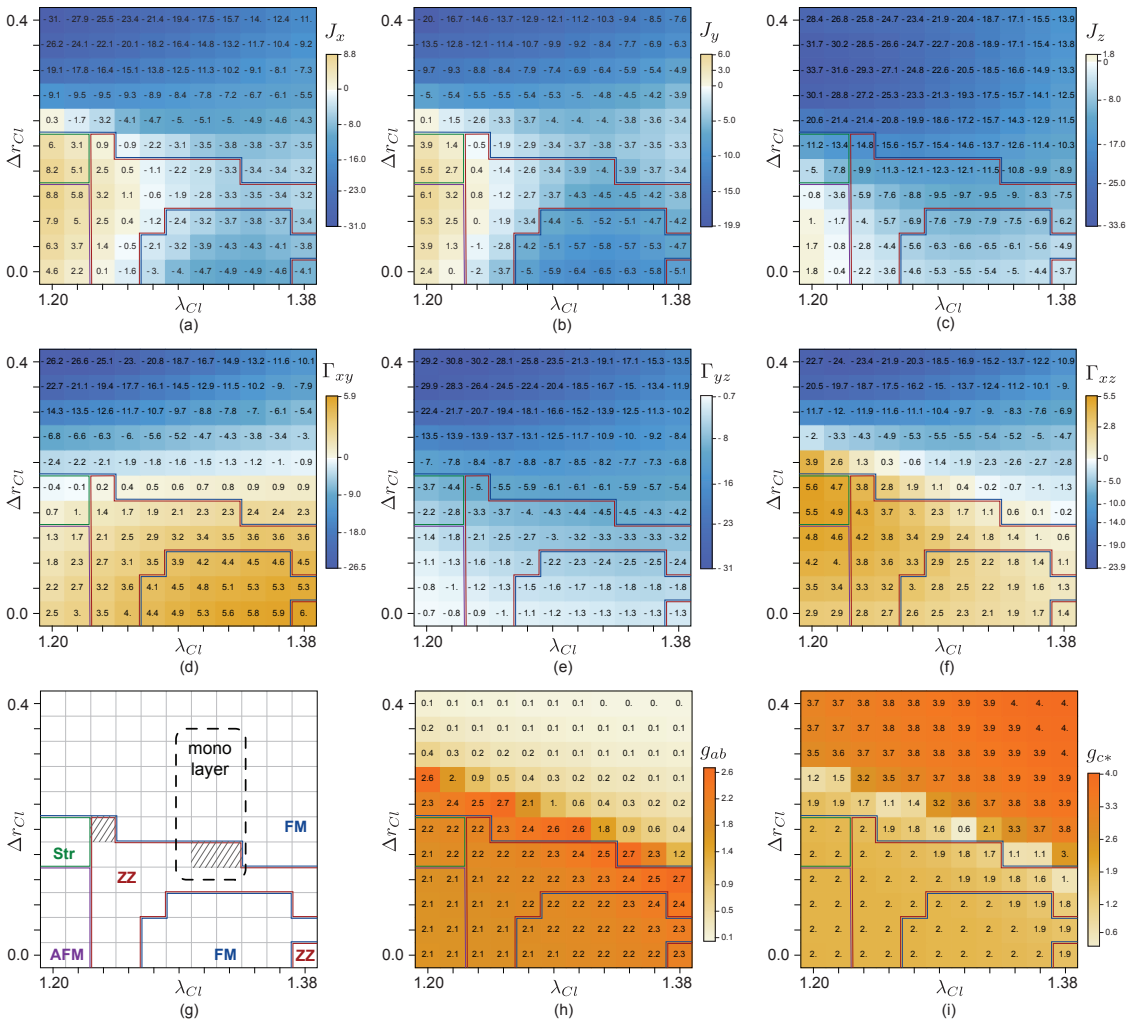

Figure 4.7: Computed structural variation of the magnetic couplings with finite buckling ($\Delta\zeta_{\mathrm{Ru}} = 0.3$ Å). (a-f): Magnetic exchange interactions. (g): Schematic phase diagram showing various ordered regions: FM = ferromagnetic, ZZ = zigzag, Str = stripy, and AFM = Neel antiferromagnetic. The experimental error range for the monolayer is indicated. Hashed areas indicate zigzag regions with easy axis anisotropy within the experimental error range. (h,i): g-tensor components.

Table 4.2: Comparison of average structural parameters obtained from experiment with theoretical structural relaxation for monolayer α-$RuCl_3$

	λ_{Cl} (Å)	$\mathbf{\Delta}r_{Cl}$ (Å)	$\Delta\zeta_{Ru}$ (Å)
Bulk R-3 [66]	1.329	0.0924	0
Bulk C2/m [114]	1.336	0.0945	0
Monolayer (exp)	1.31 ± 0.026	0.24 ± 0.12	0.30 ± 0.15
Relaxed Monolayer without h-BN	1.3380	0.0861	< 0.01
Relaxed with h-BN (no Cl vacancy)	1.3031	0.2188	< 0.01
Relaxed with h-BN (Cl vacancy)	1.2913	0.2075	0.0478

magnetic scattering. In general, tunneling occurs from occupied states in the source electrode to unoccupied states in the drain electrode, with relative Fermi energies ($\varepsilon_{F,S}$ and $\varepsilon_{F,D}$, respectively) controlled by the voltage difference, V. Elastic tunneling events lead to a background current given by:

$$I \propto \int_{\varepsilon_{F,D}}^{\varepsilon_{F,S}} D_D(\omega) D_S(\omega) d\omega = \int_{\varepsilon_{F,D}}^{\varepsilon_{F,D+V}} D_D(\omega) D_S(\omega) d\omega \tag{4.10}$$

where $D_D(\omega)$ and $D_S(\omega)$ are the electronic densities of states of the drain and source electrodes, respectively. For metallic electrodes, these can be treated as roughly constant within the narrow range of voltage employed in the experiment. Considering inelastic processes leads to additional tunneling channels with associated current:

$$I \propto \int_{\varepsilon_{F,D}}^{\varepsilon_{F,D+V}} d\omega_1 D_S(\omega_1) \int_{\varepsilon_{F,D}}^{\omega_1} d\omega_2 \, D_D(\omega_2) \, g(\omega_1 - \omega_2) \tag{4.11}$$

where $g(\omega)$ is the scattering function, which is related to the density of (magnetic) excitations in the sample, and their associated scattering matrix elements in addition to the nature of the sample / electrode interfaces and the available intermediate states in which tunneling charges exist within the sample. Under the assumption of constant $D_D(\omega)$ and $D_S(\omega)$, this implies:

$$\frac{d^2 I}{dV^2} \propto g(V) \tag{4.12}$$

Additional voltage dependence may arise from energy dependence of $D_D(\omega)$ and $D_S(\omega)$. The scattering function itself is challenging to quantitatively model, but should generally be related to various orders of local dynamical spin susceptibility of the sample. In the following, we consider the first order susceptibility:

$$g(\omega) \propto \mathrm{Im}\left[\sum_{\mu\,\varepsilon\,\{x,y,z\}} \sum_{n} \frac{|\langle 0|S_i^{\mu}|n\rangle|^2}{\omega - E_n + E_0 - i\eta}\right] \tag{4.13}$$

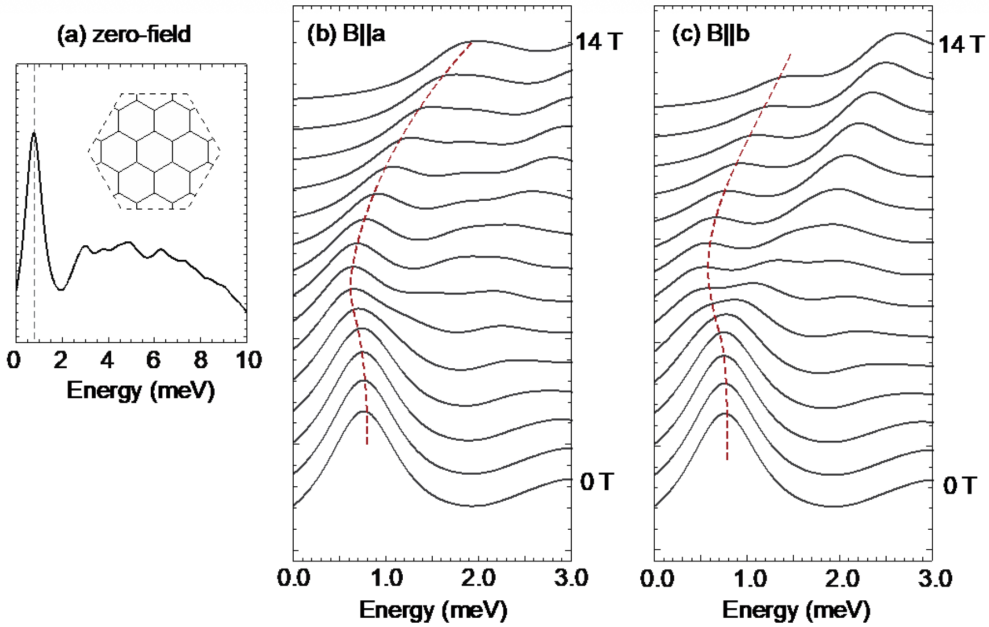

Figure 4.8: Local dynamical spin structure factor for bulk model from ref [204] computed via exact diagonalization. (a) zero-field result showing peak at lowest (Y/M-point) magnon and higher energy continuum. (b,c) evolution of low-energy response under in-plane magnetic field.

As discussed in previous works [204], linear spin-wave theory is insufficient to capture the important effects of magnon decays, which significantly alter the dynamical response in bulk α-$RuCl_3$. For this reason, we estimate $g(\omega)$ using exact diagonalization on the symmetrical 24-site cluster depicted in the inset of Fig. 4.8(a). Qualitatively similar results are obtained for all models; for simplicity, we show results for the bulk model of ref [204] to facilitate comparison with previous works ($J_1 = -0.5$, $K_1 = -5.0$, $\Gamma_1 = +2.5$, $J_3 = +0.5$). As can be seen, this approximation reproduces qualitatively the observed zero-field IETS

response in 3L samples: (i) the low-energy peak corresponds to the lowest energy magnons at the Y/M-points (which have dominant spectral weight), and (ii) the high energy continuum corresponds to one-magnon and multi- magnon continuum excitations. The evolution under in-plane applied field is depicted in Fig. 4.8(b) and 4.8(c). With increasing field, the lowest peak initially shifts to lower energy. Above the critical field $B_c \sim 7$ T, the lowest peak then increases with field. A similar qualitative behavior is indeed observed experimentally, which validates the interpretation of the IETS experiments discussed in the main text.

Chapter 5

Hybrid Spin-Orbit Exciton-Magnon Excitations in $FePS_3$

This chapter is adapted from a paper titled "Hybrid Spin-Orbit Exciton-Magnon Excitations in $FePS_3$" as published in npj Quantum Materials, ***9****, 64,(2024) [135] .*

In this chapter, we demonstrate an important unresolved role of spin-orbit coupling (SOC) in the ground state and excitations of $FePS_3$. This compound is a layered van der Waals (vdW) Ising antiferromagnet that has recently been studied in the context of true 2D magnetism, and emerged as an ideal material platform for investigating strong spin-phonon coupling, and non-linear magneto-optical phenomena. Combining first principles calculations with Linear Flavor Wave Theory (LFWT), we find strong mixing and spectral overlap of different spin-orbital single-ion states. As such, the low-lying excitations form complex mixtures of local degrees of freedom most accurately viewed as hybrid spin-orbit exciton-magnon modes. Complete parameterization of the resulting low-energy model including all such degrees of freedom requires nearly half a million coupling constants. Despite this complexity, we show that such a model can be inexpensively derived using local many-body-based approaches, which yield quantitative agreement with recent experiments. The results highlight the importance of SOC even in first row transition metals, and provide

essential insight into the properties of 2D magnets with unquenched orbital moments. It also demonstrate the power of dCEH method to treat complicated materials with low-lying J- multiplets.

5.1 Introduction

Two-dimensional (2D) van der Waals magnets have recently been intensively investigated for fundamental developments and potential applications in heterostructure devices [241–245]. One such material is $FePS_3$, which exhibits a large Ising anisotropy of the local moments [246, 247], allowing retention of (zigzag) antiferromagnetic order down to the monolayer limit [248]. This fact combined with the ease of exfoliation of few-layer samples of $FePS_3$ has facilitated recent studies of e.g. proximity effects in magnet-semiconductor heterostructures [249], cavity manipulation of electromagnetic responses via strong light-matter coupling [250], and giant nonlinear optical responses [251]. The material has also emerged as an ideal platform for studying strong spin-phonon coupling [252], as it exhibits clear formation of optical magnon-polarons [253–256], and a large modification of the lattice dynamics as a function of magnetic state [257–260]. A similar effect leads to the possibility of topologically nontrivial phonon-magnon hybrid modes [261–264] in $FePS_3$ and the isostructural $FePSe_3$.

The bulk magnetic excitations of $FePS_3$ have also been extensively studied, via inelastic neutron scattering (INS) [265–267], magneto-Raman [268], and THz spectroscopy [269]. Particulary intriguing is Ref. [269], which proposed to observe high energy 4-magnon bound states. However, to date, the majority of such works have analyzed the response of $FePS_3$ with reference to phenomenological models with spin $S = 2$, referring to the four unpaired electrons at each high-spin d^6 Fe^{2+} site. As we discuss in this work, such models ignore the unquenched local orbital degrees of freedom, which are necessary for the strong Ising anisotropy of the local moments [270, 271], and play a significant role in related Fe^{2+} materials [272, 273]. Experimental evidence for large orbital moments in $FePS_3$ can be seen in recent X-ray absorption spectroscopy branching ratio and linear dichroism measurements [274]. Thus, we raise a fundamental question: Is $FePS_3$ an $S = 2$ system? The definitive answer is, "No." Utilizing a systematic first-principles-based approach to construct

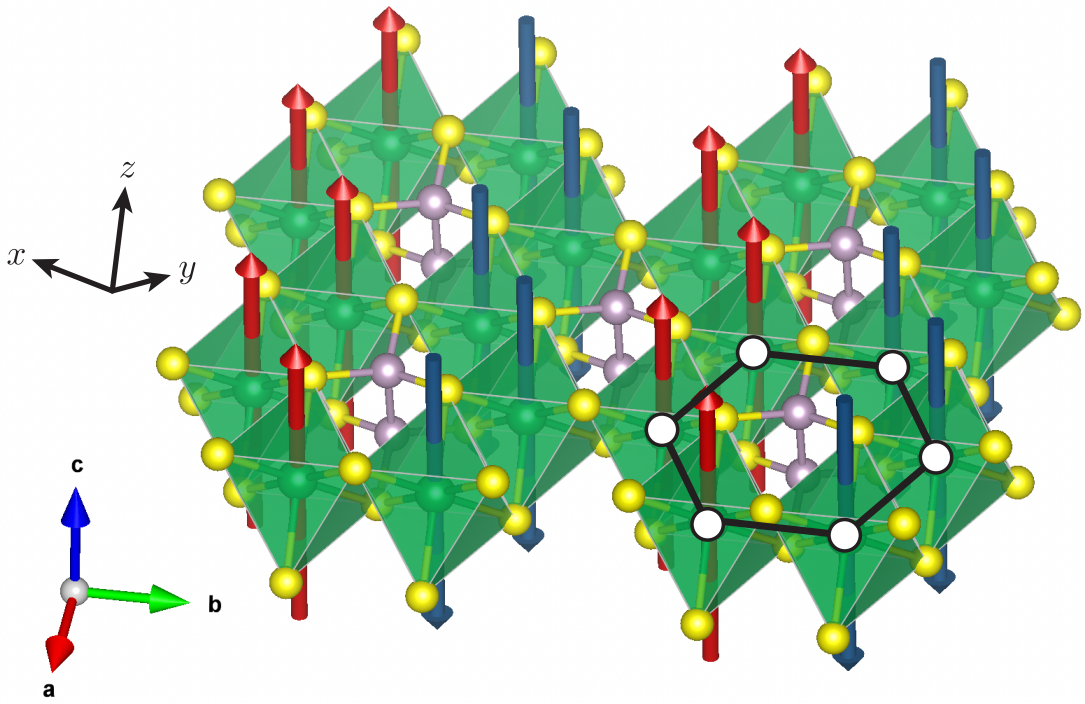

Figure 5.1: Structure of $FePS_3$ showing honeycomb motif. The (a,b,c) coordinates refer to the $C2/m$ unit cell. The (x,y,z) coordinates are the global cubic axes. Predicted ordered moment directions are indicated by red and blue arrows.

the low-energy model, we instead show that the local moments are rich mixtures of spin-orbit entangled $J_{\text{eff}} = 1, 2$, and 3 states. The low-lying magnetic excitations alter both the orbital composition and moment orientations, thus being described as hybrid spin-orbit exciton (SOE)-magnon modes. These findings are relevant for a complete microscopic understanding of the intriguing magnetic, phononic, and optical properties of $FePS_3$.

5.2 Single Site States

At the single-site level, the high-spin d^6 case has electronic configuration $(t_{2g})^4(e_g)^2$, which corresponds to $S = 2$, and $L_{\text{eff}} = 1$. The latter orbital momentum has been largely ignored in various recent works, which treated $FePS_3$ as an $S = 2$ system. Instead, when spin-orbit coupling (SOC) is considered, the low-energy single-ion states are split into $J_{\text{eff}} = 1, 2$, and 3 multiplets [270, 275], as shown in Fig. 5.2(a). These states are further split by the crystal field, which has approximately trigonal symmetry in $FePS_3$. The basis functions for the pure J_{eff} multiplets are given in [[276]]. As discussed below, due to the relative weakness of SOC,

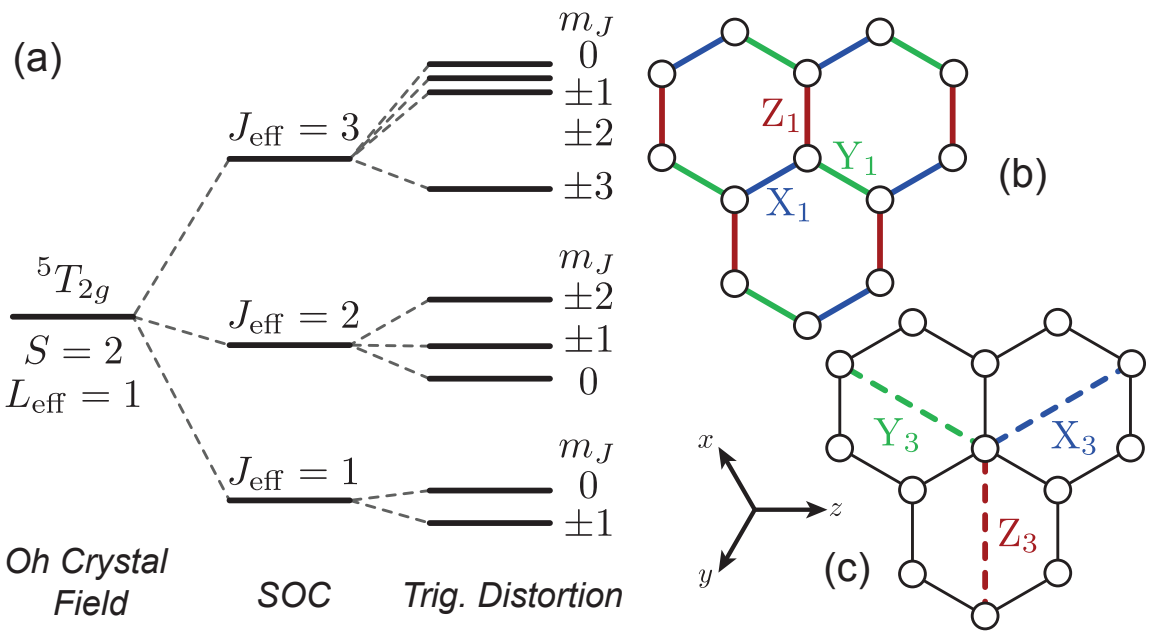

Figure 5.2: (a) Splitting of local single-ion multiplets with spin-orbit coupling (SOC) and trigonal distortion. (b) Definition of first neighbor (X_1, Y_1, Z_1) bonds. (c) Definition of third neighbor (X_3, Y_3, Z_3) bonds. The (x,y,z) coordinates are the global cubic axes.

intersite couplings are sufficiently strong to significantly mix and reorder these single-ion levels, such that the local moments and excitations develop a mixed $J_{\rm eff}$ character.

5.3 Electronic Hamiltonian

In order to develop a low-energy model for $FePS_3$, we use the des Cloizeaux effective Hamiltonian (dCEH) approach [108, 277] to compute interactions for each bond up to third neighbors. We first consider an electronic Hamiltonian in terms of Fe $3d$-orbitals, which is a sum of, respectively, one- and two-particle terms: $\mathcal{H}_{\rm el} = \mathcal{H}_{1p} + \mathcal{H}_{2p}$. The one-particle terms include intersite hopping, intrasite crystal field, and spin-orbit coupling,

$\mathcal{H}_{1p} = \mathcal{H}_{hop} + \mathcal{H}_{\mathrm{CF}} + \mathcal{H}_{\mathrm{SO}}$:

$$\mathcal{H}_{hop} = \sum_{ij\alpha\beta\sigma} t_{ij}^{\alpha\beta} c_{i,\alpha,\sigma}^{\dagger} c_{j,\beta,\sigma} \tag{5.1}$$

$$\mathcal{H}_{\mathrm{CF}} = \sum_{i\alpha\beta\sigma} d_{i}^{\alpha\beta} c_{i,\alpha,\sigma}^{\dagger} c_{i,\beta,\sigma} \tag{5.2}$$

$$\mathcal{H}_{\mathrm{SO}} = \sum_{i\alpha\beta\sigma\sigma'} \lambda_{\mathrm{Fe}} \langle \phi_{i}^{\alpha}(\sigma) | \mathbf{L} \cdot \mathbf{S} | \phi_{i}^{\beta}(\sigma') \rangle c_{i,\alpha,\sigma}^{\dagger} c_{i,\beta,\sigma'} \tag{5.3}$$

where $c_{i,\alpha,\sigma}^{\dagger}$ creates an electron at site i, in orbital α, with spin σ. To estimate $t_{ij}^{\alpha\beta}$ and $d_{i}^{\alpha\beta}$, we perform non-relativistic density functional theory (DFT) calculations, as described in the Methods section. For $\mathcal{H}_{\mathrm{SO}}$, we take the atomic value, $\lambda_{\mathrm{Fe}} = 53$ meV [278]. The same value is obtained from Wannier fitting of fully relativistic DFT calculations performed with FPLO (not shown).

For $\mathcal{H}_{2p} = \mathcal{H}_{U} + \mathcal{H}_{Jnn}$, we consider both on-site and intersite terms, respectively. The on-site contributions are given by:

$$\mathcal{H}_{U} = \sum_{i\alpha\beta\delta\gamma} \sum_{\sigma\sigma'} U_{\alpha\beta\gamma\delta} \; c_{i,\alpha,\sigma}^{\dagger} c_{i,\beta,\sigma'}^{\dagger} c_{i,\gamma,\sigma'} c_{i,\delta,\sigma} \tag{5.4}$$

In the spherically symmetric approximation [279], $U_{\alpha\beta\gamma\delta}$ are parameterized by the Slater parameters F_0, F_2, F_4. We use $F_2 = 9.11$ eV, $F_4 = 6.56$ eV, in accordance with spectroscopic studies of high energy d-d transitions in $FePS_3$ [280]. This leaves F_0 (or equivalently, $U_{t2g} = F_0 - \frac{4}{49}(F_2 + F_4)$) as a free parameter in the calculation. The effects of this choice are discussed below; we ultimately conclude that $U_{t2g} = 4.2$ eV provides a good match with experiment. For the intersite terms, we consider an additional nearest neighbor Hund's coupling:

$$\mathcal{H}_{Jnn} = \sum_{ij\alpha\beta\sigma\sigma'} J_{H,ij}^{\alpha\beta} \; c_{i,\alpha,\sigma}^{\dagger} c_{j,\beta,\sigma'}^{\dagger} c_{i,\alpha,\sigma'} c_{j,\beta,\sigma} \tag{5.5}$$

The physical origin of this term is the downfolding of the p-orbital Coulomb interactions associated with the sulfur ligands into the Fe d-orbital Wannier functions. The Wannier orbitals are, in reality, anti-bonding combinations of d- and p-orbitals. The usual ferro-

magnetic Goodenough-Kanamori superexchange [34] arises from the residual effects of the ligand Hund's coupling when d-orbitals of adjacent Fe atoms hybridize with p-orbitals of the same ligand. This term plays a primary role in establishing ferromagnetic nearest neighbor couplings in edge-sharing materials (see e.g. [281]). The intersite Hund's coupling coefficients $J^{\alpha\beta}_{H,ij}$ can, in principle, be estimated by constrained Random Phase Approximation (cRPA) calculations [282, 283]. However, we have found that cRPA tends to overestimate the coefficients by an order of magnitude. Instead we take a partially empirical approach. Projecting the p-orbital Coulomb interactions into the Wannier function basis gives the approximation:

$$J^{\alpha\beta}_{H,ij} = \sum_{n,\delta,\gamma} (U^n - J^n_H)\ \phi^{n,\delta}_{i,\alpha}\phi^{n\delta}_{j,\beta}\phi^{n,\gamma}_{i,\alpha}\phi^{n,\gamma}_{j,\beta} + J^n_H|\phi^{n,\delta}_{i,\alpha}|^2|\phi^{n,\gamma}_{j,\beta}|^2 \tag{5.6}$$

where $\phi^{n,\delta}_{i,\alpha}$ is the wavefunction coefficient for the Wannier function at Fe site i and d-orbital α corresponding to the directly-bonded sulfur atom n, and p-orbital $\delta \in \{p_x, p_y, p_z\}$. U^n is the Hubbard repulsion between electrons in the same p-orbital at site n, and J^n_H is the Hund's coupling at site n. At this point, we approximate $U^n = 2J^n_H$, and take the screened sulfur Hund's coupling to be half of the atomic value [284], namely $J^n_H = 0.27$ eV. We then evaluate the sums over bridging sulfur atoms, employing the wavefunction coefficients obtained from DFT. While these choices are physically reasonable, this approach is empirically justified because it yields intersite magnetic couplings of experimentally correct magnitude, as shown below. The full estimated intersite $J^{\alpha\beta}_{H,ij}$ tensors are given in the Supplemental Material [[276]]; the largest coefficients are ~ 2 meV, and involve the e_g orbitals, which hybridize more strongly than the t_{2g} orbitals with the ligand p-orbitals.

5.4 Intersite Low-Energy Couplings

With the electronic Hamiltonian thus defined, we obtain the low energy model by exactly diagonalizing $\mathcal{H}_{\text{el}}$ on pairs of sites up to third nearest neighbor, and projecting the lowest energy eigenstates onto pure J_{eff} states (see Supplemental Material [[276]] for full definition).

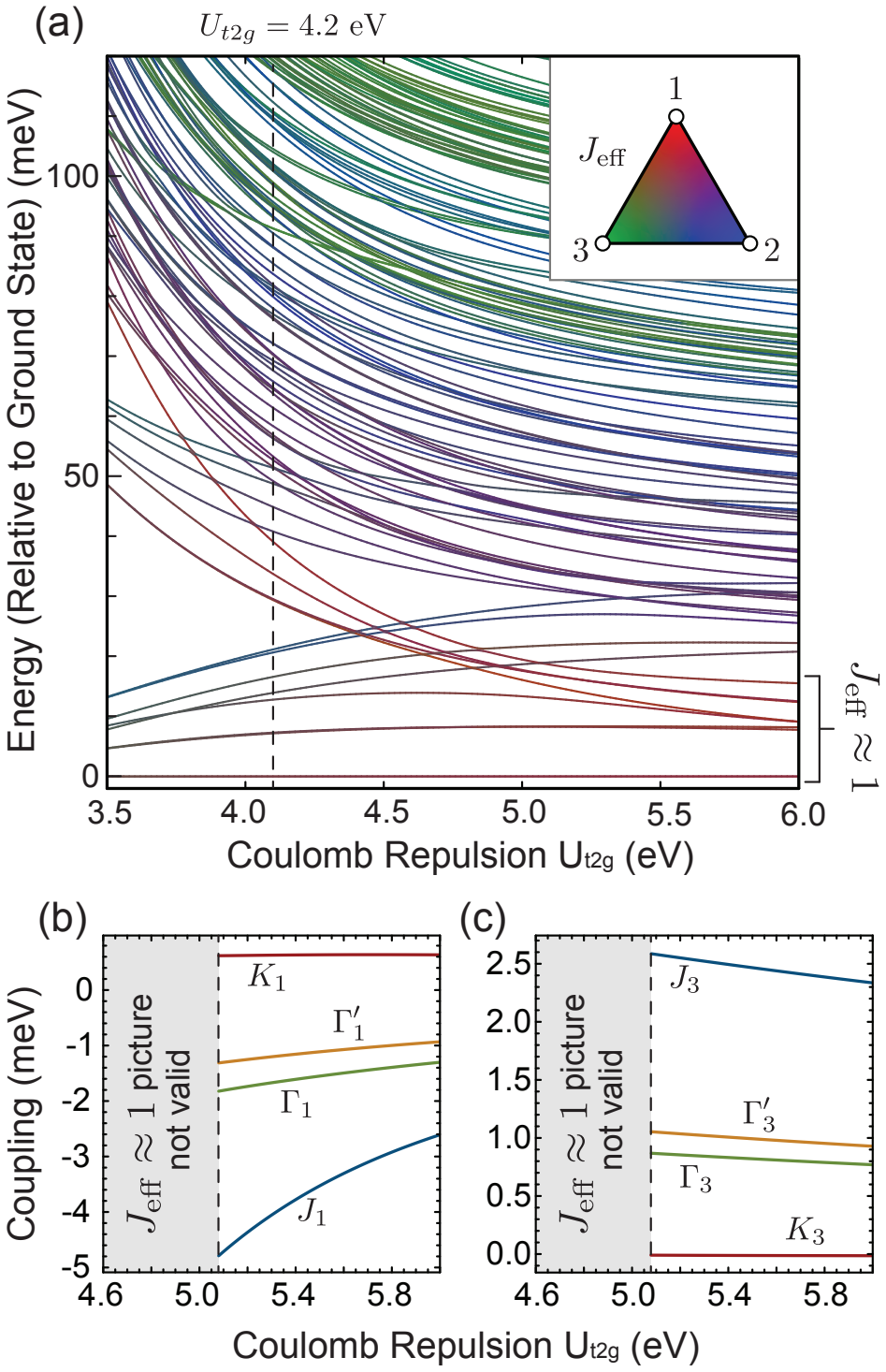

Figure 5.3: (a) Evolution of lowest energy eigenvalues for two site Z_1-bond cluster. States are colored according to their composition in terms of J_{eff} states. For $U_{t2g} \lesssim 5$ eV, $J_{\text{eff}} = 2$ states intrude into the low-energy space, invalidating a pure $J_{\text{eff}} = 1$ model. (b,c) Evolution of bilinear couplings in $J_{\text{eff}} = 1$ model for large U_{t2g} for first and third neighbors, respectively. Second neighbor couplings are an order of magnitude smaller, and are not shown.

In general, the resulting low-energy model takes the form:

$$\mathcal{H} = \sum_{i,n} A_i^n \mathcal{O}_i^n + \sum_{ij,nm} J_{ij}^{nm} \mathcal{O}_i^n \mathcal{O}_j^m \tag{5.7}$$

where $\mathcal{O}_i^n$ are local operators that act in the local basis, which may include up to $J_{\text{eff}} = 1, 2,$ and 3 states.

In Fig. 5.3(a), we first show the evolution of the state energies as a function of U_{t2g} for a two-site cluster representing the Z_1-bond. It is instructive to first consider the large U_{t2g} limit, where states of different J are somewhat separated in energy. In this limit, it is possible to constrain the low-energy model to the lowest three states on each site, which are smoothly connected to pure $J_{\text{eff}} = 1$ triplets (9 states for the pair of sites). In this case, the $\mathcal{O}_i^n$ operators may be chosen as the conventional spherical tensor (Stevens) operators for $S = 1$. The Hamiltonian may then be written:

$$\begin{aligned}\mathcal{H} = &\sum_i A(\mathbf{S}_i \cdot \hat{c}^*)^2 + \sum_{ij} \mathbf{S}_i \cdot \mathbb{J}_{ij} \cdot \mathbf{S}_j \\ &+ \sum_{ij,nm} B_{ij}^{nm}\ \mathcal{O}_i^{2,n}\ \mathcal{O}_j^{2,m}\end{aligned} \tag{5.8}$$

where the bilinear couplings are parameterized by

$$\mathbb{J}_{ij} = \begin{pmatrix} J & \Gamma & \Gamma' \\ \Gamma & J & \Gamma' \\ \Gamma' & \Gamma' & J+K \end{pmatrix} \tag{5.9}$$

for the Z-bonds, in terms of the global (x, y, z) coordinates defined in Fig. 5.1 and 5.2(b,c). In Fig. 5.3(b,c), we show the evolution of the couplings for the Z_1 and Z_3 bonds obtained by projecting the lowest 9 states onto pure $J_{\text{eff}} = 1$ states. A full discussion of the biquadratic couplings B_{ij}^{nm} is found in the Supplemental Material [sup]. There are several important observations: (i) We find a large single-ion anisotropy (SIA) with $A \approx -5.1$ meV, independent of U_{t2g}. This arises from the local trigonal distortion of the FeS_6 octahedra, which split the $J_{\text{eff}} = 1$ levels. (ii) The intersite exchange couplings are quite anisotropic. The

nearest neighbor Kitaev coupling K_1 is antiferromagnetic, but small compared to the other couplings. The third neighbor K_3 is negligible. Instead, the largest anisotropic couplings are $\Gamma_n \approx \Gamma'_n$, which have the same sign as the corresponding Heisenberg couplings J_n. This implies a significant bond-independent Ising exchange anisotropy, with the Ising axis along the c^*-axis. Microscopically, the origin of this exchange anisotropy is precisely the same as the SIA: the modification of the local moments by the trigonal crystal field. Both the exchange anisotropy and SIA must be present together. (iii) There is significant anisotropic nearest neighbor biquadratic (BQ) exchange. Full details are given in the Supplemental Material [sup]; the Z-bond BQ terms are parameterized by nine symmetry-distinct constants, which we find are typically on the order of 10% of J_1. It may be noted that large BQ exchange was recently implicated to explain the specific dispersion of excitations in inelastic neutron scattering experiments [267], although this was in the context of an $S = 2$ model.

While these observations for the large U case may provide some intuition into the intersite couplings, the $J_{\text{eff}} = 1$ picture breaks down for $U_{t2g} \lesssim 5$ eV, as the higher lying $J_{\text{eff}} = 2$ states descend into the low-energy window. This is depicted in Fig. 5.3(a). As we show below, the physically applicable value is $U_{t2g} \approx 4.2 < 5$ eV. Thus, it is not possible to map the low-energy space onto a single J multiplet, so that all 15 local $J_{\text{eff}} = 1, 2$, and 3 states need to be considered explicitly in the low-energy model. Complete specification of the Hamiltonian therefore requires $15^2 = 225$ local operators, such that each bond interaction is defined by $(15^2 - 1)^2 = 50,176$ coupling constants J_{ij}^{nm}. Fig. 5.4(a) and (b) show the distribution and magnitudes of such couplings for the Z_1 bond obtained by the dCEH method for $U_{t2g} = 4.2$ eV; the fact that there is no clear separation of magnitudes implies the need to retain all couplings. This situation highlights the utility of many-body approaches, such as the above-described dCEH approach, for the estimation of low-energy Hamiltonians (see e.g. [118, 285–288] for a survey of approaches). The many-body nature of the local spin-orbital states and large number of couplings would present a significant difficulty for more traditional pure-DFT approaches in which couplings are estimated from energy differences between suitably constrained Kohn-Sham (single determinant) wavefunctions [111, 289, 290]. In the above-described dCEH approach, all couplings are instead

obtained simultaneously for a given bond from a single diagonalization of the two-site electronic Hamiltonian, which requires at most a few minutes on a single workstation. In lieu of printing these couplings, we provide the corresponding bond-matrices in matrix market [291] (.mtx) format in the Supplemental Material [[276]] to facilitate future studies.

5.5 Model Properties

From here, we consider only the full $J_{\text{eff}} = 1, 2, 3$ model with $U_{t2g} = 4.2$ eV. In order to analyze the ground state and excitations, we employ a numerical Linear Flavor Wave Theory (LFWT) approach [292–297], described in detail in the Methods section. We find that the full model reproduces *all* aspects of the experimental response of $FePS_3$.

In agreement with experiment, the mean field model exhibits antiferromagnetic zigzag order of magnetic dipoles, which can be understood as arising from primarily ferromagnetic nearest neighbor and antiferromagnetic third neighbor couplings. The moment size is $|\langle\psi_i^0|\mathbf{L} - 2\mathbf{S}|\psi_i^0\rangle| = 5.0\mu_B$, which is enhanced compared to the spin-only value of $4\mu_B$ for $S = 2$. A similar enhancement has been reported both from neutron [298, 299] and susceptibility [300] analysis.

For the zigzag wavevector along the b-axis, the moments are oriented in the ac^*-plane, making an angle of 11° with the c^* axis, as shown in Fig. 5.1. Previous neutron scattering data was analyzed in terms of the moments oriented precisely along the c^* axis, although this is not required by symmetry. Future experiments could refine the moment direction. The composition of the MF ground state is 75% $J_{\text{eff}} = 1$, 23% $J_{\text{eff}} = 2$, and 2% $J_{\text{eff}} = 3$, demonstrating significant mixture of different spin-orbital components. This mixing is driven both by the on-site crystal field and the (mean-field) effects of intersite coupling.

In principle, there are two classes of excitations of the magnetically ordered phase: magnon-like modes within the lowest J_{eff} manifold, and spin-orbit excitons (SOE) between different J_{eff} values. In $FePS_3$, we find that these excitations are strongly mixed. The predicted dispersion of the hybrid SOE/magnon excitations is shown in Fig. 5.5(a), with the color indicating the J-composition of the mode. In Fig. 5.5(b), we show the predicted low-energy dynamical magnetic structure factor, defined by $D_{\text{mag}}(q) = \sum_\mu \int e^{i\omega t}[L^\mu_{-q}(t) -$

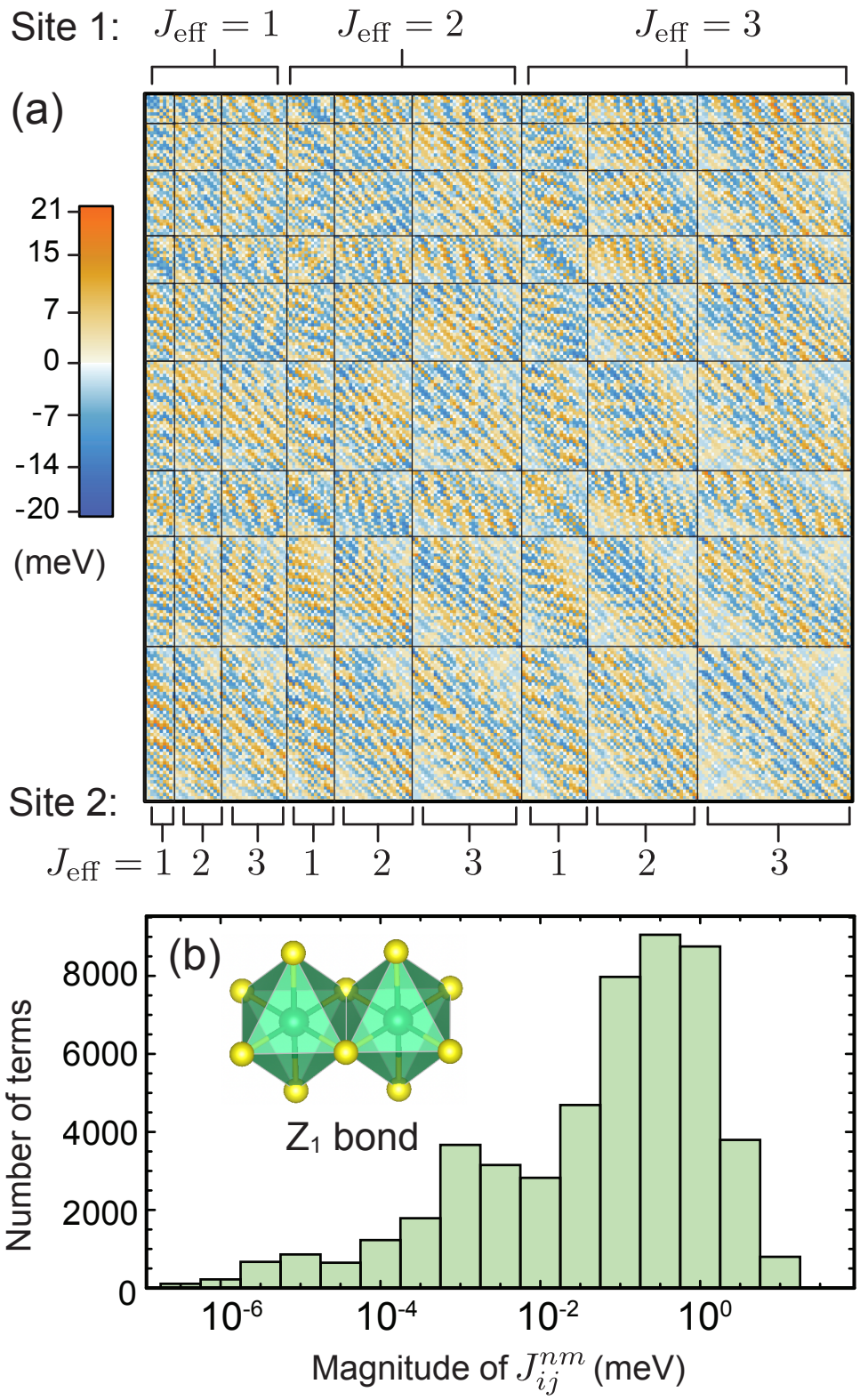

Figure 5.4: Intersite interactions for Z_1 bond and $U_{t2g} = 4.2$ eV for full $J_{\text{eff}} = 1, 2$, and 3 model. (a) Plot of interaction matrix indicating location of different J_{eff} blocks for each site. A constant has been subtracted from the diagonal to make the matrix traceless for plotting. (b) Histogram showing distribution of the magnitude of matrix elements.

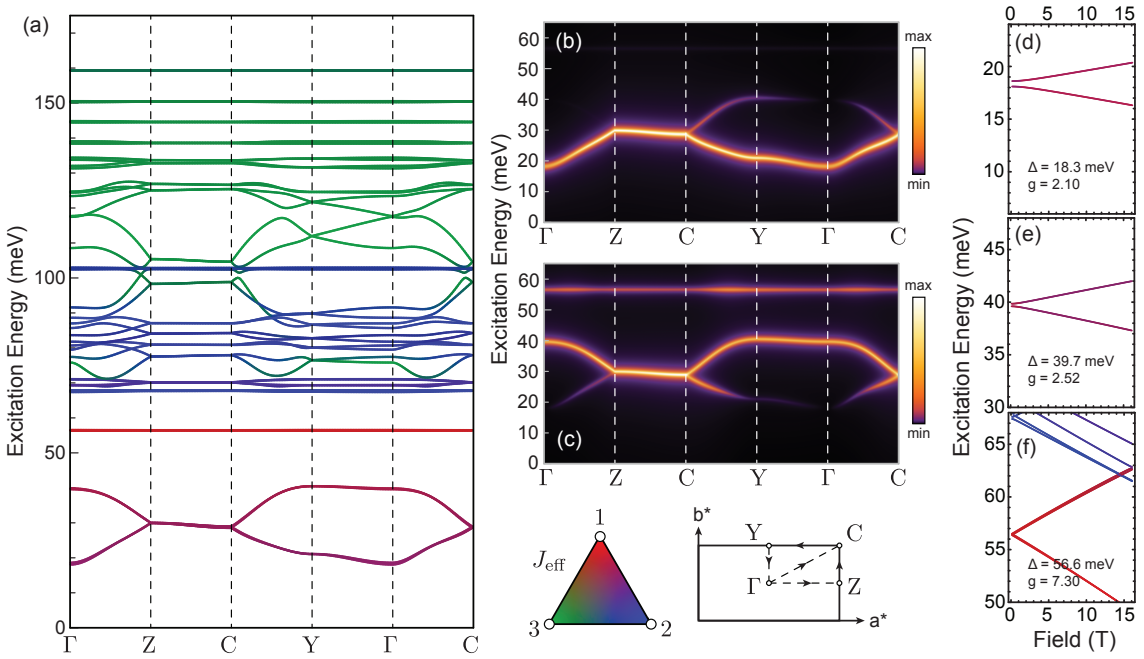

Figure 5.5: Results from LFWT. (a) Full magnon/spin-orbit exciton band structure, with bands colored according to their J_{eff} composition. (b) Dynamical magnetic structure factor $D_{\text{mag}}(q)$ for the lowest energy bands. (c) Dynamical electrical polarization structure factor $D_{\text{el}}(q)$ for the lowest energy bands (see text for definition). (d-f) Evolution of the lowest excitations with magnetic field oriented along the c^*-axis, with zero-field energy Δ and slope g indicated. To be compared with Ref. [269].

$2S^{\mu}_{-q}(t)][L^{\mu}_{q}(0) - 2S^{\mu}_{q}(0)]dt$. The intensity pattern matches well with the inelastic neutron scattering (INS) experiments [265–267].

In accordance with INS experiments, the lowest branch forms two dispersive bands. We predict the gap at the Γ-point to be $\sim$ 18 meV, which is somewhat larger than the experimental value of 15 meV. This discrepancy is likely due to an overestimation of the trigonal crystal field splitting at the DFT level. For example, a recent x-ray absorption study [274] was well-modelled with an absolute splitting of the t_{2g} orbitals on the order of $\sim$ 10 meV, while we find a value of $\sim$ 44 meV from the Wannier-interpolated crystal field terms. Apart from this discrepancy, the predicted dispersions of the excitations below 50 meV are in excellent agreement with INS experiments. Due to their differing spin-orbital composition, population of the low-energy modes alters the J-composition of the local moments. For example, at $q = 0$, the eigenvector for the lower band corresponds to a composition of 53% $J_{\text{eff}} = 1$, 38% $J_{\text{eff}} = 2$, and 9% $J_{\text{eff}} = 3$. Similarly, the upper band has

a composition of 65% $J_{\text{eff}} = 1$, 28% $J_{\text{eff}} = 2$, and 7% $J_{\text{eff}} = 3$. In both cases, relative weight is shifted from $J_{\text{eff}} = 1$ to $J_{\text{eff}} = 2$, highlighting the mixed SOE/magnon character of these modes. Another particular feature of the bands is the very weak dispersion along the $\Gamma \rightarrow$ Y and Z $\rightarrow$ C paths, which implies the excitations primarily propagate perpendicular to the ordering wavevector, i.e. along the ferromagnetic zigzag chains. This feature was discussed in Ref. [267], and is naturally reproduced here.

Above the lowest branch, there is a flat band at $\sim$ 57 meV. This band essentially represents the quadrupolar $\Delta m_J = \pm 2$ modes of the lowest $J_{\text{eff}} = 1$ single-ion level. These modes correspond to a composition of 78% $J_{\text{eff}} = 1$, 13% $J_{\text{eff}} = 2$, and 9% $J_{\text{eff}} = 3$, which is similar to the composition of the ground-state moments. Beyond the LFWT approximation, we would expect this mode to hybridize with the 2-magnon continuum, which may lead to broadening. Finally, at higher energies there are a number of modes between 70 and 170 meV, with mostly $J_{\text{eff}} = 2$ and 3 SOE character. These likely explain the broad absorption bands observed in the same region of energies via infrared and Raman measurements [275, 301].

We next consider the THz/infrared studies reported in Ref. [269]. These studies observed the main modes at 15.1, 39.6, and 57.5 meV, which correspond very well with the predicted energies of 18.3, 39.7, and 56.6 meV from LFWT (at $q = 0$). In Fig. 5.5(d-f), we show the evolution of these modes with magnetic field applied along the out-of-plane c^* direction. The modes at 18.3 and 39.7 meV each consist of a pair of excitations that are symmetrically split under applied field. These represent magnon-like excitations ($\Delta m_J \sim \pm 1$), which are essentially confined to either a spin-up or spin-down sublattice. Based on the predicted slopes, we evaluate the effective g-values for the excitations to be 2.10 and 2.52, respectively. These values are in good agreement with the experimental value of 2.15 for both modes. The quadrupolar ($\Delta m_J \sim \pm 2$) mode at 56.6 meV instead has a much larger slope, which we evaluate as $g \approx 7.3$. Experimentally, it was found to be 9.2. While, naively, one might expect the energies of the $\Delta m_J \sim \pm 2$ excitations to have twice the slope of the $\Delta m_J \sim \pm 1$ excitations with respect to field, it should be emphasized that the spin-orbital composition of the excitations is quite different. The lower energy modes have significantly higher $J_{\text{eff}} = 2$ character, which reduces the effective g-value.

Finally, it is worth considering why the 39.7 meV mode has appreciable intensity in the THz/infrared spectra? As shown in Fig. 5.5(b), this band has vanishing weight in the dynamical magnetic structure factor near $q = 0$. This is because this mode is odd under inversion, while the magnetic dipole operator is even. In principle, the finite intensity may therefore reflect a lowering of symmetry in the bulk, or a surface effect in thin samples. Here we present another possibility that arises from the orbital component of the excitations: in a sufficiently low-symmetry crystal field, these modes are electric dipole-active. In order to demonstrate this, we computed the electrical polarization operators in the dCEH basis from the matrix elements of $\mathbf{P} = -e\mathbf{r}$ between d-orbital Wannier functions on the same Fe site. In Fig. 5.5(c), we show the predicted electric dipole structure factor, defined by $D_{\mathrm{el}}(q) = \sum_{\mu} \int e^{i\omega t} P^{\mu}_{-q}(t) P^{\mu}_{q}(0) dt$. For $q = 0$, this is proportional to the electric dipole absorption intensity, which contributes to THz/infrared spectra, but not INS. Since $\mathbf{P}$ is odd under inversion, this provides a route to observe the inversion-odd "exchange modes" without lowering of symmetry, provided such excitations significantly alter the orbital composition. In the present case of $FePS_3$, where the magnons and SOEs are strongly mixed, this condition is satisfied. As shown in Fig. 5.5(c), both the 39.7 and 56.6 meV excitations are electric dipole active.

5.6 Conclusions

In this work, we have investigated the low-energy model, ground state, and excitations of $FePS_3$, which has been of growing interest in the context of 2D magnetism. Contrary to typical expectations for $3d$ transition metal compounds, SOC is very important to accurately model the low-lying excitations. In fact, the weakness of SOC compared to crystal field splitting and intersite exchange leads to spectral overlap and mixing of magnons and spin-orbit excitons to form hybrid excitations, the properties of which depend on their specific spin-orbital composition. We have shown that a comprehensive model including all local J_{eff} states, obtained from first principles calculations employing the dCEH approach, reproduces all essential experimental details with remarkable quantititive agreement. While these findings do not invalidate previous phenomenological models (of e.g. spin-phonon coupling

in $FePS_3$) in terms of an $S = 2$ system, a complete microscopic picture of the intriguing optical, magnetic, and phononic properties should account for the large orbital moment. For example, due to the relative weakness of SOC, the specific spin-orbital composition of the local moments and excitations can be strongly perturbed by structural distortions, potentially enhancing spin-lattice coupling and sensitivity to symmetry breaking at the surface. Effects such as the giant surface optical second harmonic generation [251], and strong spin-phonon coupling [253–256] may therefore be rooted in SOC. Overall, the results highlight that complex spin-orbital phenomena may be found even in first row transition metal compounds, and that we have the tools to address them.

5.7 Methods

Density Functional Theory calculations

Ab-initio DFT calculations were performed starting from the experimental $C2/m$ structure of $FePS_3$ [302] in order to parameterize the single-particle parts of the electronic Hamiltonian. These calculations employed the package FPLO [199, 200], and were performed at the GGA (PBE) level [201] using a $12 \times 12 \times 12$ k-grid for self-consistent calculations. Hopping integrals were obtained by performing non-relativistic calculations, and projecting the resulting electronic bands onto Fe d-orbitals to construct Wannier functions [303]. We also repeated this procedure for fully relativistic calculations in order to check the effects of SOC on the single-particle Wannier Hamiltonian. From the comparison of the two calculations, we find that SOC is well captured by an on-site $\lambda \mathbf{L} \cdot \mathbf{S}$ term with $\lambda = 53$ meV, which was subsequently included in the derivation of the low-energy Hamiltonian. Imaginary intersite hoppings were negligible in the fully relativistic calculation, and were subsequently omitted.

Linear Flavor Wave Theory

Calculations of the ground state and excitations of $FePS_3$ were performed within the LFWT approach. The mean-field model $\mathcal{H}_{\mathrm{MF}} = \sum_{i,n} \left(A_i^n + \sum_{jm} J_{ij}^{nm} \langle \mathcal{O}_j^m \rangle \right) \mathcal{O}_i^n$ was first solved self-consistently. From this, the local eigenstates $|\psi_i^\alpha\rangle$ were then employed to construct the LFWT Hamiltonian in terms of bosonic operators $b_{i,\alpha}^\dagger \equiv |\psi_i^\alpha\rangle\langle\psi_i^0|$ where $|\psi_i^0\rangle$ corresponds

to the local ground state of the MF model at site i. Then, we may write:

$$\begin{aligned}\mathcal{H}_{\mathrm{LFWT}} = & \sum_i \varepsilon_i^\alpha b_{i,\alpha}^\dagger b_{i,\alpha} + \sum_{ij} t_{ij}^{\alpha\beta} b_{i,\alpha}^\dagger b_{j,\beta} \\ & + \sum_{ij} \Delta_{ij}^{\alpha\beta} b_{i,\alpha}^\dagger b_{j,\beta}^\dagger + H.c. \end{aligned} \tag{5.10}$$

where:

$$\varepsilon_i^\alpha = \langle \psi_i^\alpha | \mathcal{H}_{\mathrm{MF}} | \psi_i^\alpha \rangle \tag{5.11}$$

$$t_{ij}^{\alpha\beta} = J_{ij}^{nm} \langle \psi_i^\alpha | \mathcal{O}_i^n | \psi_i^0 \rangle \langle \psi_j^0 | \mathcal{O}_j^m | \psi_j^\beta \rangle \tag{5.12}$$

$$\Delta_{ij}^{nm} = J_{ij}^{nm} \langle \psi_i^\alpha | \mathcal{O}_i^n | \psi_i^0 \rangle \langle \psi_j^\beta | \mathcal{O}_j^m | \psi_j^0 \rangle \tag{5.13}$$

The linearized model was then diagonalized utilizing the standard Cholesky decomposition approach [304, 305]. Following a similar approach, operators corresponding to the spin, orbital momentum, and electric dipole operators were constructed in terms of the bosonic operators $b_{i,\alpha}^\dagger$, and the q-dependent excitation intensities computed from the resulting eigenvectors.

5.8 Supplemental Material

5.8.1 Basis functions for J States

In order to obtain the effective Hamiltonian describing the $J_{\mathrm{eff}} = 1, 2$, and 3 states, it is necessary to project the low-energy eigenstates of a given two-site cluster onto ideal reference states, according to the standard dCEH procedure. These states can be easily derived, but are reproduced here in full detail for future convenience. The states labelled according to $|J_{\mathrm{eff}}, m_J\rangle$ can be expanded in terms of $|S, m_S; L_{\mathrm{eff}}, m_L\rangle$ states. In particular, the $J_{\mathrm{eff}} = 3$

states are:

$$|3,+3\rangle = |2,+2;1,+1\rangle \tag{5.14}$$

$$|3,+2\rangle = \sqrt{\frac{1}{3}}|2,+2;1,0\rangle + \sqrt{\frac{2}{3}}|2,+1;1,+1\rangle \tag{5.15}$$

$$\begin{aligned}|3,+1\rangle = &\sqrt{\frac{1}{15}}|2,+2;1,-1\rangle + \sqrt{\frac{8}{15}}|2,+1;1,0\rangle \\ &+ \sqrt{\frac{6}{15}}|2,0;1,+1\rangle\end{aligned} \tag{5.16}$$

$$\begin{aligned}|3,0\rangle = &\sqrt{\frac{1}{5}}|2,+1;1,-1\rangle + \sqrt{\frac{3}{5}}|2,0;1,0\rangle \\ &+ \sqrt{\frac{1}{5}}|2,-1;1,+1\rangle\end{aligned} \tag{5.17}$$

$$\begin{aligned}|3,-1\rangle = &\sqrt{\frac{1}{15}}|2,-2;1,+1\rangle + \sqrt{\frac{8}{15}}|2,-1;1,0\rangle \\ &+ \sqrt{\frac{6}{15}}|2,0;1,-1\rangle\end{aligned} \tag{5.18}$$

$$|3,-2\rangle = \sqrt{\frac{1}{3}}|2,-2;1,0\rangle + \sqrt{\frac{2}{3}}|2,-1;1,-1\rangle \tag{5.19}$$

$$|3,-3\rangle = |2,-2;1,-1\rangle \tag{5.20}$$

The $J_{\text{eff}} = 2$ states are:

$$|2,+2\rangle = \sqrt{\frac{2}{3}}|2,+2,1,0\rangle - \sqrt{\frac{1}{3}}|2,+1,1,+1\rangle \tag{5.21}$$

$$\begin{aligned}|2,+1\rangle = &\sqrt{\frac{1}{3}}|2,+2,1,-1\rangle + \sqrt{\frac{1}{6}}|2,+1,1,0\rangle \\ &- \sqrt{\frac{1}{2}}|2,0,1,+1\rangle\end{aligned} \tag{5.22}$$

$$|2,0\rangle = \sqrt{\frac{1}{2}}|2,+1,1,-1\rangle - \sqrt{\frac{1}{2}}|2,-1,1,+1\rangle \tag{5.23}$$

$$\begin{aligned}|2,-1\rangle = &-\sqrt{\frac{1}{3}}|2,-2,1,+1\rangle - \sqrt{\frac{1}{6}}|2,-1,1,0\rangle \\ &+ \sqrt{\frac{1}{2}}|2,0,1,-1\rangle\end{aligned} \tag{5.24}$$

$$|2,-2\rangle = -\sqrt{\frac{2}{3}}|2,-2,1,0\rangle + \sqrt{\frac{1}{3}}|2,-1,1,-1\rangle \tag{5.25}$$

The $J_{\text{eff}} = 1$ states are:

$$|1,+1\rangle = \sqrt{\frac{3}{5}}|2,+2,1,-1\rangle - \sqrt{\frac{3}{10}}|2,+1,1,0\rangle + \sqrt{\frac{1}{10}}|2,0,1,+1\rangle \tag{5.26}$$

$$|1,0\rangle = \sqrt{\frac{3}{10}}|2,+1,1,-1\rangle - \sqrt{\frac{2}{5}}|2,0,1,0\rangle + \sqrt{\frac{3}{10}}|2,-1,1,+1\rangle \tag{5.27}$$

$$|1,-1\rangle = \sqrt{\frac{3}{5}}|2,-2,1,+1\rangle - \sqrt{\frac{3}{10}}|2,-1,1,0\rangle + \sqrt{\frac{1}{10}}|2,0,1,-1\rangle \tag{5.28}$$

Each of the $|S, m_S; L_{\text{eff}}, m_L\rangle$ states can then be written as a linear combination of Slater determinants. For this purpose, we define the following orbitals:

$$e_a = d_{z^2} \quad , \quad e_b = d_{x^2-y^2} \quad , \quad t_0 = d_{xy} \tag{5.29}$$

$$t_+ = -\frac{1}{\sqrt{2}}(d_{yz} + id_{xz}) \quad , \quad t_- = \frac{1}{\sqrt{2}}(d_{yz} - id_{xz}) \tag{5.30}$$

Then we have:

$$|2,+2,1,+1\rangle = |e_{a\uparrow}e_{b\uparrow}t_{+\uparrow}t_{+\downarrow}t_{0\uparrow}t_{-\uparrow}\rangle \tag{5.31}$$

$$|2,+2,1,0\rangle = -|e_{a\uparrow}e_{b\uparrow}t_{+\uparrow}t_{0\uparrow}t_{0\downarrow}t_{-\uparrow}\rangle \tag{5.32}$$

$$|2,+2,1,-1\rangle = |e_{a\uparrow}e_{b\uparrow}t_{+\uparrow}t_{0\uparrow}t_{-\uparrow}t_{-\downarrow}\rangle \tag{5.33}$$

$$\begin{aligned} |2,+1,1,+1\rangle = \frac{1}{2}\,(&|e_{a\downarrow}e_{b\uparrow}t_{+\uparrow}t_{+\downarrow}t_{0\uparrow}t_{-\uparrow}\rangle \\ &+|e_{a\uparrow}e_{b\downarrow}t_{+\uparrow}t_{+\downarrow}t_{0\uparrow}t_{-\uparrow}\rangle \\ &+|e_{a\uparrow}e_{b\uparrow}t_{+\uparrow}t_{+\downarrow}t_{0\downarrow}t_{-\uparrow}\rangle \\ &+|e_{a\uparrow}e_{b\uparrow}t_{+\uparrow}t_{+\downarrow}t_{0\uparrow}t_{-\downarrow}\rangle) \end{aligned} \tag{5.34}$$

$$\begin{aligned} |2,+1,1,0\rangle = -\frac{1}{2}\,(&|e_{a\downarrow}e_{b\uparrow}t_{+\uparrow}t_{0\uparrow}t_{0\downarrow}t_{-\uparrow}\rangle \\ &+|e_{a\uparrow}e_{b\downarrow}t_{+\uparrow}t_{0\uparrow}t_{0\downarrow}t_{-\uparrow}\rangle \end{aligned}$$

$$
\begin{aligned}
&+|e_{a\uparrow}e_{b\uparrow}t_{+\downarrow}t_{0\uparrow}t_{0\downarrow}t_{-\uparrow}\rangle \\
&+|e_{a\uparrow}e_{b\uparrow}t_{+\uparrow}t_{0\uparrow}t_{0\downarrow}t_{-\downarrow}\rangle) \qquad (5.35)\\
|2,+1,1,-1\rangle = \frac{1}{2}\,(&|e_{a\downarrow}e_{b\uparrow}t_{+\uparrow}t_{0\uparrow}t_{-\uparrow}t_{-\downarrow}\rangle \\
&+|e_{a\uparrow}e_{b\downarrow}t_{+\uparrow}t_{0\uparrow}t_{-\uparrow}t_{-\downarrow}\rangle \\
&+|e_{a\uparrow}e_{b\uparrow}t_{+\downarrow}t_{0\uparrow}t_{-\uparrow}t_{-\downarrow}\rangle \\
&+|e_{a\uparrow}e_{b\uparrow}t_{+\uparrow}t_{0\downarrow}t_{-\uparrow}t_{-\downarrow}\rangle) \qquad (5.36)
\end{aligned}
$$

$$
\begin{aligned}
|2,0,1,+1\rangle = \frac{1}{\sqrt{6}}\,(&|e_{a\downarrow}e_{b\downarrow}t_{+\uparrow}t_{+\downarrow}t_{0\uparrow}t_{-\uparrow}\rangle \\
&+|e_{a\downarrow}e_{b\uparrow}t_{+\uparrow}t_{+\downarrow}t_{0\downarrow}t_{-\uparrow}\rangle \\
&+|e_{a\downarrow}e_{b\uparrow}t_{+\uparrow}t_{+\downarrow}t_{0\uparrow}t_{-\uparrow}\rangle \\
&+|e_{a\uparrow}e_{b\downarrow}t_{+\uparrow}t_{+\downarrow}t_{0\uparrow}t_{-\downarrow}\rangle \\
&+|e_{a\uparrow}e_{b\downarrow}t_{+\uparrow}t_{+\downarrow}t_{0\downarrow}t_{-\uparrow}\rangle \\
&+|e_{a\uparrow}e_{b\uparrow}t_{+\uparrow}t_{+\downarrow}t_{0\downarrow}t_{-\downarrow}\rangle) \qquad (5.37)\\
|2,0,1,0\rangle = -\frac{1}{\sqrt{6}}\,(&|e_{a\downarrow}e_{b\downarrow}t_{+\uparrow}t_{0\uparrow}t_{0\downarrow}t_{-\uparrow}\rangle \\
&+|e_{a\downarrow}e_{b\uparrow}t_{+\downarrow}t_{0\uparrow}t_{0\downarrow}t_{-\uparrow}\rangle \\
&+|e_{a\downarrow}e_{b\uparrow}t_{+\uparrow}t_{0\uparrow}t_{0\downarrow}t_{-\downarrow}\rangle \\
&+|e_{a\uparrow}e_{b\downarrow}t_{+\downarrow}t_{0\uparrow}t_{0\downarrow}t_{-\uparrow}\rangle \\
&+|e_{a\uparrow}e_{b\downarrow}t_{+\uparrow}t_{0\uparrow}t_{0\downarrow}t_{-\downarrow}\rangle \\
&+|e_{a\uparrow}e_{b\uparrow}t_{+\downarrow}t_{0\uparrow}t_{0\downarrow}t_{-\downarrow}\rangle) \qquad (5.38)\\
|2,0,1,-1\rangle = \frac{1}{\sqrt{6}}\,(&|e_{a\downarrow}e_{b\downarrow}t_{+\uparrow}t_{0\uparrow}t_{-\uparrow}t_{-\downarrow}\rangle \\
&+|e_{a\downarrow}e_{b\uparrow}t_{+\downarrow}t_{0\uparrow}t_{-\uparrow}t_{-\downarrow}\rangle \\
&+|e_{a\downarrow}e_{b\uparrow}t_{+\uparrow}t_{0\downarrow}t_{-\uparrow}t_{-\downarrow}\rangle \\
&+|e_{a\uparrow}e_{b\downarrow}t_{+\downarrow}t_{0\uparrow}t_{-\uparrow}t_{-\downarrow}\rangle \\
&+|e_{a\uparrow}e_{b\downarrow}t_{+\uparrow}t_{0\downarrow}t_{-\uparrow}t_{-\downarrow}\rangle \\
&+|e_{a\uparrow}e_{b\uparrow}t_{+\downarrow}t_{0\downarrow}t_{-\uparrow}t_{-\downarrow}\rangle) \qquad (5.39)
\end{aligned}
$$

$$
\begin{aligned}
|2,-1,1,+1\rangle = \frac{1}{2}\,(&|e_{a\uparrow}e_{b\downarrow}t_{+\uparrow}t_{+\downarrow}t_{0\downarrow}t_{-\downarrow}\rangle \\
&+|e_{a\downarrow}e_{b\uparrow}t_{+\uparrow}t_{+\downarrow}t_{0\downarrow}t_{-\downarrow}\rangle \\
&+|e_{a\downarrow}e_{b\downarrow}t_{+\uparrow}t_{+\downarrow}t_{0\uparrow}t_{-\downarrow}\rangle \\
&+|e_{a\downarrow}e_{b\downarrow}t_{+\uparrow}t_{+\downarrow}t_{0\downarrow}t_{-\uparrow}\rangle) \qquad (5.40)\\
|2,-1,1,0\rangle = -\frac{1}{2}\,(&|e_{a\uparrow}e_{b\downarrow}t_{+\downarrow}t_{0\uparrow}t_{0\downarrow}t_{-\downarrow}\rangle \\
&+|e_{a\downarrow}e_{b\uparrow}t_{+\downarrow}t_{0\uparrow}t_{0\downarrow}t_{-\downarrow}\rangle \\
&+|e_{a\downarrow}e_{b\downarrow}t_{+\uparrow}t_{0\uparrow}t_{0\downarrow}t_{-\downarrow}\rangle \\
&+|e_{a\downarrow}e_{b\downarrow}t_{+\downarrow}t_{0\uparrow}t_{0\downarrow}t_{-\uparrow}\rangle) \qquad (5.41)\\
|2,-1,1,-1\rangle = \frac{1}{2}\,(&|e_{a\uparrow}e_{b\downarrow}t_{+\downarrow}t_{0\downarrow}t_{-\uparrow}t_{-\downarrow}\rangle \\
&+|e_{a\downarrow}e_{b\uparrow}t_{+\downarrow}t_{0\downarrow}t_{-\uparrow}t_{-\downarrow}\rangle \\
&+|e_{a\downarrow}e_{b\downarrow}t_{+\uparrow}t_{0\downarrow}t_{-\uparrow}t_{-\downarrow}\rangle \\
&+|e_{a\downarrow}e_{b\downarrow}t_{+\downarrow}t_{0\uparrow}t_{-\uparrow}t_{-\downarrow}\rangle) \qquad (5.42)\\
|2,-2,1,+1\rangle = &|e_{a\downarrow}e_{b\downarrow}t_{+\uparrow}t_{+\downarrow}t_{0\downarrow}t_{-\downarrow}\rangle \qquad (5.43)\\
|2,-2,1,0\rangle = -&|e_{a\downarrow}e_{b\downarrow}t_{+\downarrow}t_{0\uparrow}t_{0\downarrow}t_{-\downarrow}\rangle \qquad (5.44)\\
|2,-2,1,-1\rangle = &|e_{a\downarrow}e_{b\downarrow}t_{+\downarrow}t_{0\downarrow}t_{-\uparrow}t_{-\downarrow}\rangle \qquad (5.45)
\end{aligned}
$$

5.8.2 Intersite Hund's Coupling Matrices

As discussed in the main text, we include the effects of intersite Hund's coupling for nearest neighbor bonds, in order to treat the ferromagnetic Goodenough-Kanamori exchange. The resulting electronic Hamiltonian takes the form:

$$
\mathcal{H}_{Jnn} = \sum_{ij\alpha\beta\sigma\sigma'} J_{H,ij}^{\alpha\beta}\; c_{i,\alpha,\sigma}^{\dagger} c_{j,\beta,\sigma'}^{\dagger} c_{i,\alpha,\sigma'} c_{j,\beta,\sigma} \qquad (5.46)
$$

where the coefficients $J^{\alpha\beta}_{H,ij}$ were approximated as:

$$J^{\alpha\beta}_{H,ij} = \sum_{n,\delta,\gamma} (U^n - J^n_H)\ \phi^{n,\delta}_{i,\alpha}\phi^{n\delta}_{j,\beta}\phi^{n,\gamma}_{i,\alpha}\phi^{n,\gamma}_{j,\beta} + J^n_H|\phi^{n,\delta}_{i,\alpha}|^2|\phi^{n,\gamma}_{j,\beta}|^2 \tag{5.47}$$

with $U^n = 2J^n_H$, and $J^n_H = 0.27$ eV. The resulting tensors are thus summarized as (in meV):

X_1 bond:

$$J^{\alpha\beta}_{H,ij} = \left(\begin{array}{c|ccccc} & d_{xy} & d_{xz} & d_{yz} & d_{z^2} & d_{x^2-y^2} \\ \hline d_{xy} & 0. & 0.03 & 0.08 & 0.2 & 0.02 \\ d_{xz} & 0.03 & 0. & 0.09 & 0.07 & 0.16 \\ d_{yz} & 0.08 & 0.09 & 0.44 & 1.2 & 0.8 \\ d_{z^2} & 0.2 & 0.07 & 1.2 & 0.7 & 1.32 \\ d_{x^2-y^2} & 0.02 & 0.16 & 0.8 & 1.32 & 0.01 \end{array}\right) \tag{5.48}$$

Y_1 bond:

$$J^{\alpha\beta}_{H,ij} = \left(\begin{array}{c|ccccc} & d_{xy} & d_{xz} & d_{yz} & d_{z^2} & d_{x^2-y^2} \\ \hline d_{xy} & 0. & 0.08 & 0.03 & 0.2 & 0.02 \\ d_{xz} & 0.08 & 0.44 & 0.09 & 1.2 & 0.8 \\ d_{yz} & 0.03 & 0.09 & 0. & 0.07 & 0.16 \\ d_{z^2} & 0.2 & 1.2 & 0.07 & 0.7 & 1.32 \\ d_{x^2-y^2} & 0.02 & 0.8 & 0.16 & 1.32 & 0.01 \end{array}\right) \tag{5.49}$$

Z_1 bond:

$$J^{\alpha\beta}_{H,ij} = \left(\begin{array}{c|ccccc} & d_{xy} & d_{xz} & d_{yz} & d_{z^2} & d_{x^2-y^2} \\ \hline d_{xy} & 0.4 & 0.08 & 0.08 & 0.57 & 1.37 \\ d_{xz} & 0.08 & 0. & 0.03 & 0.06 & 0.15 \\ d_{yz} & 0.08 & 0.03 & 0. & 0.06 & 0.15 \\ d_{z^2} & 0.57 & 0.06 & 0.06 & 0.29 & 0.7 \\ d_{x^2-y^2} & 1.37 & 0.15 & 0.15 & 0.7 & 1.71 \end{array}\right) \tag{5.50}$$

5.8.3 Biquadratic Exchange Couplings

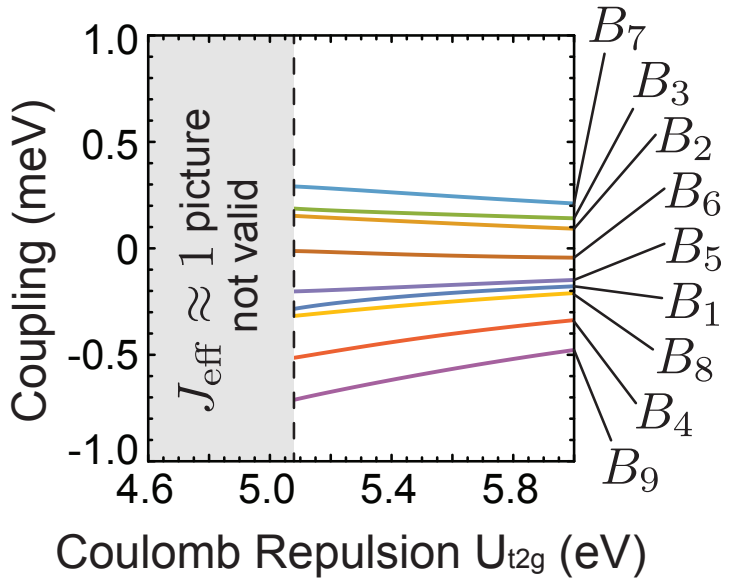

Figure 5.6: Intersite biquadratic interactions for Z_1 bond as a function of U_{t2g}.

In the limit of large U_{t2g}, the intersite interactions may be discussed in terms of states smoothly connected to the lowest $J_{\text{eff}} = 1$ levels. In this case, the biquadratic terms may

be expressed in terms of the operators:

$$\mathcal{O}_i^{2,-2} = S_i^x S_i^y + S_i^y S_i^x \tag{5.51}$$

$$\mathcal{O}_i^{2,-1} = S_i^y S_i^z + S_i^z S_i^y \tag{5.52}$$

$$\mathcal{O}^{2,0} = 3S_z^2 - 2 \tag{5.53}$$

$$\mathcal{O}_i^{2,+1} = S_i^x S_i^z + S_i^z S_i^x \tag{5.54}$$

$$\mathcal{O}_i^{2,+2} = (S_i^x)^2 - (S_i^y)^2 \tag{5.55}$$

Here, the (x, y, z) axes correspond to the cubic axes defined in Fig. 1 of the main text. Defining $\mathbf{O}_i = (\mathcal{O}_i^{2,-2}, \mathcal{O}_i^{2,-1}, \mathcal{O}_i^{2,0}, \mathcal{O}_i^{2,+1}, \mathcal{O}_i^{2,+2})$, the biquadratic interactions can be written $\mathbf{O}_i \cdot \mathbb{B}_{ij} \cdot \mathbf{O}_j$. For the nearest neighbor Z-bond, the coupling matrix can be written in terms of nine parameters as:

$$\mathbb{B}_{ij} = \begin{pmatrix} B_1 & B_2 & B_3 & B_2 & 0 \\ B_2 & B_4 & B_5 & B_6 & B_7 \\ B_3 & B_5 & B_8 & B_5 & 0 \\ B_2 & B_6 & B_5 & B_4 & -B_7 \\ 0 & B_7 & 0 & -B_7 & B_9 \end{pmatrix} \tag{5.56}$$

The computed values are given in Fig. 5.6 as a function of U_{t2g}. It can be seen that the biquadratic couplings are indeed relatively large.

Chapter 6

Spin-Phonon Coupling in Transition Metal Insulators

This chapter is adapted from the arXiv:2407.00659 preprint titled "Spin-Phonon Coupling in Transition Metal Insulators: General Computational Approach and Application to $MnPSe_3$".

In this chapter, we describe a general approach to the first principles estimation of generic spin-orbit-phonon couplings. Understanding this interaction is crucial as it is important to understand diverse range of phenomena of recent interest. Specifically, in transition metal insulators with strong spin-orbit effects, it may give rise to hybrid magnetoelastic excitations, and the controversial phonon thermal Hall effect. The method is demonstrated by application to study the temperature-dependent optical phonon lineshapes in $MnPSe_3$, for which we find quantitative agreement with recent experiments.

My role in this project was to develop a new *ab initio* method to derive a complete set of spin-phonon couplings for $MnPSe_3$. This was done by optimizing the first principles method discussed in chapter 2.

6.1 Introduction

Spin-lattice coupling underlies a wide variety of phenomena in magnetic transition metal insulators. For example, it is considered a key ingredient for optimization of relaxation times

in spin-qubits[306, 307], the thermal transport properties of magnon spintronics[308], and the properties of 2D layered magnets pursued for magnetic heterostructure devices[241, 309–311]. At a basic level, this coupling describes the dependence of magnetic couplings to the positions of atoms in the crystal, but may also include dynamical effects that couple spins to atomic momenta[312–316].

Of recent fundamental interest are a number experimental findings, which all call for a deeper understanding of spin-lattice coupling. Example phenomena include: (i) The formation of magnon-polarons (hybrid one-magnon, one-phonon excitations), such as observed in (Y/Lu)MnO_3,[317, 318] $FePS_3$,[253–255, 263] and $Fe_2Mo_3O_8$[319]. In the latter materials, the avoided crossings may give rise to topologically nontrivial magnetoelastic excitations[261, 264, 319]. (ii) Strong temperature dependence of the longitudinal (phonon) thermal conductivity and/or ultrasound attenuation[320–324] due to spin-phonon scattering, as observed in e.g. $YMnO_3$[325], $FeCr_2S_4$[326], α-$RuCl_3$[106, 327], and various MPS_3 (M = Fe, Mn) compounds[328]. (iii) The controversial phonon thermal Hall effect, now possibly observed in a wide variety of magnetic insulators including $FeCr_2S_4$[326], $FeCl_2$[329], $Fe_2Mo_3O_8$[96], VI_3[97], CrI_3[330], $YMnO_3$[325], $Na_2Co_2TeO_6$[331–334] and α-$RuCl_3$[212, 335–338]. It should be emphasized that the precise explanation of the thermal Hall effect in each material remains somewhat controversial, as there are a variety of potential contributions. These include extrinsic contributions (impurity skew-scattering)[91, 339–341] and intrinsic contributions from topological magnons[73, 342, 343] and fractional spinons[99, 344] in addition to chiral phonons. The latter may acquire chirality as a consequence of spin-lattice coupling, through topological magnon-polaron formation[345–348], dissipationless spin-phonon scattering[82–84, 86, 349–354] (often captured by a phenomenological phonon Hall viscosity), and spin-phonon skew-scattering[87, 88]. In many cases, it has been argued that phonons are likely to contribute significantly to the observed thermal Hall conductivity[97, 329, 331–333, 338, 341], but the precise mechanisms involved in each material remain unclear. What is currently missing is a comprehensive material-specific picture of spin-lattice coupling in each compound, and it's relationship to various properties. Experimentally, it is clear that all of these compounds display strong spin-lattice coupling, in addition to having unquenched orbital moments and/or relatively anisotropic exchange

interactions arising from spin-orbit coupling. Thus, we need a first principles approach capable of accurately treating the complex local spin-orbital moments and their coupling to phonons.

In this work, we describe a new *ab-initio* method for addressing these questions in a material-specific way, by computing generic spin-phonon couplings within the framework of numerical (des Cloizeaux) effective Hamiltonians (dCEHs)[108]. In the dCEH approach generally, a many-body electronic Hamiltonian is solved, and the resulting low-energy states are projected onto a reference low-energy space, in order to obtain an effective Hamiltonian that reproduces the low-energy spectrum exactly. The advantages of this approach are as follows: (i) The use of multi-reference wavefunctions allows the full many-body (spin-orbital multiplet) character of the local states to be faithfully captured, which is relevant for accurate calculations of magnetic anisotropies, and higher order interactions (e.g. ring-exchange and biquadratic exchange), (ii) The method can be applied to any sufficiently local model, and can be easily adapted to treat any combination of spin, charge, and orbital degrees of freedom, (iii) The resulting couplings necessarily retain all symmetries of the paramagnetic crystal, and are quantitatively consistent with analytical perturbation theory by construction, (iv) The method is semi-empirical; a small number of parameters, such as (screened) Coulomb interaction strengths, serve as inputs. These parameters are taken from experimental estimates, when available. While the method is therefore not "fully" *ab-initio*, it does not require very large active spaces or many-body perturbation theory to properly capture the screening of the Coulomb interactions, which is a primary limitation of fully *ab-initio* multireference approaches.

This chapter is organized as follows. In Section 6.2.1 and 6.2.2, we first motivate the form of the generic spin-lattice coupling from perturbation theory, and briefly review existing *ab-initio* approaches. In Section 6.2.3, we discuss the inclusion of phonons into dCEHs framework, and the extraction of spin-phonon couplings.

We then apply this approach to study $MnPSe_3$. This material represents a simple case of strong spin-phonon coupling, as evidenced particularly by the Raman scattering experiment of Ref. [355], which shows strong renormalization of the optical phonon lifetimes due to hybridization with a two-magnon continuum. While this material does not display all

of the spin-orbital complexity of the previously mentioned materials, it serves as an ideal benchmark for our new method. The more complex case of α-$RuCl_3$ is addressed in chapter 7. Thus, in Section 6.3.1 we provide an introduction to this material, and in Section 6.3.2 we compute the zeroth order magnetic couplings. Sections 6.3.3 and 6.3.4 address the phonons and spin-phonon couplings. Finally, in 6.3.5, we combine the computed spin-phonon couplings with semiclassical spin dynamics to compute the magnetic and phononic Raman response for comparison with Ref. [355]. We ultimately demonstrate quantitative agreement with the temperature-dependence of the phonon lifetimes. The results and perspective are summarized in Section 6.4.

6.2 Spin-Phonon Couplings Theory

6.2.1 Intuition from Perturbation Theory

In this section, we first motivate the form of the magnetoelastic couplings, with reference to perturbation theory in electron-phonon coupling. Seminal works on this topic[312–316] often only considered the effects of modulation of local crystal fields by phonons, which is likely the primary source of spin-phonon coupling in rare earth ions. For more general applications, it is instructive to consider modulation of both the crystal field and intersite hoppings. For the sake of discussion, we consider a two-orbital Hubbard model with spin-orbit coupling, with one electron per site on average. The base electronic Hamiltonian is given by:

$$\mathcal{H}_{\text{el}} = \mathcal{H}_0 + \mathcal{H}_{\text{hop}} \tag{6.1}$$

$$\begin{aligned}\mathcal{H}_0 = &\sum_{i\alpha} \epsilon_\alpha \mathbf{c}^\dagger_{i\alpha}\mathbf{c}_{i\alpha} \\ &+ U\sum_i \left(n_{i,1}n_{i,2} + \sum_\alpha n_{i,\alpha,\uparrow}n_{i,\alpha,\downarrow} \right)\end{aligned} \tag{6.2}$$

$$\mathcal{H}_{\text{hop}} = \sum_{ij\alpha\beta} \mathbf{c}^\dagger_{i\alpha}\mathbb{T}^{\alpha\beta}_{ij}\mathbf{c}_{j\beta} \tag{6.3}$$

where:

$$\mathbf{c}^{\dagger}_{i,\alpha} = \begin{pmatrix} c^{\dagger}_{i,\alpha,\uparrow} & c^{\dagger}_{i,\alpha,\downarrow} \end{pmatrix} \quad , \quad \mathbf{c}_{i,\alpha} = \begin{pmatrix} c_{i,\alpha,\uparrow} \\ c_{i,\alpha,\downarrow} \end{pmatrix} \tag{6.4}$$

and $c^{\dagger}_{i,\alpha,\sigma}$ creates an electron at site i, orbital $\alpha \in \{1,2\}$, and spin σ. The orbital energies are taken to satisfy $\epsilon_2 > \epsilon_1$. The number operators are:

$$n_{i,\alpha} = \mathbf{c}^{\dagger}_{i\alpha}\mathbf{c}_{i,\alpha} = n_{i,\alpha,\uparrow} + n_{i,\alpha,\downarrow} \tag{6.5}$$

The hopping matrices are complex as a consequence of SOC, satisfy $\mathbb{T}^{\alpha\beta}_{ij} = (\mathbb{T}^{\beta\alpha}_{ji})^{\dagger}$, and can be written:

$$\mathbb{T}^{\alpha\beta}_{ij} = t^{\alpha\beta}_{ij}\mathbb{I}_{2\times 2} + i\vec{\lambda}^{\alpha\beta}_{ij} \cdot \vec{\sigma} \tag{6.6}$$

where $\mathbb{I}_{2\times 2}$ is a 2×2 identity matrix. The linear electron-phonon coupling can be written:

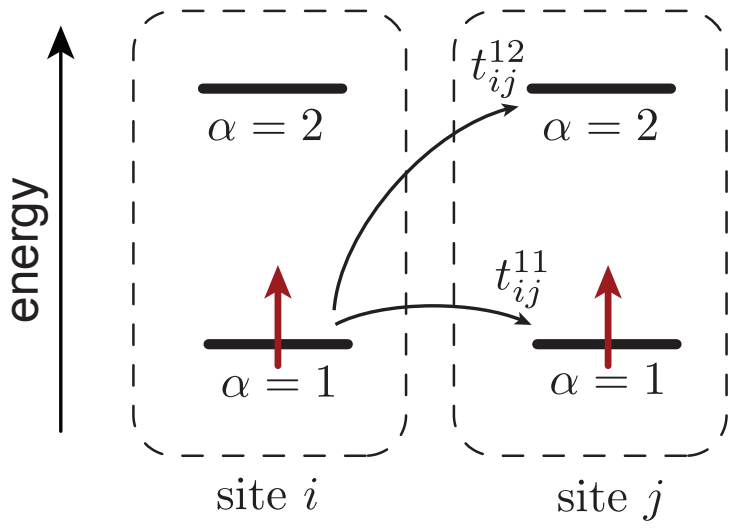

Figure 6.1: Schematic definition of two-orbital model showing two sites, with orbital labels $\alpha, \beta \in \{1,2\}$, and hoppings $t^{\alpha\beta}_{ij}$ shown. The electronic ground state is taken to consist of one electron at each site occupying the $\alpha = 1$ orbital.

$$\mathcal{H}_{\text{el}-\text{ph}} = \sum_{i,\alpha\beta,n} \mathbf{c}^{\dagger}_{i\alpha} \mathbb{D}^{\alpha\beta}_{i,n} \mathbf{c}_{i,\beta} \ \hat{u}_n + \sum_{ij,\alpha\beta,n} \mathbf{c}^{\dagger}_{i\alpha} \mathbb{M}^{\alpha\beta}_{ij,n} \mathbf{c}_{j,\beta} \ \hat{u}_n \tag{6.7}$$

where $\hat{u}_n$ is a generic operator measuring the deviation of the atomic positions from equilibrium along some distortion vector. This may be written in terms of phonon operators as:

$$\hat{u}_n = (a^{\dagger}_n + a_n) \tag{6.8}$$

$$\hat{p}_n = i\omega_n (a^{\dagger}_n - a_n) \tag{6.9}$$

$$\mathcal{H}_{\text{ph}} = \frac{1}{4} \sum_n \left(\frac{1}{\omega_n} \hat{p}^2_n + \omega_n \hat{u}^2_n \right) = \sum_n \omega_n \left(a^{\dagger}_n a_n + \frac{1}{2} \right) \tag{6.10}$$

Here, we have suppressed the units of the phonon operators for simplicity of notation; they will be restored in section 6.2.3 when discussing our *ab-initio* approach. In $\mathcal{H}_{\text{el}-\text{ph}}$, the first term $\mathbb{D}$ represents the modulation of the local crystal-field at site i, while the second term $\mathbb{M}$ represents the modulation of the intersite hopping. These may be written:

$$\mathbb{D}^{\alpha\beta}_{i,n} = d^{\alpha\beta}_{i,n} \mathbb{I}_{2\times 2} + i\vec{\delta}^{\alpha\beta}_{i,n} \cdot \vec{\sigma} \tag{6.11}$$

$$\mathbb{M}^{\alpha\beta}_{ij,n} = m^{\alpha\beta}_{ij,n} \mathbb{I}_{2\times 2} + i\vec{\xi}^{\alpha\beta}_{ij,n} \cdot \vec{\sigma} \tag{6.12}$$

This explicitly distinguishes the spin-independent terms from the spin-dependent terms induced by SOC.

We consider the terms that arise perturbatively in intersite hopping $\mathcal{H}_{\text{hop}}$ and electron-phonon coupling $\mathcal{H}_{\text{el}-\text{ph}}$ (taking the unperturbed Hamiltonian to be $\mathcal{H}_0 + \mathcal{H}_{\text{ph}}$). The low-energy manifold is taken to contain all states with exactly one electron per site occupying orbital $\alpha = 1$, as shown schematically in Fig. 6.1. We may then compute the effective Hamiltonian in this manifold using the standard Brillouin-Wigner approach:

$$\mathcal{H}_{\text{eff}} = \mathbb{P}\mathcal{H}\mathbb{P} + \mathbb{P}\mathcal{H}\mathbb{Q}(\mathcal{E} - \mathbb{Q}\mathcal{H}\mathbb{Q})^{-1}\mathbb{Q}\mathcal{H}\mathbb{P} + ... \tag{6.13}$$

where $\mathcal{E}$ is the state energy, $\mathbb{P}$ is a projection operator onto the low-energy subspace, and $\mathbb{Q} = 1 - \mathbb{P}$.

Let us first consider the effects of modulation of the intersite hopping via the phonons. For this purpose, it is useful to note (for generic $\mathbb{A}_{ij} = a_{ij} + i\vec{\alpha}_{ij} \cdot \vec{\sigma}$ and $\mathbb{B}_{ij} = b_{ij} + i\vec{\beta}_{ij} \cdot \vec{\sigma}$) that:

$$\begin{aligned}
\mathbf{c}_i^\dagger \mathbb{A}_{ij} \mathbf{c}_j \mathbf{c}_j^\dagger \mathbb{B}_{ji} \mathbf{c}_i + (i \leftrightarrow j) = \\
&- 4(a_{ij} b_{ji} + \vec{\alpha}_{ij} \cdot \vec{\beta}_{ji}) \, (\mathbf{S}_i \cdot \mathbf{S}_j) \\
&- 4(b_{ji} \vec{\alpha}_{ij} - a_{ij} \vec{\beta}_{ji}) \cdot (\mathbf{S}_i \times \mathbf{S}_j) \\
&+ 4 \, \mathbf{S}_i \cdot \left(\vec{\alpha}_{ij} \otimes \vec{\beta}_{ji} + \vec{\beta}_{ji} \otimes \vec{\alpha}_{ij} \right) \cdot \mathbf{S}_j \\
&+ 2i(a_{ij} \vec{\beta}_{ji} + b_{ji} \vec{\alpha}_{ij}) \cdot (\mathbf{S}_i - \mathbf{S}_j) \\
&- 2i(\vec{\alpha}_{ij} \times \vec{\beta}_{ji}) \cdot (\mathbf{S}_i + \mathbf{S}_j)
\end{aligned} \tag{6.14}$$

where:

$$S^\mu_{i,\alpha} = \frac{1}{2} \mathbf{c}^\dagger_{i,\alpha} \sigma_\mu \mathbf{c}_{i,\alpha} \tag{6.15}$$

are the different components of the spin operators for orbital α at site i, with $\mu \in \{x, y, z\}$.

At linear order in electron-phonon coupling, we have two types of contributions. The first involves the modulation of the hopping between the occupied $\alpha = 1$ orbitals on each site. The second involves hopping from an occupied $\alpha = 1$ orbital on one site to an unoccupied $\alpha = 2$ orbital on another site. Together, these are:

$$\begin{aligned}
\mathcal{H}_{\text{eff}} = &\sum_{ij,n} \mathbf{c}^\dagger_{i,1} \mathbb{T}^{11}_{ij} \mathbf{c}_{j,1} (\mathcal{E} - \mathcal{H})^{-1} \mathbf{c}^\dagger_{j,1} \mathbb{M}^{11}_{ji,n} \mathbf{c}_{i,1} \hat{u}_n + \hat{u}_n \mathbf{c}^\dagger_{i,1} \mathbb{M}^{11}_{ij,n} \mathbf{c}_{j,1} (\mathcal{E} - \mathcal{H})^{-1} \mathbf{c}^\dagger_{j,1} \mathbb{T}^{11}_{ji} \mathbf{c}_{i,1} \\
&+ \sum_{ij,n} \mathbf{c}^\dagger_{i,1} \mathbb{T}^{12}_{ij} \mathbf{c}_{j,2} (\mathcal{E} - \mathcal{H})^{-1} \mathbf{c}^\dagger_{j,2} \mathbb{M}^{21}_{ji,n} \mathbf{c}_{i,1} \hat{u}_n \\
&+ \hat{u}_n \mathbf{c}^\dagger_{i,1} \mathbb{M}^{12}_{ij,n} \mathbf{c}_{j,2} (\mathcal{E} - \mathcal{H})^{-1} \mathbf{c}^\dagger_{j,2} \mathbb{T}^{21}_{ji} \mathbf{c}_{i,1} + (i \leftrightarrow j)
\end{aligned} \tag{6.16}$$

The inclusion of $\mathcal{H}_{\text{ph}}$ in the denominator $(\mathcal{E} - \mathcal{H})$ has important consequences for the terms, because the energy $\mathcal{E}$ may differ from the excited state energy by the number of phonon

quanta. Accounting for this leads to equation (6.17). Substituting equation (6.14) into equation (6.17), taking $U \gg \omega$, and keeping only spin-dependent terms then gives equation (6.18):

$$\begin{aligned}
\mathcal{H}_{\text{eff}} = & -\sum_{ij,n}\left(\frac{a_n^\dagger}{U-\omega_n}+\frac{a_n}{U+\omega_n}\right)\mathbf{c}_{i,1}^\dagger \mathbb{T}_{ij}^{11}\mathbf{c}_{j,1}\mathbf{c}_{j,1}^\dagger \mathbb{M}_{ji,n}^{11}\mathbf{c}_{i,1} \\
& +\left(\frac{a_n^\dagger}{U+\omega_n}+\frac{a_n}{U-\omega_n}\right)\mathbf{c}_{i,1}^\dagger \mathbb{M}_{ij,n}^{11}\mathbf{c}_{j,1}\mathbf{c}_{j,1}^\dagger \mathbb{T}_{ji}^{11}\mathbf{c}_{i,1} \\
& -\sum_{ij,n}\left(\frac{a_n^\dagger}{U-\omega_n}+\frac{a_n}{U+\omega_n}\right)\mathbf{c}_{i,1}^\dagger \mathbb{T}_{ij}^{12}\mathbb{M}_{ji,n}^{21}\mathbf{c}_{i,1} \\
& +\left(\frac{a_n^\dagger}{U+\omega_n}+\frac{a_n}{U-\omega_n}\right)\mathbf{c}_{i,1}^\dagger \mathbb{M}_{ij,n}^{12}\mathbb{T}_{ji}^{21}\mathbf{c}_{i,1}+(i\leftrightarrow j) \\
= & \sum_{ij,n}\frac{8\hat{u}_n}{U}\Big[\left(t_{ij}^{11}m_{ji,n}^{11}+\vec{\lambda}_{ij}^{11}\cdot\vec{\xi}_{ji,n}^{11}\right)(\mathbf{S}_i\cdot\mathbf{S}_j) \\
& +\left(m_{ji,n}^{11}\vec{\lambda}_{ij}^{11}-t_{ij}^{11}\vec{\xi}_{ji,n}^{11}\right)\cdot(\mathbf{S}_i\times\mathbf{S}_j)-\mathbf{S}_i\cdot\left(\vec{\lambda}_{ij}^{11}\otimes\vec{\xi}_{ji,n}^{11}+\vec{\xi}_{ji,n}^{11}\otimes\vec{\lambda}_{ij}^{11}\right)\cdot\mathbf{S}_j \\
& +\sum_{a\in\{1,2\}}\frac{4\hat{p}_n}{U^2}\Big[(\vec{\lambda}_{ij}^{1a}\times\vec{\xi}_{ji,n}^{a1}-t_{ij}^{1a}\vec{\xi}_{ji,n}^{a1}-m_{ji,n}^{a1}\vec{\lambda}_{ij}^{1a})\cdot\mathbf{S}_i \\
& +(\vec{\lambda}_{ij}^{a1}\times\vec{\xi}_{ji,n}^{1a}+t_{ij}^{a1}\vec{\xi}_{ji,n}^{1a}+m_{ji,n}^{1a}\vec{\lambda}_{ij}^{a1})\cdot\mathbf{S}_j
\end{aligned} \tag{6.17, 6.18}$$

The first three terms in equation (6.18) give the static modification to the Heisenberg, Dzyalloshinskii-Moriya, and symmetric anisotropic exchange that is linearly proportional to the displacement $\hat{u}_n$. These arise from the fact that intersite exchange couplings depend on the atomic positions. The terms arising proportional to $\hat{p}_n$ deserve special mention. These reflect the fact that the specific spin-orbital composition of the ground-state doublets at each site may be altered by the displacement of the atoms. To understand the consequences, it is useful to consider applying a strong magnetic field in order to split the doublet into $\psi_{i,1,\uparrow}(x_n)$ and $\psi_{i,1,\downarrow}(x_n)$ states. Suppose that $\psi_{i,1,\uparrow}(x_n)$ is the ground state. If the atoms are displaced very slowly (i.e. adiabatically), then the system will tend to stay in this state. This corresponds to the limit $\omega_n \to 0$, in which case the terms with $\hat{p}_n$ vanish. However, if the atoms are rapidly displaced to a new coordinate x_n', as long as $\langle\psi_{i,1,\uparrow}(x_n)|\psi_{i,1,\downarrow}(x_n')\rangle \neq 0$ the displacement may induce a transition from $\uparrow$ to $\downarrow$, corresponding to the application

of S_i^-. From this intuition, one can expect the appearance of single-site spin operators multiplying the *time derivative* of the displacement, i.e. $\propto \hat{p}_n$. Similar conclusions were drawn in Refs [312–316], although in the context of two-phonon processes discussed below.

Looking now at the hopping modulation terms second order with respect to the electron-phonon coupling, we have:

$$\begin{aligned}\mathcal{H}_{\text{eff}} = & \sum_{ij,nm} \hat{u}_n \mathbf{c}_{i,1}^\dagger \mathbb{M}_{ij,n}^{11} \mathbf{c}_{j,1} (\mathcal{E}-\mathcal{H})^{-1} \mathbf{c}_{j,1}^\dagger \mathbb{M}_{ji,m}^{11} \mathbf{c}_{i,1} \hat{u}_m \\ & + \hat{u}_n \mathbf{c}_{i,1}^\dagger \mathbb{M}_{ij,n}^{12} \mathbf{c}_{j,2} (\mathcal{E}-\mathcal{H})^{-1} \mathbf{c}_{j,2}^\dagger \mathbb{M}_{ji,n}^{21} \mathbf{c}_{i,1} \hat{u}_m + (i \leftrightarrow j) \qquad (6.19) \\ = & -\sum_{ij,nm} \left(\frac{a_n^\dagger a_m^\dagger}{U-\omega_n+\omega_m} + \frac{a_n^\dagger a_m}{U-\omega_n-\omega_m} + \frac{a_n a_m^\dagger}{U+\omega_n+\omega_m} + \frac{a_n a_m}{U+\omega_n-\omega_m} \right) \\ & \left[\mathbf{c}_{i,1}^\dagger \mathbb{M}_{ij,n}^{11} \mathbf{c}_{j,1} \mathbf{c}_{j,1}^\dagger \mathbb{M}_{ji,m}^{11} \mathbf{c}_{i,1} + \mathbf{c}_{i,1}^\dagger \mathbb{M}_{ij,n}^{12} \mathbb{M}_{ji,m}^{21} \mathbf{c}_{i,1} \right] + (i \leftrightarrow j) \qquad (6.20)\end{aligned}$$

Taking the limit $U \gg \omega$, and keeping only spin-phonon coupling terms gives:

$$\begin{aligned}\mathcal{H}_{\text{eff}} = & \sum_{ij,nm} \frac{4\hat{u}_n \hat{u}_m}{U} \Big[(m_{ij,n}^{11} m_{ji,m}^{11} + \vec{\xi}_{ij,n}^{11} \cdot \vec{\xi}_{ji,m}^{11}) (\mathbf{S}_i \cdot \mathbf{S}_j) \\ & + (m_{ji,m}^{11} \vec{\xi}_{ij,n}^{11} - m_{ij,n} \vec{\xi}_{ji,m}^{11}) \cdot (\mathbf{S}_i \times \mathbf{S}_j) - \mathbf{S}_i \cdot \left(\vec{\xi}_{ij,n}^{11} \otimes \vec{\xi}_{ji,m}^{11} + \vec{\xi}_{ji,n}^{11} \otimes \vec{\xi}_{ij,n}^{11} \right) \cdot \mathbf{S}_j \\ & + \sum_{ij,n,m\neq n} \frac{2}{U^2} (\hat{p}_n \hat{u}_m - \hat{u}_n \hat{p}_m) \sum_{a\in\{1,2\}} \Big[(\vec{\xi}_{ij,n}^{1a} \times \vec{\xi}_{ji,m}^{a1} - m_{ij,n}^{1a} \vec{\xi}_{ji,m}^{a1} - m_{ji,m}^{a1} \vec{\xi}_{ij,n}^{1a}) \cdot \mathbf{S}_i \\ & + (\vec{\xi}_{ij,n}^{a1} \times \vec{\xi}_{ji,m}^{1a} + m_{ij,n}^{a1} \vec{\xi}_{ji,m}^{1a} + m_{ji,m}^{1a} \vec{\xi}_{ij,n}^{a1}) \cdot \mathbf{S}_j \Big] \qquad (6.21)\end{aligned}$$

Here, the first sum gives the static modification of the Heisenberg, Dzyalloshinskii-Moriya and symmetric anisotropic exchange that is quadratic in atomic displacements. The second sum in equation (6.21) arises via a similar mechanism to the spin-momentum coupling in equation (6.18). The modification of the spin-orbital composition of the ground state doublets with atomic position introduces terms related to the time derivative of those positions. Due to the antisymmetric combination of $\hat{u}$ and $\hat{p}$, this term resembles the coupling of the phonon angular momentum to the spin. Indeed, this is the microscopic origin of the phenomenological "Raman" spin-phonon coupling $\propto (\vec{x} \times \vec{p}) \cdot \mathbf{S}$, which has been implicated

in models of the phonon thermal Hall effect[82–84, 349, 350, 352–354]. However, as implied by equation (6.21), the actual form of this coupling in real materials is sensitive to the microscopic details of the phonons and spin-orbit effects, such that it may be strongly anisotropic and dependent on the phonon mode.

Finally, let us consider the effects of modulating the crystal field. The lowest order contribution arises at second order with respect to $\mathcal{H}_{\text{el}-\text{ph}}$, and takes the form:

$$\mathcal{H}_{\text{eff}} = \sum_{i,n,m} \hat{u}_n \mathbf{c}_{i,1}^{\dagger} \mathbb{D}_{i,n}^{12} \mathbf{c}_{i,2} (\mathcal{E} - \mathcal{H})^{-1} \mathbf{c}_{i,2}^{\dagger} \mathbb{D}_{i,m}^{21} \mathbf{c}_{i,1} \hat{u}_m \tag{6.22}$$

Expanding in the limit $\Delta_{12} = \epsilon_2 - \epsilon_1 \gg \omega$, and keeping only spin-dependent terms gives:

$$\begin{aligned} \mathcal{H}_{\text{eff}} = \frac{2}{\Delta_{12}^2} \sum_{i,n,m \neq n} & (\hat{p}_n \hat{u}_m - \hat{u}_n \hat{p}_m) \cdot \\ & \cdot (\vec{\delta}_{i,n}^{12} \times \vec{\delta}_{i,m}^{21} - d_{i,n}^{12} \vec{\delta}_{i,m}^{21} - \vec{\delta}_{i,n}^{12} d_{i,m}^{21}) \cdot \mathbf{S}_i \end{aligned} \tag{6.23}$$

Here, again, we find a contribution to the "Raman" spin-phonon coupling. It may be noted that the energy denominator may satisfy $\Delta_{12} \ll U$ for many materials, such that modulation of the crystal field makes the dominant contribution to the "Raman" term. This may be particularly true for systems with unquenched orbital momentum and weak SOC (such as first-row transition metals), as there may be very low-lying crystal field levels that can contribute to equation (6.23).

While this simple two-orbital model is not sufficiently elaborate to model most real materials, it provides several insights: (i) In the absence of SOC, one can expect the spin-phonon coupling to modulate only the intersite Heisenberg coupling, through static terms proportional to u, u^2, ... This can be anticipated on the basis of symmetry analysis; the phonon displacements can coupling only to time-reversal even products of spin operators. (ii) In the presence of SOC, not only are the full intersite anisotropic exchange couplings modulated via static displacements u, u^2, ..., but also additional terms with phonon momentum p arise due to modulation of the ground state spin-orbital composition. By symmetry, these terms must couple to odd order spin operators.

Given the potential for significant complexity in the spin-phonon couplings in real mate-

rials, it is desirable to have a general numerical method for evaluating arbitrary spin-phonon couplings.

6.2.2 General Form of Spin-Phonon Operators and Inadequacy of Static Approaches

Following from the previous section, the spin-phonon coupling for general S takes the form:

$$\begin{aligned}\mathcal{H} = &\sum_{i,\alpha\ell n}\left[\left(\mathbf{D}_i^{\alpha\ell n}\cdot\vec{\mathcal{O}}_i\right)\hat{u}_\alpha(\ell n)+\left(\mathbf{G}_i^{\alpha\ell n}\cdot\vec{\mathcal{O}}_i\right)\hat{p}_\alpha(\ell n)\right]\\ &+\sum_{ij,\alpha\ell n}\left[\left(\vec{\mathcal{O}}_i\cdot\mathbb{A}_{ij}^{\alpha\ell n}\cdot\vec{\mathcal{O}}_j\right)\hat{u}_\alpha(\ell n)+\left(\vec{\mathcal{O}}_i\cdot\mathbb{B}_{ij}^{\alpha\ell n}\cdot\vec{\mathcal{O}}_j\right)\hat{p}_\alpha(\ell n)\right]\\ &+\sum_{i,\alpha\ell n,\beta km}\left[\left(\mathbf{R}_i^{\alpha\ell n;\beta km}\cdot\vec{\mathcal{O}}_i\right)\hat{u}_\alpha(\ell n)\hat{u}_\beta(km)+\left(\mathbf{L}_i^{\alpha\ell n;\beta km}\cdot\vec{\mathcal{O}}_i\right)\hat{u}_\alpha(\ell n)\hat{p}_\beta(km)\right]\\ &+\sum_{ij,\alpha\ell n,\beta km}\left[\left(\vec{\mathcal{O}}_i\cdot\mathbb{K}_{ij}^{\alpha\ell n;\beta km}\cdot\vec{\mathcal{O}}_j\right)\hat{u}_\alpha(\ell n)\hat{u}_\beta(km)+\left(\vec{\mathcal{O}}_i\cdot\mathbb{N}_{ij}^{\alpha\ell n;\beta km}\cdot\vec{\mathcal{O}}_j\right)\hat{u}_\alpha(\ell n)\hat{p}_\beta(km)\right]\end{aligned} \tag{6.24}$$

where $\hat{u}_\alpha(\ell n)$ refers to the displacement from equilibrium of the atom in unit cell ℓ with index n, in the $\alpha\in\{x,y,z\}$ direction. The vector $\vec{\mathcal{O}}_i$ contains all local multipole operators appropriate for the local degrees of freedom. The couplings with boldface font, such as $\mathbf{D}_i^{\alpha\ell n}$, are vectors; the couplings with blackboard bold font, such as $\mathbb{A}_{ij}^{\alpha\ell n}$ are matrices. As in the previous section, time-reversal symmetry restricts many terms to vanish. For example, $\mathbf{D}$ represents the linear modulation of the single-ion anisotropy terms with atomic displacement, and is thus finite for even multipole operators, but vanishes for all odd multipoles. If

we consider only spin dipole operators $\vec{\mathcal{O}}_i \approx (S_i^x, S_i^y, S_i^z)$, then the form simplifies to:

$$\begin{aligned}\mathcal{H} = & \sum_{i,\alpha\ell n} \left(\mathbf{G}_i^{\alpha\ell n} \cdot \mathbf{S}_i\right) \hat{p}_\alpha(\ell n) \\ & + \sum_{ij,\alpha\ell n} \left(\mathbf{S}_i \cdot \mathbb{A}_{ij}^{\alpha\ell n} \cdot \mathbf{S}_j\right) \hat{u}_\alpha(\ell n) \\ & + \sum_{\substack{ij \\ \alpha\ell n,\beta km}} \left(\mathbf{S}_i \cdot \mathbb{K}_{ij}^{\alpha\ell n;\beta km} \cdot \mathbf{S}_j\right) \hat{u}_\alpha(\ell n)\hat{u}_\beta(km) \\ & + \sum_{\substack{i \\ \alpha\ell n,\beta km}} \left(\mathbf{L}_i^{\alpha\ell n;\beta km} \cdot \mathbf{S}_i\right) \hat{u}_\alpha(\ell n)\hat{p}_\beta(km) \end{aligned} \tag{6.25}$$

The estimation of $\mathbb{A}$ and $\mathbb{K}$ has been previously demonstrated using *static* first principles approaches, i.e. frozen phonon and/or frozen magnon methods. Various approaches have been demonstrated for this purpose, and have been widely employed with notable successes in modelling e.g. spin relaxation in single molecule magnets[306, 356, 357, 357–361], and spin-phonon couplings in 2D magnets[263, 362, 363]. For example, $\mathbb{A}$ and $\mathbb{K}$ can be computed from the differences between nuclear force matrices in different static magnetic configurations[364–367]. Alternatively, the changes in magnetic couplings for small static atomic displacements may be computed, either from the total electronic energies of multiple different magnetic configurations for each displacement[363, 368], or magnetic force theorem approaches[369–372]. The latter approach can also provide higher multipole-lattice couplings [289, 373]. A combined magneto-structural force theorem approach has also been reported[374], and a similar framework has been demonstrated that can address $\mathbf{G}$ and $\mathbf{L}$ terms by relating them to nuclear Berry curvatures[375, 376]. To our knowledge, this latter approach is the first *ab-initio* method capable of treating the full range of spin-phonon couplings, provided the effects are accurately captured in the Kohn-Sham (single-determinant) energies. However, in order to complement these approaches, it is desirable to have a many-body method that fully captures the local many-body nature of the single-ion states, and is able to treat $\mathbf{G}$ and $\mathbf{L}$, which are experimentally relevant, for example, for the phonon thermal Hall effect[82–84, 349, 350, 352–354]. This can be accomplished by treating the phonons as genuine dynamical variables.

6.2.3 Spin-Phonon Implementation Details

In this section, we describe the inclusion of phonons explicitly in the dCEH approach. We first compute the linear electron-phonon coupling in real space, defined by:

$$\mathcal{H}_{\text{el}-\text{ph}} = \sum_{\alpha \ell n} \mathcal{H}_{\Delta}^{\alpha \ell n} \hat{u}_{\alpha}(\ell n) \tag{6.26}$$

$$\mathcal{H}_{\Delta}^{\alpha \ell n} = \sum_{i \sigma j \sigma'} \Delta_{i \sigma j \sigma'}^{\mu \nu; \ell \alpha n} \; c_{i,\mu,\sigma}^{\dagger} c_{j,\nu,\sigma'} \tag{6.27}$$

where $c_{i,\mu,\sigma}^{\dagger}$ creates an electron at metal site i, in orbital μ, with spin σ. The phonon operator $\hat{u}_{\alpha}(\ell n)$ refers to displacement of atom n, in the unit cell labelled ℓ, in the direction $\alpha \in \{x, y, z\}$. The elements $\Delta_{i \sigma j \sigma'}^{\mu \nu; \ell \alpha n}$ refer to changes in the single-particle matrix elements due to such a displacement. In the present work, these are estimated via a finite displacement (frozen phonon) approach, as described in Section 6.3.4. Hopping matrix elements are computed using density functional theory for different atomic geometries, and Δ is determined from their differences. Alternately, if one is interested in a small selection of phonon bands at specific q-points, the displacements may be taken along the relevant phonon eigenvectors.

We are now ready to compute the spin-phonon couplings. We first describe the calculation of $\mathbf{D}$, $\mathbf{G}$, $\mathbb{A}$, and $\mathbb{B}$, which are linear in phonon operators. To include the effects of the real space displacements in the dCEH calculation of the magnetic couplings, we treat $u_{\alpha}(\ell j)$ and $p_{\alpha}(\ell j)$ formally in terms of fictitious phonon operators, given by:

$$a = \sqrt{\frac{m_n \omega}{2\hbar}} \left(\hat{u}_{\alpha}(\ell n) + \frac{i}{m_n \omega} \hat{p}_{\alpha}(\ell n) \right) \tag{6.28}$$

$$a^{\dagger} = \sqrt{\frac{m_n \omega}{2\hbar}} \left(\hat{u}_{\alpha}(\ell n) - \frac{i}{m_n \omega} \hat{p}_{\alpha}(\ell n) \right) \tag{6.29}$$

$$\hat{u}_{\alpha}(\ell n) = \sqrt{\frac{\hbar}{2 m_n \omega}} \left(a^{\dagger} + a \right) \tag{6.30}$$

$$\hat{p}_{\alpha}(\ell n) = i \sqrt{\frac{\hbar m_n \omega}{2}} \left(a^{\dagger} - a \right) \tag{6.31}$$

In all calculations, we take:

$$r_0 \equiv \sqrt{\frac{\hbar}{2m\omega}} = 0.02 \text{ Å} \tag{6.32}$$

$$\hbar\omega = 10 \text{ meV} \tag{6.33}$$

As discussed below, provided electron-phonon coupling is in the perturbative regime, the computed spin-phonon couplings are linear in electron-phonon coupling. As a consequence, the specific values of the fictitious phonon constants are not important computationally, provided $\hbar\omega \ll U$ and $r_0\Delta \ll U$, where Δ is the electron-phonon coupling defined in eq'n (7.40), and U is the energy scale of the electronic excited states contributing at lowest order. The ficticious phonons are treated as hard-core bosons. A separate dCEH calculation is performed for each cluster included in the cluster expansion, and each atomic displacement defined by α, ℓ, n. The full Hamiltonian for each such calculation is constructed in the following way:

$$\mathcal{H} = \begin{pmatrix} 1 & a^\dagger \end{pmatrix} \left(\begin{array}{c|c} \mathcal{H}_0 & r_0\ \mathcal{H}_\Delta^{\alpha\ell n} \\ \hline r_0\ \mathcal{H}_\Delta^{\alpha\ell n} & \mathcal{H}_0 + \hbar\omega \end{array}\right) \begin{pmatrix} \mathbb{P}_{n=0} \\ a\ \mathbb{P}_{n=1} \end{pmatrix} \tag{6.34}$$

where $\mathcal{H}_0$ is the regular full electronic Hamiltonian including single-particle and Coulomb terms relevant for the cluster. The Hilbert space is now doubled in size, and includes explicitly states with zero and one fictitious phonon. The projection operators $\mathbb{P}_{n=0}$ and $\mathbb{P}_{n=1}$ project onto subspaces with zero and one phonon, respectively. The idealized low-energy basis is also doubled in size; the projection operator can be constructed as:

$$\mathbb{P} = \left(\begin{array}{c|c} \mathbb{P}_{\text{spin}} & 0 \\ \hline 0 & \mathbb{P}_{\text{spin}} \end{array}\right) \tag{6.35}$$

where $\mathbb{P}_{\text{spin}}$ refers to the ideal low-energy space of the spin-only basis. The different blocks corresponds to the projection onto the sectors with nominally zero or one phonon. Then, the low-energy Hamiltonian for each cluster can be numerically computed following section

2.1:

$$\mathcal{H}_{\text{eff}} = \mathbb{P}\mathbf{S}^{-1/2}\mathcal{H}_{\text{low}}\mathbf{S}^{-1/2}\mathbb{P} \tag{6.36}$$

$$= \begin{pmatrix} 1 & a^\dagger \end{pmatrix} \left(\begin{array}{c|c} \mathcal{H}^0_{\text{eff}} & \mathcal{O}_{\alpha\ell n} \\ \hline \mathcal{O}^\dagger_{\alpha\ell n} & \mathcal{H}^0_{\text{eff}} + \mathcal{H}^1_{\text{eff}} \end{array}\right) \begin{pmatrix} \mathbb{P}_{n=0} \\ a\ \mathbb{P}_{n=1} \end{pmatrix} \tag{6.37}$$

$$= \mathcal{H}^0_{\text{eff}} + \mathcal{H}^1_{\text{eff}}\ a^\dagger a + \mathcal{O}^\dagger_{\alpha\ell n}\ a^\dagger + \mathcal{O}_{\alpha\ell n}\ a \tag{6.38}$$

where $\mathcal{H}^0_{\text{eff}}$, $\mathcal{H}^1_{\text{eff}}$, and $\mathcal{O}_{\alpha\ell n}$ act only on the spin degrees of freedom. For one-site clusters,

$$\frac{\mathcal{O}^\dagger_{\alpha\ell n} + \mathcal{O}_{\alpha\ell n}}{2r_0} = \mathbf{D}^{\alpha\ell n}_{i()} \cdot \vec{\mathcal{O}}_i \tag{6.39}$$

$$\frac{\mathcal{O}^\dagger_{\alpha\ell n} - \mathcal{O}_{\alpha\ell n}}{2ir_0 m_n \omega} = \mathbf{G}^{\alpha\ell n}_{i()} \cdot \vec{\mathcal{O}}_i \tag{6.40}$$

where $\mathbf{D}^{\alpha\ell n}_{i()}$ and $\mathbf{G}^{\alpha\ell n}_{i()}$ include all essential contributions in the cluster expansion from site i (see section 2.1 for cluster-expansion notation). For two-site clusters,

$$\begin{aligned} \frac{\mathcal{O}^\dagger_{\alpha\ell n} + \mathcal{O}_{\alpha\ell n}}{2r_0} &= \mathbf{D}^{\alpha\ell n}_{i(j)} \cdot \vec{\mathcal{O}}_i + \mathbf{D}^{\alpha\ell n}_{j(i)} \cdot \vec{\mathcal{O}}_j \\ &\quad + \vec{\mathcal{O}}_i \cdot \mathbb{A}^{\alpha\ell n}_{ij()} \cdot \vec{\mathcal{O}}_j \end{aligned} \tag{6.41}$$

$$\begin{aligned} \frac{\mathcal{O}^\dagger_{\alpha\ell n} - \mathcal{O}_{\alpha\ell n}}{2i\omega r_0} &= m_n \Big[\mathbf{G}^{\alpha\ell n}_{i(j)} \cdot \vec{\mathcal{O}}_i + \mathbf{G}^{\alpha\ell n}_{j(i)} \cdot \vec{\mathcal{O}}_j \\ &\quad + \vec{\mathcal{O}}_i \cdot \mathbb{B}^{\alpha\ell n}_{ij()} \cdot \vec{\mathcal{O}}_j \Big] \end{aligned} \tag{6.42}$$

Then, up to two-site clusters, we have:

$$\mathbf{D}^{\alpha\ell n}_{i} \approx \mathbf{D}^{\alpha\ell n}_{i()} + \sum_j \left(\mathbf{D}^{\alpha\ell n}_{i(j)} - \mathbf{D}^{\alpha\ell n}_{i()} \right) \tag{6.43}$$

$$\mathbb{A}^{\alpha\ell n}_{ij} \approx \mathbb{A}^{\alpha\ell n}_{ij()} \tag{6.44}$$

and analogous expressions for $m_n\mathbf{G}$ and $m_n\mathbb{B}$. At lowest order, all four sets of couplings are independent of the choice of $\hbar\omega$ and r_0. This can be seen from the fact that $(\mathcal{O}^\dagger_{\alpha\ell n} - \mathcal{O}_{\alpha\ell n}) \propto i\omega r_0$, and $(\mathcal{O}^\dagger_{\alpha\ell n} + \mathcal{O}_{\alpha\ell n}) \propto r_0$ at lowest order. For this reason, the specific choices of $\hbar\omega$ and r_0 do not affect the computed couplings.

The computed spin-phonon couplings may then be Fourier transformed using phonon eigenvectors and frequencies derived from *ab-initio* phonon calculations. The displacement and momentum operators are written:

$$\hat{u}_\alpha(\ell n) = \sqrt{\frac{\hbar}{2Nm_n}} \sum_{qv} \frac{e^{iq\cdot r_{\ell n}}}{\sqrt{\omega_{qv}}} \; (a^\dagger_{-qv} + a_{qv}) \; e_\alpha(n, qv) \tag{6.45}$$

$$\hat{p}_\alpha(\ell n) = i\sqrt{\frac{\hbar m_n}{2N}} \sum_{qv} \sqrt{\omega_{qv}} \; e^{iq\cdot r_{\ell n}} (a^\dagger_{-qv} - a_{qv}) \; e_\alpha(n, qv) \tag{6.46}$$

where q is the wavevector, v is the phonon band index, N = the number of unit cells, m_n is the mass of atom n, and e_α are unitless coefficients appearing in the phonon eigenvectors. For example,

$$\sum_{i,\alpha\ell n} (\mathbf{D}_i^{\alpha\ell n} \cdot \vec{\mathcal{O}}_i)\hat{u}_\alpha(\ell n) \equiv \sum_{q\nu} \hat{\mathcal{D}}_{q\nu}(a^\dagger_{-q\nu} + a_{q\nu}) \tag{6.47}$$

$$\sum_{i,\alpha\ell n} (\mathbf{G}_i^{\alpha\ell n} \cdot \vec{\mathcal{O}}_i)\hat{p}_\alpha(\ell n) \equiv i \sum_{q\nu} \hat{\mathcal{G}}_{q\nu}(a^\dagger_{-q\nu} - a_{q\nu}) \tag{6.48}$$

where:

$$\hat{\mathcal{D}}_{q\nu} = \sqrt{\frac{\hbar}{2N\omega_{q\nu}}} \sum_{i,\alpha\ell n} \sqrt{\frac{1}{m_n}} e^{iq\cdot r_{\ell n}} (\mathbf{D}_i^{\alpha\ell n} \cdot \vec{\mathcal{O}}_i) e_\alpha(n, q\nu) \tag{6.49}$$

$$\hat{\mathcal{G}}_{q\nu} = \sqrt{\frac{\hbar\omega_{q\nu}}{2N}} \sum_{i,\alpha\ell n} \sqrt{\frac{1}{m_n}} e^{iq\cdot r_{\ell n}} (m_n \mathbf{G}_i^{\alpha\ell n} \cdot \vec{\mathcal{O}}_i) e_\alpha(n, q\nu) \tag{6.50}$$

To compute the $\mathbf{R}$, $\mathbf{L}$, $\mathbb{K}$, and $\mathbb{N}$ couplings, which are quadratic in phonon operators, we take a similar approach. For each cluster and pair of phonons $(\alpha\ell n) \neq (\beta km)$, we define:

$$\hat{u}_\alpha(\ell n) = r_0 \left(a_1^\dagger + a_1\right) \tag{6.51}$$

$$\hat{p}_\alpha(\ell n) = i \; r_0 \; m_1 \; \omega \left(a_1^\dagger - a_1\right) \tag{6.52}$$

$$\hat{u}_\beta(km) = r_0 \left(a_2^\dagger + a_2\right) \tag{6.53}$$

$$\hat{p}_\beta(km) = i \; r_0 \; m_2 \; \omega \left(a_2^\dagger - a_2\right) \tag{6.54}$$

The Hamiltonian of the cluster is then:

$$\mathcal{H} = \mathcal{H}_0 + a^\dagger \left(\begin{array}{c|c|c|c} 0 & r_0\mathcal{H}_{\Delta,1} & r_0\mathcal{H}_{\Delta,2} & 0 \\ \hline r_0\mathcal{H}_{\Delta,1} & \omega & 0 & r_0\mathcal{H}_{\Delta,2} \\ \hline r_0\mathcal{H}_{\Delta,2} & 0 & \omega & r_0\mathcal{H}_{\Delta,1} \\ \hline 0 & r_0\mathcal{H}_{\Delta,2} & r_0\mathcal{H}_{\Delta,1} & 2\omega \end{array}\right) b \tag{6.55}$$

where:

$$a^\dagger = \left(1 \;\; a_1^\dagger \;\; a_2^\dagger \;\; a_1^\dagger a_2^\dagger\right) \;,\; b = \left(\begin{array}{c} \mathbb{P}_{n_1=0}^{n_2=0} \\ a_1 \; \mathbb{P}_{n_1=1}^{n_2=0} \\ a_2 \; \mathbb{P}_{n_1=0}^{n_2=1} \\ a_1 a_2 \; \mathbb{P}_{n_1=1}^{n_2=1} \end{array}\right) \tag{6.56}$$

Now, the Hilbert space explicitly includes states with zero or one quanta in each fictitious phonon mode. The low-energy projection operator is simply:

$$\mathbb{P} = \left(\begin{array}{c|c|c|c} \mathbb{P}_{\text{spin}} & 0 & 0 & 0 \\ \hline 0 & \mathbb{P}_{\text{spin}} & 0 & 0 \\ \hline 0 & 0 & \mathbb{P}_{\text{spin}} & 0 \\ \hline 0 & 0 & 0 & \mathbb{P}_{\text{spin}} \end{array}\right) \tag{6.57}$$

and the low-energy effective Hamiltonian is defined as:

$$\mathcal{H}_{\text{eff}} = \mathbb{P}\mathbf{S}^{-1/2}\mathcal{H}_{\text{low}}\mathbf{S}^{-1/2}\mathbb{P} \tag{6.58}$$

$$= \mathcal{H}_{\text{eff}}^0 + \mathcal{H}_{\text{eff}}^1 n_1 + \mathcal{H}_{\text{eff}}^2 n_2 + \mathcal{H}_{\text{eff}}^3 n_1 n_2 + a^\dagger \left(\begin{array}{c|c|c|c} 0 & \mathcal{O}_1 & \mathcal{O}_2 & \mathcal{O}_{1;2}^{--} \\ \hline \mathcal{O}_1^+ & 0 & \mathcal{O}_{1;2}^{+-} & \mathcal{O}_{1;2}^{0-} \\ \hline \mathcal{O}_2^+ & \mathcal{O}_{1;2}^{-+} & 0 & \mathcal{O}_{1;2}^{-0} \\ \hline \mathcal{O}_{1;2}^{++} & \mathcal{O}_{1;2}^{0+} & \mathcal{O}_{1;2}^{+0} & 0 \end{array}\right) b \tag{6.59}$$

From this, we see for one-site clusters:

$$\frac{\mathcal{O}^{++}_{1;2} + \mathcal{O}^{+-}_{1;2} + \mathcal{O}^{-+}_{1;2} + \mathcal{O}^{--}_{1;2}}{4r_0^2} = \mathbf{R}^{\alpha\ell n;\beta km}_{i()} \cdot \vec{\mathcal{O}}_i \tag{6.60}$$

$$\frac{\mathcal{O}^{++}_{1;2} + \mathcal{O}^{+-}_{1;2} - \mathcal{O}^{-+}_{1;2} - \mathcal{O}^{--}_{1;2}}{4ir_0^2\omega} = m_1 \left[\mathbf{L}^{\beta km;\alpha\ell n}_{i()} \cdot \vec{\mathcal{O}}_i\right] \tag{6.61}$$

$$\frac{\mathcal{O}^{++}_{1;2} - \mathcal{O}^{+-}_{1;2} + \mathcal{O}^{-+}_{1;2} - \mathcal{O}^{--}_{1;2}}{4ir_0^2\omega} = m_2 \left[\mathbf{L}^{\alpha\ell n;\beta km}_{i()} \cdot \vec{\mathcal{O}}_i\right] \tag{6.62}$$

and for two-site clusters:

$$\begin{aligned}
&\frac{\mathcal{O}^{++}_{1;2} + \mathcal{O}^{+-}_{1;2} + \mathcal{O}^{-+}_{1;2} + \mathcal{O}^{--}_{1;2}}{4r_0^2} \\
&\quad = \vec{\mathcal{O}}_i \cdot \mathbb{K}^{\alpha\ell n;\beta km}_{ij()} \cdot \vec{\mathcal{O}}_j + \mathbf{R}^{\alpha\ell n;\beta km}_{i(j)} \cdot \vec{\mathcal{O}}_i \\
&\qquad\qquad + \mathbf{R}^{\alpha\ell n;\beta km}_{j(i)} \cdot \vec{\mathcal{O}}_i
\end{aligned} \tag{6.63}$$

$$\begin{aligned}
&\frac{\mathcal{O}^{++}_{1;2} + \mathcal{O}^{+-}_{1;2} - \mathcal{O}^{-+}_{1;2} - \mathcal{O}^{--}_{1;2}}{4ir_0^2\omega} \\
&= m_1 \Big[\vec{\mathcal{O}}_i \cdot \mathbb{N}^{\beta km;\alpha\ell n}_{ij()} \cdot \vec{\mathcal{O}}_j + \mathbf{L}^{\beta km;\alpha\ell n}_{i(j)} \cdot \vec{\mathcal{O}}_i \\
&\qquad\qquad + \mathbf{L}^{\beta km;\alpha\ell n}_{j(i)} \cdot \vec{\mathcal{O}}_i\Big]
\end{aligned} \tag{6.64}$$

$$\begin{aligned}
&\frac{\mathcal{O}^{++}_{1;2} - \mathcal{O}^{+-}_{1;2} + \mathcal{O}^{-+}_{1;2} - \mathcal{O}^{--}_{1;2}}{4ir_0^2\omega} \\
&= m_2 \Big[\vec{\mathcal{O}}_i \cdot \mathbb{N}^{\alpha\ell n;\beta km}_{ij()} \cdot \vec{\mathcal{O}}_j + \mathbf{L}^{\alpha\ell n;\beta km}_{i(j)} \cdot \vec{\mathcal{O}}_i \\
&\qquad\qquad + \mathbf{L}^{\alpha\ell n;\beta km}_{j(i)} \cdot \vec{\mathcal{O}}_i\Big]
\end{aligned} \tag{6.65}$$

Then, we have:

$$\mathbf{R}^{\alpha\ell n;\beta km}_{i} \approx \mathbf{R}^{\alpha\ell n;\beta km}_{i()} + \sum_j \left(\mathbf{R}^{\alpha\ell n;\beta km}_{i(j)} - \mathbf{R}^{\alpha\ell n;\beta km}_{i()}\right) \tag{6.66}$$

$$\mathbb{K}^{\alpha\ell n;\beta km}_{ij} \approx \mathbb{K}^{\alpha\ell n;\beta km}_{ij()} \tag{6.67}$$

and analogous expressions for $\mathbf{L}$ and $\mathbb{N}$. It may be noted that the anharmonic terms involving three phonon $a^\dagger$ or a operators in equation (6.59) are expected to be small, and have thus been ignored in the later expressions.

Altogether, this method gives a recipe for the numerical estimation of generic spin-

phonon couplings within an explicitly many-body framework, including both static and dynamic phonon terms. It can provide all multipole tensor interactions in the full q-space spin-phonon Hamiltonian, including modulation of single-ion anisotropies, g-tensors, intersite bilinear couplings, biquadratic couplings, etc. However, given the relatively large number of calculations in the cluster and phonon flavor expansion, it may appear to be very computationally heavy. In this context, it is worth noting that the most expensive step in dCEH calculations is the diagonalization of the combined electron phonon Hamiltonian on each cluster. It is typically possible to truncate the cluster expansion at two sites for magnetic insulators, and achieve quantitative results with small active spaces of orbitals for suitably constructed electronic Hamiltonians. For example, for transition metals, it is necessary to retain only the five d-orbital Wannier functions on each site; at half-filling and two phonon flavors, two-site clusters require diagonalization of a sparse matrix of dimension less than 10^6, which can typically be accomplished within a few minutes on a single workstation without prohibitive memory requirements. The cluster expansion is easily parallelized. In practice, for moderately sized unit cells, the full spin-phonon dCEH calculation to achieve full q-dependent couplings demands similar computational commitment as *ab-initio* phonon calculations.

In order to validate the proposed method, in the next sections, we apply it to compute the linear spin-phonon couplings for $MnPSe_3$, and compare with experimental measurements of temperature- and band-dependent phonon renormalization.

6.3 Study of $MnPSe_3$

6.3.1 Introduction

$MnPSe_3$ is a layered van der Waals (vdW) material, with Mn sites forming a honeycomb lattice, as depicted in Fig. 7.5. The material orders[377] as a Néel antiferromagnet below $T_N = 74$ K, below which there is a rapid increase in the longitudinal (phonon) thermal conductivity[328] and the lifetimes of some optical phonons[355], suggesting both are strongly influenced by spin-phonon scattering. Similar behavior is also observed in $MnPS_3$[377, 378]. The detailed Raman scattering study of these effects in $MnPSe_3$ in

Ref. [355] provides the opportunity to benchmark our *ab-initio* approach via a comprehensive investigation of the magnetic couplings, lowest order spin-phonon couplings, and consequent temperature-dependent phonon lineshapes.

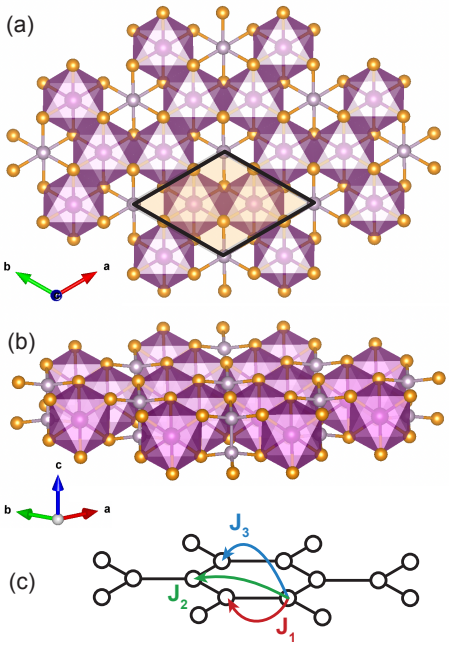

Figure 6.2: Structure of $MnPSe_3$ monolayer viewed (a) along c-axis, with two-site honeycomb unit cell highlighted, and (b) from the side. (c) Definition of first, second, and third neighbor interactions between Mn sites.

Given that the Mn^{2+} in $MnPSe_3$ is in a high-spin $S = 5/2$ state, there is no significant orbital moment. As a consequence, the magnetic couplings are expected to be only weakly anisotropic, and spin-orbit coupling effects should be negligible. Powder neutron scattering[379] was shown to be compatible with the isotropic Heisenberg Hamiltonian containing couplings up to third neighbor:

$$\mathcal{H} = \sum_{\langle ij \rangle} J_1 \, \mathbf{S}_i \cdot \mathbf{S}_j + \sum_{\langle\langle ij \rangle\rangle} J_2 \, \mathbf{S}_i \cdot \mathbf{S}_j + \sum_{\langle\langle\langle ij \rangle\rangle\rangle} J_3 \, \mathbf{S}_i \cdot \mathbf{S}_j \tag{6.68}$$

with values of $J_1 = 0.90$ meV, $J_2 = 0.06$ meV, and $J_3 = 0.38$ meV being motivated from previous *ab-initio* estimates[380, 381] using DFT+U total energy analysis.

It may be emphasized that this material, as a consequence of negligible SOC effects, should have a relatively simple form of the spin-phonon coupling. For this reason, it provides

a "simple" material to benchmark our approach, even though it does not show the full range of couplings discussed in section 6.2.2. In chapter 7, we address α-$RuCl_3$, which displays more complex spin-orbital coupled moments[382].

6.3.2 Base Magnetic Hamiltonian

Treatment in Ab-initio

In order to develop a low-energy model for $MnPSe_3$, we first consider an electronic Hamiltonian in terms of Mn $3d$-orbitals, which is a sum of, respectively, one- and two-particle terms: $\mathcal{H}_{\rm el} = \mathcal{H}_{1p} + \mathcal{H}_{2p}$. The one-particle terms include intersite hopping, intrasite crystal field, and spin-orbit coupling, $\mathcal{H}_{1p} = \mathcal{H}_{hop} + \mathcal{H}_{\rm CF} + \mathcal{H}_{\rm SO}$:

$$\mathcal{H}_{hop} = \sum_{ij\alpha\beta\sigma} t_{ij}^{\alpha\beta} c_{i,\alpha,\sigma}^{\dagger} c_{j,\beta,\sigma} \tag{6.69}$$

$$\mathcal{H}_{\rm CF} = \sum_{i\alpha\beta\sigma} d_{i}^{\alpha\beta} c_{i,\alpha,\sigma}^{\dagger} c_{i,\beta,\sigma} \tag{6.70}$$

$$\mathcal{H}_{\rm SO} = \sum_{i\alpha\beta\sigma\sigma'} \lambda_{\rm Mn} \langle \phi_i^{\alpha}(\sigma) | \mathbf{L}\cdot\mathbf{S} | \phi_i^{\beta}(\sigma') \rangle c_{i,\alpha,\sigma}^{\dagger} c_{i,\beta,\sigma'} \tag{6.71}$$

where $c_{i,\alpha,\sigma}^{\dagger}$ creates an electron at Mn site i, in d-orbital α, with spin σ. For this purpose, we use $\lambda_{\rm Mn} = 41$ meV, which is the atomic value. As we see below, the high-spin d^5 configuration has no unquenched orbital momentum, such that SOC has only minor effects on the magnetic couplings. In order to estimate the hopping integrals ($\mathcal{H}_{hop}$) and crystalline electric field ($\mathcal{H}_{\rm CF}$), we started by taking a relaxed idealized monolayer structure with a vacuum gap of 11.98 Å (see section 6.3.3 for details). The in-plane lattice parmater was found to be 6.345 Å. The non-spin polarized density functional theory (DFT) calculation was carried out at Perdew–Burke–Ernzerhof generalized gradient approximation (PBE-GGA)[201] level as provided in a a full-potential local-orbital (FPLO) code[199, 200]. We performed these calculations at non-relativistic limit by taking the dense k-point grid of $12\times12\times12$. Finally, $\mathcal{H}_{hop}$ and ($\mathcal{H}_{\rm CF}$) terms were calculated by using Wannier projection, where the Wannier functions are assumed to have d-only basis[303].

For the two-particle terms, we consider both on-site and (long-range) intersite terms:

$\mathcal{H}_{2p} = \mathcal{H}_U + \mathcal{H}_J^{\mathrm{LR}}$, respectively. The on-site contributions are given by:

$$\mathcal{H}_U = \sum_{i\alpha\beta\delta\gamma} \sum_{\sigma\sigma'} U_{\alpha\beta\gamma\delta}\ c^\dagger_{i,\alpha,\sigma} c^\dagger_{i,\beta,\sigma'} c_{i,\gamma,\sigma'} c_{i,\delta,\sigma} \tag{6.72}$$

In the spherically symmetric approximation [279], $U_{\alpha\beta\gamma\delta}$ are parameterized by the Slater parameters $F_0^{dd}, F_2^{dd}, F_4^{dd}$. For the (screened) on-site metal Coulomb interactions, we took $F_2^{dd} = 6.81$ eV, and $F_4^{dd} = 4.78$ eV, obtained from the fitting of low-temperature optical spectra of the related compound $MnPS_3$ in Ref. [383]. Similar estimates were reported in other experimental studies[280, 384] for $MnPS_3$, and are not expected to differ significantly in $MnPSe_3$.

For the long-range intersite Hund's coupling, we define:

$$\mathcal{H}_J^{\mathrm{LR}} = \sum_{ij\alpha\beta\sigma\sigma'} J^{\alpha\beta}_{H,ij}\ c^\dagger_{i,\alpha,\sigma} c^\dagger_{j,\beta,\sigma'} c_{i,\alpha,\sigma'} c_{j,\beta,\sigma} \tag{6.73}$$

The origin of this term is as follows. There are various exchange processes that contribute to the magnetic couplings, which have been discussed specifically in the context of MPS_3 materials[281, 380, 381], as well as extensively for various other edge-sharing materials[43, 208, 385–388]. If one considers explicitly the d-orbitals on the metal sites and the p-orbitals on the bridging ligands, the exchange processes can be grouped into two categories. The first category are those involving direct metal-metal hopping, giving $J \propto t_{dd}^2$. The second category are those involving metal-ligand hybridization, resulting in terms $J \propto t_{pd}^4$. This latter category includes the usual ferromagnetic Goodenough-Kanamori exchange[32–34], which is typically important for edge-sharing compounds[281]. All of these contributions can be downfolded, in principle, into the more convenient basis of metal-centered Wannier functions derived from the d-orbitals only. This reduced basis is more convenient from the standpoint of computational efficiency, but also because experimental on-site F_2 and F_4 parameters estimated from optical spectra refer to the Wannier basis implicitly. The Wannier functions are, in reality, anti-bonding combinations of metal d- and ligand p-orbitals following standard ligand field theory. Since Wannier functions of different metal sites may share density on the same ligand, the downfolding produces longer-ranged

intersite Coulomb terms. For the purpose of magnetic exchange, the long-range Hund's coupling should be considered explicitly – this is the essence of the Goodenough-Kanamori mechanism. Here, we take a partially empirical approach to account for this contribution. Projecting the p-orbital Coulomb interactions into the d-orbital Wannier function basis gives the approximation:

$$J_{H,ij}^{\alpha\beta} = \gamma \sum_{n,\delta,\gamma} (U^n - J_H^n)\ \phi_{i,\alpha}^{n,\delta}\phi_{j,\beta}^{n\delta}\phi_{i,\alpha}^{n,\gamma}\phi_{j,\beta}^{n,\gamma} + J_H^n|\phi_{i,\alpha}^{n,\delta}|^2|\phi_{j,\beta}^{n,\gamma}|^2 \tag{6.74}$$

where $\phi_{i,\alpha}^{n,\delta}$ is the wavefunction coefficient for the Wannier function at Mn site i and d-orbital α corresponding to the Se atom n, and p-orbital $\delta \in \{p_x, p_y, p_z\}$. U^n is the Hubbard repulsion between electrons in the same p-orbital at site n, and J_H^n is the Hund's coupling at site n, and γ is a renormalization factor that ostensibly accounts for screening of the interactions relative to their atomic values. We consider intersite Hund's coupling up to third neighbors, summing over all Se sites n within 12Å of each of sites i and j. We approximate $U^n = 2J_H^n$, and take the selenium Hund's coupling to be the atomic value[389], namely $J_H^n = 0.51$ eV. The wavefunction coefficients were taken from the DFT calculations of the hoppings, computed with FPLO as described above. A similar approach[135] was taken recently by the present authors in order to model the related compound $FePS_3$, where excellent agreement was demonstrated between computed and experimental excitations in the magnetically ordered phase.

Finally, we vary the renormalization factor γ and on-site repulsion F_0^{dd} within a realistic range, and find good agreement with previous experimental couplings[379] for $\gamma = 0.65$, and $F_0^{dd} = 5.05$ eV. The latter value corresponds to $U_{t2g} = F_0^{dd} + (4/49)(F_2^{dd} + F_4^{dd}) = 6.0$ eV. The final intersite Hund's matrices are given in Appendix 6.5. At this point, it should be emphasized that this approach is not strictly fully *ab-initio*, since we have varied U_{t2g} and γ to best reproduce the experimental values of the base magnetic couplings in Ref. [379]. This is similar to the common practice of varying U and/or J_H in DFT+U calculations of magnetic couplings to achieve reasonable experimental agreement. In the present case, U_{t2g},

and γ control the relative contributions from antiferromagnetic and ferromagnetic exchange processes in addition to the overall scale of the couplings. Since we are primarily interested in studying the spin-phonon couplings, the utilization of experimental input in the selection of model parameters helps ensure accuracy of the resulting approach. These are the only two free parameters in our study, and all later magnetic and spin-phonon couplings derive from them.

In order to determine the magnetic exchange constants, we exactly diagonalize the described electronic Hamiltonian on one-site and two-site clusters corresponding to first, second, and third neighbor bonds. For each cluster, we retain the lowest energy states, and then project the resulting low-energy Hamiltonian onto idealized pure-spin states representing the ${}^6A_1$ electronic ground states of each Mn site.

Results

Using the approach outlined in Section 6.3.2, we obtain the following estimates for the magnetic couplings. For a given bond, the bilinear couplings can be written:

$$\mathcal{H} = \sum_{ij} \mathbf{S}_i \cdot \mathbb{J}_{ij} \cdot \mathbf{S}_j \tag{6.75}$$

in terms of the 3×3 exchange matrix $\mathbb{J}_{ij}$. For the nearest neighbor bond highlighted in Fig. 7.5(c), we compute:

$$\mathbb{J}_1 = \begin{pmatrix} 0.9281 & 0.0002 & 0.0 \\ 0.0002 & 0.9281 & 0.0 \\ 0.0 & 0.0 & 0.9276 \end{pmatrix} \tag{6.76}$$

which indeed shows very weak anisotropy. Similarly, for the second neighbor bond highlighted in Fig. 7.5(c):

$$\mathbb{J}_2 = \begin{pmatrix} 0.0352 & -0.0007 & -0.0005 \\ 0.0006 & 0.0352 & 0.0004 \\ 0.0005 & -0.0004 & 0.0352 \end{pmatrix} \tag{6.77}$$

Here, the nonzero off-diagonal components represent a nearly vanishing but symmetry-allowed Dzyalloshinkii-Moriya interaction, which we subsequently neglect due to it's exceedingly small magnitude. Finally, for the third neighbor bond highlighted in Fig. 7.5(c), we estimate:

$$\mathbb{J}_3 = \begin{pmatrix} 0.3791 & 0.0 & 0.0 \\ 0.0 & 0.3791 & 0.0 \\ 0.0 & 0.0 & 0.3789 \end{pmatrix} \tag{6.78}$$

From the same calculations, we also obtain higher order couplings, but can constrain all higher multipole couplings (such as biquadratic interactions) to be less than 10^{-5} meV. The single ion anisotropy terms are also found to be small, and take the form:

$$\mathcal{H}_{\text{SIA}} = D \sum_i (S_i^c)^2 \tag{6.79}$$

where we estimate $D = -2.6 \times 10^{-4}$ meV, implying extremely weak Ising anisotropy. Such anisotropy is sufficiently weak that long-range dipolar interactions between the $S = 5/2$ spins likely play a stronger role. Experimentally, $MnPSe_3$ shows weak easy-plane anisotropy. Neglecting these very small contributions, we find that the Hamiltonian does take the form of equation (6.68), with $J_1 = 0.93$ meV, $J_2 = 0.035$ meV, and $J_3 = 0.38$ meV. The computed couplings agree well with the values obtained from powder inelastic neutron scattering (partially by construction, as described above).

In Fig. 6.3, we show the expected magnon bands for these couplings at the level of linear spin-wave theory. Notably, the magnon bands are relatively dispersionless along the edge of the Brillouin zone at ~ 9 meV, which results in a large peak in the 2-magnon density of states (DOS) at ~ 18 meV. The latter peak is relevant to spin-phonon scattering, as discussed in subsequent sections.

6.3.3 Phonons

To obtain the phonon eigenvectors, we carried out *ab-initio* phonon calculations on a monolayer structure of $MnPSe_3$ using the Vienna *Ab Initio* Simulation Package (VASP)

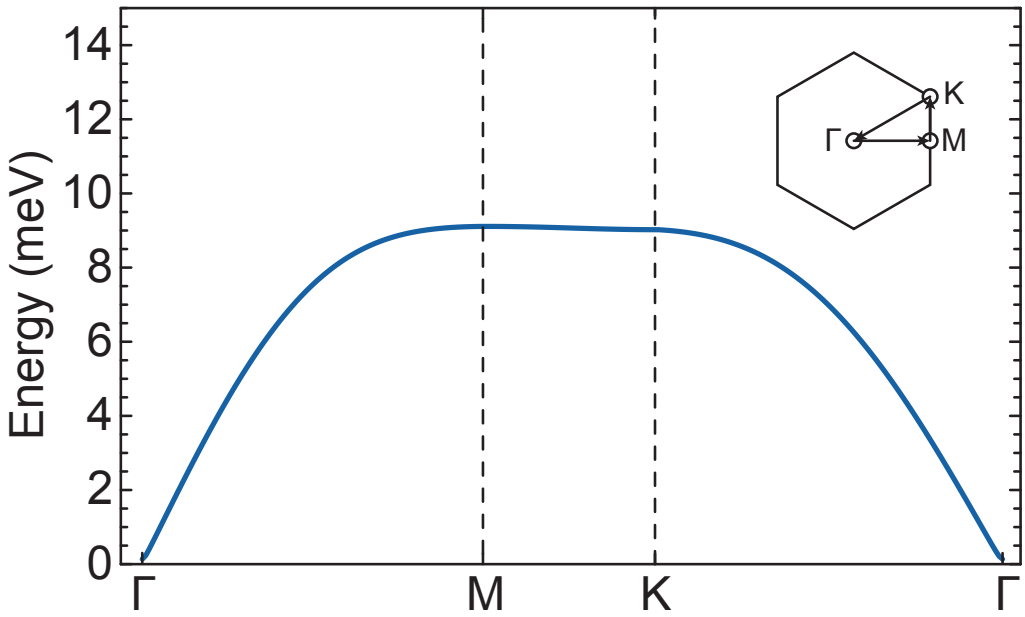

Figure 6.3: Computed one-magnon dispersion for $MnPSe_3$ at the level of linear spin-wave theory.

[239, 390, 391] within the framework of DFT. The Projector augmented wave (PAW) pseudopotential [392, 393] was chosen for all the elements as available in the VASP. The modified Perdew-Burke-Ernzerhof generalized gradient approximation functional for solid (PBEsol GGA)[394] was used for the better approximation of exchange correlation potential. The DFT-D3 method of Grimme with zero-damping function[395] was implemented to account the correction due to van der Waals forces. The kinetic energy cutoff for basis set and electronic self-consistent cycle (SCF) threshold was adjusted to 500 eV and 10^{-8} eV respectively. A robust mixture of Blocked-Davidson and RMM-DIIS iteration scheme [396, 397] was used for electronic minimization algorithm. The spin polarized calculation was carried out with initial anti-ferromagnetic spin configuration in Mn sites and the electronic correlation was treated by implementing simplified rotationally invariant DFT+U as suggested by Dudarev *et al.*[398]. For this purpose, we applied a $U - J$ value of 4 eV to the d-orbitals of Mn atoms.

To carry out phonon calculation, we started with structural relaxation of $MnPSe_3$ unit-cell without assuming any symmetry. The starting geometry was taken from the reported $R\bar{3}$ structure[399], with layers removed to produce a monolayer structure with a vacuum

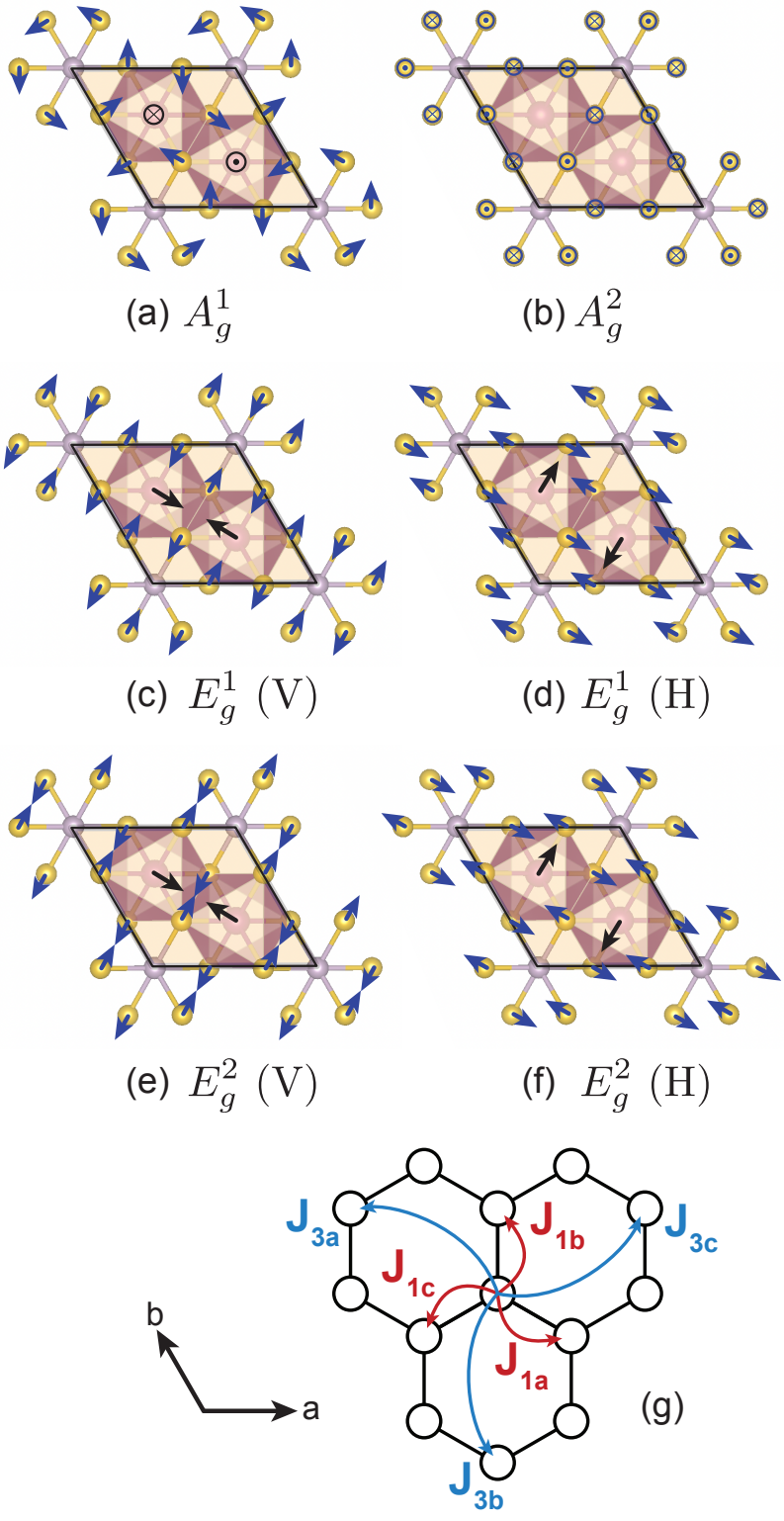

Figure 6.4: (a-f) View of the displacements of the Mn and Se atoms for the lowest energy Raman-active optical $q = 0$ phonons. For the E_g modes, vertically (V) and horizontally (H) polarized combinations are indicated. (g) Definition of the individual first and third neighbor bonds referred to in Table 6.1.

Table 6.1: Summary of lowest energy Raman active phonons and their computed $q = 0$ spin-phonon couplings. For the doubly degenerate E_g modes, the phonons have been symmetrized into horizontal (H) and vertical (V) polarizations. See Fig. 6.4(g) for definition of bonds.

Phonon	Phonon Energy (cm^{-1})		Computed $q = 0$ Spin-Phonon Couplings (meV)						
Label	Experiment[355]	Computed (Monolayer)	Pol.	A_{1a}	A_{1b}	A_{1c}	A_{3a}	A_{3b}	A_{3c}
A_g^1	48.3	33.0		≈ 0	≈ 0	≈ 0	≈ 0	≈ 0	≈ 0
E_g^1	84.0	74.3	V	+0.437	-0.218	-0.218	+0.020	-0.010	-0.010
			H	0	+0.378	-0.378	0	+0.017	-0.017
E_g^2	109.6	103.1	V	+0.502	-0.251	-0.251	+0.121	-0.061	-0.061
			H	0	+0.434	-0.434	0	+0.105	-0.105
A_g^2	149.0	138.9		≈ 0	≈ 0	≈ 0	≈ 0	≈ 0	≈ 0

gap of ~ 12Å between layers. The ionic relaxation was carried out until the forces became less than 0.001 eV/Å. The Monkhorst-Pack grid of $12 \times 12 \times 4$ was taken for the structure relaxation purpose whereas less dense k-point grid of $6 \times 6 \times 4$ was chosen for the phonon calculation due to the supercell size of $2 \times 2 \times 1$. The phonon calculations were carried out by implementing finite displacement method[140, 400] with an atomic displacement of 0.02 Å using Phonopy code[401, 402].

In Table 6.1, we show a comparison of the computed $q = 0$ monolayer phonon energies for the lowest Raman active modes with bulk experimental energies from Ref. [355]. A reasonable agreement is found, despite taking a monolayer structure. In Fig. 6.4, we show the atomic displacements associated with such phonon modes. The A_g^1 phonon corresponds to out-of-plane modulation of the Mn atoms, and rotations of the P_2Se_6 anions. The A_g^2 phonon is a symmetric P_2Se_6 stretching mode that does not involve the Mn atoms. The E_g^1 and E_g^2 modes correspond to in-plane motions of the Mn atoms coupled to bending modes of the P_2Se_6 anions.

6.3.4 Spin-Phonon Couplings

Treatment in ab-initio

In order to model the Raman scattering experiment of Ref. [355], we focus on the $q = 0$ phonons. For this purpose, we need only the electron-phonon coupling operator of equation (7.40) at $q = 0$, which can be computed without use of supercells. Therefore, to estimate the $\Delta_{i\sigma j\sigma'}^{\mu\nu;\ell\alpha n}$ parameters, we employed a finite difference (frozen phonon method). DFT

calculations were performed with FPLO on a series of geometries with each atom displaced ± 0.02Å along each of the cartesian directions $\alpha \in \{x, y, z\}$. For each calculation, the hoppings were extracted via Wannier interpolation. The parameters of each calculation were otherwise identical to those described in Section 6.3.2. The linear electron-phonon couplings were then estimated by taking the differences between calculations displaced in the $+\alpha$ and $-\alpha$ directions. In the future, such calculations could employ more sophisticated approaches, such as those implemented in the EPW code[403–405].

In order to compute the linear spin-phonon couplings $\mathbb{A}$, $\mathbb{B}$, $\mathbf{D}$, and $\mathbf{G}$, we followed the approach outlined in section 6.2.3. One- and two-Mn site clusters were exactly diagonalized, and the low-energy states were projected onto the ${}^6A_1$ electronic ground states.

Γ-point Results

Here, we consider the spin-phonon couplings linear in displacement u for $q = 0$ phonons, which is relevant for modelling the Raman measurements in Ref. [355]. We found numerically that the couplings $\mathbf{D}, \mathbf{G}$, and $\mathbb{B}$ are vanishing ($< 10^{-5}$ meV/Å) for $MnPSe_3$, as expected due to the weak effect of SOC. However, the couplings $\mathbb{A}$ are large. It is instructive to consider these couplings in mixed real-momentum space representation. The relevant coupling for the $q = 0$ phonons is:

$$\mathcal{H}_{sp} = \sum_{(ij)} \sum_{\nu} \mathcal{A}_{\nu,q=0} \, (a^{\dagger}_{\nu,q=0} + a_{\nu,q=0}) \tag{6.80}$$

The spin-phonon coupling operator is:

$$\mathcal{A}_{\nu,q=0} = \frac{1}{\sqrt{N}} \sum_{\text{u.c.}}^{N} \sum_{(ij)} \mathbf{S}_i \cdot \mathbb{A}^{\nu,q=0}_{(ij)} \cdot \mathbf{S}_j \tag{6.81}$$

where the summation over (ij) refers to the six types of first and third neighbor bonds in Fig. 6.4(g). The summation over u.c. refers to unit cells. $\mathbb{A}^{\nu,q=0}_{(ij)}$ gives the change in the magnetic coupling between spins i and j associated with the motion of the atoms along the coordinate of phonon band ν and momentum $q = 0$. The q-space couplings for a given

bond are related to the real-space couplings via:

$$\mathbb{A}_{(ij)}^{\nu,q=0} = \sum_{\alpha\ell n} \sqrt{\frac{\hbar}{2m_n\omega_{qv}}}\ \mathbb{A}_{(ij)}^{\alpha\ell n}\ e_\alpha(n, q=0, \nu) \tag{6.82}$$

where m_n is the mass of the nth nucleus, $\omega_{q\nu}$ is the phonon frequency, and $e_\alpha(n, q\nu)$ is the phonon eigenvector coefficients.

The results for different phonon bands are summarized in Table 6.1. As might be expected from the zeroth order magnetic Hamiltonian, the spin-phonon coupling matrices $\mathbb{A}_{(ij)}^{\nu,q=0}$ take the form of Heisenberg interactions for all phonon bands. For this reason, we present only the diagonal element of $\mathbb{A}$ in Table 6.1, denoted $A_{(ij)}^{v,q=0}$. There are a few immediate observations.

1. The motion of the atoms, in principle, modulates both the hoppings and the intersite Hund's coupling terms. However, in the present case, we find that the contribution to $A_{(ij)}^{\nu,q=0}$ from the intersite Coulomb terms is small, such that it can be neglected at first approximation. This is because the intersite Coulomb tensors are not strongly modified by small atomic displacements. Instead, it is the (antiferromagnetic) kinetic exchange contributions associated with direct metal-metal hopping that are most strongly modulated.

2. In the high-spin d^5 configuration of Mn^{2+}, all d-orbitals are singly occupied, such that the spin-density is essentially spherically symmetric around the Mn atom. The exchange contributions associated with direct metal-metal hopping are therefore primarily sensitive to the absolute Mn–Mn distances, rather than the relative orientations of the $MnSe_6$ octahedra. As such, the relative magnitudes of particular $A_{(ij)}^{\nu,q=0}$ follow from the amount to which the phonon mode ν modulates a particular bond distance $|\vec{r}_i - \vec{r}_j|$. For example, the A_g^1 and A_g^2 modes are not associated with in-plane motion of the Mn atoms (see Fig. 6.4). These phonons do not significantly modulate any of the Mn-Mn bond distances at linear order, and therefore do not couple strongly to the spins.

3. The spin-phonon coupling associated with the third neighbor bonds is significantly

weaker than might be anticipated from the zeroth order J_1/J_3 ratio. For third neighbors, the primary exchange pathway involves ligand-mediated hoppings exclusively, which are modulated less than the nearest neighbor direct metal-metal hoppings. As a consequence, the spin-phonon coupling is largely dominated by nearest neigbor contributions. This feature may also tend to enhance spin-phonon coupling in edge-sharing or face-sharing geometries, in comparison to edge-sharing geometries. For the latter case, direct metal-metal hopping is typically weak due to the larger distance between metal ions.

6.3.5 Modelling Raman Scattering

In order to validate the computed spin-phonon couplings, we investigated theoretically the temperature-dependence of the $q = 0$ phonon lineshapes in $MnPSe_3$, observed in recent Raman scattering experiments[355]. The Raman spectra contain contributions from both phonons and two-magnon excitations via conventional Fleury-Loudon scattering[406]. The intensity of the latter may be approximated by:

$$I_{2\mathrm{mag}}(\omega) \propto \int dt\ e^{i\omega t} \langle \hat{\mathcal{R}}(t) \hat{\mathcal{R}}(0) \rangle \tag{6.83}$$

where the Raman operators $\hat{\mathcal{R}}$ depend on the polarization of the incoming and outgoing light $\hat{e}_{\mathrm{in}}$ and $\hat{e}_{\mathrm{out}}$, according to:

$$\hat{\mathcal{R}} \propto \sum_{ij} J_{ij}\ \mathbf{S}_i \cdot \mathbf{S}_j\ (\vec{r}_{ij} \cdot \hat{e}_{\mathrm{in}})(\vec{r}_{ij} \cdot \hat{e}_{\mathrm{out}}) \tag{6.84}$$

where $\vec{r}_{ij}$ is the vector between sites i and j. In the absence of strong SOC effects, Raman scattering probes bond-bond correlations, which are primarily sensitive to two-magnon excitations in colinear antiferromagnets. Strictly speaking, given the different contributions to the intersite exchange, the precise proportionality of the bond operators in $\hat{\mathcal{R}}$ to the intersite J_{ij} does not hold (see Ref. [407]). However, for $MnPSe_3$, this is a sufficiently reasonable approximation.

By virtue of the form of the first order spin-phonon coupling, the scattering of the

phonons by spin excitations also generates a contribution to the phonon self-energy related to bond-bond spin correlations. The phonon Greens function is given by:

$$D_{q,\nu}(i\nu_n) = \frac{1}{[D^0_{q,\nu}(i\nu_n)]^{-1} - \Pi_{q,\nu}(i\nu_n)} \tag{6.85}$$

where $\nu_n = 2n\pi k_B T$, the phonon self-energy is $\Pi_{q,\nu}$ and the zeroth order Greens function is:

$$D^0_{q,\nu}(i\nu_n) = \frac{1}{i\nu_n - \omega^0_{q\nu}} - \frac{1}{i\nu_n + \omega^0_{q\nu}} \tag{6.86}$$

where $\omega^0_{q\nu}$ is the bare phonon frequency. The phonon contribution to the Raman intensity is then:

$$I_{ph}(\omega) \propto \sum_{\nu} [1 + n_B(\omega)] |R_\nu|^2 B_{0,\nu}(\omega) \tag{6.87}$$

where $n_B(\omega) = (e^{\beta\omega} - 1)^{-1}$ is the Bose distribution, $\beta = 1/(k_B T)$, and $|R_\nu|^2$ is the band-dependent Raman phonon intensity. $B_{0,\nu}(\omega)$ is the phonon spectral density, given by:

$$B_{q,\nu}(\omega) = -\frac{1}{\pi} \mathrm{Im}\left[D_{q,\nu}(i\nu_n)|_{i\nu_n \to \omega + i\Gamma}\right] \tag{6.88}$$

where Γ is a bare broadening (unrelated to spin-phonon scattering). Accounting for the lowest order spin-phonon scattering diagram shown in the inset of Fig. 6.6(b), the band-dependent phonon self-energy is:

$$\Pi_{q,\nu}(i\nu_n) = -\int_0^\beta d\tau \; e^{i\nu_n \tau} \langle \mathcal{A}_{q\nu}(\tau) \mathcal{A}_{-q\nu}(0) \rangle \tag{6.89}$$

This represents the decay of phonons into two-magnon excitations.

In order to estimate the temperature-dependent bond-bond correlation functions appearing in equations (6.83) and (6.89), we employ classical Landau-Lifshitz (LL) spin dynamics, implemented in a modified version of the Sunny.jl package[408–411]. In this approach, a distribution of initial spin states is sampled according to classical thermal equilibrium

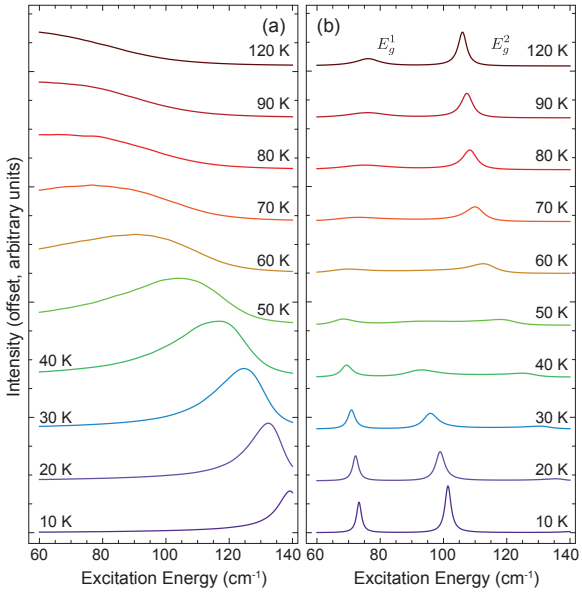

Figure 6.5: (a) Computed 2-magnon Raman scattering intensity in the VV polarization (other polarizations are nearly identical) as a function of temperature. (b) Computed phonon Raman lineshapes (2-magnon intensity omitted).

at a given temperature T. For each initial configuration, the LL equations of motion ($d\mathbf{S}_i/dt = (d\mathcal{H}/d\mathbf{S}_i) \times \mathbf{S}_i$) are iterated over a series of small time steps to generate trajectories $\mathbf{S}_i(t)$ in real time. From these trajectories, classical correlation functions of interest are computed as:

$$C^R(\omega) = \int_0^\infty dt\ e^{i\omega t} \langle \mathcal{R}(t)\mathcal{R}(0)\rangle_{\text{classical}} \tag{6.90}$$

$$C_\nu^\Pi(\omega) = \int_0^\infty dt\ e^{i\omega t} \langle \mathcal{A}_v(t)\mathcal{A}_v(0)\rangle_{\text{classical}} \tag{6.91}$$

The two-magnon Raman intensity and imaginary part of the phonon self-energy are then approximated by:

$$I_{2\text{mag}}(\omega) \propto \frac{|\omega|}{k_B T}[1 + n_B(\omega)]C^R(\omega) \tag{6.92}$$

$$\Pi_{q,\nu}(i\nu_n) = -\int_{-\infty}^\infty d\omega\ \frac{|\omega|}{k_B T}\frac{C_{q,\nu}^\Pi(\omega)}{i\nu_n - \omega} \tag{6.93}$$

It may be noted that the specific relationship between quantum and classical correlation functions is somewhat ambiguous; the prefactor of $\frac{|\omega|}{k_B T}[1 + n_B(\omega)]$ in equation (6.92) is the

"harmonic approximation", familiar in molecular dynamics[412], and represents the standard approach for dynamical spin correlations in Sunny.jl. While the harmonic approximation does not precisely reproduce the expected quantum sum rules at elevated temperatures (see Ref. [413]), in the present case of $S = 5/2$, there exist relatively small discrepancies between the quantum and classical sum rules due to the large value of S. For the purpose of benchmarking the computed spin-phonon couplings, we find the LL dynamics to be suitably accurate. For each temperature, we perform dynamics calculations on 2D systems with 100×100 unit cells (200 sites), averaging over 1000 initial spin states. We employ a time step of $\Delta t = 0.02/J_1$. We use a total of 240 frequency points with a maximum frequency of 25 meV while calculating the intensity.

In Fig. 6.5(a), we first show the computed temperature dependence of the magnetic Raman scattering response. As previously explained in Ref. [355], the magnon dispersion is relatively flat near the top of the band at ~ 9 meV, which results in a large peak in the two-magnon density of states at roughly twice this energy (18 meV $\approx$ 145 cm^{-1}). With increasing temperature, this peak broadens and softens continuously, eventually becoming quasi-elastic for $T > T_N$.

In Fig. 6.6(a-d), we show the computed temperature dependence of the $q = 0$ phonon self-energy for the E_g^1 and E_g^2 bands. The imaginary part of $\Pi_{Eg1}(\omega, T)$ and $\Pi_{Eg2}(\omega, T)$ have nearly identical form as the Raman scattering intensity, as all three quantities probe dynamical bond-bond correlations of similar form. The self-energy for the E_g^2 band is moderately larger than that of the E_g^1 band due to larger magnitude of the spin-phonon couplings $A_{(ij)}$. Very small wiggles in the computed self-energies, particularly at higher temperatures, are the result of numerical noise.

In Fig. 6.6(e,f), we show the derived phonon lifetimes τ_ν and approximate renormalized center frequency $\tilde{\omega}_\nu$, evaluated from the analytic continuation of the self-energy:

$$\tau_\nu \equiv \frac{2\pi\hbar}{\mathrm{Im}[\Pi_{0,\nu}(\omega_\nu^0 + i\eta)]} \tag{6.94}$$

$$\tilde{\omega}_\nu \equiv \omega_\nu^0 - \mathrm{Re}[\Pi_{0,\nu}(\omega_\nu^0 + i\eta)] \tag{6.95}$$

where ω_ν^0 is the bare phonon frequency obtained from the *ab-initio* phonon calculations.

Remarkably, we see a nearly quantitative agreement with the experiment of Ref. [355]. For the E_g^1 phonons, the computed minimum lifetime is $\tau_{\min} \sim 4.6$ ps, which occurs at $T \sim 65$ K. Experimentally, this minimum was estimated to be ~ 5 ps, occurring at ~ 70 K. This temperature coincides with the main peak of $\mathrm{Im}[\Pi_{Eg1}(\omega)]$ passing the bare phonon frequency. In both experiment and our calculations, the lifetime is weakly temperature dependent above the minimum temperature. For the E_g^2 phonons, the computed lifetime minimum occurs instead at ~ 50 K, with a value of $\tau_{\min} \sim 2.1$ ps. This coincides with the experimentally estimated minimum of ~ 4 ps, also at 50 K. In both experiment and our calculations, the lifetime increases rapidly with temperature above 50 K.

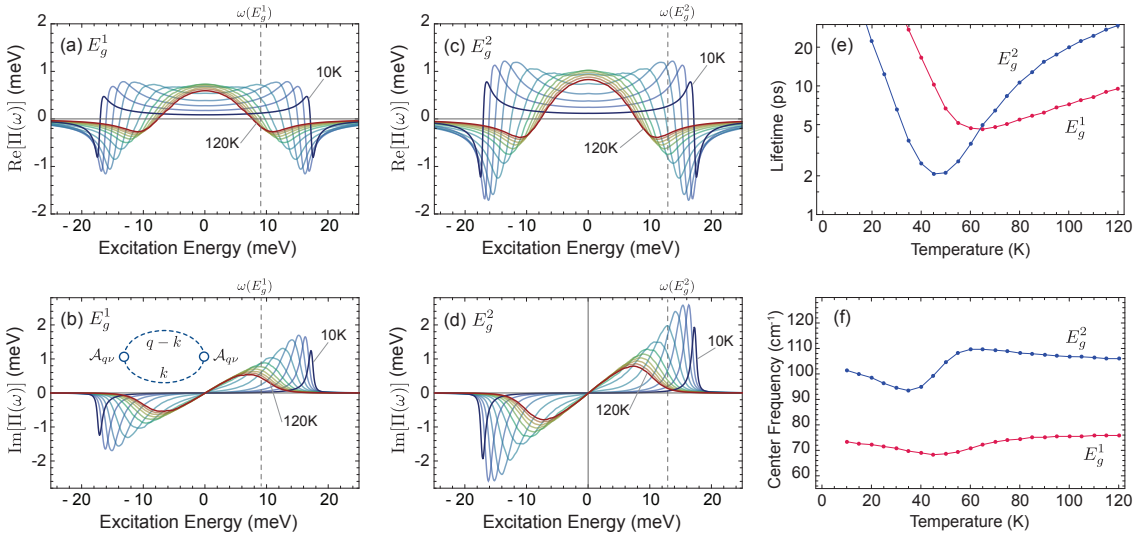

Figure 6.6: (a-d) Computed $q = 0$ phonon self-energy as a function of temperature: (a) $\mathrm{Re}[\Pi(\omega+i\eta)]$ for E_g^1, (b) $\mathrm{Im}[\Pi(\omega+i\eta)]$ for E_g^1, (c) $\mathrm{Re}[\Pi(\omega+i\eta)]$ for E_g^2, (d) $\mathrm{Im}[\Pi(\omega+i\eta)]$ for E_g^2. Curves are drawn for every 10 degrees from 10 K to 120 K. The bare phonon frequency of each mode, computed from *ab-initio*, is indicated. The inset of (b) shows the one-loop self-energy diagram associated with decay of a phonon with momentum q into two-magnon excitations with momenta $q-k$ and k. (e) Computed phonon lifetime τ_ν. (f) computed center frequency $\tilde{\omega}_\nu$.

The computed shifting of the center frequency (Fig. 6.6(f)) reproduces well the overall trends observed in experiment, although we predict somewhat larger shifts at intermediate temperatures than reported in Ref. [355]. On this point, it may be noted that the broad, multi-peaked experimental lineshapes with both phononic and magnetic contributions can make precise definition of the phonon peak position somewhat ambiguous. We also do

not account theoretically for regular magnetostriction effects, i.e. the shifting of phonons due to changes in the crystal geometry resulting from the temperature dependence of the magnetic order parameter. Such effects are associated mostly with the $\mathbb{K}$ spin-phonon couplings, which reflect spin-dependent changes to the atomic forces. Experimentally, all optical phonons are observed to shift moderately with temperature due to this effect[414], which is independent of the two magnon-phonon avoided crossing effect included here. It was noted by the authors of Ref. [355] that their experimental fits could be slightly improved by including additional temperature-dependent shifts of the phonons. We take this to imply an additional effect of magnetostriction, not included here.

For the purpose of comparison with experiment, in Fig. 6.5(b), we show the predicted temperature evolution of the phonon lineshapes, according to equation (6.87). For the bare phonon frequencies ω_ν^0, we use those obtained from the *ab-initio* phonon calculations. We take the bare width to be $\Gamma = 0.1$ meV, which is consistent with the experimental resolution in Ref. [355]. We also take the phonon oscillator strengths to satisfy $|R_{Eg2}|^2 = 2|R_{Eg1}|^2$, in order to match the appearance of the experimental spectrum. Within the magnetically ordered state ($T < T_N = 74$ K), with increasing temperature, the E_g^1 phonons broaden significantly, as the maximum of the two-magnon DOS descends to lower energy. For $T > T_N$, the E_g^1 phonons remain broad, as they fall well within the energy range of the quasielastic tail of the incoherent spin dynamics in the paramagnetic phase. For the higher energy E_g^2 phonons, the maximum of the two-magnon DOS passes the phonon energy at $T \sim 50$ K. Around this temperature, the phonon lineshape develops a very broad double-peaked form reminiscent of an avoided two-magnon/phonon crossing. Above 50 K, the peak on the higher energy side evolves into the main phonon peak, and the width of the resonance continuously decreases, until the low-temperature linewidth is recovered. Above T_N, these phonons lie at the energetic edge of the quasi-elastic spin response, such that they are mostly energetically decoupled from the spin fluctuations.

Altogether, these findings agree with and support the findings of Ref. [355]. The remarkable agreement between the computed values and experiment should lend significant confidence to the above described *ab-initio* spin-phonon coupling approach.

6.4 Conclusions and Outlook

In this work, we have motivated the need to consider spin-phonon scattering in various contexts. The form of the spin-phonon coupling was discussed with reference to generic multipolar operators, and motivated by a simple model using analytical perturbation theory. Importantly, the full spin-phonon Hamiltonian contains terms that couple spin degrees of freedom with atomic displacement and atomic momenta. The appearance of the momentum couplings (such as $\mathbf{S} \cdot (\mathbf{u} \times \mathbf{p})$) was shown to be related to structural dependence of the specific spin-orbital composition of the ground state moments. Given that such terms are implicated in the controversial phonon Hall effect, their understanding is crucial. While we leave detailed discussion of these terms in specific materials for future works, here we have introduced a generic and relatively inexpensive *ab-initio* scheme for computing arbitrary multipole-phonon couplings with full q-dependence. This approach overcomes various deficiencies of more traditional DFT frozen phonon total energy approaches, including: (i) Providing estimates for the momentum couplings through inclusion of the phonons as genuine dynamical variables, and (ii) Including the full many-body structure of the local magnetic degrees of freedom, which is important for capturing their precise spin-orbital structure. We note that very recent developments[375, 376] have also provided DFT-based approaches for estimating generic spin dipole-phonon couplings. It will be interesting to benchmark the current approach with these novel methods in the future.

In the present manuscript, we benchmarked the described method for the layered honeycomb material $MnPSe_3$, which (by choice) does not have strong spin-orbit effects, leading to a relatively simple magnetic Hamiltonian and form of the spin-phonon coupling. Combining the computed spin-phonon couplings with classical Landau-Lifshitz dynamics to estimate the dynamical bond-bond correlations allows for the evaluation of the temperature and frequency dependent phonon self-energy. This approach was shown to capture many aspects of the experimental response, including (i) distinguishing phonon modes that couple strongly or weakly with the spins, and (ii) reproducing the temperature-dependent, and band-dependent $q = 0$ optical phonon lifetimes reported in Ref. [355]. These successes validate both the computed couplings and dynamical bond-bond correlations. Alto-

gether, this approach allows for the estimation of general q-, and T-dependent spin-phonon scattering rates, which are also relevant for thermal transport[415–417] and ultrasound attenuation[320–324].

At this point, one may ask whether the effort to implement spin-phonon couplings within a dCEH framework is truly necessary. Indeed, the material at focus in this work ($MnPSe_3$) could likely be well described by more traditional DFT approaches. However, this is not the case for many vdW materials and other quantum magnets of current interest. For example, the present authors recently showed that the isostructural compound $FePS_3$ has strongly spin-orbital coupled local moments[135], and that the low-lying excitations should be viewed as complex mixtures of magnons and spin-orbital excitons. This material exhibits strong spin-phonon coupling as implied by avoided energetic crossings of phonons and spin excitations under magnetic field[253–255]. $FePS_3$ has also been implicated as a possibly hosting topological spin/phonon hybridized modes[261, 263, 264]. However, a key element for microscopic understanding of these effects is that the rich spin-orbital nature of the low-lying states must have consequences for the spin-phonon coupling; direct hybridization of one-magnon and one-phonon excitations is otherwise unlikely because a naive coupling like $\mathbf{u}\cdot\mathbf{S}$ is forbidden due to being odd under time reversal. Consistently, $MnPSe_3$ does not form magnon-polarons[418]; the fact that the primary form of spin-phonon coupling is $A_{ij}\mathbf{S}_i\cdot\mathbf{S}_j$, and the magnetic order is collinear implies a lack of mixing of one-magnon and one-phonon modes. Various phenomenological couplings have been proposed for materials like $FePS_3$ that do form magnon-polarons, which include noncolinear couplings in the intersite exchange or single-ion anisotropy terms, but these currently lack a microscopic basis. The same holds for many of the other materials mentioned in the introduction that exhibit signatures of spin-phonon coupling in their transport and excitations.

An important corollary of this work is that one can use the temperature-dependent properties of the phonons as internal probes of spin correlation functions, provided the form of the spin-phonon coupling is known. In the present example, the magnetic Raman scattering and $q = 0$ phonon lifetimes probe essentially the same two-magnon excitations, such that the phonons themselves do not provide access to additional correlation functions. However, measurements of phonon lifetimes at finite momentum, for example via ultrasound attenu-

ation, can provide access to low-energy bond-bond correlations at finite momentum, which would be otherwise difficult to probe. Here, robust first principles spin-phonon methods are of significant utility for analyzing such experiments.

In summary, the goal of this work has been to demonstrate an *ab-initio* approach capable of addressing a myriad of questions regarding spin-phonon coupling, hybrid spin-phonon excitations, and thermal transport including in materials with strong spin-orbit coupling. We look forward to pursuing these phenomena in future studies.

6.5 Intersite Coulomb Tensors

Here, we give the estimated intersite Hund's coupling tensors, which represent the down-folded ferromagnetic Goodenough-Kanamori exchange in the d-orbital Wannier functions discussed in Section 6.3.2. These are written with respect to cubic coordinates, in which $x + y + z \mid\mid c^*$, and x, y, and z are otherwise aligned with the Mn-Se bond axes. For the nearest neighbor Mn-Mn bond in which the cubic z-axis is perpendicular to the plane of the edge-sharing bond [denoted by J_{1a} in Fig. 6.4(g)], we use:

$$J_{H,ij}^{\alpha\beta} = \left(\begin{array}{r|ccccc} & d_{xy} & d_{xz} & d_{yz} & d_{z^2} & d_{x^2-y^2} \\ \hline d_{xy} & 0.51 & 0.10 & 0.11 & 0.71 & 1.64 \\ d_{xz} & 0.10 & 0.05 & 0.09 & 0.24 & 0.19 \\ d_{yz} & 0.11 & 0.09 & 0.05 & 0.23 & 0.19 \\ d_{z^2} & 0.71 & 0.24 & 0.23 & 1.00 & 0.83 \\ d_{x^2-y^2} & 1.64 & 0.19 & 0.19 & 0.83 & 1.80 \end{array}\right) \tag{6.96}$$

(in units of meV). For the high-spin d^5 case, all orbitals are equally occupied, such that the impact of these intersite Coulomb interactions on the final magnetic couplings can be estimated via $J_{FM} = \frac{1}{2S^2}\sum_{\alpha,\beta} J_{H,ij}^{\alpha\beta} = -0.96$ meV. That is to say, we estimate the effect of the ferromagnetic ligand exchange contributions on the nearest neighbor exchange to be roughly half the antiferromagnetic exchange contribution. It may be noted that this matrix is dominated by the e_g orbitals, which hybridize most strongly with the ligand p-orbitals.

For the second neighbor bond perpendicular to this bond, we have:

$$J^{\alpha\beta}_{H,ij} = \left(\begin{array}{c|ccccc} & d_{xy} & d_{xz} & d_{yz} & d_{z^2} & d_{x^2-y^2} \\ \hline d_{xy} & 0. & 0.04 & 0.06 & 0.29 & 0.01 \\ d_{xz} & 0.01 & 0.02 & 0.02 & 0.09 & 0.01 \\ d_{yz} & 0.02 & 0.01 & 0.01 & 0.02 & 0.01 \\ d_{z^2} & 0.08 & 0.04 & 0.06 & 0.23 & 0.03 \\ d_{x^2-y^2} & 0.01 & 0.09 & 0.07 & 0.37 & 0.02 \end{array}\right) \tag{6.97}$$

Here, the effective Coulomb interactions are significantly smaller. $J_{FM} = -0.13$ meV. This is sufficient to nearly completely compensate the second neighbor antiferromagnetic contribution to the exchange. Finally, For the third neighbor bond denoted by J_{3a} in Fig. 6.4(g), we use:

$$J^{\alpha\beta}_{H,ij} = \left(\begin{array}{c|ccccc} & d_{xy} & d_{xz} & d_{yz} & d_{z^2} & d_{x^2-y^2} \\ \hline d_{xy} & 0.05 & 0.03 & 0.04 & 0.1 & 0.31 \\ d_{xz} & 0.03 & 0. & 0.04 & 0.07 & 0.13 \\ d_{yz} & 0.04 & 0.04 & 0. & 0.08 & 0.12 \\ d_{z^2} & 0.1 & 0.07 & 0.08 & 0.16 & 0.47 \\ d_{x^2-y^2} & 0.31 & 0.13 & 0.12 & 0.47 & 1.22 \end{array}\right) \tag{6.98}$$

which leads to $J_{FM} = -0.34$ meV. Thus, similar to the first neighbor couplings, we estimate the ferromagnetic correction is roughly half of the antiferromagnetic contribution. As noted in the main text, the structural dependence of these matrices is weak compared to the modulation of the direct $d - d$ hopping between nearest neighbors, such that they are not a significant source of spin-phonon coupling.

Chapter 7

Phonon Thermal Hall Effect in Magnetic Insulators

This chapter is based on the arXiv:2407.00660 preprint titled "Theory of Intrinsic Phonon Thermal Hall Effect in α-$RuCl_3$".

In this chapter, We apply the method discussed in chapter 6 for treating generic spin-phonon couplings in materials with strong spin-orbit coupling to study α-$RuCl_3$. Of particular focus is the potential for this material to exhibit a phonon thermal Hall effect induced by spin-phonon interactions. We find that spin-orbit coupling significantly enriches the form of these interactions, and imbues them with chirality that is conducive to generating finite phonon Berry curvatures. We show that this leads to a phonon thermal Hall effect that qualitatively reproduces the measured field dependence of κ_{xy} without requiring a field-induced spin liquid.

My role in this project was to implement the *ab initio* method developed in chapter 6 to derive full q, ν-dependent spin-phonon Hamiltonian for α-$RuCl_3$.

7.1 Introduction

Reports of a large thermal Hall effect (THE) in α-$RuCl_3$ [211, 212, 335–338, 419–422], and an increasing range of other magnetic insulators [73, 96, 97, 325, 326, 329–334, 423], has led to intensive discussions on the nature of the heat carriers contributing to the THE,

which may include magnetic excitations (e.g. spinons [54, 99, 211, 212, 335, 344, 419] and topological magnons [337, 424–428]) as well as phonons. Various mechanisms have been proposed to generate a finite phonon thermal Hall conductivity κ_{xy}. These include *extrinsic* skew-scattering from magnetic impurities [91, 339, 340, 429] as well as *intrinsic* effects such as direct coupling of charged ions to external magnetic fields [90, 350, 352, 430], the formation of topological magnon-polarons [86, 319, 345, 348], spin-phonon scattering from bulk magnetic excitations [87, 88, 351, 353, 354, 431], and anomalous phonon velocities induced by phenomenological two-phonon "Raman" spin-phonon interactions [82, 84, 349]. The varying phenomenology of different materials points to possible contributions from different heat carriers and mechanisms. For α-$RuCl_3$, initial reports of κ_{xy}/T on the order of the half-quantum of thermal conductivity at intermediate fields led to speculation about possible contributions of Majorana spinon edge currents. However, subsequent studies also raised the possibility of non-negligible contributions from phonons [338, 341], which are compatible with experimental evidence for strong magnetoelastic coupling [327, 432–434]. Part of the continuing ambiguity stems from a lack of detailed understanding of the form and magnitude of the spin-phonon couplings, and their consequences on thermal transport. Due to the importance of the THE in identifying topologically ordered ground states [54, 435, 436], a complete understanding of phononic contributions is vital.

While the theory of spin-lattice coupling is well-developed [312–316], recent advancements in first principles methods [375, 376, 437] now make it possible to address these questions in material-specific studies. In this work, we provide a comprehensive analysis of spin-phonon couplings in α-$RuCl_3$ via first principles calculations [437] and address with them the phononic contribution to the THE due to the *intrinsic* phonon Hall viscosity [351, 353, 438]. We first review the origin of the phonon Hall viscosity, and identify the relevant spin-phonon couplings. We then present the computed couplings, focusing on the acoustic phonon modes relevant to low-temperature transport. Finally, we evaluate the longitudinal and transversal phonon thermal conductivity as a function of magnetic field. We ultimately find that the intrinsic phonon Hall effect can reproduce all aspects of the experimental low-temperature κ_{xy}.

In the low energy description of lattice phonons, the phonon Hall viscosity is the leading

term capturing time-reversal symmetry breaking. In an effective phonon Hamiltonian $\mathcal{H}_{\text{eff}}$ such a term is obtained after integrating out electronic degrees of freedom and acts as an emergent gauge field on the phonons due to electron-phonon coupling [438, 439]. Including this effect, $\mathcal{H}_{\text{eff}}$ takes the form:

$$\mathcal{H}_{\text{eff}} = \mathcal{H}_0 - \frac{1}{2}\sum_q \left(\mathbf{u}_q^\dagger \mathbb{N}_q \mathbb{M}_q^{-1} \mathbf{p}_q - \mathbf{p}_q^\dagger \mathbb{M}_q^{-1} \mathbb{N}_q \mathbf{u}_q\right) \tag{7.1}$$

where $\mathcal{H}_0$ is the unperturbed phonon Hamiltonian, $\mathbf{u}_q^\dagger = [u_{q,1}^\dagger \; u_{q,2}^\dagger \; ...]$ and $\mathbf{p}_q^\dagger = [p_{q,1}^\dagger \; p_{q,2}^\dagger \; ...]$ are the phonon displacement and momentum operators for different phonon bands, and $\mathbb{M}_q$ is the diagonal mass tensor. $\mathbb{N}_q$ is an antisymmetric matrix, whose long-wavelength limit reduces to the phonon Hall viscosity tensor discussed in Ref. [351, 353, 438].

To account for the effects of electron-phonon coupling on phonon dynamics in magnetic insulators, we start by considering the linear coupling of the electronic and lattice degrees of freedom via:

$$\mathcal{H}_{\text{el}-\text{ph}} = \sum_{q\nu} \mathcal{O}_{q\nu} u_{q\nu} \tag{7.2}$$

where $\mathcal{O}_{q\nu}$ is a generic operator acting on the electronic system, and $u_{q\nu}$ is the phonon displacement operator for momentum q and band index ν. After integrating out the electronic degrees of freedom, the lowest-order contribution to the phonon self-energy is [351, 353]:

$$\Pi_q^{\nu\nu'}(i\omega_n) = -\frac{1}{2\hbar}\int_{-\hbar\beta}^{\hbar\beta} d\tau \, e^{i\omega_n \tau} \langle \mathcal{T}_\tau [\mathcal{O}_{q\nu}(\tau) \mathcal{O}_{q\nu'}^\dagger(0)] \rangle \tag{7.3}$$

In the adiabatic limit ($i\omega_n \to 0$), the self-energy defines the effective phonon Hamiltonian of Eq. (7.1), where:

$$[\mathbb{N}_q]_{\nu,\nu'} = \frac{1}{2}\lim_{i\omega_n \to 0} \frac{i}{i\omega_n} \Pi_q^{\nu\nu'}(i\omega_n) \tag{7.4}$$

It is instructive to expand this in terms of unperturbed electronic states $|n\rangle, |m\rangle$:

$$[\mathbb{N}_q]_{\nu\nu'} = \frac{i\hbar}{4} \sum_{nm} \frac{e^{-\beta E_n} - e^{-\beta E_m}}{Z_{\text{el}}} \left[\frac{\langle n|\mathcal{O}^\dagger_{q\nu}|m\rangle\langle m|\mathcal{O}_{q\nu'}|n\rangle - \langle n|\mathcal{O}_{q\nu'}|m\rangle\langle m|\mathcal{O}^\dagger_{q\nu}|n\rangle}{(E_n - E_m)^2} \right] \tag{7.5}$$

where Z_{el} is the unperturbed electronic partition function. It is immediately recognized that:

$$\mathbb{N}_q = \frac{i\hbar}{2} \langle \nabla_{\mathbf{u}_q^\dagger} \Psi_{\text{el}}(\mathbf{u})| \wedge |\nabla_{\mathbf{u}_q} \Psi_{\text{el}}(\mathbf{u})\rangle = \frac{\hbar}{2} \Omega_q \tag{7.6}$$

where Ω_q is the "nuclear Berry curvature", which quantifies the geometric phase acquired by electronic wavefunctions under adiabatic motion of the atomic nuclei. As seen in Eq. (7.1), the nuclear Berry curvature couples to the phonon orbital momentum analogously to a magnetic field; its presence has various effects on vibrational dynamics [376, 439]. The full derivation of the above results is given in 7.3.1. The relationship between $\mathbb{N}$ and the long-wavelength viscosity tensor is discussed in 7.3.4.

It may be noted that various proposed *intrinsic* [350, 351, 353, 354] and *extrinsic* (impurity) [82, 340] mechanisms for the phonon THE can be understood within the Hall viscosity context. However, the adiabatic approximation does not include higher order skew-scattering vertex corrections or topological magnon-phonon crossings, which appear at finite energy. Nonetheless, we show that the adiabatic approximation is sufficient to capture the phenomenology of the phonon THE in α-$RuCl_3$.

7.2 Results

7.2.1 Spin-Phonon Couplings

For magnetic insulators, there are two distinct spin-dependent *intrinsic* contributions to the Hall viscosity at lowest order. These are associated with spin-phonon couplings of the form

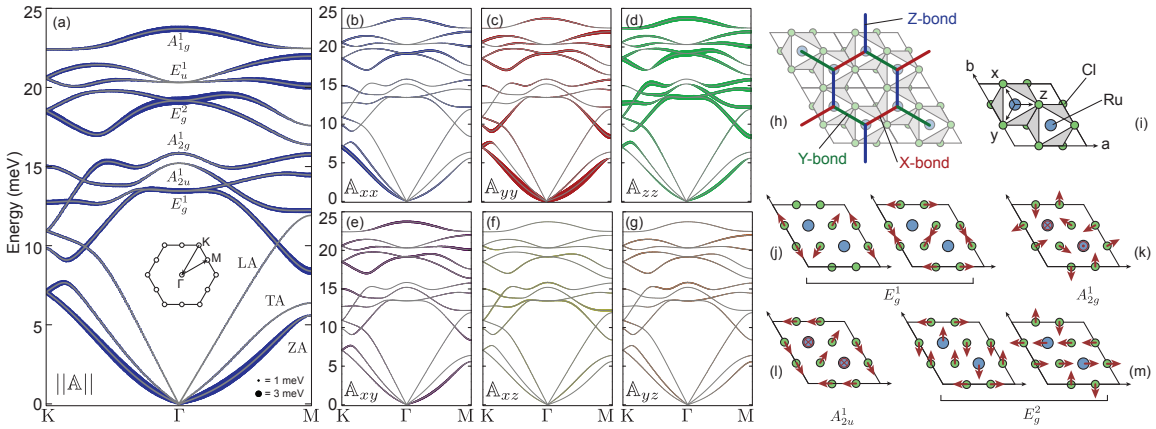

Figure 7.1: **Momentum dependence of the computed spin-phonon couplings.** $\mathbb{A}_{ij}^{q\nu}$ is depicted for the nearest-neighbor Z-bond along the high symmetry K-Γ-M path. (a): Frobenius norm $||\mathbb{A}||$. (b)-(g): Magnitude of different components of $\mathbb{A}$ in cubic coordinates. (h): Four unit cells of α-$RuCl_3$ showing definition of nearest-neighbor X-, Y-, and Z-bonds. (i): Unit cell showing definition of cubic x, y, z coordinates. (j)-(m): Primary displacements associated with $q = 0$ optical phonons.

[437]:

$$\mathcal{H}_{\text{sp-ph}} = \sum_{q\nu} \bar{u}_{q\nu}\ \mathcal{A}_{q\nu} - \sum_{q\nu q'\nu'} \bar{u}_{q\nu}\bar{p}_{q'\nu'}\ \mathcal{L}_{q\nu;q'\nu'} \tag{7.7}$$

where $\bar{u}_{q\nu} = (a^\dagger_{-q\nu} + a_{q\nu})$ and $\bar{p}_{q\nu} = i(a^\dagger_{-q\nu} - a_{q\nu})$, and $a^\dagger_{q\nu}$ creates a phonon with momentum q in band ν. The units for the phonon operators have been absorbed into the $\mathcal{A}$ and $\mathcal{L}$ operators, so that the latter have units of energy. For α-$RuCl_3$, the q-space spin and bond operators are:

$$\mathcal{A}_{q\nu} = \frac{1}{\sqrt{N}} \sum_{ij} \left(\mathbf{S}_i \cdot \mathbb{A}_{ij}^{q\nu} \cdot \mathbf{S}_j \right)\ e^{-iq\cdot(r_i + r_j)/2} \tag{7.8}$$

$$\mathcal{L}_{q\nu;q'\nu'} = \frac{\hbar\omega_{q'\nu'}}{N} \sum_{i} \left(\mathbf{L}_i^{q\nu;q'\nu'} \cdot \mathbf{S}_i \right)\ e^{-i(q+q')\cdot r_i} \tag{7.9}$$

where N is the number of unit cells, and $\mathbf{S}_i$ describe the $j_{1/2}$ moments. The $\mathcal{A}$ operators parameterize the modulation of the intersite magnetic interactions by the phonons, with $\mathbb{A}$ being the change of the 3×3 magnetic coupling tensor. The $\mathcal{L}$-operators parameterize the "two-phonon Raman" coupling, where $\mathbf{L}$ is a vector. This term arises from modulation of the local geometry around each Ru ion by the phonons, which alters the specific spin-orbital

composition of the local moments [312–316].

In order to evaluate the relative importance of the contributions, we first estimated the spin-phonon couplings following the approach of [437]. Full details are given in the 7.3.2. Briefly, we perform exact diagonalization of a coupled electron-phonon d-orbital Hamiltonian on each Ru site or bond of interest, and project the resulting low-energy Hamiltonians onto ideal $j_{1/2}$ states with different numbers of phonon quanta. The inclusion of phonons explicitly allows for the extraction of generic spin-phonon couplings in addition to the usual spin-spin couplings. These results are combined with *ab-initio* phonon calculations to yield the full q, ν-dependent spin-phonon Hamiltonian.

To reduce the complexity of the computations, we utilize a relaxed and symmetrized $P\bar{3}1m$ structure with AA stacking of adjacent layers, which aids in the symmetry analysis below. In this structure, each Ru site has D_3 point group symmetry, and each nearest-neighbor bond has C_{2h} symmetry. For the symmetrized structure, with reference to the spin Hamiltonian $\mathcal{H}_{\rm s} = \sum_{ij} \mathbf{S}_i \cdot \mathbb{J}_{ij} \cdot \mathbf{S}_j$, we compute the zeroth-order spin couplings as $(J, K, \Gamma, \Gamma') = (-2.79, -5.96, +3.06, -0.12)\,\text{meV}$, where:

$$\mathbb{J}_{\text{Z-bond}} = \begin{pmatrix} J & \Gamma & \Gamma' \\ \Gamma & J & \Gamma' \\ \Gamma' & \Gamma' & J+K \end{pmatrix} \tag{7.10}$$

for the nearest-neighbor Z-bonds [Fig. 7.1(h)]. The other bonds are related by symmetry [117, 209]. The computed couplings are sufficiently close to reported bulk values [236, 440–442] to provide confidence in the *ab-initio* methodology.

In Fig. 7.1, we first show the computed phonon dispersions and $\mathbb{A}_{ij}^{q\nu}$ couplings for the nearest-neighbor Z-bond. Despite consideration of the artificial $P\bar{3}1m$ structure, the dispersion of the phonons for in-plane momenta reproduces experimental measurements relatively well [443]. From Fig. 7.1(b)-(g), one can see that the magnitude of the different components of the spin-phonon bond operators are strongly momentum- and band-dependent. The specific coupling for each band can be rationalized from their real-space displacements, pictured in Fig 7.1(j)-(m). For example, the lowest optical mode at $q = 0$, labelled E_g^1, primarily in-

volves the symmetric motion of the Cl atoms bridging the nearest-neighbor bonds. For the Z-bond, this modulates the ligand-assisted hopping between d_{yz} and d_{xz} orbitals, which is the primary source of the Kitaev coupling K [117, 209]. As a consequence, $\mathbb{A}_{zz}$ is the largest component of the spin-phonon coupling on the Z-bond for that particular band, as shown in Fig. 7.1(d). The optical E_g^2 mode involves a similar in-plane motion of the Cl atoms, but also a modulation of the Ru positions along the bond direction. The latter motion affects the direct $d_{xy} - d_{xy}$ hopping, which alters the Γ and J couplings. For this reason, finite contributions to $\mathbb{A}_{xx}$ and $\mathbb{A}_{xy}$ are apparent. While we leave full analysis of the optical phonon couplings to future work, this discussion is meant to emphasize that the competing exchange processes in $j_{1/2}$ systems provide *strongly anisotropic and band-dependent* forms of the spin-phonon coupling.

For α-$RuCl_3$, the $\mathbf{L}$ couplings are found to be several orders of magnitude weaker than the $\mathbb{A}$ couplings, and are presented in full detail in 7.3.3. Their weakness stems from the relatively strong spin-orbit coupling, which suppresses the mixing of the $j_{1/2}$ and $j_{3/2}$ states.

We now discuss how each spin-phonon coupling contributes to the nuclear Berry curvature Eq. 7.5. The two-phonon Raman terms $\mathcal{L}$ arise from integrating out higher lying multiplet states, where $\mathcal{O}$ in Eq. (7.5) are electron-phonon coupling operators, and $|m\rangle$ are excited $j_{3/2}$ spin-orbital multiplets. This coupling is featured prominently in phenomenological models of the phonon THE [82, 84, 349], where it is often approximated by $\mathcal{H}_{\text{eff}} \sim \mathbf{S} \cdot (\mathbf{u} \times \mathbf{p})$. The $\mathcal{L}$-operators represent the generalization of these effects. They lead to a contribution to Hall viscosity of $[\mathbb{N}_q]_{\nu,\nu'} \propto \frac{1}{N} \sum_i \langle \mathbf{L}_i^{-q\nu;q\nu'} \cdot \mathbf{S}_i \rangle$, which is linear in a static $q = 0$ magnetic order parameter such as the bulk magnetization (or altermagnetic order parameter if symmetry allows). This leads to the phonon equivalent of the anomalous Hall effect. However, it requires low-lying excited multiplets $|m\rangle$ for the phonons to couple to, which are not present in α-$RuCl_3$. We thus find that the "Raman" coupling mechanism is not relevant for the phonon THE in α-$RuCl_3$, which explains why experiments do not observe a contribution to κ_{xy} that scales with the magnetization.

A second contribution to the nuclear Berry curvature comes from integrating out the magnetic excitations spanned by the lowest spin-orbital multiplet on each site. This produces a contribution to the Hall viscosity $\mathbb{N}$ where $\mathcal{O}$ in Eq. (7.5) are the spin-phonon

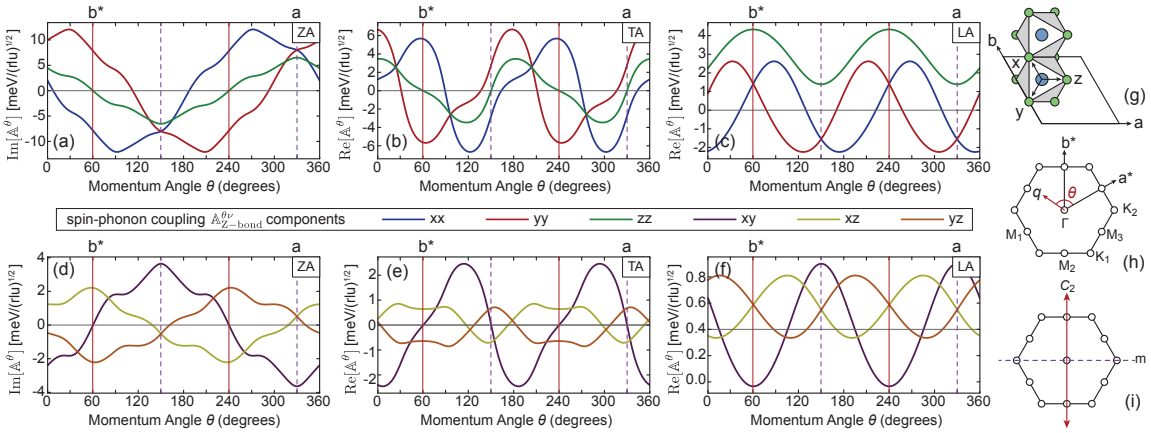

Figure 7.2: **Low-momentum angle dependence of acoustic-mode spin-phonon couplings.** Computed $\mathbb{A}^{\theta\nu}_{ij}$ for the nearest-neighbor Z-bond are shown as a function of the momentum angle θ. (a)-(c): diagonal $\mathbb{A}_{xx}$, $\mathbb{A}_{yy}$, and $\mathbb{A}_{zz}$ components. (d)-(e): off-diagonal $\mathbb{A}_{xy}$, $\mathbb{A}_{xz}$, and $\mathbb{A}_{yz}$ components. The acoustic modes ZA, TA, and LA are labelled in the upper right of each panel. (g): Z-bond in real space showing definition of the unit cell a, b axes and cubic (x, y, z) coordinates. (h): first Brillouin zone showing definition of the a^*, b^* axes, and θ (measured from the a^* axis). (i): orientation, in q-space, of the relevant symmetry operations for the Z-bond. 1 rlu $= 4\pi/(\sqrt{3}a)$.

coupling operators $\mathcal{A}$ and $|m\rangle$ are excitations like magnons, spinons, or paramagnetic fluctuations of the $j_{1/2}$ moments. This leads to a Hall viscosity contribution related to antisymmetric dynamical bond-bond correlations $\langle \mathcal{T}_\tau[\mathcal{A}_{q\nu}(\tau)\mathcal{A}^\dagger_{q\nu'}(0)]\rangle$ (see 7.3.5). For α-$RuCl_3$, we find that this contribution dominates, as discussed below.

To address the low-temperature thermal transport properties, we focus on the acoustic phonon modes. These three modes nominally correspond to out-of-plane motion of the atoms transverse to the q-vector (labelled ZA), in-plane transverse motion (TA), and in-plane longitudinal motion (LA). In the long-wavelength limit ($q \to 0$), assuming linear dispersion of the acoustic phonons, the spin-phonon couplings scale as:

$$\lim_{q\to 0} \mathbb{A}^{q\nu}_{ij} \approx \mathbb{A}^{\theta\nu}_{ij}\ |q|^{1/2} \tag{7.11}$$

where θ denotes the angle in q-space measured from the a^*-axis [Fig. 7.2(h)]. Note that there is a gauge-freedom in the complex phases of these couplings. As detailed in 7.3.2, we choose a gauge by enforcing smoothness of the couplings at small finite $|q|$, which leads to $\mathrm{Re}[\mathbb{A}^{\theta;\mathrm{ZA}}_{ij}] = \mathrm{Im}[\mathbb{A}^{\theta;\mathrm{TA}}_{ij}] = \mathrm{Im}[\mathbb{A}^{\theta;\mathrm{LA}}_{ij}] = 0$.

Fig. 7.2 shows the computed θ-dependence of the $\mathbb{A}_{ij}^{\theta\nu}$ matrices for the nearest-neighbor Z-bond. At each q-point, the time-reversal and inversion symmetry of the Hamiltonian ensures that $\mathbb{A}_{\alpha\beta} = \mathbb{A}_{\beta\alpha}$. In real space, the Z-bond is symmetric with respect to $C_2 \parallel b^*$ and $m \perp b^*$ [Fig. 7.2(i)]. This restricts the spin-phonon couplings for certain high-symmetry momenta. For $q \parallel b^*$ (parallel to the bond), the ZA and TA modes are odd with respect to the C_2, while the LA modes are even. For $q \perp b^*$ (perpendicular to the bond), the TA modes are odd with respect to m, while the ZA and LA modes are even. This means that symmetry enforces some of the couplings to change sign when rotating the momentum direction around the Brillouin zone. For example [as seen in Fig. 7.2(a)], for the ZA mode: at $q \parallel a$, $\mathbb{A}_{xx} = \mathbb{A}_{yy}$, while at $q \parallel b^*$, $\mathbb{A}_{xx} = -\mathbb{A}_{yy}$. The net result is that the spin-phonon couplings tend to wind around the origin of the Brillouin zone. Symmetry-enforced sign changes can be seen in most of the Z-bond spin-phonon couplings in Fig. 7.2(a-f).

The physical consequence of the strong θ-dependence of $\mathbb{A}_{ij}^{\theta\nu}$ can be understood as follows. In the effective phonon Hamiltonian Eq. 7.1, the Hall viscosity $\mathbb{N}_q$ enters as an antisymmetric off-diagonal term that mixes phonon modes of differing polarization. As elaborated in [353], this leads to the acoustic Faraday effect, which has now been experimentally confirmed in α-$RuCl_3$ [444]. Due to the q-dependence of $\mathbb{N}_q$, the resulting phonon eigenvectors can also wind around the Brillouin zone, which is reflected in a finite Berry curvature for the phonon bands, and thus a finite κ_{xy}. The finding that the $\mathcal{A}$ couplings have a q-dependence conducive to such winding suggest a finite phonon Berry curvature can arise from spin-phonon coupling under relatively generic conditions, as elaborated below.

7.2.2 Phonon Longitudinal Thermal Conductivity

We now consider the effects of the computed spin-phonon couplings on the field-dependence of the low-temperature thermal transport. For this purpose, we employ exact diagonalization on the 24-site periodic cluster depicted in Fig. 7.3(b; inset) to evaluate the bond correlations appearing in the acoustic phonon self-energy [Eq. (7.3) with $\mathcal{O}_{q\nu} = \mathcal{A}_{q\nu}$]. We

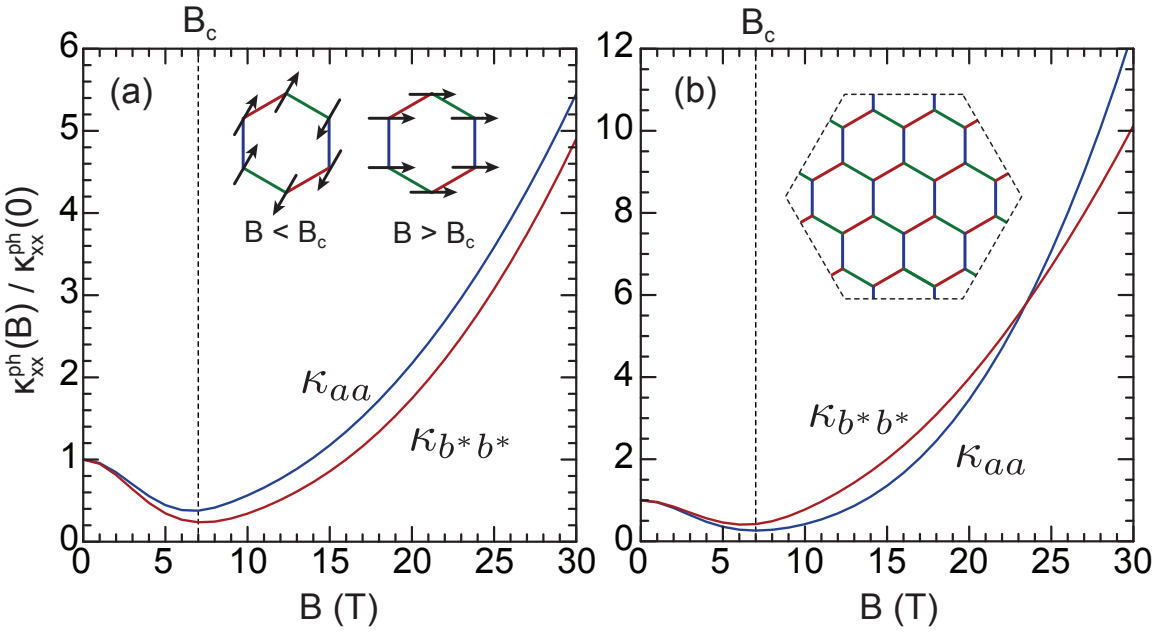

Figure 7.3: **Longitudinal phonon thermal conductivity.** Shown for (a): magnetic field $\mathbf{B} \parallel a$ and (b): $\mathbf{B} \parallel b^*$. Inset in (a) shows zigzag ($B < B_c$) and polarized ($B > B_c$) magnetic states. Inset in (b) shows 24 site cluster used in ED.

consider the bare spin Hamiltonian with an in-plane magnetic field $\mathbf{B}$:

$$\mathcal{H}_{\rm s} = \sum_{ij} \mathbf{S}_i \cdot \mathbb{J}_{ij} \cdot \mathbf{S}_j - \mu_{\rm B} g_{ab} \sum_i \mathbf{B} \cdot \mathbf{S}_i \tag{7.12}$$

with the nearest-neighbor couplings computed for the relaxed structure, plus a third-neighbor Heisenberg coupling $J_3 = +0.8\,\text{meV}$, and an in-plane g-value of $g_{ab} = 2.3$. These fall into the range of reported values in the literature [442]. For in-plane fields, this model has two phases [Fig. 7.3(a; inset)]. For $B < B_c \approx 7\,\text{T}$, it is nominally in an antiferromagnetic zigzag phase; for $B > B_c$ it adopts an asymptotically polarized phase. No intermediate phase is found.

Since ED does not allow a fine q-dependence, we approximate $\mathcal{A}_{q\nu}|_{q\approx 0} \approx \frac{1}{\sqrt{N}} \sum_{ij} (\mathbf{S}_i \cdot \mathbb{A}_{ij}^{\theta\nu} \cdot \mathbf{S}_j) |q|^{1/2}$ [cf. Eq. (7.11)]. This corresponds to retaining the q-dependence of the spin-phonon coupling operators, but approximating the relevant low-q bond correlations by their $q \to 0$ limits. With this approximation, the q-dependence of the phonon self-energy and Hall viscosity arises only from the spin-phonon couplings. The computed ED bond correlations strictly correspond to zero temperature, but serve as an approximation for their

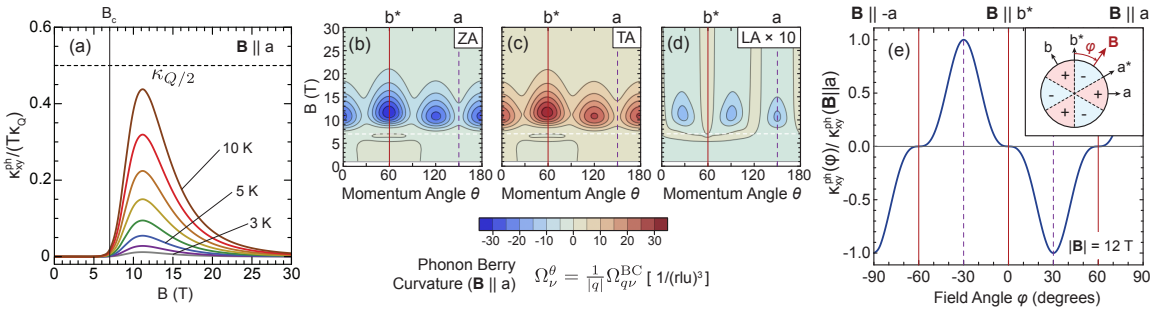

Figure 7.4: **Phonon thermal Hall conductivity.** (a): Evolution of phonon thermal Hall conductivity $\kappa_{xy}^{\rm ph}$ as a function of field for $\mathbf{B} \parallel a$ computed using ED bond correlations. (b-d): Phonon Berry curvature Ω_ν^θ as a function of field and momentum direction for three acoustic phonon bands; $1\,\text{rlu} = 4\pi/(\sqrt{3}a)$. (e): Field angle dependence of $\kappa_{xy}^{\rm ph}$ at $|\mathbf{B}| = 12\,\text{T}$. Inset: Sign of $\kappa_{xy}^{\rm ph}$ as a function of in-plane field direction, with definition of field angle ϕ.

low-temperature forms.

At fixed low temperature, assuming spin-phonon coupling is the dominant scattering mechanism, the in-plane longitudinal phonon thermal conductivity $\kappa_{\alpha\alpha}^{\rm ph}$ in the long-wavelength limit follows (7.3.5):

$$\kappa_{\alpha\alpha}^{\rm ph} \propto \sum_\nu \int_0^{2\pi} d\theta\ (\hat{q}\cdot\hat{\alpha})^2\ \tau_\nu^\theta \tag{7.13}$$

where $(\hat{q}\cdot\hat{\alpha})$ indicates the projection of the momentum on the transport direction, and τ_ν^θ is the band-dependent relative phonon lifetime, given by:

$$\tau_\nu^\theta \equiv \frac{\hbar c_\nu |q|}{\text{Im}[\Pi_q^{\nu\nu}(\omega_{q\nu})]} \tag{7.14}$$

where $c_\nu = \partial\omega_{q\nu}/\partial|q|$ is the speed of sound for each band, obtained from the *ab-initio* phonon calculations. Since $\text{Im}[\Pi_q^{\nu\nu}(\omega_{q\nu})] \propto |q|$, the relative lifetime depends only on the momentum direction. To compute $\kappa_{\alpha\alpha}$, the discrete poles of $\Pi_q^{\nu\nu}(\omega)$ were Lorentzian broadened with a width of $\gamma = 0.5\,\text{meV}$ to extrapolate to low frequency. This produces an unavoidable dependence of the computed phonon lifetimes on the broadening γ. For this reason, we plot $\kappa_{xx}^{\rm ph}$ relative to its zero-field value, which is insensitive to γ (Supplemental Note 5).

Fig. 7.3 shows the computed field-dependence of the in-plane $\kappa_{aa}^{\rm ph}$ and $\kappa_{b^*b^*}^{\rm ph}$ for $\mathbf{B} \parallel a$ and $\mathbf{B} \parallel b^*$. For both field directions and both propagation directions, the longitudinal thermal

conductivity reaches a minimum near the critical field. This behavior is consistent with experimental measurements [106, 211, 212, 327, 445], which report reduction of $\kappa^{\rm ph}_{\alpha\alpha}$ at B_c by factors of 2 - 5 compared to the zero-field value. This can be simply understood. At both low field and high field, the spin excitations are gapped and well separated in energy from the low-q acoustic phonons. At the critical field, the reduction of the spin gap implies an increased density of low-energy spin excitations, which enhances scattering. Since $\Pi^{\nu\nu}_q$ is a dynamical bond-bond correlation, the closure of a one-magnon gap at any q-point enhances scattering for phonons near $q = 0$ due to contributions from multi-magnons at low-q. ED reproduces this effect, but does not capture a complete gap-closing due to finite size effects, resulting in a broader minimum in $\kappa_{\alpha\alpha}(B)$ than found in experiments. In the high-field phase, we find $\kappa^{\rm ph}_{\alpha\alpha}$ is larger for $\mathbf{B} \,||\, b^*$ than for $\mathbf{B} \,||\, a$ as a consequence of the details of the spin-phonon couplings. At all fields, $\kappa^{\rm ph}_{\alpha\alpha}$ is dominated by the LA phonons, which have the largest sound velocity and the weakest spin-phonon coupling (see Fig 7.1).

7.2.3 Phonon Thermal Hall Conductivity

To estimate the field-dependence of the thermal Hall conductivity $\kappa^{\rm ph}_{xy}$, we computed the Hall viscosity matrix $\mathbb{N}$ for the acoustic phonons in the zero temperature limit by summing Eq. (7.4) over the ED poles without broadening. We then numerically evaluated the phonon Berry curvature $\Omega^{\rm BC}_{q\nu}$ by diagonalizing the phonon effective Hamiltonian [Eq. (7.1)]. We find that the Berry curvature of the acoustic phonons is proportional to $|q|$ for small momenta, and thus define $\Omega^{\theta}_{\nu} = \Omega^{\rm BC}_{q\nu}/|q|$. Following [85, 99, 341, 353]:

$$\frac{\kappa^{\rm ph}_{xy}}{T\kappa_Q} \approx -2.00655 \sum_{\nu} \left(\frac{k_{\rm B}T}{\hbar c_\nu}\right)^3 \int_0^{2\pi} \Omega^{\theta}_{\nu}\, d\theta \tag{7.15}$$

where $\kappa_Q = \pi k_{\rm B}^2/(6\hbar)$ is the quantum of thermal conductance.

Fig. 7.4(a) depicts the qualitative evolution of $\kappa^{\rm ph}_{xy}$, for $\mathbf{B} \,||\, a$. Here, we have employed the $T = 0$ spin correlations to evaluate the phonon Berry curvature in Eq. (7.15), so that the depicted temperature dependence is approximate (as discussed further below). We find that $\kappa^{\rm ph}_{xy}$ rapidly increases above the critical field, reaches a maximum near 11 T, and then

decays with increasing field. This can be understood from the evolution of the phonon Berry curvature Ω_ν^θ, depicted in Fig. 7.4(b-d). Above the critical field, there is a rapid increase in Ω_ν^θ for the ZA and TA phonon for all momentum directions (while the LA phonons develop nearly no Berry curvature). Ultimately, $\kappa_{xy}^{\rm ph}$ is dominated by the ZA phonons, which have the smallest sound velocity (the largest thermal population), and develop the largest Berry curvature. An interesting consequence is that κ_{xx} and κ_{xy} do not probe the same phonons at low temperatures.

In Fig. 7.4(e), we show the computed dependence of $\kappa_{xy}^{\rm ph}$ on the direction of the in-plane field, for $|\mathbf{B}| = 12$ T. We find that in-plane field-angle dependence agrees with experimental reports [212, 337, 419], with $\kappa_{xy}^{\rm ph}$ changing sign as the field is rotated through a^*, b^* and symmetry-related directions. While this mimics the expected angle-dependence of κ_{xy} contributed by Majorana spinons in the pure Kitaev spin-liquid, it is also the simplest sign structure compatible with the symmetries of the crystal. For $\mathbf{B} \parallel a^*, b^*$, it is required that $\kappa_{xy} = 0$ due to the 2-fold rotational symmetry [427, 446]. The overall sign of $\kappa_{xy}^{\rm ph}$ agrees with experiment, and is determined by the combined effect of the spin-phonon couplings and bond correlations. It is likely non-universal.

Together, these results reveal that a *planar* phonon THE is possible in α-$RuCl_3$ due to *intrinsic* Hall viscosity. In contrast with the electronic Hall effect, an out-of-plane component of the magnetic field is not necessary, because the phonons couple to the emergent gauge field generated by the nuclear Berry curvature, not to the actual magnetic field. As we show in 7.3.5, the Hall conductivity scales roughly as $\kappa_{xy}^{\rm ph} \propto \mathbb{N}^3 \sim (\mathcal{A}/\Delta_s)^6$, where $\mathcal{A}$ is the spin-phonon coupling, and Δ_s is the spin-gap [see also Eq. (7.4-7.5)]. It is thus expected that the reduction of the spin-gap in the vicinity of B_c enhances $\kappa_{xy}^{\rm ph}$ because the phonons are more strongly dressed by the low-lying spin excitations. However, we find that the maximum in $\kappa_{xy}^{\rm ph}$ occurs above the critical field, in the asymptotically polarized phase (at 11 T). This occurs due to the specific field-dependence of the bond susceptibilities, which lead to a peak in the Hall viscosities within the polarized phase. It may be noted that $\kappa_{xy}^{\rm ph}$ does not saturate at a constant value, as would be expected for dominant $\mathbf{L}$ couplings.

Lastly, we address the magnitude of $\kappa_{xy}^{\rm ph}$. Due to the sharp scaling noted above [$\kappa_{xy}^{\rm ph} \propto (\mathcal{A}/\Delta_s)^6$], precise estimates of the magnitude require accurate modeling of the magnetic

excitation spectrum and its temperature dependence. As noted above, we have estimated $\kappa_{xy}^{\mathrm{ph}}$ employing the zero-temperature spin correlations, which leads to $\kappa_{xy}^{\mathrm{ph}}/T \propto T^3$ due to the thermal population of phonons according to Eq. (7.15). The predicted $\kappa_{xy}^{\mathrm{ph}}/T$ falls within an order of magnitude of $\frac{1}{2}\kappa_Q$, which agrees very well with experimental data. While a more precise calculation should account for the temperature dependence of the Hall viscosity in addition to the phonon population, we conclude that intrinsic phononic contributions are likely a significant portion of the observed κ_{xy} in α-$RuCl_3$ at low temperatures.

In summary, taking careful account of the effects of microscopic spin-phonon couplings reveals that the intrinsic phonon Hall effect is consistent with the low-temperature $\kappa_{xy}(B)$ in α-$RuCl_3$. This mechanism reproduces all essential experimental features including the field-dependence, sign, and order of magnitude. The intrinsic phonon THE considered here does not arise from real-space spin textures or non-trivial topology of the bare spin excitations. Instead, it arises from the momentum-dependence of the spin-phonon couplings, which can induce a finite phonon Berry curvature even if the electronic system is topologically trivial. A finite intrinsic Hall viscosity can likely be found in a variety of magnetic and non-magnetic insulators, for which differing phenomenology can be attributed to differences in the specific form of electron-phonon (or spin-phonon) coupling. The present results highlight a significant utility of first-principles spin-phonon coupling methods in disentangling the microscopic details underlying the phonon THE in specific materials.

7.3 Supplementary Materials

7.3.1 Phonon Hall Viscosity as Electronic Nuclear Berry Curvature

In this first supplemental section, we discuss the connection between the phonon Hall viscosity and nuclear Berry curvature from the perspective of an effective phonon action. The total action for a coupled phonon and electronic system can be written:

$$S \equiv \int dt\ \mathcal{L} = \int dt\ \langle \Psi | i\hbar \frac{\partial}{\partial t} - \mathcal{H} | \Psi \rangle \tag{7.16}$$

where $\mathcal{L}$ is the Lagrangian and $|\Psi\rangle$ is the full wavefunction including both electronic and lattice degrees of freedom. The trajectory of a vibrational wavepacket is determined by the stationary point of the phase $iS/\hbar = \gamma_{\text{geo}} + \gamma_{\text{dyn}}$. The first contribution $\gamma_{\text{geo}} = -\int dt\ \langle\Psi|\frac{\partial}{\partial t}|\Psi\rangle$ is the geometric phase, while the second contribution $\gamma_{\text{dyn}} = (i/\hbar)\int dt\ \langle\Psi|\mathcal{H}|\Psi\rangle$ is the dynamical phase. We consider the adiabatic approximation for the total wavefunction $|\Psi\rangle = |\Psi_{\text{ph}}\rangle|\Psi_{\text{el}}[\mathbf{u}(t)]\rangle$, where $|\Psi_{\text{ph}}\rangle$ denotes the phonon (lattice) wavefunction, $|\Psi_{\text{el}}\rangle$ denotes the electronic wavefunction, and $\mathbf{u}(t)$ are the time-dependent displacements of the atoms from equilibrium. If the dynamics of the lattice are slow compared to the electronic system, then $|\Psi_{\text{el}}\rangle$ remains in the ground state. However, the explicit dependence of the ground state $|\Psi_{\text{el}}\rangle$ on $\mathbf{u}(t)$ gives an additional contribution to the geometric phase $\gamma_{\text{el-ph}} = -\int dt\ \langle\Psi_{\text{el}}|\nabla_{\mathbf{u}}\Psi_{\text{el}}\rangle \cdot \frac{\partial \mathbf{u}}{\partial t}$. Putting everything together leads to:

$$\mathcal{L} = \sum_{q\nu} \frac{1}{2} m_{q\nu} \dot{u}^{\dagger}_{q\nu} \dot{u}_{q\nu} - \frac{1}{2} m_{q\nu} \omega^2_{q\nu} u^{\dagger}_{q\nu} u_{q\nu} + \langle\Psi_{\text{el}}|i\hbar \frac{\partial}{\partial u_{q\nu}}|\Psi_{\text{el}}\rangle\ \dot{u}_{q\nu} - \langle\Psi_{\text{el}}|\mathcal{H}_{\text{el}}[\mathbf{u}(t)]|\Psi_{\text{el}}\rangle \tag{7.17}$$

where $\dot{u} = \partial u/\partial t$ and $u^{\dagger}_{q\nu} = u_{-q\nu}$. The summation is over wavevectors q and phonon band indices ν. The third term represents a modification to the effective phonon Lagrangian. The essence of this result is that vibrational wavepackets are "dressed" by the electronic system, and can acquire an additional geometric phase due to the evolution of the "dressing". The quantity $i\langle\Psi_{\text{el}}|\nabla_{\mathbf{u}}\Psi_{\text{el}}\rangle$ plays an analogous role to the magnetic vector potential for charged particles. The specific details of this emergent gauge field are determined by the details of electron-phonon coupling and the electronic ground state. If the electronic ground state breaks time-reversal symmetry (either spontaneously or in response to an external magnetic field), this can lead to a finite phonon THE [350].

The nuclear Berry connection can be evaluated perturbatively in powers of the electron-phonon coupling $\sum_{q\nu} \mathcal{O}_{q\nu} u_{q\nu}$. Taking $|g\rangle$ to be the unperturbed electronic ground state (in the absence of spin-phonon coupling), and $|m\rangle$ to be unperturbed excited states, then:

$$|\Psi_{\text{el}}\rangle \approx |g\rangle + \sum_{q\nu} \sum_{m} |m\rangle \frac{\langle m|\mathcal{O}_{q\nu}|g\rangle}{E_g - E_m} u_{q\nu} \tag{7.18}$$

This leads to:

$$i\hbar \left\langle \Psi_{\rm el} \left| \frac{\partial \Psi_{\rm el}}{\partial u_{q\nu}} \right\rangle \approx i\hbar \sum_{\nu',m} u^{\dagger}_{q\nu'} \frac{\langle g|\mathcal{O}^{\dagger}_{q\nu'}|m\rangle\langle m|\mathcal{O}_{q\nu}|g\rangle}{(E_g - E_m)^2} = i\hbar \sum_{\nu'} \left\langle \frac{\partial \Psi_{\rm el}}{\partial u^{\dagger}_{q\nu'}} \left| \frac{\partial \Psi_{\rm el}}{\partial u_{q\nu}} \right\rangle u^{\dagger}_{q\nu'} \right. \quad (7.19)$$

$$i\hbar \left\langle \frac{\partial \Psi_{\rm el}}{\partial u_{q\nu}} \left| \Psi_{\rm el} \right\rangle \right. \approx i\hbar \sum_{\nu',m} \frac{\langle g|\mathcal{O}_{q\nu}|m\rangle\langle m|\mathcal{O}^{\dagger}_{q\nu'}|g\rangle}{(E_g - E_m)^2} u^{\dagger}_{q\nu'} = i\hbar \sum_{\nu'} \left\langle \frac{\partial \Psi_{\rm el}}{\partial u_{q\nu}} \left| \frac{\partial \Psi_{\rm el}}{\partial u^{\dagger}_{q\nu'}} \right\rangle u^{\dagger}_{q\nu'} \right. \quad (7.20)$$

One may note that normalization of the electronic wavefunction for all values of displacements requires that $\frac{\partial}{\partial u}\langle \Psi_{\rm el}|\Psi_{\rm el}\rangle = \langle \frac{\partial \Psi_{\rm el}}{\partial u}|\Psi_{\rm el}\rangle + \langle \Psi_{\rm el}|\frac{\partial \Psi_{\rm el}}{\partial u}\rangle = 0$, such that $\langle \frac{\partial \Psi_{\rm el}}{\partial u}|\Psi_{\rm el}\rangle = -\langle \Psi_{\rm el}|\frac{\partial \Psi_{\rm el}}{\partial u}\rangle$. As a consequence:

$$i\hbar \left\langle \Psi_{\rm el} \left| \frac{\partial \Psi_{\rm el}}{\partial u_{q\nu}} \right\rangle \approx \frac{i\hbar}{2} \sum_{\nu'} \left(\left\langle \frac{\partial \Psi_{\rm el}}{\partial u^{\dagger}_{q\nu'}} \left| \frac{\partial \Psi_{\rm el}}{\partial u_{q\nu}} \right\rangle - \left\langle \frac{\partial \Psi_{\rm el}}{\partial u_{q\nu}} \left| \frac{\partial \Psi_{\rm el}}{\partial u^{\dagger}_{q\nu'}} \right\rangle \right) u^{\dagger}_{q\nu'} = \frac{\hbar}{2} \sum_{\nu'} \Omega_q^{\nu'\nu} u^{\dagger}_{q\nu'} \right. \quad (7.21)$$

Here, we have introduced the nuclear Berry curvature in q-space:

$$\begin{aligned} \Omega_q^{\nu'\nu} &= i \left(\left\langle \frac{\partial \Psi_{\rm el}}{\partial u^{\dagger}_{q\nu'}} \left| \frac{\partial \Psi_{\rm el}}{\partial u_{q\nu}} \right\rangle - \left\langle \frac{\partial \Psi_{\rm el}}{\partial u_{q\nu}} \left| \frac{\partial \Psi_{\rm el}}{\partial u^{\dagger}_{q\nu'}} \right\rangle \right) \right. \\ &= i \sum_m \frac{\langle g|\mathcal{O}^{\dagger}_{q\nu'}|m\rangle\langle m|\mathcal{O}_{q\nu}|g\rangle - \langle g|\mathcal{O}_{q\nu}|m\rangle\langle m|\mathcal{O}^{\dagger}_{q\nu'}|g\rangle}{(E_g - E_m)^2} \end{aligned} \quad (7.22)$$

For reasons made clear below, it is convenient to absorb the prefactors of the Fourier transformed phonon operators, and represent the nuclear Berry curvature in terms of the reduced Hall viscosity $\overline{\eta}_q^{\nu'\nu} = -\overline{\eta}_{-q}^{\nu\nu'}$:

$$\overline{\eta}_q^{\nu'\nu} = \sqrt{\frac{\hbar}{2m_{q\nu}\omega_{q\nu}}} \sqrt{\frac{\hbar}{2m_{q\nu'}\omega_{q\nu'}}}\ \Omega_q^{\nu'\nu} \quad (7.23)$$

such that:

$$i\hbar \left\langle \Psi_{\rm el} \left| \frac{\partial \Psi_{\rm el}}{\partial u_{q\nu}} \right\rangle \right. \approx \sum_{\nu'} \sqrt{m_{q\nu}\omega_{q\nu} m_{q\nu'}\omega_{q\nu'}}\ \overline{\eta}_q^{\nu'\nu}\ u^{\dagger}_{q\nu'} \quad (7.24)$$

The above expressions are analogous to the symmetric Coulomb gauge for the electromagnetic vector potential, wherein $\vec{A} = -\frac{1}{2}\vec{r}\times\vec{B}$, except that $\Omega_q^{\nu'\nu}$ plays the role of the magnetic

field. As defined, Ω has units of inverse length squared, and $\overline{\eta}$ is unitless. The relationship between this quantity and the usual definition of the viscosity in the long-wavelength elastic theory is discussed in 7.3.4.

Returning to the effective phonon Lagrangian, we find:

$$\mathcal{L}_{\text{eff}} = \sum_{q\nu} \frac{1}{2} m_{q\nu} \dot{u}^{\dagger}_{q\nu} \dot{u}_{q\nu} - \frac{1}{2} m_{q\nu} \omega^2_{q\nu} u^{\dagger}_{q\nu} u_{q\nu} + \sum_{q\nu\nu'} \sqrt{m_{q\nu}\omega_{q\nu} m_{q\nu'}\omega_{q\nu'}}\ u^{\dagger}_{q\nu'} \overline{\eta}^{\nu'\nu}_{q} \dot{u}_{q\nu} \tag{7.25}$$

From this, we define the phonon momenta:

$$p^{\dagger}_{q\nu} = \frac{\partial \mathcal{L}_{\text{eff}}}{\partial \dot{u}_{q\nu}} = m_{q\nu} \dot{u}^{\dagger}_{q\nu} + \sum_{\nu'} \sqrt{m_{q\nu}\omega_{q\nu} m_{q\nu'}\omega_{q\nu'}}\ u^{\dagger}_{q\nu'} \overline{\eta}^{\nu'\nu}_{q} \tag{7.26}$$

The resulting effective phonon Hamiltonian up to linear order in η is:

$$\mathcal{H}_{\text{eff}} = \sum_{q\nu} \frac{p^{\dagger}_{q\nu} p_{q\nu}}{2m_{q\nu}} + \frac{1}{2} m_{q\nu} \omega^2_{q\nu} u^{\dagger}_{q\nu} u_{q\nu} - \sum_{q\nu\nu'} \frac{\sqrt{m_{q\nu}\omega_{q\nu} m_{q\nu'}\omega_{q\nu'}}}{2} \left(u^{\dagger}_{q\nu} \overline{\eta}^{\nu\nu'}_{q} \frac{p_{q\nu'}}{m_{q\nu'}} - \frac{p^{\dagger}_{q\nu}}{m_{q\nu}} \overline{\eta}^{\nu\nu'}_{q} u_{q\nu'} \right) \tag{7.27}$$

We see that the nuclear Berry curvature couples to an antisymmetric combination of the phonon displacement and momentum resembling a phonon angular momentum.

As discussed in Ref. ye2020phonon,ye2021phonon, the Hall viscosity can be separately identified with the antisymmetric part of the adiabatic limit of the phonon self-energy. At one loop order in the spin-phonon coupling, the self-energy is defined by:

$$\Pi^{\nu\nu'}_{q}(i\omega_n) = -\frac{1}{2\hbar} \int_{-\hbar\beta}^{\hbar\beta} d\tau\ e^{i\omega_n \tau} \langle \mathcal{T}_{\tau} [\mathcal{O}_{q\nu}(\tau) \mathcal{O}^{\dagger}_{q\nu'}(0)] \rangle \tag{7.28}$$

$$= \frac{1}{2} \sum_{nm} \frac{e^{-\beta E_n} - e^{-\beta E_m}}{Z_{\text{el}}} \left[\frac{\langle n|\mathcal{O}^{\dagger}_{q\nu'}|m\rangle\langle m|\mathcal{O}_{q\nu}|n\rangle}{E_n - E_m - \hbar\ i\omega_n} + \frac{\langle n|\mathcal{O}_{q\nu}|m\rangle\langle m|\mathcal{O}^{\dagger}_{q\nu'}|n\rangle}{E_n - E_m + \hbar\ i\omega_n} \right] \tag{7.29}$$

where $|n\rangle$ and $|m\rangle$ are unperturbed electronic states and Z_{el} is the unperturbed electronic

partition function. The reduced Hall viscosity is then given by:

$$\overline{\eta}_q^{\nu'\nu} = \sqrt{\frac{1}{2m_{q\nu}\omega_{q\nu}}}\sqrt{\frac{1}{2m_{q\nu'}\omega_{q\nu'}}}\lim_{i\omega_n\to 0}\frac{i}{i\omega_n}\Pi_q^{\nu\nu'} \tag{7.30}$$

$$= \frac{i}{2}\sqrt{\frac{\hbar}{2m_{q\nu}\omega_{q\nu}}}\sqrt{\frac{\hbar}{2m_{q\nu'}\omega_{q\nu'}}}\sum_{nm}\frac{e^{-\beta E_n}-e^{-\beta E_m}}{Z_{\text{el}}} \left[\frac{\langle n|\mathcal{O}^\dagger_{q\nu'}|m\rangle\langle m|\mathcal{O}_{q\nu}|n\rangle - \langle n|\mathcal{O}_{q\nu}|m\rangle\langle m|\mathcal{O}^\dagger_{q\nu'}|n\rangle}{(E_n-E_m)^2}\right] \tag{7.31}$$

which is simply the finite-temperature analogue of the nuclear Berry curvature defined above.

7.3.2 Details of First Principles Calculations

In this section, we describe the full computational details of the spin-phonon couplings. There are four essential steps.

1. The structure is relaxed to obtain a starting geometry for further calculations.

2. *Ab-initio* phonon calculations are performed on the relaxed structure to obtain phonon frequencies and eigenvectors. A gauge transformation is applied to the eigenvectors to ensure a smooth definition at finite $|q|$.

3. Linear electron-phonon couplings are computed on the relaxed structure for a Wannier basis of d-orbitals on each Ru site using a finite displacement approach.

4. Exact diagonalization of the d-orbital electron+phonon Hamiltonian including electronic interactions and electron-phonon coupling is performed for small clusters of Ru atoms. The resulting low-energy states are projected onto pure $j_{1/2}$ states with variable numbers of phonon quanta, and the low-energy Hamiltonian is analyzed to extract generic spin-phonon couplings.

Structural Relaxation: We first relaxed an idealized structure of α-$RuCl_3$ with AA stacking in the space group $P\bar{3}1m$, starting from a similar out-of-plane layer-to-layer distance as observed in the reported $R\bar{3}$ structure. For this purpose, the Vienna *Ab Initio* Simulation Package (VASP) [239, 390, 391] was used for the DFT calculations with PBE-GGA [201]

exchange correlation functional. The Projector augmented wave (PAW) pseudopotential [392, 393] was implemented for the given elements as provided in VASP. To account the van der Waals interaction, we used the DFT-D3 method of Grimme with zero-damping function [395] and for the electronic minimization algorithm, we choose a mixture of the blocked-Davidson and RMM-DIIS algorithms [396, 397]. To approximately treat the strongly correlated d-electrons, we employed the rotationaly invariant DFT+U of Liechtenstein *et al.* [447] with U = 1.80 eV and J = 0.40 eV on d orbitals of Ru atoms (method adapted from [443]). The relaxation was performed with an initial antiferromagnetic (Neél) spin configuration on the Ru sites. A k-mesh sampling of $8\times8\times8$ was chosen for the first Brillouin zone and the structural relaxation was performed until the forces were less than 0.005 eV/Å. The resulting structure is depicted in Fig. 7.5, and has a c-axis lattice constant of 5.7389 Å and in-plane lattice constant of 6.0577 Å.

Ab-initio Phonons: To carry out the phonon calculations, we prepared a super-cell of $2\times2\times2$ and utilized the finite displacement method [140, 400] as implemented in Phonopy [401, 402]. Here, we chose a less dense k-mesh of $4\times4\times4$ due to the reduced Brillouin zone size of supercell. From these calculations, we obtain the phonon eigenvectors $e^{q\nu}_{\alpha n}$ and eigenenergies $\hbar\omega_{q\nu}$. In terms of $q-$space operators, the real-space atomic displacement and momentum operators may be written:

$$\hat{u}_\alpha(\ell n) = \sqrt{\frac{\hbar}{2Nm_n}}\sum_{q\nu}\frac{e^{iq\cdot r_{\ell n}}}{\sqrt{\omega_{q\nu}}}\,(a^\dagger_{-q\nu}+a_{q\nu})\;e^{q\nu}_{\alpha n} = \frac{1}{\sqrt{N}}\sum_{q\nu}e^{iq\cdot r_{\ell n}}\sqrt{\frac{m_{q\nu}}{m_n}}\;e^{q\nu}_{\alpha n}\;\hat{u}_{q\nu} \tag{7.32}$$

$$\hat{p}_\alpha(\ell n) = i\sqrt{\frac{\hbar m_n}{2N}}\sum_{q\nu}\sqrt{\omega_{q\nu}}\;e^{iq\cdot r_{\ell n}}(a^\dagger_{-q\nu}-a_{q\nu})\;e^{q\nu}_{\alpha n} = \frac{1}{\sqrt{N}}\sum_{q\nu}e^{iq\cdot r_{\ell n}}\sqrt{\frac{m_n}{m_{q\nu}}}\;e^{q\nu}_{\alpha n}\;\hat{p}_{q\nu} \tag{7.33}$$

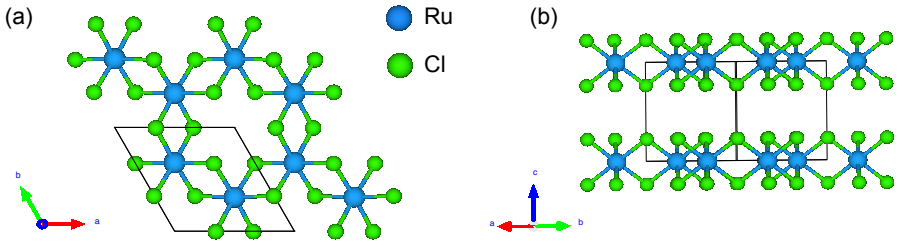

Figure 7.5: Relaxed high-symmetry crystal structure of α-$RuCl_3$ with the $P\bar{3}1m$ symmetry (a): view along c-axis showing honeycomb planes. (b): side view showing AA stacking. Ru and Cl atoms are shown in blue and green colors respectively.

where $\hat{u}_\alpha(\ell n)$ refers to the displacement of the nth atom in the ℓth unit cell, in the $\alpha \in \{x, y, z\}$ direction. $r_{\ell n}$ is the position of such atom, m_n is it's mass, and $e^{q\nu}_{\alpha n} = (e^{-q\nu}_{\alpha n})^*$ are the phonon eigenvectors associated with momentum q and band index ν.

Phonon Gauge Choice: For the acoustic modes, we then make a gauge transformation to ensure a smooth definition of $e^{q\nu}_{\alpha n}$ at finite in-plane $|q|$. The gauge transformation is equivalent to making a q, ν-dependent shift of the origin of the Fourier transform, which results in:

$$e^{q\nu}_{\alpha n} \to e^{q\nu}_{\alpha n} e^{-i\phi_{q\nu}} \tag{7.34}$$

$$\mathcal{A}_{q\nu} \to \mathcal{A}_{q\nu} e^{i\phi_{q\nu}} \tag{7.35}$$

$$\mathcal{L}_{q\nu;q'\nu'} \to \mathcal{L}_{q\nu;q'\nu'} e^{i(\phi_{q\nu}+\phi_{q'\nu'})} \tag{7.36}$$

which retains the feature that $e^{q\nu}_{\alpha n} = (e^{-q\nu}_{\alpha n})^*$ provided $\phi_{q\nu} = -\phi_{-q\nu}$. As depicted in Fig. 7.6, it is not possible for both the real and imaginary parts of the phonon eigenvectors to be continuous at both $q = 0$ and finite q if $e^{q\nu}_{\alpha n} = (e^{-q\nu}_{\alpha n})^*$ is satisfied. For example, there is an obstruction on $\mathrm{Re}[e^{q\nu}_{\alpha n}]$ for the LA and TA modes that can be seen from the requirement that the primary direction of atomic displacement should rotate with the q-vector if it is to remain parallel or transverse to q. A smooth gauge therefore requires $e^{q\nu}_{\alpha n} = -e^{-q\nu}_{\alpha n}$ which excludes a real component to the eigenvector since $\mathrm{Re}[e^{q\nu}_{\alpha n}] = \mathrm{Re}[e^{-q\nu}_{\alpha n}]$. In the conventional gauge choice employed in most *ab-initio* phonon codes, the eigenvectors are defined such that $\mathrm{Im}[e^{q\nu}_{\alpha n}]$ vanishes in the limit $q \to 0$. In this case, it is necessary for the eigenvectors of the TA and LA modes to have branch cuts in $\mathrm{Re}[e^{q\nu}_{\alpha n}]$ at finite q, leading to corresponding branch cuts in the spin-phonon couplings. For these modes, it is more convenient to make a gauge transformation that makes the eigenvectors continuous at all finite q. The eigenvectors of the TA and LA modes can be made continuous everywhere in the 2D Brillouin zone except exactly at $q = 0$ via a transformation that makes $e^{q\nu}_{\alpha n}$ primarily imaginary, such that $\lim_{q\to 0} \mathrm{Re}[e^{q\nu}_{\alpha n}] = 0$. Similarly, the eigenvectors for the ZA modes are made continuous by ensuring that the imaginary component vanishes in the small momentum limit $\lim_{q\to 0} \mathrm{Im}[e^{q\nu}_{\alpha n}] = 0$. The consequences for the spin-phonon couplings is discussed below.

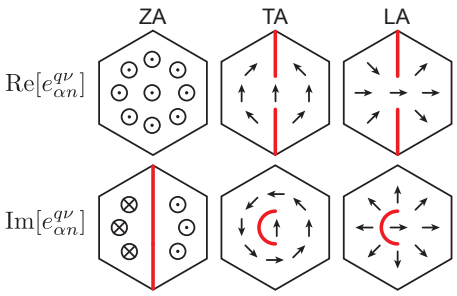

Figure 7.6: Evolution of the real and imaginary parts of the phonon eigenvectors $e^{q\nu}_{\alpha n}$ for ZA, TA, and LA modes in the chosen gauge. Arrows indicate the dominant direction of atomic displacement corresponding to eigenvectors at different q-points in the Brillouin zone. Transforming the ZA eigenvectors to be purely real and the TA and LA eigenvectors to be purely imaginary in the limit $q \to 0$ ensures smooth spin-phonon couplings in the same limit.

Wannier Hamiltonian: In order to estimate the spin-phonon couplings, we first estimate the one-particle contributions to the Hamiltonian in a basis of d-orbital Wannier functions on each Ru site. Formally, the one-particle Hamiltonian includes intersite hopping, intrasite crystal field, and spin-orbit coupling, $\mathcal{H}_{1p} = \mathcal{H}_{hop} + \mathcal{H}_{\rm CF} + \mathcal{H}_{\rm SO}$:

$$\mathcal{H}_{hop} = \sum_{ij\alpha\beta\sigma} t_{ij}^{\alpha\beta} c^{\dagger}_{i,\alpha,\sigma} c_{j,\beta,\sigma} \tag{7.37}$$

$$\mathcal{H}_{\rm CF} = \sum_{i\alpha\beta\sigma} d_{i}^{\alpha\beta} c^{\dagger}_{i,\alpha,\sigma} c_{i,\beta,\sigma} \tag{7.38}$$

$$\mathcal{H}_{\rm SO} = \sum_{i\alpha\beta\sigma\sigma'} \lambda_{\rm Ru} \langle \phi_i^{\alpha}(\sigma) | \mathbf{L}\cdot\mathbf{S} | \phi_i^{\beta}(\sigma') \rangle c^{\dagger}_{i,\alpha,\sigma} c_{i,\beta,\sigma'} \tag{7.39}$$

where $c^{\dagger}_{i,\alpha,\sigma}$ creates an electron at Ru site i, in d-orbital α, with spin σ. Here, $\mathbf{L}$ is the orbital momentum operator (not to be confused with the spin-phonon coupling addressed below). The linear electron-phonon coupling represents the modulation of these terms that is linear in atomic displacements:

$$\mathcal{H}_{\rm el-ph} = \sum_{\alpha\ell n} \mathcal{H}_{\Delta}^{\alpha\ell n} \hat{u}_{\alpha}(\ell n) \tag{7.40}$$

$$\mathcal{H}_{\Delta}^{\alpha\ell n} = \sum_{i\sigma j\sigma'} \Delta_{i\sigma j\sigma'}^{\mu\nu;\ell\alpha n}\ c^{\dagger}_{i,\mu,\sigma} c_{j,\nu,\sigma'} \tag{7.41}$$

The phonon displacement operators $\hat{u}_{\alpha}(\ell n)$ are defined above in Eq. (7.32) and refer to

displacement of atom n, in the unit cell labelled ℓ, in the direction $\alpha \in \{x, y, z\}$. The elements $\Delta_{i\sigma j\sigma'}^{\mu\nu;\ell\alpha n}$ refer to changes in the single-particle matrix elements due to such a displacement, including all the hopping, CF, and SOC terms.

In order to estimate all of the undisplaced one-particle terms, we perform fully relativistic density functional theory calculations on a 2×2×1 supercell of the relaxed $P\bar{3}1m$ structure using FPLO [200], and project [303] the resulting Kohn-Sham bands onto Ru d-orbitals to obtain the electronic Hamiltonian in terms of Ru Wannier functions. For this purpose, we employ the PBE functional[201], and a 6×6×1 k-point mesh.

To estimate the electron-phonon coupling (in real-space), we take a supercell approach similar to that described in Ref. togo2023first. Using the same 2×2×1 supercell, we compute the changes in the single-particle terms between sites in the full supercell induced by small displacements of each atom in the parent primitive cell. For this purpose, we displace each atom along the cartesian x, y, z directions by ±0.02 Å, and perform a DFT calculation on each geometry using FPLO and Wannier projection. The changes in the hoppings are then obtained by taking finite differences of the displaced and undisplaced Hamiltonians in the Wannier basis. Finally, each orbital in the supercell is translated back to the parent cell to identify the corresponding $\Delta_{i\sigma j\sigma'}^{\mu\nu;\ell\alpha n}$ term with respect to the primitive cell. This provides an estimate of the electron-phonon coupling associated with any pair of orbitals, and an atomic displacement within a supercell distance of one of those orbitals. This coupling falls off rapidly with distance between the orbital site and the displaced atom, such that a 2×2×1 supercell suffices to capture the relevant effects within the monolayer.

Spin-Phonon Couplings: Finally, we employ the des Cloizeaux effective Hamiltonian (dCEH) approach outlined in Ref. [437] to obtain the spin-phonon couplings. As noted in the main text, the spin-phonon Hamiltonian is defined as:

$$\mathcal{H}_{\mathrm{sp-ph}} = \sum_{q\nu} \bar{u}_{q\nu}\ \mathcal{A}_{q\nu} + \sum_{q\nu q'\nu'} \bar{u}_{q\nu}\bar{p}_{q'\nu'}\ \mathcal{L}_{q\nu;q'\nu'} \tag{7.42}$$

where $\bar{u}_{q\nu} = (a^{\dagger}_{-q\nu} + a_{q\nu})$ and $\bar{p}_{q\nu} = i(a^{\dagger}_{-q\nu} - a_{q\nu})$, and $a^{\dagger}_{q\nu}$ creates a phonon with momentum q in band ν. Here, the units for the phonon operators have been absorbed into the $\mathcal{A}$ and $\mathcal{L}$ operators, so that the latter have units of energy. The q-space spin and bond operators

are:

$$\mathcal{A}_{q\nu} = \frac{1}{\sqrt{N}} \sum_{ij} \left(\mathbf{S}_i \cdot \mathbb{A}_{ij}^{q\nu} \cdot \mathbf{S}_j \right) \; e^{-iq\cdot(r_i+r_j)/2} \tag{7.43}$$

$$\mathcal{L}_{q\nu;q'\nu'} = \frac{\hbar\omega_{q'\nu'}}{N} \sum_{i} \left(\mathbf{L}_i^{q\nu;q'\nu'} \cdot \mathbf{S}_i \right) \; e^{-i(q+q')\cdot r_i} \tag{7.44}$$

where N is the number of unit cells, and $\mathbf{S}_i$ describe the $j_{1/2}$ moments. To compute $\mathbf{L}$ and $\mathbb{A}$, we implemented a real-space and momentum-space formulation of this approach, which have different merits. For the $\mathcal{A}$ couplings, we emlpoyed the real-space formulation. For each bond of interest, and each elementary real-space displacement $(\alpha\ell n)$, we construct a local many-body model including two Ru sites. The Hamiltonian of the local models takes the form:

$$\mathcal{H}_{ij}(\alpha\ell n) = \mathcal{H}_{1p} + \mathcal{H}_{2p} + \mathcal{H}_{\Delta}^{\alpha\ell n} \; (a^\dagger + a) \; \delta u + \hbar\omega_0 a^\dagger a \tag{7.45}$$

where $\mathcal{H}_{1p}$ and $\mathcal{H}_{\Delta}^{\alpha\ell n}$ are obtained as described above. The operator $a^\dagger$ creates an auxiliary phonon, which is included as a degree of freedom corresponding to a displacement of $\delta u =$ 0.01 Å and energy $\hbar\omega_0 = 1$ meV. The two-particle interactions are taken to be:

$$\mathcal{H}_{2p} = \sum_{i\alpha\beta\delta\gamma} \sum_{\sigma\sigma'} U_{\alpha\beta\gamma\delta} \; c_{i,\alpha,\sigma}^\dagger c_{i,\beta,\sigma'}^\dagger c_{i,\gamma,\sigma'} c_{i,\delta,\sigma} \tag{7.46}$$

where $U_{\alpha\beta\gamma\delta}$ are parameterized by the Slater parameters $F_0^{dd}, F_2^{dd}, F_4^{dd}$, following the spherically symmetric approximation [279]. In terms of these parameters, the Kanamori parameters for the t_{2g} orbitals satisfy:

$$U_{t2g} = F_0^{dd} + \frac{4}{49}(F_2^{dd} + F_4^{dd}) \tag{7.47}$$

$$J_{t2g} = \frac{3}{49} F_2^{dd} + \frac{20}{441} F_4^{dd} \tag{7.48}$$

We use $U_{t2g} = 2.58$ eV, $J_{t2g} = 0.29$ eV, and $F_4^{dd} = (5/8)F_2^{dd}$, which are taken from previous theoretical estimates from constrained RPA [236], and roughly compatible with estimates from optical studies [448–450]. The electron/phonon Hamiltonian $\mathcal{H}$ is then

exactly diagonalized within a basis including $n = 0$ or 1 phonon quanta, and the resulting low-energy states projected onto ideal $j_{1/2}$ states with variable number of phonon quanta as described in Ref. [437]. The low-energy Hamiltonian obtained takes the form:

$$\begin{aligned}\mathcal{H}_{\text{low}} = (\mathbf{S}_i \cdot \mathbb{J}_{ij} \cdot \mathbf{S}_j) + \left(\mathbf{S}_i \cdot \mathbb{A}_{ij}^{\alpha\ell n} \cdot \mathbf{S}_j\right)(a^\dagger + a)\,\delta u \\ + i\hbar\omega_0 \left(\mathbf{G}_i^{\alpha\ell n} \cdot \mathbf{S}_i + \mathbf{G}_j^{\alpha\ell n} \cdot \mathbf{S}_j\right)(a^\dagger - a)\;\delta u + \mathcal{O}(\delta u^2)\end{aligned} \tag{7.49}$$

Here, $\mathbb{A}_{ij}^{\alpha\ell n}$ is the change in the intersite coupling matrix that is linear in atomic displacement. This is obtained by dividing the terms symmetric in $a^\dagger$ and a by δu. It may be noted that the computed $\mathbb{A}_{ij}^{\alpha\ell n}$ matrices are insensitive to the specific choice of δu provided it is sufficiently small to correspond to a linear perturbative regime. We confirmed linear scaling by checking different values of δu in the range of 0.01 Åto 0.05 Å. $\mathbf{G}_i$ is a symmetry allowed coupling of the local spin to the phonon momentum, which is obtained by dividing the terms antisymmetric in $a^\dagger$ and a by $i\hbar\omega_0\delta u$. The origin and scaling of this term is discussed in Ref. [437]. We compute it to be small $\lesssim 10^{-2}$ meV for all bands, and thus neglect it in our analysis.

After repeating the calculation for all elementary displacements in real-space, the q-space operator is then constructed via:

$$\mathbb{A}_{ij}^{qv} = \sum_{\alpha\ell n} \sqrt{\frac{\hbar}{2m_n\omega_{qv}}}\; e_{\alpha n}^{qv}\; \mathbb{A}_{ij}^{\alpha\ell n}\; e^{iq\cdot r_{\ell n}} \tag{7.50}$$

This yields the full q- and band-dependence of the $\mathbb{A}_{ij}^{qv}$ couplings. For a given bond, we included displacements of atoms within 4.0 Å for the crystal field electron-phonon coupling, and 4.64 Å of the bond center for the hopping electron-phonon terms. The electron-phonon couplings fall off rapidly with distance, so this truncation does not introduce significant errors. However, to mitigate small spurious effects associated with the finite distance cutoff, we subtract from each electron-phonon coupling (separately for each direction α) the average value of $\Delta_{i\sigma j\sigma'}^{\mu\nu;\ell\alpha n}$ over the atoms included within the cutoff. This ensures that any uniform translation of all atoms under consideration corresponds to no modification of the

Hamiltonian (which ensures $\lim_{q\to 0} \mathbb{A} = 0$). The advantage of the real-space approach is that a relatively small number of exact diagonalization calculations (3 $\times$ number of bonds $\times$ number of atoms within cutoff) is required to obtain the full q-dependent spin-phonon couplings.

In order to estimate the two-phonon $\mathbf{L}$ couplings, we employed a different approach explicitly in q-space, which requires two ED calculations for each pair of phonon bands and q-point of interest. This formulation is less efficient unless one is interested in a small subset of bands or q-points. However, it has the advantage of mitigating numerical rounding errors accumulated over the summation of the real space spin-phonon couplings in the Fourier transform. For α-$RuCl_3$, the $\mathbf{L}$ couplings are orders of magnitude smaller than the $\mathbb{A}$ couplings, and require two Fourier transforms, making them more susceptible to rounding errors. We start by Fourier transforming the electron-phonon coupling to q-space:

$$\mathcal{H}_{\text{el}-\text{ph}} = \sum_{q\nu} \mathcal{H}_{\Delta}^{q\nu}\ u_{q\nu} = \sum_{q\nu} \mathcal{H}_{\Delta}^{q\nu} a_{q\nu} + \mathcal{H}_{\Delta}^{-q\nu} a_{q\nu}^{\dagger} \tag{7.51}$$

$$\mathcal{H}_{\Delta}^{q\nu} = \sum_{\alpha\ell n} \sqrt{\frac{\hbar}{2Nm_n}} \frac{e^{iq\cdot r_{\ell n}}}{\sqrt{\omega_{q\nu}}}\ e_{\alpha n}^{q\nu}\ \mathcal{H}_{\Delta}^{\alpha\ell n} \tag{7.52}$$

where $\mathcal{H}_{\Delta}^{-q\nu} = (\mathcal{H}_{\Delta}^{q\nu})^{\dagger}$. We then consider one-site models for each pair of phonon bands:

$$\begin{aligned}\mathcal{H}_i(q\nu q'\nu') = \mathcal{H}_{1p} + \mathcal{H}_{2p} + \left[\mathcal{H}_{\Delta}^{-q\nu} a_{-q\nu} + (\mathcal{H}_{\Delta}^{-q\nu})^{\dagger} a_{-q\nu}^{\dagger}\right] \delta u + \left[\mathcal{H}_{\Delta}^{q'\nu'} a_{q'\nu'} + (\mathcal{H}_{\Delta}^{q'\nu'})^{\dagger} a_{q'\nu'}^{\dagger}\right] \delta u' \\ + \hbar\omega_0 \left(a_{q\nu}^{\dagger} a_{q\nu} + a_{q'\nu'}^{\dagger} a_{q'\nu'}\right)\end{aligned} \tag{7.53}$$

The electron/phonon Hamiltonian $\mathcal{H}_i$ is then exactly diagonalized within a basis including $n_{-q\nu}, n_{q\nu'} = 0$ or 1 phonon quanta, and the resulting low-energy states projected onto ideal $j_{1/2}$ states with variable number of phonon quanta. For $j_{1/2}$ moments, the resulting low-energy Hamiltonian is written:

$$\begin{aligned}\mathcal{H}_{\text{low}} = i\hbar\omega_0 \delta u \left(\mathbf{G}_i^{-q\nu} \cdot \mathbf{S}_i\right)\left(a_{-q\nu}^{\dagger} - a_{-q\nu}\right) + i\hbar\omega_0' \delta u' \left(\mathbf{G}_i^{q\nu'} \cdot \mathbf{S}_i\right)\left(a_{q\nu'}^{\dagger} - a_{q\nu'}\right) \\ + \delta u \delta u' \left(\mathbf{B}_{i;++}^{-q\nu;q'\nu'} a_{-q\nu}^{\dagger} a_{q'\nu'}^{\dagger} + \mathbf{B}_{i;+-}^{-q\nu;q'\nu'} a_{-q\nu}^{\dagger} a_{q'\nu'}\right. \\ \left. + \mathbf{B}_{i;-+}^{-q\nu;q'\nu'} a_{-q\nu} a_{q'\nu'}^{\dagger} + \mathbf{B}_{i;--}^{-q\nu;q'\nu'} a_{-q\nu} a_{q'\nu'}\ \right) \cdot \mathbf{S}_i + ...\end{aligned} \tag{7.54}$$

We then approximate the $\mathbf{L}$ coupling relevant for the Hall viscosity via:

$$\mathbf{L}_i^{-q\nu;q\nu'} \approx \frac{i}{4\hbar\omega_0}\left(\mathbf{B}_{i;++}^{q\nu;-q\nu'} + \mathbf{B}_{i;+-}^{-q\nu;-q\nu'} - \mathbf{B}_{i;-+}^{q\nu;q\nu'} - \mathbf{B}_{i;--}^{-q\nu;q\nu'}\right) \tag{7.55}$$

In practice, this requires two ED calculations to evaluate, one with $q' = q$, and one with $q' = -q$. This follows from the fact that $\mathbf{B}_{i;++}^{q\nu;-q\nu'} = -\mathbf{B}_{i;--}^{-q\nu;q\nu'}$ and $\mathbf{B}_{i;+-}^{-q\nu;-q\nu'} = -\mathbf{B}_{i;-+}^{q\nu;q\nu'}$. Results of calculations of $\mathbf{L}$ are given in Fig. 7.7 in 7.3.3.

7.3.3 Numerical Results for L Couplings for Acoustic Phonons

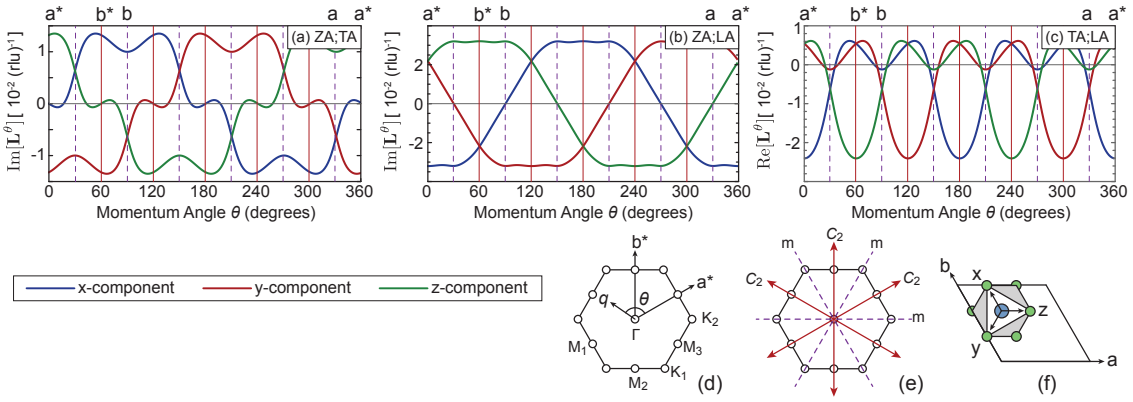

Figure 7.7: Momentum angle dependence of the computed $\mathbf{L}_i^{\theta\nu;\nu'}$ spin-phonon couplings. (a)-(c): (x, y, z) components of $\mathbf{L}_i^{\theta\nu;\nu'}$. The pairs of acoustic modes $\nu;\nu' =$ ZA, TA, and LA are labelled in the upper right of each panel. (d): first Brillouin zone showing the definition of a^* and b^* axes and θ (measured from the a^* axis). (e): orientation, in q-space, of the relevant symmetry operations for the single-site couplings. (f) Single Ru site showing definition of cubic axes. 1 rlu $= 4\pi/(\sqrt{3}a)$, reciprocal lattice unit.

Here, we discuss the computed q-dependence of the $\mathbf{L}$ couplings for the acoustic modes. As noted in the main text, these couplings are sufficiently small in α-$RuCl_3$ as to have negligible consequence on the thermal transport. As demonstrated in 7.3.4, $\mathbf{L} \propto |q|$ for low momentum acoustic phonons. In the limit of small q, for the chosen gauge, the coupling is also equal at both Ru sites in the unit cell. Thus, we write:

$$\mathbf{L}_i^{-q\nu;q\nu'} = \mathbf{L}_{\nu;\nu'}^{\theta}|q| \tag{7.56}$$

Fig. 7.7(a-c) shows the computed momentum-dependence of $\mathbf{L}_{\nu;\nu'}^{\theta}$. This quantity has units

of inverse wavevector. The order of magnitude should be compared with the total angle-dependent reduced Hall viscosity $\overline{\eta}_\theta$ defined in 7.3.5. The contribution to the latter quantity from $\mathcal{A}-\mathcal{A}$ bond-bond correlations reaches several $(\text{rlu})^{-1}$ at maximum. In contrast, the order of magnitude of the contribution from $\mathbf{L}$ interactions is 10^{-3} to 10^{-2} $(\text{rlu})^{-1}$. For this reason, the two-phonon Raman interaction $\mathbf{L}$ does not make a significant contribution to the phonon thermal Hall effect.

To investigate why these couplings are so small in α-$RuCl_3$, we performed calculations employing model electron-phonon couplings and idealized crystal fields, and confirmed that the largest contribution to $\mathbf{L}$ scales like $(\mathcal{H}_{\text{el}-\text{ph}})^2/\lambda_{\text{Ru}}^2$. The $\mathbf{L}$ couplings represent the nuclear Berry curvature associated with the evolution of the spin-orbital composition of the ground-state doublet at each site. The primary mechanism for this evolution is mixing of the $j_{1/2}$ states with $j_{3/2}$ states. The relatively large value of the SOC constant λ_{Ru} reduces this effect in α-$RuCl_3$. Thus, one can expect $\mathbf{L}$ to be suppressed in materials with strong SOC or otherwise energetically separated single-ion states.

The couplings depicted in Fig. 7.7 display the expected symmetries. $\mathbf{L}^\theta_{\text{ZA;TA}}$ is even with respect to C_2 and odd with respect to m. $\mathbf{L}^\theta_{\text{ZA;LA}}$ is odd with respect to C_2 and even with respect to m. $\mathbf{L}^\theta_{\text{TA;LA}}$ is odd with respect to both C_2 and m. Within the chosen gauge, the leading contributions to $\mathbf{L}^\theta_{\text{ZA;TA}}$ and $\mathbf{L}^\theta_{\text{ZA;LA}}$ are imaginary, while $\mathbf{L}^\theta_{\text{TA;LA}}$ is real. The combinations of the symmetries and gauge choice ensure that the $\mathbf{L}$ vectors wind around $q=0$. For each combination of bands, there is a component of $\mathbf{L}$ in the direction $\mathbf{u}_{q\nu}\times\mathbf{p}_{q\nu'}$, which corresponds to a spin-phonon coupling like $\mathbf{S}\cdot(\mathbf{u}\times\mathbf{p})$ [82]. For example, the primary atomic motion for the LA mode is in-plane, parallel to q. The primary motion for the TA mode is in-plane, perpendicular to q. There is a component of $\mathbf{L}^\theta_{\text{TA;LA}}$ that points out of plane (along the cubic $\hat{x}+\hat{y}+\hat{z}$ direction). However, we also find significant contributions to the θ-dependence of $\mathbf{L}$ that depart from this form, which highlight the subtleties of spin-phonon coupling of spin-orbital moments.

7.3.4 Low-q Scaling and Connection to Long-Wavelength Elastic Theory

In this section, we discuss the low-q scaling of various quantities for the acoustic phonons, and the relationship between the reduced Hall viscosity $\overline{\eta}_q$ and the long-wavelength viscosity

tensor. In the long-wavelength limit, the Lagrangian density of an elastic medium is given by:

$$\frac{\mathcal{L}}{V} = \frac{\rho}{2}\sum_{\alpha}\dot{u}_{\alpha} - \frac{1}{2}\sum_{\alpha\beta\delta\gamma} C_{\alpha\beta\delta\gamma}\epsilon_{\alpha\beta}\epsilon_{\delta\gamma} + \sum_{\alpha\beta\delta\gamma}\eta_{\alpha\beta\delta\gamma}\epsilon_{\alpha\beta}\dot{\epsilon}_{\delta\gamma} \tag{7.57}$$

where $\dot{\epsilon} = \partial\epsilon/\partial t$ and ρ is the mass density, $C_{\alpha\beta\delta\gamma}$ is the elasticity tensor, $\eta_{\alpha\beta\delta\gamma}$ is the viscosity tensor, and the strain field is:

$$\epsilon_{\alpha\beta} = \frac{1}{2}\left(\frac{\partial u_{\alpha}}{\partial r_{\beta}} + \frac{\partial u_{\beta}}{\partial r_{\alpha}}\right) \tag{7.58}$$

This form of the Langrangian density can be recovered by taking the long-wavelength limit of equation (7.27). For illustrative purpose, we neglect the q-dependence of the phonon eigenvectors by approximating $\partial e^{q\nu}_{\alpha n}/\partial q = 0$. This leads to the long-wavelength approximation:

$$e^{q\nu}_{\alpha n}\; e^{iq\cdot r_{\ell n}} \approx \sqrt{\frac{m_n N}{\rho V}}\;\varepsilon^{q}_{\alpha\nu}\left[\,1 + i\;\vec{r}_{\ell n}\cdot\vec{q}\,\right] + O(q^2) \tag{7.59}$$

such that the displacement field is:

$$\hat{u}_{\alpha}(\vec{r}) \approx \frac{1}{\sqrt{N}}\sum_{q\nu}\hat{u}_{q\nu}\;\varepsilon^{q}_{\alpha\nu}\left[1 + i\;\vec{r}\cdot\vec{q}\,\right] + O(q^2) \tag{7.60}$$

where the phonon polarization coefficients $\varepsilon^{q}_{\alpha\nu}$ depend on the direction of the q-vector. We have utilized $\lim_{q\to 0} m_{q\nu} = \rho(V/N)$ for the acoustic modes, where V/N is the volume of a unit cell. The gauge choice described in 7.3.2 corresponds to choosing $\varepsilon^{q}_{\alpha\nu}$ to be completely real for the ZA modes and completely imaginary for the TA and LA modes. In particular, for in-plane momenta:

$$\varepsilon^{q}_{x,\mathrm{LA}} = i\frac{\vec{q}\cdot\hat{x}}{|\vec{q}|} \quad , \quad \varepsilon^{q}_{y,\mathrm{LA}} = i\frac{\vec{q}\cdot\hat{y}}{|\vec{q}|} \quad , \quad \varepsilon^{q}_{z,\mathrm{LA}} = 0 \tag{7.61}$$

$$\varepsilon^{q}_{x,\mathrm{TA}} = -i\frac{\vec{q}\cdot\hat{y}}{|\vec{q}|} \quad , \quad \varepsilon^{q}_{y,\mathrm{TA}} = i\frac{\vec{q}\cdot\hat{x}}{|\vec{q}|} \quad , \quad \varepsilon^{q}_{z,\mathrm{TA}} = 0 \tag{7.62}$$

$$\varepsilon^{q}_{x,\mathrm{ZA}} = 0 \quad , \quad \varepsilon^{q}_{y,\mathrm{ZA}} = 0 \quad , \quad \varepsilon^{q}_{z,\mathrm{ZA}} = 1 \tag{7.63}$$

In the limit $q \to 0$, the spin-phonon couplings for the acoustic modes must vanish, since those modes correspond to a uniform translation of the lattice. As a consequence,

$$\lim_{q\to 0} \mathbb{A}_{ij}^{qv} = \sum_{\alpha\ell n} \sqrt{\frac{\hbar N}{2\rho V \omega_{qv}}}\ \mathbb{A}_{ij}^{\alpha\ell n}\ \varepsilon_{\alpha\nu}^{q} = 0 \tag{7.64}$$

which leads to:

$$\mathbb{A}_{ij}^{qv} \approx i \sum_{\alpha\ell n} \sqrt{\frac{\hbar N}{2\rho V \omega_{qv}}}\ \mathbb{A}_{ij}^{\alpha\ell n}\ [\ \varepsilon_{\alpha\nu}^{q}\ (\vec{r}_{\ell n} \cdot \vec{q})\ ] \equiv \mathbb{A}_{ij}^{\theta\nu}\ |q|^{1/2} \tag{7.65}$$

Here, we have assumed that $\omega_q \propto |q|$. This is satisfied for all acoustic modes at sufficiently small $|q|$. As a consequence, $\mathbb{A}_{ij}^{qv} \propto |q|^{1/2}$. A similar argument leads to the following scaling of the couplings and operators:

$$\mathbb{A} \propto |q|^{1/2} \tag{7.66}$$

$$\mathcal{A} \propto |q|^{1/2} \tag{7.67}$$

$$\mathbf{L} \propto |q| \tag{7.68}$$

$$\mathcal{L} \propto |q|^{2} \tag{7.69}$$

$$\overline{\eta} \propto |q| \tag{7.70}$$

The extra factor of q in the $\mathcal{L}$ operators compared to the $\mathbf{L}$ couplings arises from the factor of ω_q in equation (7.44). We have verified that this scaling is satisfied in our numerical results.

In the same long-wavelength limit, the strain field is:

$$\epsilon_{\alpha\beta} = \frac{i}{2}\frac{1}{\sqrt{N}} \sum_{q\nu} u_{q\nu} \left(\varepsilon_{\alpha\nu}^{q} q_\beta + \varepsilon_{\beta\nu}^{q} q_\alpha \right) \tag{7.71}$$

By comparing equations (7.25) and (7.57), we identify:

$$\overline{\eta}_{q}^{\nu\nu'} = \sum_{\alpha\beta\delta\gamma} \frac{\left(\varepsilon_{\alpha\nu}^{-q} q_\beta + \varepsilon_{\beta\nu}^{-q} q_\alpha \right) \left(\varepsilon_{\delta\nu'}^{q} q_\gamma + \varepsilon_{\gamma\nu'}^{q} q_\delta \right)}{8\rho\sqrt{\omega_{q\nu}\omega_{q\nu'}}} \left(\eta_{\alpha\beta\delta\gamma} - \eta_{\delta\gamma\alpha\beta} \right) \tag{7.72}$$

It it then instructive to consider the approximate angular dependence of the reduced Hall viscosity. We define:

$$\eta^H_{\alpha\beta\delta\gamma} = \frac{1}{8}\left(\eta_{\alpha\beta\delta\gamma} + \eta_{\alpha\beta\gamma\delta} + \eta_{\beta\alpha\delta\gamma} + \eta_{\beta\alpha\gamma\delta} - \eta_{\delta\gamma\alpha\beta} - \eta_{\gamma\delta\alpha\beta} - \eta_{\delta\gamma\beta\alpha} - \eta_{\gamma\delta\beta\alpha}\right) \tag{7.73}$$

Then, for $q_x \mid\mid a$, and $q_y \mid\mid b^*$:

$$\begin{aligned}\overline{\eta}_q^{\mathrm{ZA;TA}} = \frac{i}{\rho\sqrt{c_{\mathrm{ZA}}c_{\mathrm{TA}}}|q|^2}\big[&\eta^H_{xzxy}q_x^3 + (\eta^H_{xxxz} + \eta^H_{xzyy} + \eta^H_{yzxy})q_x^2 q_y \\ &+(\eta^H_{xyxz} + \eta^H_{xxyz} + \eta^H_{yzyy})q_x q_y^2 + \eta^H_{xyyz}q_y^3\big]\end{aligned} \tag{7.74}$$

$$\overline{\eta}_q^{\mathrm{ZA;LA}} = \frac{i}{\rho\sqrt{c_{\mathrm{ZA}}c_{\mathrm{LA}}}|q|^2}\left[\eta^H_{xzxx}q_x^3 + \left(2\eta^H_{xzxy} + \eta^H_{yzxx}\right)q_x^2 q_y + \left(2\eta^H_{yzxy} + \eta^H_{xzyy}\right)q_x q_y^2 + \eta^H_{yzyy}q_y^3\right] \tag{7.75}$$

$$\overline{\eta}_q^{\mathrm{TA;LA}} = \frac{1}{\rho\sqrt{c_{\mathrm{TA}}c_{\mathrm{LA}}}|q|}\left[\eta^H_{xyxx}\ q_x^2 + \eta^H_{yyxx}\ q_x q_y + \eta^H_{yyxy}\ q_y^2\right] \tag{7.76}$$

where $c_\nu = \partial\omega_{q\nu}/(\partial q)$ is the speed of sound for each band. From this, we see that the reduced Hall viscosities are particular angle-dependent linear combinations of the long-wavelength Hall viscosities. As discussed in 7.3.5, the numerical estimates of $\overline{\eta}$ follow approximately these forms, but additional momentum-dependence of the phonon eigenvectors $e^{q\nu}_{\alpha n}$ not included equation (7.59) somewhat enriches the angular-dependence of $\overline{\eta}$.

7.3.5 Evaluation of Acoustic Phonon Thermal Conductivities

Effective Hamiltonian: At sufficiently low temperatures, only the acoustic phonon bands contribute significantly to the phonon thermal transport. Focusing on these bands, the effective phonon Hamiltonian may be written:

$$\mathcal{H}_{\mathrm{eff}} = \frac{1}{2}\sum_q \begin{pmatrix}\mathbf{a}_q^\dagger & \mathbf{a}_{-q}\end{pmatrix}\mathcal{H}_q\begin{pmatrix}\mathbf{a}_q \\ \mathbf{a}_{-q}^\dagger\end{pmatrix} \tag{7.77}$$

$$\mathcal{H}_q = \begin{pmatrix}\Lambda_q + \frac{i}{2}\left(\Lambda_q\mathbb{N}_q + \mathbb{N}_q\Lambda_q\right) & \frac{i}{2}\left(\Lambda_q\mathbb{N}_q - \mathbb{N}_q\Lambda_q\right) \\ -\frac{i}{2}\left(\Lambda_q\mathbb{N}_q - \mathbb{N}_q\Lambda_q\right) & \Lambda_q - \frac{i}{2}\left(\Lambda_q\mathbb{N}_q + \mathbb{N}_q\Lambda_q\right)\end{pmatrix} \tag{7.78}$$

where $\mathbf{a}_q$ is a column vector of $a_{q\nu}$ operators for different phonon bands ν, and Λ_q is a

diagonal matrix of phonon energies:

$$\Lambda_q = \hbar \begin{pmatrix} \omega_{q,\mathrm{ZA}} & 0 & 0 \\ 0 & \omega_{q,\mathrm{TA}} & 0 \\ 0 & 0 & \omega_{q,\mathrm{LA}} \end{pmatrix} = \hbar \begin{pmatrix} c_{\mathrm{ZA}} & 0 & 0 \\ 0 & c_{\mathrm{TA}} & 0 \\ 0 & 0 & c_{\mathrm{LA}} \end{pmatrix} |q| \tag{7.79}$$

Here, we have defined $\hbar\omega_{q\nu} = \hbar c_\nu |q|$, where $c_\nu = \partial\omega_{q\nu}/\partial|q|$ is the speed of sound for each band, which we estimate as $\hbar c_{\mathrm{ZA}} = 6.6\,\mathrm{meV/rlu}$, $\hbar c_{\mathrm{TA}} = 11.7\,\mathrm{meV/rlu}$, and $\hbar c_{\mathrm{LA}} = 28.2\,\mathrm{meV/rlu}$ from the *ab-initio* phonon calculations described in 7.3.2. We have ignored the symmetric part of the phonon self-energy in the adiabatic limit because it only results in a very weak renormalization of the phonon velocities. The reduced Hall viscosity matrix is:

$$\mathbb{N}_q = \begin{pmatrix} 0 & \overline{\eta}_q^{\mathrm{ZA;TA}} & \overline{\eta}_q^{\mathrm{ZA;LA}} \\ \overline{\eta}_q^{\mathrm{TA;ZA}} & 0 & \overline{\eta}_q^{\mathrm{TA;LA}} \\ \overline{\eta}_q^{\mathrm{LA;ZA}} & \overline{\eta}_q^{\mathrm{LA;TA}} & 0 \end{pmatrix} = \begin{pmatrix} 0 & \overline{\eta}_\theta^{\mathrm{ZA;TA}} & \overline{\eta}_\theta^{\mathrm{ZA;LA}} \\ \overline{\eta}_\theta^{\mathrm{TA;ZA}} & 0 & \overline{\eta}_\theta^{\mathrm{TA;LA}} \\ \overline{\eta}_\theta^{\mathrm{LA;ZA}} & \overline{\eta}_\theta^{\mathrm{LA;TA}} & 0 \end{pmatrix} |q| \tag{7.80}$$

where:

$$\begin{aligned} \overline{\eta}_q^{\nu\nu'}(T) = & \sum_n \frac{e^{-\beta E_n}}{\mathcal{Z}} \left[\frac{1}{N} \sum_i \langle n | \mathbf{L}_i^{-q\nu;q\nu'} \cdot \mathbf{S}_i | n \rangle \right] \\ & + \frac{i}{2} \sum_{nm} \frac{e^{-\beta E_n} - e^{-\beta E_m}}{\mathcal{Z}} \left[\frac{\langle n|\mathcal{A}_{q\nu}^\dagger|m\rangle\langle m|\mathcal{A}_{q\nu'}|n\rangle - \langle n|\mathcal{A}_{q\nu'}|m\rangle\langle m|\mathcal{A}_{q\nu}^\dagger|n\rangle}{(E_n - E_m)^2} \right] \end{aligned} \tag{7.81}$$

and $\mathcal{A}$ are the linear spin-phonon coupling operators and $\mathbf{L}$ are the vectors defining the two-phonon Raman interaction. $|n\rangle$ and $|m\rangle$ are unperturbed spin states, and $\mathcal{Z}$ is the unperturbed spin partition function. As described in 7.3.4, $\overline{\eta}_q \propto |q|$; we therefore define $\overline{\eta}_q = \overline{\eta}_\theta |q|$, where $\overline{\eta}_\theta$ captures the dependence on in-plane momentum direction. In the chosen gauge, $\overline{\eta}_\theta^{\mathrm{ZA;TA}} = \overline{\eta}_\theta^{\mathrm{TA;ZA}}$ and $\overline{\eta}_\theta^{\mathrm{ZA;LA}} = \overline{\eta}_\theta^{\mathrm{LA;ZA}}$ are purely imaginary, while $\overline{\eta}_\theta^{\mathrm{TA;LA}} = -\overline{\eta}_\theta^{\mathrm{LA;TA}}$ is purely real. The approximate form of the reduced Hall viscosity in terms of the long-wavelength viscosity tensor is described in 7.3.4. We have defined the spin-phonon coupling operators $\mathcal{A}$ and $\mathcal{L}$ to have units of energy for convenience, which leads to $\overline{\eta}_q$ being

unitless, while $\overline{\eta}_\theta$ has units of inverse wavevector.

Comparison with long-wavelength limit: Returning to the long-wavelength approximation in 7.3.4, the approximate form of the reduced Hall viscosities for different field directions can be deduced from symmetry [451]. In the high-field polarized phase for a magnetic field $\mathbf{B} \,||\, a$, the magnetic point group is $2'/m'$, which leads to:

$$\overline{\eta}_\theta^{\mathrm{ZA;TA}} = \frac{i}{\rho\sqrt{c_{\mathrm{ZA}}c_{\mathrm{TA}}}|q|^3}\left[\eta^H_{xzxy}q_x^3 - (\eta^H_{yyyz} + \eta^H_{xzxy} + \eta^H_{yzxx})q_x q_y^2\right] \tag{7.82}$$

$$\overline{\eta}_\theta^{\mathrm{ZA;LA}} = \frac{i}{\rho\sqrt{c_{\mathrm{ZA}}c_{\mathrm{LA}}}|q|^3}\left[\left(2\eta^H_{xzxy} + \eta^H_{yzxx}\right) q_x^2 q_y - \eta^H_{yyyz}q_y^3\right] \tag{7.83}$$

$$\overline{\eta}_\theta^{\mathrm{TA;LA}} = \frac{1}{\rho\sqrt{c_{\mathrm{TA}}c_{\mathrm{LA}}}|q|^2}\left[\eta^H_{xyxx}\ q_x^2 + \eta^H_{yyxy}\ q_y^2\right] \tag{7.84}$$

where $q_x \,||\, a$, and $q_y \,||\, b^*$. This allows a finite κ_{xy}. In contrast, in the zero-field zigzag phase or high-field polarized phase with magnetic field $\mathbf{B} \,||\, b^*$, the magnetic point group is $2/m$, which allows:

$$\overline{\eta}_\theta^{\mathrm{ZA;TA}} = \frac{i}{\rho\sqrt{c_{\mathrm{ZA}}c_{\mathrm{TA}}}|q|^3}\left[(\eta^H_{xxxz} + \eta^H_{xzyy} + \eta^H_{yzxy})q_x^2 q_y - \eta^H_{yzxy}q_y^3\right] \tag{7.85}$$

$$\overline{\eta}_\theta^{\mathrm{ZA;LA}} = \frac{i}{\rho\sqrt{c_{\mathrm{ZA}}c_{\mathrm{LA}}}|q|^3}\left[\left(2\eta^H_{yzxy} + \eta^H_{xzyy}\right) q_x q_y^2 - \eta^H_{xxxz}q_x^3\right] \tag{7.86}$$

$$\overline{\eta}_\theta^{\mathrm{TA;LA}} = \frac{1}{\rho\sqrt{c_{\mathrm{TA}}c_{\mathrm{LA}}}|q|^2}\left[\eta^H_{yyxx}\ q_x q_y\right] \tag{7.87}$$

In our numerical results, we find that $\overline{\eta}_\theta^{\nu;\nu'}$ follow these forms approximately, but also have additional higher order $\sin 4\theta$, $\cos 4\theta$, $\sin 6\theta$, $\cos 6\theta$, etc. contributions resulting from the momentum-dependence of the phonon eigenvectors. Nonetheless, we may estimate the long-wavelength Hall viscosity tensor components by fitting the computed θ-dependence of $\overline{\eta}_\theta^{\nu;\nu'}$. The results are shown in Fig. 7.8. As expected, all components of $\eta^H_{\alpha\beta\delta\gamma}$ vanishes at zero field. For $\mathbf{B} \,||\, a$, all components of the Hall viscosity tensor are enhanced for $B > B_c$, reaching a maximum magnitude in the range $10 - 12$ T. This corresponds to the maximum in $\kappa_{xy}(B)$. For $\mathbf{B} \,||\, b^*$, instead several components of the Hall viscosity tensor change sign at B_c, displaying maximum magnitudes both above and below B_c. Although $\kappa_{xy} = 0$ for this field direction, the Hall viscosity is finite.

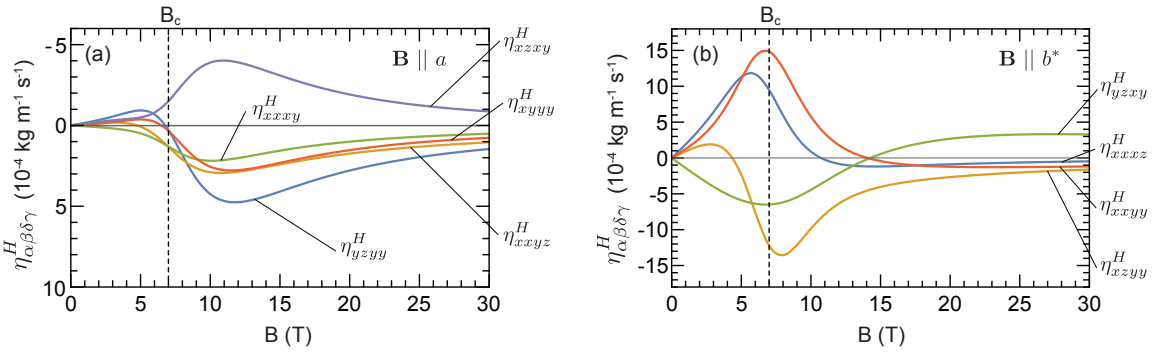

Figure 7.8: Evolution of different components of the long-wavelength Hall viscosity tensor obtained by fitting computed $\overline{\eta}_\theta^{\nu;\nu'}$ to approximate long-wavelength forms for (a): $\mathbf{B} \parallel a$ and (b): $\mathbf{B} \parallel b^*$. Results based on zero-temperature bond correlations computed using exact diagonalization of the spin model discussed in the main text.

Evaluation of κ_{xy}: Following [305, 452, 453], we define a matrix $\mathbf{g}$, which is:

$$\mathbf{g} = \left[\begin{pmatrix} \mathbf{a}_q \\ \mathbf{a}^\dagger_{-q} \end{pmatrix}, \begin{pmatrix} \mathbf{a}^\dagger_q & \mathbf{a}_{-q} \end{pmatrix} \right] = \begin{pmatrix} \mathbb{I}_{N\times N} & 0 \\ 0 & -\mathbb{I}_{N\times N} \end{pmatrix} \tag{7.88}$$

where $\mathbb{I}_{N\times N}$ is the identity matrix of dimension $N = 3$, which is the number of phonon bands. The phonon eigenvectors $\xi^L_{q\nu}$ and $\xi^R_{q\nu}$ are the left and right eigenvectors of $\mathbf{g}\mathcal{H}_q$ with eigenvalues $\lambda_{q\nu} \approx \pm\omega_{q\nu}$, and the 2D phonon Berry curvature is given by:

$$\Omega^{\rm BC}_{q\nu} = -\text{sign}(\lambda_{q\nu})\ \text{Im}\left[\left(\frac{\partial}{\partial q_x}\xi^L_{q\nu}\right) \mathbf{g} \left(\frac{\partial}{\partial q_y}\xi^R_{q\nu}\right) - \left(\frac{\partial}{\partial q_y}\xi^L_{q\nu}\right) \mathbf{g} \left(\frac{\partial}{\partial q_x}\xi^R_{q\nu}\right) \right] \equiv \Omega^\theta_\nu |q| \tag{7.89}$$

This is the Berry curvature of the phonon bands associated with a q-dependent remixing of the phonons induced by the Hall viscosity terms in $\mathcal{H}_q$ [not to be confused with the nuclear Berry curvature defined in equation (7.22), which determines the Hall viscosity]. As discussed in more detail below, we find $\Omega^{\rm BC}_{q\nu} \propto |q|$. Thus, following [341]:

$$\frac{\kappa^{\rm 2D}_{xy}}{T} = -\frac{3\kappa_Q}{2\pi^3} \sum_\nu \int_{\rm BZ(2D)} d\vec{q}\ c_2\left[n_{\rm B}(\hbar\omega_{q\nu})\right] \Omega^{\rm BC}_{q\nu} \tag{7.90}$$

where:

$$c_2(x) = (1+x)\left[\ln\left(\frac{1+x}{x}\right)\right]^2 - [\ln(x)]^2 - 2\mathrm{Li}_2(-x) \tag{7.91}$$

$$n_{\mathrm{B}}(E) = \frac{1}{e^{\frac{E}{k_{\mathrm{B}}T}} - 1} \tag{7.92}$$

where $\kappa_Q = \pi k_{\mathrm{B}}^2/(6\hbar)$ is the quantum of thermal conductivity and Li_2 is the polylog function. For low temperatures, the acoustic phonons at the edge of the Brillouin contribute little to the integral, because they are sufficiently high in energy. As such, the integral can be extended to infinite $|q|$, and written:

$$\frac{\kappa_{xy}^{\mathrm{2D}}}{T} \approx -\frac{3\kappa_Q}{2\pi^3}\sum_\nu \int_0^{2\pi} \Omega_\nu^\theta \, d\theta \int_0^\infty |q|^2 \, c_2(f(\hbar c_\nu |q|)) \, d|q| \tag{7.93}$$

using $\Omega_{q\nu}^{\mathrm{BC}} = \Omega_\nu^\theta |q|$ and $\hbar\omega_{q\nu} = \hbar c_\nu |q|$. Introducing $x = \frac{\hbar c_\nu |q|}{k_{\mathrm{B}}T}$ gives:

$$\frac{\kappa_{xy}^{\mathrm{2D}}}{T} \approx -\frac{3\kappa_Q}{2\pi^3}\sum_\nu \left(\frac{k_{\mathrm{B}}T}{\hbar c_\nu}\right)^3 \int_0^{2\pi} \Omega_\nu^\theta \, d\theta \int_0^\infty x^2 \, c_2\left[\frac{1}{e^x - 1}\right] \, dx \tag{7.94}$$

$$\approx -2.00655 \, \kappa_Q \sum_\nu \left(\frac{k_{\mathrm{B}}T}{\hbar c_\nu}\right)^3 \int_0^{2\pi} \Omega_\nu^\theta \, d\theta \tag{7.95}$$

Conditions for finite κ_{xy}: It is finally instructive to consider the restrictions on $\overline{\eta}_q$ that allow for a finite κ_{xy}. To do so, we consider the case where the three phonon bands are non-degenerate, and treat the effects of the Hall viscosity perturbatively. In particular,

$$\mathcal{H}_q^{(0)} = \begin{pmatrix} \Lambda_q & 0 \\ 0 & \Lambda_q \end{pmatrix} \quad , \quad \mathcal{H}_q^{(1)} = \begin{pmatrix} \frac{i}{2}\left(\Lambda_q \mathbb{N}_q + \mathbb{N}_q \Lambda_q\right) & \frac{i}{2}\left(\Lambda_q \mathbb{N}_q - \mathbb{N}_q \Lambda_q\right) \\ -\frac{i}{2}\left(\Lambda_q \mathbb{N}_q - \mathbb{N}_q \Lambda_q\right) & -\frac{i}{2}\left(\Lambda_q \mathbb{N}_q + \mathbb{N}_q \Lambda_q\right) \end{pmatrix} \tag{7.96}$$

We then consider the perturbative expansion of the eigenvectors of $\mathbf{g}\mathcal{H}_q$:

$$\xi_{q\nu}^R \approx \xi_{q\nu}^{R,0} + \sum_{\nu' \neq \nu} \xi_{q\nu'}^{R,0} \frac{\xi_{q\nu'}^{L,0} \mathcal{H}_q^{(1)} \xi_{q\nu}^{R,0}}{\lambda_{q\nu}^0 - \lambda_{q\nu'}^0} + \sum_{\nu'', \nu' \neq \nu} \xi_{q\nu'}^{R,0} \frac{\xi_{q\nu'}^{L,0} \mathcal{H}_q^{(1)} \xi_{q\nu''}^{R,0} \xi_{q\nu''}^{L,0} \mathcal{H}_q^{(1)} \xi_{q\nu}^{R,0}}{(\lambda_{q\nu}^0 - \lambda_{q\nu''}^0)(\lambda_{q\nu}^0 - \lambda_{q\nu'}^0)} + \ldots \tag{7.97}$$

and finally compute the phonon Berry curvature $\Omega_{q\nu}^{\mathrm{BC}}$ using equation (7.89). We find the leading contribution to scale linearly with $|q|$, such that $\Omega_{q\nu}^{\mathrm{BC}} = \Omega_\nu^\theta |q|$. The latter quantity

is:

$$\Omega_\nu^\theta = \left[f_{1\nu}\ \overline{\eta}_\theta^{\mathrm{ZA;TA}} \overline{\eta}_\theta^{\mathrm{TA;LA}} \frac{\partial \overline{\eta}_\theta^{\mathrm{ZA;LA}}}{\partial \theta} + f_{2\nu}\ \overline{\eta}_\theta^{\mathrm{ZA;TA}} \frac{\partial \overline{\eta}_\theta^{\mathrm{TA;LA}}}{\partial \theta} \overline{\eta}_\theta^{\mathrm{ZA;LA}} + f_{3\nu}\ \frac{\partial \overline{\eta}_\theta^{\mathrm{ZA;TA}}}{\partial \theta} \overline{\eta}_\theta^{\mathrm{TA;LA}} \overline{\eta}_\theta^{\mathrm{ZA;LA}} \right] \tag{7.98}$$

where $f_{1\nu}$, $f_{2\nu}$, and $f_{3\nu}$ are real band-dependent functions that depend only on the relative sound velocities of the bands (not on the θ or q). There are several important observations underlying this expression. First, as noted above, $\Omega_{q\nu}^{\mathrm{BC}} \propto |q|$. This agrees with our numerical, which confirms the perturbative regime is appropriate. Second, we see that a finite $\Omega_{q\nu}^{\mathrm{BC}}$ requires all three elements of the Hall viscosity matrix $\mathbb{N}_q$ to be finite. That is, the coupling of any two bands is not sufficient to induce a finite Berry curvature in any of the bands in the 2D limit. This is true because a smooth gauge exists at low q (except at $q = 0$) such that all $\overline{\eta}_q$ are either completely real or completely imaginary. At first order in $\mathcal{H}_q^{(1)}$, the complex phases of the phonon eigenvectors therefore do not wind as a function of θ. Instead, the Berry curvature arises from the combination of the first and second order terms in equation (7.97). For example, the ZA phonon band may acquire a finite mixture of the TA mode due to the interband Hall viscosity matrix elements $i\ \mathbb{N}_q$. The first order contribution to the mixing corresponds to $i\overline{\eta}_\theta^{\mathrm{ZA;TA}}$, which is real. The second order contribution corresponds to $(i\overline{\eta}_\theta^{\mathrm{ZA;LA}})(i\overline{\eta}_\theta^{\mathrm{LA;TA}})$, which is imaginary. Thus the phase of the complex coefficient representing the small mixing of the TA mode into the ZA eigenvector can wind around the Brillouin zone provided the first and second order terms have complementary momentum-angle dependence.

As can be seen above, $\kappa_{xy}^{\mathrm{ph}} \propto \int \Omega_\nu^\theta \propto \overline{\eta}^3$, which scales roughly as $\overline{\eta}^3 \sim \sum_n (\langle n|\mathcal{A}|g\rangle/\Delta_n)^6$, where Δ_n is the energy of the nth excited state of the spin system. For this reason, accurate estimates of the magnitude of $\kappa_{xy}^{\mathrm{ph}}$ require precise modeling of the evolution of the spin excitation energies.

Evaluation of κ_{xx}: In the 2D limit, the longitudinal conductivity is given by:

$$\kappa_{\alpha\alpha}^{\mathrm{2D}} = \sum_\nu \int_{\mathrm{BZ(2D)}} d\vec{q}\ \frac{\hbar^2 \omega_{q\nu}^2}{k_B T^2} \frac{e^{\frac{\hbar\omega_{q\nu}}{k_B T}}}{\left(e^{\frac{\hbar\omega_{q\nu}}{k_B T}} - 1\right)^2} (\nabla_q \omega_{q\nu} \cdot \hat{\alpha})^2 \tau_{q\nu} \tag{7.99}$$

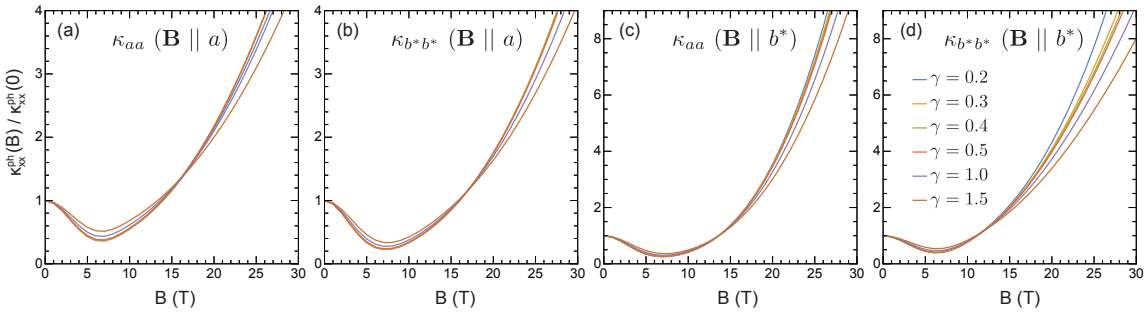

Figure 7.9: Comparison of computed longitudinal phonon thermal conductivity as a function of Lorentzian broadening (γ in meV) of the poles of the dynamical bond correlation functions obtained from exact diagonalization. $\kappa_{xx}^{\rm ph}(B)/\kappa_{xx}(0)$ is relatively insensitive to choice of broadening. $\gamma = 0.5\,$meV is employed in the main text.

where $\tau_{q\nu}$ is the phonon lifetime. Introducing $x = \frac{\hbar c_\nu |q|}{k_{\rm B} T}$:

$$\kappa_{\alpha\alpha}^{\rm 2D} = \frac{1}{(2\pi)^2} \frac{k_B^2 T}{\hbar^2} \sum_\nu \int_0^\infty dx \frac{x^2 e^x}{(e^x - 1)^2} \int_0^{2\pi} d\theta (\hat{q} \cdot \hat{\alpha})^2 \, (\hbar c_\nu |q| \tau_{q\nu}) \tag{7.100}$$

$$= \frac{k_B^2 T}{12 \hbar^2} \sum_\nu \int_0^{2\pi} d\theta \; (\hat{q} \cdot \hat{\alpha})^2 \; \tau_\nu^\theta \tag{7.101}$$

where $\tau_\nu^\theta \equiv \hbar c_\nu |q| \tau_{q\nu}$ is the angle-dependent relative phonon lifetime. It is approximately given by the imaginary part of the diagonal components of the phonon self-energy evaluated at the bare phonon frequency:

$$\tau_\nu^\theta = \frac{\hbar c_\nu |q|}{{\rm Im}[\Pi_q^{\nu\nu}(\omega_{q\nu})]} \tag{7.102}$$

which is independent of $|q|$. Here, we assume that spin-phonon scattering is the most significant mechanism affecting the thermal transport lifetime at low temperatures. Additional contributions to the scattering rate from impurities and phonon anharmonicity may be relevant for quantitative calculations. Finally, we comment on the numerical evaluation of ${\rm Im}[\Pi_q^{\nu\nu}(\omega_{q\nu})]$ using exact diagonalization (ED) of the spin model discussed in the main text. From ED, we obtain $\Pi_q^{\nu\nu}(\omega_{q\nu})$ as discrete poles, which are Lorentzian broadened to extrapolate to low frequency:

$${\rm Im}[\Pi_q^{\nu\nu}(\omega)] \approx \sum_n \frac{1}{\pi} \frac{\gamma A_n}{(E_n - \omega)^2 + \gamma^2} \tag{7.103}$$

where γ is the broadening, and A_n is the amplitude of the correlation function for excited state $|n\rangle$. The discrete poles contributing to this function remain above $E_n = 1\,\mathrm{meV}$ even at B_c due to finite size effects, which is above the energies of the phonons with appreciable population at low temperatures. The broadening results in an approximately linear dependence of the low-frequency $\mathrm{Im}[\Pi_q^{\nu\nu}(\omega_{q\nu})]$ on γ. As a consequence, absolute magnitudes of the spin-phonon scattering rate cannot be resolved, but relative values remain robust. This is demonstrated in Fig. 7.9, where we plot $\kappa_{xx}^{\mathrm{ph}}(B)/\kappa_{xx}^{\mathrm{ph}}(0)$ derived from different choices of broadening. The qualitative field dependence is preserved over a wide range of choices of γ.

Chapter 8

Selected Co-authored Projects

8.1 Characterization of Pyrochlore Compound $Ba_3Tm_2Zn_5O_{11}$

*This project is published as "Synthesis and characterization of the novel breathing pyrochlore compound $Ba_3Tm_2Zn_5O_{11}$ in Physical Review Materials, **8**, 123401 (2024) [454].*

In this project, I helped our experimental colleagues to understand the nature of low energy excitations in $Ba_3Tm_2Zn_5O_{11}$ compound, a material which falls under the family of breathing pyrochlore. My contribution was to perform an *ab initio* phonon calculation to rule out the phononic nature of low energy modes that were observed in inelastic neutron scattering experiment. I also analyzed the data, and wrote the manuscript in collaboration with the other coauthors.

8.2 Pressure-dependent Magnetism in Li_2RhO_3

*This project is published as "Pressure-dependent magnetism of the Kitaev candidate Li_2RhO_3 in npj Quantum Materials, **10**, 9,(2025) [455].*

For this project, I analyzed how external pressure affect the magnetic interactions in Li_2RhO_3 compound. To better understand the pressure dependence of the measured magnetization, I comprehensively investigated the evolution of magnetic couplings using dCEH approach at different pressure. In addition, I also discussed and analyzed the experimental and theoretical results, and contributed to writing the manuscript with coauthors.

Chapter 9

Conclusions and Future Outlook

In this thesis, we have developed a comprehensive theoretical framework to compute spin-phonon interactions in transition metal-insulators. The spin-phonon Hamiltonian thus derived contains terms that couple spin degrees of freedom with atomic displacement and atomic momenta. Such treatment allows us to estimate generic spin phonon couplings within an explicitly many-body framework, including both static and dynamic phonon terms. Understanding dynamical contributions, for example the "two phonon Raman" contribution ($\mathbf{S} \cdot \mathbf{u} \times \mathbf{p}$), is crucial because they are believed to be important for the phonon thermal Hall effect in magnetic insulators. This approach is benchmarked by computing temperature and frequency dependent optical phonons lifetimes of layered honeycomb compound $MnPSe_3$, for which we find excellent agreement with experiment.

The developed formalism is subsequently used to estimate the magnitude and sign of phonon thermal Hall conductivity κ_{xy}^{ph} in α-$RuCl_3$. Previous studies had identified multiple possible heat carriers in this material, such as phonons, magnons, and spinons. In our work, we focused on examining whether phonons—the simplest among them—could explain the observed thermal Hall effect via spin–orbit–driven spin–phonon coupling. Understanding this phenomenon is of fundamental importance, as the quantized thermal Hall effect reported in controversial experiments had been interpreted as a "smoking-gun" signature of Majorana fermions. Our study shows that the strong spin-orbit coupling induces phonon chirality giving rise to a finite Berry curvature, which in turn leads to the phonon thermal Hall effect. This proposed mechanism is consistent with observed experimental features

including the field-dependence, sign, and order of magnitude.

We have also examined the magnetic response of magnetic insulators under structural disorder and distortion. For this purpose, we first considered structurally disordered honeycomb cobalt compound $Na_2Co_2TeO_6$, which has been identified as Heisenberg-Kitaev quantum magnet. To understand the observed anisotropic magnetic excitations, we developed a microscopic model by considering all unique Na occupancies. We demonstrated that the couplings and g- tensors are strongly affected by the disorder in this compound owing to its relatively weak spin-orbit interaction. This results in a rich spectra of magnetic excitations with remarkably large number of modes in this compound.

In order to examine the role of the structural distortion on the magnetic response, we chose α-$RuCl_3$ as a candidate material. The layer dependent magnetic anisotropy observed in atomically thin samples of this compound was rationalized by investigating the trends in the magnetic couplings via ab-initio calculations for different distorted structures. We demonstrated that in-plane Cl distortion can lead to magnetic anisotropy reversal in the monolayer by suppressing off-diagonal exchange terms in the spin Hamiltonian. By constructing distortion-dependent magnetic phase diagram, we illustrated that ground state of monolayer α-$RuCl_3$ lies in the vicinity of several competing spin orders, and has larger Kitaev interaction compared to its bulk counterpart. These features might be important to realize quantum spin liquid phase for out of plane fields in α-$RuCl_3$.

In addition, by considering van der Waals Ising antiferromagnet $FePS_3$ as a representative materials, we underscored the importance of spin-orbit coupling even in $3d$-transition metal compounds. In most of the literature that studied bulk magnetic excitations of this compound, it was treated as a spin $S = 2$ system, owing to the four unpaired electrons at each high-spin d^6 Fe^{2+} site. By explicitly incorporating the unquenched local orbital degrees of freedom, we demonstrated that local moments are rich mixtures of spin-orbit entangled $J_{\text{eff}} = 1$, 2, and 3 states. Due to the relatively weak spin-orbit interaction compared to crystalline electric field and intersite exchange, there is a strong mixing and spectral overlap of magnon and spin-orbit excitons to form hybrid excitations. Despite the inherent complexity of the low energy model, we illustrated that local many-body based approaches can derive such model inexpensively.

To conclude, we investigated several magnetic insulators in the context of spin-phonon coupling, thermal Hall effect, the nature and sensitivity of magnetic response to disorder and distortion, and the importance of spin-orbit interaction on the ground state of local spin-orbital single-ion states. As a result, we have developed the microscopic mechanisms and necessary tools that are required to address and understand several relevant phenomena in magnetic insulators.

This framework can be naturally extended to address several key experimental observations of magnetic insulators and related materials. For example, we noted that the "two phonon Raman" contribution is negligible for the thermal Hall effect, in the case of α-$RuCl_3$ due to the large splitting of local single-ion states. This contribution can be important in $3d$-transtion metal compounds due to relatively weak spin-orbit interaction. As a consequence, contribution arising from "two phonon Raman" process can be significant for the thermal Hall of $3d$-layered materials like VI_3. This mechanism is also considered important in spin-relaxation, chiral phonons, and chirality selective magnon-phonon hybridization.

In our work, we have studied the evolution of phonon thermal Hall conductivity κ_{xy}^{ph} as a function of field. Due to finite size effect in exact diagonalization method, we have adopted the long wavelength limit ($q \to 0$) to compute various quantities for acoustic phonons. Another possible extension could be the study of field and temperature dependent response of κ_{xy}^{ph} retaining the full q-dependence. This can, in principle, be evaluated by estimating temperature-dependent bond-bond correlation functions, derived from solving classical Landau-Lifshitz equation of motion.

An interesting, though ambitious, direction for future work would be to consider contributions from extrinsic skew-scattering and various intrinsic effects to obtain a comprehensive quantitative theory of thermal Hall effect. Also, the recent reports of thermal Hall effect in black phosphorus and a variety of other non-magnetic insulators warrants a closer examination due to possibly new underlying mechanism. A natural extension of spin-phonon coupling would be to look at the relevant interactions such as exciton-magnon, magnon-magnon, and exciton-phonon interactions.

Bibliography

[1] S. Blundell, *Magnetism in condensed matter* (OUP Oxford, 2001).

[2] D. C. Mattis, *Theory Of magnetism made simple: An introduction to physical concepts and to some useful mathematical methods* (World Scientific Publishing Company, 2006).

[3] K. Yosida, *Theory of magnetism.: Edition en anglais*, Vol. 122 (Springer Science & Business Media, 1996).

[4] R. P. Feynman, R. B. Leighton, and M. Sands, *The Feynman Lectures on Physics, Vol. II: Mainly Electromagnetism and Matter* (Addison-Wesley Publishing Company, Inc., Reading, Massachusetts; Palo Alto; London, 1964).

[5] C. Timm, *Theory of Magnetism* (Technische Univ. Dresden, Institute for Theoretical Physics, Dresden, Germany, 2011).

[6] A. Tsirlin, *Theory of Magnetism* (Felix Bloch Institute, University of Augsburg, Germany, 2020).

[7] W. Gerlach and O. Stern, in *Walther Gerlach (1889–1979) Eine Auswahl aus seinen Schriften und Briefen* (Springer, 1989) pp. 26–29.

[8] G. E. Uhlenbeck and S. Goudsmit, Die Naturwissenschaften **13**, 953 (1925).

[9] P. A. M. Dirac, Proceedings of the Royal Society of London. Series A, Containing Papers of a Mathematical and Physical Character **117**, 610 (1928).

[10] S. N. Bose, Zeitschrift für Physik **26**, 178 (1924).

[11] E. Fermi, Zeitschrift für Physik **36**, 902 (1926).

[12] P. A. M. Dirac, Proceedings of the Royal Society of London. Series A, Containing Papers of a Mathematical and Physical Character **112**, 661 (1926).

[13] W. Pauli, Zeitschrift für Physik **31**, 765 (1925).

[14] J. C. Slater, Physical Review **34**, 1293 (1929).

[15] W. Heisenberg, Zeitschrift für Physik **49**, 619 (1928).

[16] P. A. M. Dirac, Proceedings of the Royal Society of London. Series A, Containing Papers of a Mathematical and Physical Character **123**, 714 (1929).

[17] W. Heitler and F. London, Zeitschrift für Physik **44**, 455 (1927).

[18] F. Bloch, Zeitschrift für Physik **61**, 206 (1930).

[19] W. Pauli Jr, Zeitschrift für Physik **41**, 81 (1927).

[20] L. Landau, Zeitschrift für Physik **64**, 629 (1930).

[21] W. De Haas and P. Van Alphen, in *Proc. Netherlands Roy. Acad. Sci*, Vol. 33 (1930) p. 170.

[22] J. C. Slater, Physical Review **49**, 537 (1936).

[23] J. C. Slater, Physical Review **49**, 931 (1936).

[24] J. C. Slater, Physical Review **52**, 198 (1937).

[25] E. C. Stoner, Proceedings of the Royal Society of London. Series A. Mathematical and Physical Sciences **165**, 372 (1938).

[26] E. C. Stoner, Proceedings of the Royal Society of London. Series A. Mathematical and Physical Sciences **169**, 339 (1939).

[27] J. H. de Boer and E. J. Verwey, Proceedings of the Physical Society **49**, 59 (1937).

[28] N. F. Mott, Proceedings of the Physical Society. Section A **62**, 416 (1949).

[29] J. Hubbard, Proceedings of the Royal Society of London. Series A. Mathematical and Physical Sciences **276**, 238 (1963).

[30] H. Kramers, Physica **1**, 182 (1934).

[31] P. W. Anderson, Physical Review **79**, 350 (1950).

[32] J. B. Goodenough, Physical Review **100**, 564 (1955).

[33] J. B. Goodenough, Journal of Physics and chemistry of Solids **6**, 287 (1958).

[34] J. Kanamori, Journal of Physics and chemistry of Solids **10**, 87 (1959).

[35] L. Néel, Journal de Physique et le Radium **3**, 160 (1932).

[36] P. Anderson, Journal of Applied Physics **50**, 7281 (1979).

[37] H. Bethe, Zeitschrift für Physik **71**, 205 (1931).

[38] L. Hulthén, *Über das austauschproblem eines kristalles*, Ph.D. thesis, Almqvist & Wiksell (1938).

[39] C. G. Shull, W. Strauser, and E. Wollan, Physical Review **83**, 333 (1951).

[40] P. W. Anderson, Physical Review **86**, 694 (1952).

[41] P. W. Anderson, Materials Research Bulletin **8**, 153 (1973).

[42] D. I. Khomskii, *Transition metal compounds* (Cambridge University Press, 2014).

[43] S. M. Winter, Journal of Physics: Materials **5**, 045003 (2022).

[44] I. Dzyaloshinsky, Journal of physics and chemistry of solids **4**, 241 (1958).

[45] T. Moriya, Physical Review **120**, 91 (1960).

[46] P. W. Anderson, Physical Review **115**, 2 (1959).

[47] D. C. Tsui, H. L. Stormer, and A. C. Gossard, Physical Review Letters **48**, 1559 (1982).

[48] R. B. Laughlin, Physical Review Letters **50**, 1395 (1983).

[49] C. Broholm, R. J. Cava, S. Kivelson, D. Nocera, M. Norman, and T. Senthil, Science **367**, eaay0668 (2020).

[50] Y. Zhou, K. Kanoda, and T.-K. Ng, Reviews of Modern Physics **89**, 025003 (2017).

[51] L. Savary and L. Balents, Reports on Progress in Physics **80**, 016502 (2017).

[52] L. Balents, nature **464**, 199 (2010).

[53] T. Lancaster, Contemporary Physics **64**, 127 (2023).

[54] A. Kitaev, Annals of Physics **321**, 2 (2006).

[55] S. Trebst and C. Hickey, Physics Reports **950**, 1 (2022).

[56] S. M. Winter, A. A. Tsirlin, M. Daghofer, J. van den Brink, Y. Singh, P. Gegenwart, and R. Valentí, Journal of Physics: Condensed Matter **29**, 493002 (2017).

[57] Y. Matsuda, T. Shibauchi, and H.-Y. Kee, Reviews of Modern Physics **97**, 045003 (2025).

[58] H. Takagi, T. Takayama, G. Jackeli, G. Khaliullin, and S. E. Nagler, Nature Reviews Physics **1**, 264 (2019).

[59] M. Hermele, T. Senthil, M. Fisher, P. A. Lee, N. Nagaosa, and X.-G. Wen, arXiv preprint cond-mat/0404751 (2004).

[60] A. Y. Kitaev, Annals of Physics **303**, 2 (2003).

[61] Y.-C. He, D. Sheng, and Y. Chen, Physical Review Letters **112**, 137202 (2014).

[62] Z. Yan, R. Samajdar, Y.-C. Wang, S. Sachdev, and Z. Y. Meng, Nature Communications **13**, 5799 (2022).

[63] G. Jackeli and G. Khaliullin, Physical Review Letters **102**, 017205 (2009).

[64] J. Chaloupka, G. Jackeli, and G. Khaliullin, Physical Review Letters **105**, 027204 (2010).

[65] A. Banerjee, C. Bridges, J.-Q. Yan, A. Aczel, L. Li, M. Stone, G. Granroth, M. Lumsden, Y. Yiu, J. Knolle, *et al.*, Nature materials **15**, 733 (2016).

[66] A. Banerjee, J. Yan, J. Knolle, C. A. Bridges, M. B. Stone, M. D. Lumsden, D. G. Mandrus, D. A. Tennant, R. Moessner, and S. E. Nagler, Science **356**, 1055 (2017).

[67] Y. Singh and P. Gegenwart, Physical Review B—Condensed Matter and Materials Physics **82**, 064412 (2010).

[68] Y. Singh, S. Manni, J. Reuther, T. Berlijn, R. Thomale, W. Ku, S. Trebst, and P. Gegenwart, Physical Review Letters **108**, 127203 (2012).

[69] A. Glamazda, P. Lemmens, S.-H. Do, Y. Choi, and K.-Y. Choi, Nature Communications **7**, 12286 (2016).

[70] T. Amundsen, Physics Letters A **29**, 209 (1969).

[71] S. Lipson, Proceedings of the Royal Society of London. Series A. Mathematical and Physical Sciences **293**, 275 (1966).

[72] D. Lovett and D. Ballentyne, British Journal of Applied Physics **18**, 1399 (1967).

[73] X.-T. Zhang, Y. H. Gao, and G. Chen, Physics Reports **1070**, 1 (2024).

[74] C. Strohm, G. Rikken, and P. Wyder, Physical Review Letters **95**, 155901 (2005).

[75] K. Sugii, M. Shimozawa, D. Watanabe, Y. Suzuki, M. Halim, M. Kimata, Y. Matsumoto, S. Nakatsuji, and M. Yamashita, Physical Review Letters **118**, 145902 (2017).

[76] M. Akazawa, M. Shimozawa, S. Kittaka, T. Sakakibara, R. Okuma, Z. Hiroi, H.-Y. Lee, N. Kawashima, J. H. Han, and M. Yamashita, Physical Review X **10**, 041059 (2020).

[77] Y. Hirokane, Y. Nii, Y. Tomioka, and Y. Onose, Physical Review B **99**, 134419 (2019).

[78] X. Li, B. Fauqué, Z. Zhu, and K. Behnia, Physical Review Letters **124**, 105901 (2020).

[79] G. Grissonnanche, S. Thériault, A. Gourgout, M.-E. Boulanger, E. Lefrançois, A. Ataei, F. Laliberté, M. Dion, J.-S. Zhou, S. Pyon, *et al.*, Nature Physics **16**, 1108 (2020).

[80] É. Lefrançois, G. Grissonnanche, J. Baglo, P. Lampen-Kelley, J.-Q. Yan, C. Balz, D. Mandrus, S. Nagler, S. Kim, Y.-J. Kim, *et al.*, Physical Review X **12**, 021025 (2022).

[81] X. Li, Y. Machida, A. Subedi, Z. Zhu, L. Li, and K. Behnia, Nature Communications **14**, 1027 (2023).

[82] L. Sheng, D. Sheng, and C. Ting, Physical Review Letters **96**, 155901 (2006).

[83] Y. Kagan and L. Maksimov, Physical Review Letters **100**, 145902 (2008).

[84] L. Zhang, J. Ren, J.-S. Wang, and B. Li, Physical Review Letters **105**, 225901 (2010).

[85] T. Qin, J. Zhou, and J. Shi, Physical Review B **86**, 104305 (2012).

[86] X. Zhang, Y. Zhang, S. Okamoto, and D. Xiao, Physical Review Letters **123**, 167202 (2019).

[87] L. Mangeolle, L. Balents, and L. Savary, Physical Review X **12**, 041031 (2022).

[88] L. Mangeolle, L. Balents, and L. Savary, Physical Review B **106**, 245139 (2022).

[89] J.-Y. Chen, S. A. Kivelson, and X.-Q. Sun, Physical Review Letters **124**, 167601 (2020).

[90] B. Flebus and A. MacDonald, Physical Review B **105**, L220301 (2022).

[91] H. Guo, D. G. Joshi, and S. Sachdev, Proceedings of the National Academy of Sciences **119**, e2215141119 (2022).

[92] H. Yang, C. Kim, Y. Choi, J. H. Lee, G. Lin, J. Ma, M. Kratochvílová, P. Proschek, E.-G. Moon, K. H. Lee, *et al.*, Physical Review B **106**, L081116 (2022).

[93] H. Doki, M. Akazawa, H.-Y. Lee, J. H. Han, K. Sugii, M. Shimozawa, N. Kawashima, M. Oda, H. Yoshida, and M. Yamashita, Physical Review Letters **121**, 097203 (2018).

[94] M. Hirschberger, J. W. Krizan, R. Cava, and N. Ong, Science **348**, 106 (2015).

[95] M. Hirschberger, P. Czajka, S. Koohpayeh, W. Wang, and N. P. Ong, arXiv preprint arXiv:1903.00595 (2019).

[96] T. Ideue, T. Kurumaji, S. Ishiwata, and Y. Tokura, Nature Materials **16**, 797 (2017).

[97] H. Zhang, C. Xu, C. Carnahan, M. Sretenovic, N. Suri, D. Xiao, and X. Ke, Physical Review Letters **127**, 247202 (2021).

[98] L. Chen, M.-E. Boulanger, Z.-C. Wang, F. Tafti, and L. Taillefer, Proceedings of the National Academy of Sciences **119**, e2208016119 (2022).

[99] H. Katsura, N. Nagaosa, and P. A. Lee, Physical Review Letters **104**, 066403 (2010).

[100] T. Qin, Q. Niu, and J. Shi, Physical Review Letters **107**, 236601 (2011).

[101] H. Lee, J. H. Han, and P. A. Lee, Physical Review B **91**, 125413 (2015).

[102] J. H. Han and H. Lee, Journal of the Physical Society of Japan **86**, 011007 (2017).

[103] R. Samajdar, S. Chatterjee, S. Sachdev, and M. S. Scheurer, Physical Review B **99**, 165126 (2019).

[104] Y. Teng, Y. Zhang, R. Samajdar, M. S. Scheurer, and S. Sachdev, Physical Review Research **2**, 033283 (2020).

[105] S. Murakami and A. Okamoto, Journal of the Physical Society of Japan **86**, 011010 (2017).

[106] I. A. Leahy, C. A. Pocs, P. E. Siegfried, D. Graf, S.-H. Do, K.-Y. Choi, B. Normand, and M. Lee, Physical Review Letters **118**, 187203 (2017).

[107] C. A. Pocs, I. A. Leahy, H. Zheng, G. Cao, E.-S. Choi, S.-H. Do, K.-Y. Choi, B. Normand, and M. Lee, Physical Review Research **2**, 013059 (2020).

[108] J. Des Cloizeaux, Nuclear Physics **20**, 321 (1960).

[109] A. Togo and I. Tanaka, Scripta Materialia **108**, 1 (2015).

[110] A. Togo, Journal of the Physical Society of Japan **92**, 012001 (2023).

[111] A. Szilva, Y. Kvashnin, E. A. Stepanov, L. Nordström, O. Eriksson, A. I. Lichtenstein, and M. I. Katsnelson, Reviews of Modern Physics **95**, 035004 (2023).

[112] V. M. Katukuri, S. Nishimoto, V. Yushankhai, A. Stoyanova, H. Kandpal, S. Choi, R. Coldea, I. Rousochatzakis, L. Hozoi, and J. Van Den Brink, New Journal of Physics **16**, 013056 (2014).

[113] V. M. Katukuri, V. Yushankhai, L. Siurakshina, J. Van Den Brink, L. Hozoi, and I. Rousochatzakis, Physical Review X **4**, 021051 (2014).

[114] R. Yadav, N. A. Bogdanov, V. M. Katukuri, S. Nishimoto, J. Van Den Brink, and L. Hozoi, Scientific Reports **6**, 37925 (2016).

[115] P. Bhattacharyya, N. A. Bogdanov, S. Nishimoto, S. D. Wilson, and L. Hozoi, arXiv preprint arXiv:2212.09365 (2022).

[116] M. Pizzochero, R. Yadav, and O. V. Yazyev, 2d Materials **7**, 035005 (2020).

[117] S. M. Winter, Y. Li, H. O. Jeschke, and R. Valentí, Physical Review B **93**, 214431 (2016).

[118] K. Riedl, Y. Li, R. Valentí, and S. M. Winter, Physica Status Solidi B **256**, 1800684 (2019).

[119] F. Neese, L. Lang, V. G. Chilkuri, and M. an der Ruhr, in *Lecture Notes of the Autumn School on Correlated Electrons* (Forschungszentrum Jülich GmbH Institute for Advanced Simulation, 2020).

[120] C. J. Calzado, J. Cabrero, J. P. Malrieu, and R. Caballol, The Journal of Chemical Physics **116**, 2728 (2002).

[121] C. J. Calzado, J. Cabrero, J. P. Malrieu, and R. Caballol, The Journal of Chemical Physics **116**, 3985 (2002).

[122] P. Durand and J.-P. Malrieu, Advances in Chemical Physics **67**, 321 (2007).

[123] C. J. Calzado, C. Angeli, D. Taratiel, R. Caballol, and J.-P. Malrieu, The Journal of Chemical Physics **131**, 044327 (2009).

[124] J. P. Malrieu, R. Caballol, C. J. Calzado, C. De Graaf, and N. Guihery, Chemical Reviews **114**, 429 (2014).

[125] R. Maurice, R. Bastardis, C. d. Graaf, N. Suaud, T. Mallah, and N. Guihery, Journal of Chemical Theory and Computation **5**, 2977 (2009).

[126] R. Maurice, N. Guihéry, R. Bastardis, and C. d. Graaf, Journal of Chemical Theory and Computation **6**, 55 (2010).

[127] R. Maurice, C. de Graaf, and N. Guihéry, The Journal of Chemical Physics **133**, 084307 (2010).

[128] R. Maurice, C. De Graaf, and N. Guihery, Physical Chemistry Chemical Physics **15**, 18784 (2013).

[129] R. Ruamps, R. Maurice, C. De Graaf, and N. Guihéry, Inorganic Chemistry **53**, 4508 (2014).

[130] R. Maurice, R. Broer, N. Guihéry, and C. de Graaf, in *Handbook of Relativistic Quantum Chemistry* (Springer Berlin, Heidelberg, 2016).

[131] J. Oitmaa, C. Hamer, and W. Zheng, *Series expansion methods for strongly interacting lattice models* (Cambridge University Press, 2006).

[132] B. Yang, Y. M. Goh, S. H. Sung, G. Ye, S. Biswas, D. A. Kaib, R. Dhakal, S. Yan, C. Li, S. Jiang, F. Chen, H. Lei, R. He, R. Valentí, S. M. Winter, R. Hovden, and A. W. Tsen, Nature Materials **22**, 50 (2023).

[133] K. Riedl, R. Valentí, and S. M. Winter, Nature Communications **10**, 2561 (2019).

[134] K. Riedl, E. Gati, D. Zielke, S. Hartmann, O. M. Vyaselev, N. D. Kushch, H. O. Jeschke, M. Lang, R. Valentí, M. V. Kartsovnik, and S. M. Winter, Physical Review Letters **127**, 147204 (2021).

[135] R. Dhakal, S. Griffith, and S. M. Winter, npj Quantum Materials **9**, 64 (2024).

[136] P. Hohenberg and W. Kohn, Physical Review **136**, B864 (1964).

[137] W. Kohn and L. J. Sham, Physical Review **140**, A1133 (1965).

[138] S. Baroni, P. Giannozzi, and A. Testa, Physical Review Letters **58**, 1861 (1987).

[139] S. Baroni, S. De Gironcoli, A. Dal Corso, and P. Giannozzi, Reviews of Modern Physics **73**, 515 (2001).

[140] K. Parlinski, Z. Li, and Y. Kawazoe, Physical Review Letters **78**, 4063 (1997).

[141] K. Kunc and R. M. Martin, Physical Review Letters **48**, 406 (1982).

[142] W. Frank, C. Elsässer, and M. Fähnle, Physical review letters **74**, 1791 (1995).

[143] L. Xiang, R. Dhakal, M. Ozerov, Y. Jiang, B. S. Mou, A. Ozarowski, Q. Huang, H. Zhou, J. Fang, S. M. Winter, *et al.*, Physical Review Letters **131**, 076701 (2023).

[144] P. W. Anderson, Materials Research Bulletin **8**, 153 (1973).

[145] A. Kitaev, Annals of Physics **321**, 2 (2006).

[146] L. Balents, nature **464**, 199 (2010).

[147] Y. Zhou, K. Kanoda, and T.-K. Ng, Reviews of Modern Physics **89**, 025003 (2017).

[148] C. Broholm, R. J. Cava, S. Kivelson, D. Nocera, M. Norman, and T. Senthil, Science **367**, eaay0668 (2020).

[149] A. Banerjee, C. Bridges, J.-Q. Yan, A. Aczel, L. Li, M. Stone, G. Granroth, M. Lumsden, Y. Yiu, J. Knolle, *et al.*, Nature materials **15**, 733 (2016).

[150] S.-H. Do, S.-Y. Park, J. Yoshitake, J. Nasu, Y. Motome, Y. S. Kwon, D. Adroja, D. Voneshen, K. Kim, T.-H. Jang, *et al.*, Nature Physics **13**, 1079 (2017).

[151] K. Ran, J. Wang, W. Wang, Z.-Y. Dong, X. Ren, S. Bao, S. Li, Z. Ma, Y. Gan, Y. Zhang, *et al.*, Physical Review Letters **118**, 107203 (2017).

[152] S.-H. Baek, S.-H. Do, K.-Y. Choi, Y. S. Kwon, A. Wolter, S. Nishimoto, J. Van Den Brink, and B. Büchner, Physical Review Letters **119**, 037201 (2017).

[153] Z. Wang, S. Reschke, D. Hüvonen, S.-H. Do, K.-Y. Choi, M. Gensch, U. Nagel, T. Rõõm, and A. Loidl, Physical Review Letters **119**, 227202 (2017).

[154] R. Hentrich, A. U. Wolter, X. Zotos, W. Brenig, D. Nowak, A. Isaeva, T. Doert, A. Banerjee, P. Lampen-Kelley, D. G. Mandrus, *et al.*, Physical Review Letters **120**, 117204 (2018).

[155] A. Ponomaryov, L. Zviagina, J. Wosnitza, P. Lampen-Kelley, A. Banerjee, J.-Q. Yan, C. Bridges, D. Mandrus, S. Nagler, and S. Zvyagin, Physical Review Letters **125**, 037202 (2020).

[156] Y. Kasahara, T. Ohnishi, Y. Mizukami, O. Tanaka, S. Ma, K. Sugii, N. Kurita, H. Tanaka, J. Nasu, Y. Motome, *et al.*, Nature **559**, 227 (2018).

[157] D. Wulferding, Y. Choi, S.-H. Do, C. H. Lee, P. Lemmens, C. Faugeras, Y. Gallais, and K.-Y. Choi, Nature Communications **11**, 1603 (2020).

[158] A. Sahasrabudhe, D. Kaib, S. Reschke, R. German, T. Koethe, J. Buhot, D. Kamenskyi, C. Hickey, P. Becker, V. Tsurkan, *et al.*, Physical Review B **101**, 140410 (2020).

[159] P. Maksimov and A. Chernyshev, Physical Review Research **2**, 033011 (2020).

[160] P. Laurell and S. Okamoto, npj Quantum Materials **5**, 2 (2020).

[161] H. Liu and G. Khaliullin, Physical Review B **97**, 014407 (2018).

[162] R. Sano, Y. Kato, and Y. Motome, Physical Review B **97**, 014408 (2018).

[163] H. Liu, J. Chaloupka, and G. Khaliullin, Physical Review Letters **125**, 047201 (2020).

[164] H. Liu, International Journal of Modern Physics B **35**, 2130006 (2021).

[165] L. Viciu, Q. Huang, E. Morosan, H. Zandbergen, N. Greenbaum, T. McQueen, and R. Cava, Journal of Solid State Chemistry **180**, 1060 (2007).

[166] E. Lefrançois, M. Songvilay, J. Robert, G. Nataf, E. Jordan, L. Chaix, C. Colin, P. Lejay, A. Hadj-Azzem, R. Ballou, *et al.*, Physical Review B **94**, 214416 (2016).

[167] A. Bera, S. Yusuf, A. Kumar, and C. Ritter, Physical Review B **95**, 094424 (2017).

[168] G. Xiao, Z. Xia, W. Zhang, X. Yue, S. Huang, X. Zhang, F. Yang, Y. Song, M. Wei, H. Deng, *et al.*, Crystal Growth & Design **19**, 2658 (2019).

[169] X. Hong, M. Gillig, R. Hentrich, W. Yao, V. Kocsis, A. R. Witte, T. Schreiner, D. Baumann, N. Pérez, A. U. Wolter, *et al.*, Physical Review B **104**, 144426 (2021).

[170] R. Zhong, M. Chung, T. Kong, L. T. Nguyen, S. Lei, and R. J. Cava, Physical Review B **98**, 220407 (2018).

[171] H. S. Nair, J. Brown, E. Coldren, G. Hester, M. Gelfand, A. Podlesnyak, Q. Huang, and K. Ross, Physical Review B **97**, 134409 (2018).

[172] R. Zhong, T. Gao, N. P. Ong, and R. J. Cava, Science advances **6**, eaay6953 (2020).

[173] S. Das, S. Voleti, T. Saha-Dasgupta, and A. Paramekanti, Physical Review B **104**, 134425 (2021).

[174] C. Kim, H.-S. Kim, and J.-G. Park, Journal of Physics: Condensed Matter **34**, 023001 (2022).

[175] L. Shi, X. Wang, R. Zhong, Z. Wang, T. Hu, S. Zhang, Q. Liu, T. Dong, F. Wang, and N. Wang, Physical Review B **104**, 144408 (2021).

[176] P. A. Maksimov, A. V. Ushakov, Z. V. Pchelkina, Y. Li, S. M. Winter, and S. V. Streltsov, Physical Review B **106**, 165131 (2022).

[177] X. Zhang, Y. Xu, T. Halloran, R. Zhong, C. Broholm, R. Cava, N. Drichko, and N. Armitage, Nature Materials **22**, 58 (2023).

[178] T. Halloran, F. Desrochers, E. Z. Zhang, T. Chen, L. E. Chern, Z. Xu, B. Winn, M. Graves-Brook, M. Stone, A. I. Kolesnikov, *et al.*, Proceedings of the National Academy of Sciences **120**, e2215509119 (2023).

[179] G. Lin, J. Jeong, C. Kim, Y. Wang, Q. Huang, T. Masuda, S. Asai, S. Itoh, G. Günther, M. Russina, *et al.*, Nature Communications **12**, 5559 (2021).

[180] W. Yao, Y. Zhao, Y. Qiu, C. Balz, J. R. Stewart, J. W. Lynn, and Y. Li, arXiv preprint arXiv:2211.16941 (2022).

[181] M. Songvilay, J. Robert, S. Petit, J. Rodriguez-Rivera, W. Ratcliff, F. Damay, V. Balédent, M. Jiménez-Ruiz, P. Lejay, E. Pachoud, *et al.*, Physical Review B **102**, 224429 (2020).

[182] A. M. Samarakoon, Q. Chen, H. Zhou, and V. O. Garlea, Physical Review B **104**, 184415 (2021).

[183] C. Kim, J. Jeong, G. Lin, P. Park, T. Masuda, S. Asai, S. Itoh, H.-S. Kim, H. Zhou, J. Ma, *et al.*, Journal of Physics: Condensed Matter **34**, 045802 (2022).

[184] A. L. Sanders, R. A. Mole, J. Liu, A. J. Brown, D. Yu, C. D. Ling, and S. Rachel, Physical Review B **106**, 014413 (2022).

[185] W. Chen, X. Li, Z. Hu, Z. Hu, L. Yue, R. Sutarto, F. He, K. Iida, K. Kamazawa, W. Yu, *et al.*, Physical Review B **103**, L180404 (2021).

[186] W. Yao, K. Iida, K. Kamazawa, and Y. Li, Physical Review Letters **129**, 147202 (2022).

[187] W. G. Krüger, W. Chen, X. Jin, Y. Li, and L. Janssen, arXiv preprint arXiv:2211.16957 (2022).

[188] S. Zhang, S. Lee, A. J. Woods, W. Peria, S. M. Thomas, R. Movshovich, E. Brosha, Q. Huang, H. Zhou, V. S. Zapf, *et al.*, arXiv preprint arXiv:2212.03849 (2022).

[189] X. Liu and H.-Y. Kee, Physical Review B **107**, 054420 (2023).

[190] L. Wu, A. Little, E. E. Aldape, D. Rees, E. Thewalt, P. Lampen-Kelley, A. Banerjee, C. A. Bridges, J.-Q. Yan, D. Boone, *et al.*, Physical Review B **98**, 094425 (2018).

[191] S. M. Winter, K. Riedl, D. Kaib, R. Coldea, and R. Valentí, Physical Review Letters **120**, 077203 (2018).

[192] S. M. Winter, K. Riedl, P. A. Maksimov, A. L. Chernyshev, A. Honecker, and R. Valentí, Nature Communications **8**, 1152 (2017).

[193] G. Xiao, Z. Xia, Y. Song, and L. Xiao, Journal of Physics: Condensed Matter **34**, 075801 (2022).

[194] W. Yao and Y. Li, Physical Review B **101**, 085120 (2020).

[195] C. Lee, S. Lee, Y. Choi, Z. Jang, R. Kalaivanan, R. Sankar, and K.-Y. Choi, Physical Review B **103**, 214447 (2021).

[196] J. A. Sears, Y. Zhao, Z. Xu, J. W. Lynn, and Y.-J. Kim, Physical Review B **95**, 180411 (2017).

[197] A. Banerjee, P. Lampen-Kelley, J. Knolle, C. Balz, A. A. Aczel, B. Winn, Y. Liu, D. Pajerowski, J. Yan, C. A. Bridges, *et al.*, npj Quantum Materials **3**, 8 (2018).

[198] A. Hassan, L. Pardi, J. Krzystek, A. Sienkiewicz, P. Goy, M. Rohrer, and L.-C. Brunel, Journal of Magnetic Resonance **142**, 300 (2000).

[199] K. Koepernik and H. Eschrig, Physical Review B **59**, 1743 (1999).

[200] I. Opahle, K. Koepernik, and H. Eschrig, Physical Review B **60**, 14035 (1999).

[201] J. P. Perdew, K. Burke, and M. Ernzerhof, Physical Review Letters **77**, 3865 (1996).

[202] S. Sugano, *Multiplets of transition-metal ions in crystals* (Elsevier, 2012).

[203] E. Pavarini, *in Many-Electron Approaches in Physics, Chemistry and Mathematics* (Springer, 2014) pp. 321–341.

[204] N. D. Patel and N. Trivedi, Proceedings of the National Academy of Sciences **116**, 12199 (2019).

[205] C. Hickey and S. Trebst, Nature Communications **10**, 530 (2019).

[206] D. A. Kaib, S. M. Winter, and R. Valentí, Physical Review B **100**, 144445 (2019).

[207] M. Freedman, A. Kitaev, M. Larsen, and Z. Wang, Bulletin of the American Mathematical Society **40**, 31 (2003).

[208] J. Chaloupka, G. Jackeli, and G. Khaliullin, Physical Review Letters **110**, 097204 (2013).

[209] J. G. Rau, E. K.-H. Lee, and H.-Y. Kee, Physical Review Letters **112**, 077204 (2014).

[210] K. Plumb, J. Clancy, L. Sandilands, V. V. Shankar, Y. Hu, K. Burch, H.-Y. Kee, and Y.-J. Kim, Physical Review B **90**, 041112 (2014).

[211] Y. Kasahara, T. Ohnishi, Y. Mizukami, O. Tanaka, S. Ma, K. Sugii, N. Kurita, H. Tanaka, J. Nasu, Y. Motome, *et al.*, Nature **559**, 227 (2018).

[212] T. Yokoi, S. Ma, Y. Kasahara, S. Kasahara, T. Shibauchi, N. Kurita, H. Tanaka, J. Nasu, Y. Motome, C. Hickey, *et al.*, Science **373**, 568 (2021).

[213] L. J. Sandilands, Y. Tian, K. W. Plumb, Y.-J. Kim, and K. S. Burch, Physical Review Letters **114**, 147201 (2015).

[214] Y.-F. Jiang, T. P. Devereaux, and H.-C. Jiang, Physical Review B **100**, 165123 (2019).

[215] L. E. Chern, R. Kaneko, H.-Y. Lee, and Y. B. Kim, Physical Review Research **2**, 013014 (2020).

[216] S.-S. Zhang, G. B. Halász, and C. D. Batista, Nature Communications **13**, 399 (2022).

[217] H. Li, H.-K. Zhang, J. Wang, H.-Q. Wu, Y. Gao, D.-W. Qu, Z.-X. Liu, S.-S. Gong, and W. Li, Nature Communications **12**, 4007 (2021).

[218] K. A. Modic, R. D. McDonald, J. Ruff, M. D. Bachmann, Y. Lai, J. C. Palmstrom, D. Graf, M. K. Chan, F. Balakirev, J. Betts, *et al.*, Nature Physics **17**, 240 (2021).

[219] X.-G. Zhou, H. Li, Y. H. Matsuda, A. Matsuo, W. Li, N. Kurita, G. Su, K. Kindo, and H. Tanaka, Nature Communications **14**, 5613 (2023).

[220] S. Biswas, Y. Li, S. M. Winter, J. Knolle, and R. Valentí, Physical Review Letters **123**, 237201 (2019).

[221] S.-Y. Park, S.-H. Do, K.-Y. Choi, D. Jang, T.-H. Jang, J. Schefer, C.-M. Wu, J. Gardner, J. Park, J.-H. Park, *et al.*, arXiv preprint arXiv:1609.05690 (2016).

[222] H. B. Cao, A. Banerjee, J.-Q. Yan, C. Bridges, M. Lumsden, D. Mandrus, D. Tennant, B. Chakoumakos, and S. Nagler, Physical Review B **93**, 134423 (2016).

[223] D. R. Klein, D. MacNeill, J. L. Lado, D. Soriano, E. Navarro-Moratalla, K. Watanabe, T. Taniguchi, S. Manni, P. Canfield, J. Fernández-Rossier, *et al.*, Science **360**, 1218 (2018).

[224] H. H. Kim, B. Yang, S. Li, S. Jiang, C. Jin, Z. Tao, G. Nichols, F. Sfigakis, S. Zhong, C. Li, *et al.*, Proceedings of the National Academy of Sciences **116**, 11131 (2019).

[225] L. Shi, Y. Liu, T. Lin, M. Zhang, S. Zhang, L. Wang, Y. Shi, T. Dong, and N. Wang, Physical Review B **98**, 094414 (2018).

[226] C. Balz, P. Lampen-Kelley, A. Banerjee, J. Yan, Z. Lu, X. Hu, S. M. Yadav, Y. Takano, Y. Liu, D. A. Tennant, *et al.*, Physical Review B **100**, 060405 (2019).

[227] T. Harada, I. Ohkubo, M. Lippmaa, Y. Sakurai, Y. Matsumoto, S. Muto, H. Koinuma, and M. Oshima, Physical Review Letters **109**, 076602 (2012).

[228] J. Lambe and R. Jaklevic, Physical Review **165**, 821 (1968).

[229] H. Li, T. Zhang, A. Said, G. Fabbris, D. G. Mazzone, J. Yan, D. Mandrus, G. B. Halász, S. Okamoto, S. Murakami, *et al.*, Nature Communications **12**, 3513 (2021).

[230] N. D. Mermin and H. Wagner, Physical Review Letters **17**, 1133 (1966).

[231] D. A. Kaib, S. Biswas, K. Riedl, S. M. Winter, and R. Valentí, Physical Review B **103**, L140402 (2021).

[232] S. Bachus, D. A. Kaib, Y. Tokiwa, A. Jesche, V. Tsurkan, A. Loidl, S. M. Winter, A. A. Tsirlin, R. Valenti, and P. Gegenwart, Physical Review Letters **125**, 097203 (2020).

[233] Y. Wang, J. Balgley, E. Gerber, M. Gray, N. Kumar, X. Lu, J.-Q. Yan, A. Fereidouni, R. Basnet, S. J. Yun, *et al.*, Nano Letters **20**, 8446 (2020).

[234] Z. Dai, J.-X. Yu, B. Zhou, S. A Tenney, P. Lampen-Kelley, J. Yan, D. Mandrus, E. A Henriksen, J. Zang, K. Pohl, *et al.*, 2D Materials **7**, 035004 (2020).

[235] H. Eschrig, M. Richter, and I. Opahle, in *Theoretical and Computational Chemistry*, Vol. 14 (Elsevier, 2004) pp. 723–776.

[236] C. Eichstaedt, Y. Zhang, P. Laurell, S. Okamoto, A. G. Eguiluz, and T. Berlijn, Physical Review B **100**, 075110 (2019).

[237] K. S. Pedersen, J. Bendix, A. Tressaud, E. Durand, H. Weihe, Z. Salman, T. J. Morsing, D. N. Woodruff, Y. Lan, W. Wernsdorfer, *et al.*, Nature Communications **7**, 12195 (2016).

[238] F. Neese, Wiley Interdisciplinary Reviews: Computational Molecular Science **8**, e1327 (2018).

[239] G. Kresse and J. Hafner, Physical Review B **47**, 558 (1993).

[240] S. Grimme, Journal of computational chemistry **27**, 1787 (2006).

[241] K. S. Burch, D. Mandrus, and J.-G. Park, Nature **563**, 47 (2018).

[242] K. F. Mak, J. Shan, and D. C. Ralph, Nature Reviews Physics **1**, 646 (2019).

[243] H. Li, S. Ruan, and Y.-J. Zeng, Advanced Materials **31**, 1900065 (2019).

[244] M. A. McGuire, Journal of Applied Physics **128** (2020).

[245] H. Kurebayashi, J. H. Garcia, S. Khan, J. Sinova, and S. Roche, Nature Reviews Physics **4**, 150 (2022).

[246] A. Wildes, D. Lançon, M. K. Chan, F. Weickert, N. Harrison, V. Simonet, M. Zhitomirsky, M. Gvozdikova, T. Ziman, and H. Rønnow, Physical Review B **101**, 024415 (2020).

[247] M. Nauman, D. H. Kiem, S. Lee, S. Son, J.-G. Park, W. Kang, M. J. Han, and Y. Jo, 2D Materials **8**, 035011 (2021).

[248] J.-U. Lee, S. Lee, J. H. Ryoo, S. Kang, T. Y. Kim, P. Kim, C.-H. Park, J.-G. Park, and H. Cheong, Nano Letters **16**, 7433 (2016).

[249] C. Gong, P. Zhang, T. Norden, Q. Li, Z. Guo, A. Chaturvedi, A. Najafi, S. Lan, X. Liu, Y. Wang, *et al.*, Nature Communications **14**, 3839 (2023).

[250] H. Zhang, Z. Ni, C. E. Stevens, A. Bai, F. Peiris, J. R. Hendrickson, L. Wu, and D. Jariwala, Nature Photonics **16**, 311 (2022).

[251] Z. Ni, N. Huang, A. V. Haglund, D. G. Mandrus, and L. Wu, Nano Letters **22**, 3283 (2022).

[252] K. Wang, K. Ren, Y. Hou, Y. Cheng, and G. Zhang, Physical Chemistry Chemical Physics **25**, 21802 (2023).

[253] S. Liu, A. Granados del Águila, D. Bhowmick, C. K. Gan, T. Thu Ha Do, M. A. Prosnikov, D. Sedmidubský, Z. Sofer, P. C. M. Christianen, P. Sengupta, and Q. Xiong, Physical Review Letters **127**, 097401 (2021).

[254] Q. Zhang, M. Ozerov, E. V. Boström, J. Cui, N. Suri, Q. Jiang, C. Wang, F. Wu, K. Hwangbo, J.-H. Chu, D. Xiao, A. Rubio, and X. Xu, arXiv preprint arXiv:2108.11619 (2021).

[255] D. Vaclavkova, M. Palit, J. Wyzula, S. Ghosh, A. Delhomme, S. Maity, P. Kapuscinski, A. Ghosh, M. Veis, M. Grzeszczyk, C. Faugeras, M. Orlita, S. Datta, and M. Potemski, Physical Review B **104**, 134437 (2021).

[256] Y.-J. Sun, J.-M. Lai, S.-M. Pang, X.-L. Liu, P.-H. Tan, and J. Zhang, The Journal of Physical Chemistry Letters **13**, 1533 (2022).

[257] A. Ghosh, M. Palit, S. Maity, V. Dwij, S. Rana, and S. Datta, Physical Review B **103**, 064431 (2021).

[258] F. Zhou, K. Hwangbo, Q. Zhang, C. Wang, L. Shen, J. Zhang, Q. Jiang, A. Zong, Y. Su, M. Zajac, *et al.*, Nature Communications **13**, 6598 (2022).

[259] E. Ergeçen, B. Ilyas, J. Kim, J. Park, M. B. Yilmaz, T. Luo, D. Xiao, S. Okamoto, J.-G. Park, and N. Gedik, Proceedings of the National Academy of Sciences **120**, e2208968120 (2023).

[260] A. Zong, Q. Zhang, F. Zhou, Y. Su, K. Hwangbo, X. Shen, Q. Jiang, H. Liu, T. E. Gage, D. A. Walko, *et al.*, Nature **620**, 988 (2023).

[261] D.-Q. To, C. Ameyaw, A. Suresh, S. Bhatt, M. Ku, M. Jungfleisch, J. Xiao, J. Zide, B. Nikolić, and M. Doty, Physical Review B **108**, 085435 (2023).

[262] J. N. Kløgetvedt and A. Qaiumzadeh, Physical Review B **108**, 224424 (2023).

[263] J. Cui, E. V. Boström, M. Ozerov, F. Wu, Q. Jiang, J.-H. Chu, C. Li, F. Liu, X. Xu, A. Rubio, *et al.*, Nature Communications **14**, 3396 (2023).

[264] J. Luo, S. Li, Z. Ye, R. Xu, H. Yan, J. Zhang, G. Ye, L. Chen, D. Hu, X. Teng, *et al.*, Nano Letters **23**, 2023 (2023).

[265] A. Wildes, K. C. Rule, R. Bewley, M. Enderle, and T. J. Hicks, Journal of Physics: Condensed Matter. **24**, 416004 (2012).

[266] D. Lançon, H. Walker, E. Ressouche, B. Ouladdiaf, K. Rule, G. McIntyre, T. Hicks, H. M. Rønnow, and A. Wildes, Physical Review B **94**, 214407 (2016).

[267] A. Wildes, M. Zhitomirsky, T. Ziman, D. Lançon, and H. Walker, Journal of Applied Physics **127** (2020).

[268] A. McCreary, J. R. Simpson, T. T. Mai, R. D. McMichael, J. E. Douglas, N. Butch, C. Dennis, R. V. Aguilar, and A. R. H. Walker, Physical Review B **101**, 064416 (2020).

[269] J. Wyzula, I. Mohelsky, D. Václavková, P. Kapuscinski, M. Veis, C. Faugeras, M. Potemski, M. E. Zhitomirsky, and M. Orlita, Nano Letters **22**, 9741 (2022).

[270] N. Chandrasekharan and S. Vasudevan, Pramana **43**, 21 (1994).

[271] T. Y. Kim and C.-H. Park, Nano Letters **21**, 10114 (2021).

[272] Y.-J. Song, K.-W. Lee, and W. E. Pickett, Physical Review B **92**, 125109 (2015).

[273] X. Bai, S.-S. Zhang, Z. Dun, H. Zhang, Q. Huang, H. Zhou, M. B. Stone, A. I. Kolesnikov, F. Ye, C. D. Batista, *et al.*, Nature Physics **17**, 467 (2021).

[274] Y. Lee, S. Son, C. Kim, S. Kang, J. Shen, M. Kenzelmann, B. Delley, T. Savchenko, S. Parchenko, W. Na, *et al.*, Advanced Electronic Materials **9**, 2200650 (2023).

[275] M. Sanjuán, M. Kanehisa, and M. Jouanne, Physical Review B **46**, 11501 (1992).

[276] See supplemental material for complete definition of J_{eff} states, intersite Hund's coupling matrices employed, estimated biquadratic exchange constants for large U_{t2g}, and mtx files for intersite couplings in full $J_{\text{eff}} = 1, 2, 3$ model for $U_{t2g} = 4.2$.

[277] C. E. Soliverez, Physical Review A **24**, 4 (1981).

[278] M. Montalti, A. Credi, L. Prodi, and M. T. Gandolfi, *Handbook of photochemistry* (CRC press, 2006).

[279] S. Sugano, Y. Tanabe, and H. Kamimura, eds., *Multiplets of Transition-Metal Ions in Crystals*, Pure and Applied Physics, Vol. 33 (Elsevier, 1970) pp. 294–301.

[280] P. Joy and S. Vasudevan, Physical Review B **46**, 5134 (1992).

[281] C. Autieri, G. Cuono, C. Noce, M. Rybak, K. M. Kotur, C. E. Agrapidis, K. Wohlfeld, and M. Birowska, The Journal of Physical Chemistry C **126**, 6791 (2022).

[282] E. Şaşıoğlu, C. Friedrich, and S. Blügel, Physical Review B **83**, 121101 (2011).

[283] L. Vaugier, H. Jiang, and S. Biermann, Physical Review B **86**, 165105 (2012).

[284] M. Liska, P. Pelikán, and L. T. Nagy, Chemical Papers **29**, 577 (1975).

[285] C. J. Calzado, J. Cabrero, J. P. Malrieu, and R. Caballol, The Journal of Chemical Physics **116**, 2728 (2002).

[286] C. J. Calzado, J. Cabrero, J. P. Malrieu, and R. Caballol, The Journal of Chemical Physics **116**, 3985 (2002).

[287] L. Pourovskii, Physical Review B **94**, 115117 (2016).

[288] L. V. Pourovskii, D. F. Mosca, and C. Franchini, Physical Review Letters **127**, 237201 (2021).

[289] S.-T. Pi, R. Nanguneri, and S. Savrasov, Physical Review Letters **112**, 077203 (2014).

[290] D. F. Mosca, L. V. Pourovskii, and C. Franchini, Physical Review B **106**, 035127 (2022).

[291] R. F. Boisvert, R. F. Boisvert, and K. A. Remington, *The matrix market exchange formats: Initial design*, Vol. 5935 (Citeseer, 1996).

[292] A. Joshi, M. Ma, F. Mila, D. Shi, and F. Zhang, Physical Review B **60**, 6584 (1999).

[293] A. Läuchli, F. Mila, and K. Penc, Physical Review Letters **97**, 087205 (2006).

[294] T. A. Tóth, A. M. Läuchli, F. Mila, and K. Penc, Physical Review Letters **105**, 265301 (2010).

[295] C. Luo, T. Datta, and D.-X. Yao, Physical Review B **93**, 235148 (2016).

[296] F. H. Kim, K. Penc, P. Nataf, and F. Mila, Physical Review B **96**, 205142 (2017).

[297] S. Koyama and J. Nasu, arXiv preprint arXiv:2308.01711 (2023).

[298] K. Kurosawa, S. Saito, and Y. Yamaguchi, Journal of the Physical Society of Japan **52**, 3919 (1983).

[299] M. J. Coak, D. M. Jarvis, H. Hamidov, A. R. Wildes, J. A. Paddison, C. Liu, C. R. Haines, N. T. Dang, S. E. Kichanov, B. N. Savenko, *et al.*, Physical Review X **11**, 011024 (2021).

[300] P. Joy and S. Vasudevan, Physical Review B **46**, 5425 (1992).

[301] M. Jouanne and C. Julien, Journal of Applied Physics **64**, 3637 (1988).

[302] G. Ouvrard, R. Brec, and J. Rouxel, Materials Research Bulletin **20**, 1181 (1985).

[303] K. Koepernik, O. Janson, Y. Sun, and J. Van Den Brink, Physical Review B **107**, 235135 (2023).

[304] J. Colpa, Physica A **93**, 327 (1978).

[305] S. Toth and B. Lake, Journal of Physics: Condensed Matter. **27**, 166002 (2015).

[306] A. Lunghi, Science Advances **8**, eabn7880 (2022).

[307] J. G. Kragskow, A. Mattioni, J. K. Staab, D. Reta, J. M. Skelton, and N. F. Chilton, Chemical Society Reviews (2023).

[308] D. Bozhko, V. Vasyuchka, A. Chumak, and A. Serga, Low Temperature Physics **46**, 383 (2020).

[309] Q. H. Wang, A. Bedoya-Pinto, M. Blei, A. H. Dismukes, A. Hamo, S. Jenkins, M. Koperski, Y. Liu, Q.-C. Sun, E. J. Telford, H. H. Kim, M. Augustin, U. Vool, J.-X. Yin, L. H. Li, A. Falin, C. R. Dean, F. Casanova, R. F. L. Evans, M. Chshiev, A. Mishchenko, C. Petrovic, R. He, L. Zhao, A. W. Tsen, B. D. Gerardot, M. Brotons-Gisbert, Z. Guguchia, X. Roy, S. Tongay, Z. Wang, M. Z. Hasan, J. Wrachtrup, A. Yacoby, A. Fert, S. Parkin, K. S. Novoselov, P. Dai, L. Balicas, and E. J. G. Santos, ACS Nano **16**, 6960 (2022).

[310] D. Zhong, K. L. Seyler, X. Linpeng, R. Cheng, N. Sivadas, B. Huang, E. Schmidgall, T. Taniguchi, K. Watanabe, M. A. McGuire, W. Yao, D. Xiao, K.-M. C. Fu, and X. Xu, Science Advances **3**, e1603113 (2017).

[311] L. Hu, K.-z. Du, Y. Chen, Y. Zhai, X. Wang, and Q. Xiong, National Science Open **2**, 20230002 (2023).

[312] J. Van Vleck, Physical Review **57**, 426.

[313] R. Orbach, Proceedings of the Royal Society of London. Series A. Mathematical and Physical Sciences **264**, 458 (1961).

[314] T. Ray and D. Ray, Physical Review **164**, 420 (1967).

[315] H. Capellmann and S. Lipinski, Zeitschrift für Physik B Condensed Matter **83**, 199 (1991).

[316] A. Ioselevich and H. Capellmann, Physical Review B **51**, 11446 (1995).

[317] S. Petit, F. Moussa, M. Hennion, S. Pailhes, L. Pinsard-Gaudart, and A. Ivanov, Physical Review Letters **99**, 266604 (2007).

[318] J. Oh, M. D. Le, H.-H. Nahm, H. Sim, J. Jeong, T. Perring, H. Woo, K. Nakajima, S. Ohira-Kawamura, Z. Yamani, *et al.*, Nature Communications **7**, 13146 (2016).

[319] S. Bao, Z.-L. Gu, Y. Shangguan, Z. Huang, J. Liao, X. Zhao, B. Zhang, Z.-Y. Dong, W. Wang, R. Kajimoto, *et al.*, Nature Communications **14**, 6093 (2023).

[320] Y. Zhou and P. A. Lee, Physical Review Letters **106**, 056402 (2011).

[321] M. Poirier, M. de Lafontaine, K. Miyagawa, K. Kanoda, and Y. Shimizu, Physical Review B **89**, 045138 (2014).

[322] S. Streib, P. Kopietz, P. T. Cong, B. Wolf, M. Lang, N. van Well, F. Ritter, and W. Assmus, Physical Review B **91**, 041108 (2015).

[323] A. Metavitsiadis and W. Brenig, Physical Review B **101**, 035103 (2020).

[324] K. Feng, A. Shiralieva, and N. B. Perkins, Physical Review B **106**, 144424 (2022).

[325] H.-L. Kim, T. Saito, H. Yang, H. Ishizuka, M. J. Coak, J. H. Lee, H. Sim, Y. S. Oh, N. Nagaosa, and J.-G. Park, Nature Communications **15**, 243 (2024).

[326] X. Zhou, W. Wu, Y. Sui, Y.-f. Yang, and J. Luo, Advanced Functional Materials , 2304921 (2024).

[327] R. Hentrich, A. U. Wolter, X. Zotos, W. Brenig, D. Nowak, A. Isaeva, T. Doert, A. Banerjee, P. Lampen-Kelley, D. G. Mandrus, *et al.*, Physical Review Letters **120**, 117204 (2018).

[328] A. Haglund, (2019).

[329] C. Xu, C. Carnahan, H. Zhang, M. Sretenovic, P. Zhang, D. Xiao, and X. Ke, Physical Review B **107**, L060404 (2023).

[330] C. Xu, H. Zhang, C. Carnahan, P. Zhang, D. Xiao, and X. Ke, Physical Review B **109**, 094415 (2024).

[331] M. Gillig, X. Hong, C. Wellm, V. Kataev, W. Yao, Y. Li, B. Büchner, and C. Hess, Physical Review Research **5**, 043110 (2023).

[332] N. Li, R. Neumann, S. Guang, Q. Huang, J. Liu, K. Xia, X. Yue, Y. Sun, Y. Wang, Q. Li, *et al.*, Physical Review B **108**, L140402 (2023).

[333] L. Chen, É. Lefrançois, A. Vallipuram, Q. Barthélemy, A. Ataei, W. Yao, Y. Li, and L. Taillefer, arXiv preprint arXiv:2309.17231 (2023).

[334] S. Guang, N. Li, R. L. Luo, Q. Huang, Y. Wang, X. Yue, K. Xia, Q. Li, X. Zhao, G. Chen, *et al.*, Physical Review B **107**, 184423 (2023).

[335] Y. Kasahara, K. Sugii, T. Ohnishi, M. Shimozawa, M. Yamashita, N. Kurita, H. Tanaka, J. Nasu, Y. Motome, T. Shibauchi, *et al.*, Physical Review Letters **120**, 217205 (2018).

[336] J. Bruin, R. Claus, Y. Matsumoto, N. Kurita, H. Tanaka, and H. Takagi, Nature Physics **18**, 401 (2022).

[337] P. Czajka, T. Gao, M. Hirschberger, P. Lampen-Kelley, A. Banerjee, N. Quirk, D. G. Mandrus, S. E. Nagler, and N. P. Ong, Nature Materials **22**, 36 (2023).

[338] É. Lefrançois, G. Grissonnanche, J. Baglo, P. Lampen-Kelley, J.-Q. Yan, C. Balz, D. Mandrus, S. Nagler, S. Kim, Y.-J. Kim, *et al.*, Physical Review X **12**, 021025 (2022).

[339] M. Mori, A. Spencer-Smith, O. P. Sushkov, and S. Maekawa, Physical Review Letters **113**, 265901 (2014).

[340] H. Guo and S. Sachdev, Physical Review B **103**, 205115 (2021).

[341] S. Li, H. Yan, and A. H. Nevidomskyy, arXiv preprint arXiv:2301.07401 (2023).

[342] Y. Onose, T. Ideue, H. Katsura, Y. Shiomi, N. Nagaosa, and Y. Tokura, Science **329**, 297 (2010).

[343] P. A. McClarty, Annual Review of Condensed Matter Physics **13**, 171 (2022).

[344] J. Nasu, J. Yoshitake, and Y. Motome, Physical Review Letters **119**, 127204 (2017).

[345] E. Thingstad, A. Kamra, A. Brataas, and A. Sudbø, Physical Review Letters **122**, 107201 (2019).

[346] S. Park and B.-J. Yang, Physical Review B **99**, 174435 (2019).

[347] B. Sheikhi, M. Kargarian, and A. Langari, Physical Review B **104**, 045139 (2021).

[348] H. Huang and Z. Tian, Physical Review B **104**, 064305 (2021).

[349] J.-S. Wang and L. Zhang, Physical Review B **80**, 012301 (2009).

[350] T. Saito, K. Misaki, H. Ishizuka, and N. Nagaosa, Physical Review Letters **123**, 255901 (2019).

[351] M. Ye, R. M. Fernandes, and N. B. Perkins, Physical Review Research **2**, 033180 (2020).

[352] K. Sun, Z. Gao, and J.-S. Wang, Physical Review B **103**, 214301 (2021).

[353] M. Ye, L. Savary, and L. Balents, arXiv preprint arXiv:2103.04223 (2021).

[354] Y. Zhang, Y. Teng, R. Samajdar, S. Sachdev, and M. S. Scheurer, Physical Review B **104**, 035103 (2021).

[355] T. T. Mai, K. F. Garrity, A. McCreary, J. Argo, J. R. Simpson, V. Doan-Nguyen, R. V. Aguilar, and A. R. H. Walker, Science Advances **7**, eabj3106 (2021).

[356] A. Lunghi, F. Totti, S. Sanvito, and R. Sessoli, Chemical Science **8**, 6051 (2017).

[357] A. Albino, S. Benci, L. Tesi, M. Atzori, R. Torre, S. Sanvito, R. Sessoli, and A. Lunghi, Inorganic Chemistry **58**, 10260 (2019).

[358] F.-S. Guo, B. M. Day, Y.-C. Chen, M.-L. Tong, A. Mansikkamäki, and R. A. Layfield, Science **362**, 1400 (2018).

[359] A. Lunghi, F. Totti, R. Sessoli, and S. Sanvito, Nature Communications **8**, 14620 (2017).

[360] L. Escalera-Moreno, N. Suaud, A. Gaita-Arino, and E. Coronado, The Journal of Physical Chemistry Letters **8**, 1695 (2017).

[361] D. Reta, J. G. Kragskow, and N. F. Chilton, Journal of the American Chemical Society **143**, 5943 (2021).

[362] B. Zhang, Y. Hou, Z. Wang, and R. Wu, Physical Review B **100**, 224427 (2019).

[363] P. Delugas, O. Baseggio, I. Timrov, S. Baroni, and T. Gorni, Physical Review B **107**, 214452 (2023).

[364] C. J. Fennie and K. M. Rabe, Physical Review Letters **96**, 205505 (2006).

[365] T. Shen, K. Cao, G.-C. Guo, and L. He, Physical Review B **78**, 134413 (2008).

[366] A. Kumar, C. Fennie, and K. Rabe, Physical Review B **86**, 184429 (2012).

[367] A. Paul, P. Sharma, and U. V. Waghmare, Physical Review B **92**, 054106 (2015).

[368] A. Paul and U. V. Waghmare, Physical Review B **107**, 174403 (2023).

[369] J. Hellsvik, D. Thonig, K. Modin, D. Iuşan, A. Bergman, O. Eriksson, L. Bergqvist, and A. Delin, Physical Review B **99**, 104302 (2019).

[370] B. Sadhukhan, A. Bergman, Y. O. Kvashnin, J. Hellsvik, and A. Delin, Physical Review B **105**, 104418 (2022).

[371] S. Mankovsky, S. Polesya, H. Lange, M. Weißenhofer, U. Nowak, and H. Ebert, Physical Review Letters **129**, 067202 (2022).

[372] H. Lange, S. Mankovsky, S. Polesya, M. Weißenhofer, U. Nowak, and H. Ebert, Physical Review B **107**, 115176 (2023).

[373] S.-T. Pi, R. Nanguneri, and S. Savrasov, Physical Review B **90**, 045148 (2014).

[374] S. Mankovsky, H. Lange, S. Polesya, and H. Ebert, Physical Review B **107**, 144428 (2023).

[375] J. Bonini, S. Ren, D. Vanderbilt, M. Stengel, C. E. Dreyer, and S. Coh, Physical Review Letters **130**, 086701 (2023).

[376] S. Ren, J. Bonini, M. Stengel, C. E. Dreyer, and D. Vanderbilt, Physical Review X **14**, 011041 (2024).

[377] K. Kim, S. Y. Lim, J. Kim, J.-U. Lee, S. Lee, P. Kim, K. Park, S. Son, C.-H. Park, J.-G. Park, *et al.*, 2d Materials **6**, 041001 (2019).

[378] D. Vaclavkova, A. Delhomme, C. Faugeras, M. Potemski, A. Bogucki, J. Suffczyński, P. Kossacki, A. R. Wildes, B. Grémaud, and A. Saúl, 2d Materials **7**, 035030 (2020).

[379] S. Calder, A. Haglund, A. I. Kolesnikov, and D. Mandrus, Physical Review B **103**, 024414 (2021).

[380] N. Sivadas, M. W. Daniels, R. H. Swendsen, S. Okamoto, and D. Xiao, Physical Review B **91**, 235425 (2015).

[381] J. Yang, Y. Zhou, Q. Guo, Y. Dedkov, and E. Voloshina, RSC Advances **10**, 851 (2020).

[382] R. Dhakal, D. A. Kaib, S. Biswas, R. Valenti, and S. M. Winter, arXiv preprint arXiv:2407.00660 (2024).

[383] V. Grasso, F. Neri, P. Perillo, L. Silipigni, and M. Piacentini, Physical Review B **44**, 11060 (1991).

[384] V. Grasso, F. Neri, L. Silipigni, and M. Piacentini, Physical Review B **40**, 5529 (1989).

[385] K. Foyevtsova, H. O. Jeschke, I. Mazin, D. Khomskii, and R. Valentí, Physical Review B **88**, 035107 (2013).

[386] H. Liu and G. Khaliullin, Physical Review B **97**, 014407 (2018).

[387] H. Liu, J. Chaloupka, and G. Khaliullin, Physical Review B **105**, 214411 (2022).

[388] H. Liu, J. Chaloupka, and G. Khaliullin, Physical Review Letters **125**, 047201 (2020).

[389] K. Wittel and R. Manne, Theoretica Chimica Acta **33**, 347 (1974).

[390] G. Kresse and J. Furthmüller, Physical Review B **54**, 11169 (1996).

[391] G. Kresse and J. Furthmüller, Computational materials science **6**, 15 (1996).

[392] G. Kresse and D. Joubert, Physical Review B **59**, 1758 (1999).

[393] P. E. Blöchl, Physical Review B **50**, 17953 (1994).

[394] J. P. Perdew, A. Ruzsinszky, G. I. Csonka, O. A. Vydrov, G. E. Scuseria, L. A. Constantin, X. Zhou, and K. Burke, Physical Review Letters **100**, 136406 (2008).

[395] S. Grimme, J. Antony, S. Ehrlich, and H. Krieg, The Journal of Chemical Physics **132** (2010).

[396] D. Wood and A. Zunger, Journal of Physics A: Mathematical and General **18**, 1343 (1985).

[397] P. Pulay, Chemical Physics Letters **73**, 393 (1980).

[398] S. L. Dudarev, G. A. Botton, S. Y. Savrasov, C. Humphreys, and A. P. Sutton, Physical Review B **57**, 1505 (1998).

[399] A. Wiedenmann, J. Rossat-Mignod, A. Louisy, R. Brec, and J. Rouxel, Solid State Communications **40**, 1067 (1981).

[400] G. Kresse, J. Furthmüller, and J. Hafner, Europhysics Letters **32**, 729 (1995).

[401] A. Togo, L. Chaput, T. Tadano, and I. Tanaka, Journal of Physics: Condensed Matter **35**, 353001 (2023).

[402] A. Togo, Journal of the Physical Society of Japan **92**, 012001 (2023).

[403] F. Giustino, M. L. Cohen, and S. G. Louie, Physical Review B **76**, 165108 (2007).

[404] J. Noffsinger, F. Giustino, B. D. Malone, C.-H. Park, S. G. Louie, and M. L. Cohen, Computer Physics Communications **181**, 2140 (2010).

[405] H. Lee, S. Poncé, K. Bushick, S. Hajinazar, J. Lafuente-Bartolome, J. Leveillee, C. Lian, J.-M. Lihm, F. Macheda, H. Mori, *et al.*, Npj Compututational Materials **9**, 156 (2023).

[406] P. Fleury and R. Loudon, Physical Review **166**, 514 (1968).

[407] Y. Yang, M. Li, I. Rousochatzakis, and N. B. Perkins, Physical Review B **104**, 144412 (2021).

[408] Original Sunny.jl code available at https://github.com/SunnySuite/Sunny.jl.

[409] H. Zhang and C. D. Batista, Physical Review B **104**, 104409 (2021).

[410] D. Dahlbom, H. Zhang, C. Miles, X. Bai, C. D. Batista, and K. Barros, Physical Review B **106**, 054423 (2022).

[411] D. Dahlbom, C. Miles, H. Zhang, C. D. Batista, and K. Barros, Physical Review B **106**, 235154 (2022).

[412] R. Ramırez, T. López-Ciudad, P. Kumar P, and D. Marx, The Journal of Chemical Physics **121**, 3973 (2004).

[413] D. Dahlbom, F. Brooks, M. Wilson, S. Chi, A. Kolesnikov, M. Stone, H. Cao, Y.-W. Li, K. Barros, M. Mourigal, *et al.*, Physical Review B **109**, 014427 (2024).

[414] D. J. Gillard, D. Wolverson, O. M. Hutchings, and A. I. Tartakovskii, npj 2D Materials and Applications **8**, 6 (2024).

[415] C. Hess, The European Physical Journal Special Topics **151**, 73 (2007).

[416] A. Chernyshev and W. Brenig, Physical Review B **92**, 054409 (2015).

[417] A. Chernyshev and A. Rozhkov, Physical Review Letters **116**, 017204 (2016).

[418] J. Liao, Z. Huang, Y. Shangguan, B. Zhang, S. Cheng, H. Xu, R. Kajimoto, K. Kamazawa, S. Bao, and J. Wen, Physical Review B **109**, 224411 (2024).

[419] K. Imamura, S. Suetsugu, Y. Mizukami, Y. Yoshida, K. Hashimoto, K. Ohtsuka, Y. Kasahara, N. Kurita, H. Tanaka, P. Noh, *et al.*, Science Advances **10**, eadk3539 (2024).

[420] R. Hentrich, M. Roslova, A. Isaeva, T. Doert, W. Brenig, B. Büchner, and C. Hess, Physical Review B **99**, 085136 (2019).

[421] Y. Kasahara, S. Suetsugu, T. Asaba, S. Kasahara, T. Shibauchi, N. Kurita, H. Tanaka, and Y. Matsuda, Physical Review B **106**, L060410 (2022).

[422] H. Zhang, M. A. McGuire, A. F. May, H.-Y. Chao, Q. Zheng, M. Chi, B. C. Sales, D. G. Mandrus, S. E. Nagler, H. Miao, *et al.*, Physical Review Materials **8**, 014402 (2024).

[423] M. Nawwar, R. R. Neumann, J. Wen, I. Mertig, A. Mook, and J. P. Heremans, Reports on Progress in Physics **88**, 080503 (2025).

[424] A. Mook, J. Henk, and I. Mertig, Physical Review B **89**, 134409 (2014).

[425] P. McClarty, X.-Y. Dong, M. Gohlke, J. Rau, F. Pollmann, R. Moessner, and K. Penc, Physical Review B **98**, 060404 (2018).

[426] E. Z. Zhang, L. E. Chern, and Y. B. Kim, Physical Review B **103**, 174402 (2021).

[427] L. E. Chern, E. Z. Zhang, and Y. B. Kim, Physical Review Letters **126**, 147201 (2021).

[428] S. Li and S. Okamoto, Physical Review B **106**, 024413 (2022).

[429] X.-Q. Sun, J.-Y. Chen, and S. A. Kivelson, Physical Review B **106**, 144111 (2022).

[430] B. Flebus and A. MacDonald, Physical Review Letters **131**, 236301 (2023).

[431] S. Singh, P. P. Stavropoulos, and N. B. Perkins, Physical Review B **110**, 094431 (2024).

[432] S. Gass, P. M. Cônsoli, V. Kocsis, L. T. Corredor, P. Lampen-Kelley, D. G. Mandrus, S. E. Nagler, L. Janssen, M. Vojta, B. Büchner, and A. U. B. Wolter, Physical Review B **101**, 245158 (2020).

[433] R. Schönemann, S. Imajo, F. Weickert, J. Yan, D. G. Mandrus, Y. Takano, E. L. Brosha, P. F. S. Rosa, S. E. Nagler, K. Kindo, and M. Jaime, Physical Review B **102**, 214432 (2020).

[434] V. Kocsis, D. A. S. Kaib, K. Riedl, S. Gass, P. Lampen-Kelley, D. G. Mandrus, S. E. Nagler, N. Pérez, K. Nielsch, B. Büchner, A. U. B. Wolter, and R. Valentí, Physical Review B **105**, 094410 (2022).

[435] C. Kane and M. P. Fisher, Physical Review B **55**, 15832 (1997).

[436] M. Banerjee, M. Heiblum, V. Umansky, D. E. Feldman, Y. Oreg, and A. Stern, Nature **559**, 205 (2018).

[437] R. Dhakal, S. Griffith, K. Choi, and S. M. Winter, arXiv preprint arXiv:2407.00659 (2024).

[438] M. Barkeshli, S. B. Chung, and X.-L. Qi, Physical Review B—Condensed Matter and Materials Physics **85**, 245107 (2012).

[439] C. A. Mead, Reviews of Modern Physics **64**, 51 (1992).

[440] S. M. Winter, K. Riedl, P. A. Maksimov, A. L. Chernyshev, A. Honecker, and R. Valentí, Nature Communications **8**, 1152 (2017).

[441] D. A. Kaib, K. Riedl, A. Razpopov, Y. Li, S. Backes, I. I. Mazin, and R. Valentí, npj Quantum Materials **7**, 75 (2022).

[442] P. Maksimov and A. Chernyshev, Physical Review Research **2**, 033011 (2020).

[443] B. W. Lebert, S. Kim, D. A. Prishchenko, A. A. Tsirlin, A. H. Said, A. Alatas, and Y.-J. Kim, Physical Review B **106**, L041102 (2022).

[444] A. Shragai, E. Horsley, S. Kim, Y.-J. Kim, and B. Ramshaw, arXiv preprint arXiv:2510.06443 (2025).

[445] Y. Yu, Y. Xu, K. Ran, J. Ni, Y. Huang, J. Wang, J. Wen, and S. Li, Physical Review Letters **120**, 067202 (2018).

[446] T. Kurumaji, Physical Review Research **5**, 023138 (2023).

[447] A. Liechtenstein, V. I. Anisimov, and J. Zaanen, Physical Review B **52**, R5467 (1995).

[448] L. J. Sandilands, Y. Tian, A. A. Reijnders, H.-S. Kim, K. W. Plumb, Y.-J. Kim, H.-Y. Kee, and K. S. Burch, Physical Review B **93**, 075144 (2016).

[449] L. J. Sandilands, C. H. Sohn, H. J. Park, S. Y. Kim, K. W. Kim, J. A. Sears, Y.-J. Kim, and T. W. Noh, Physical Review B **94**, 195156 (2016).

[450] B. W. Lebert, S. Kim, B. H. Kim, S. H. Chun, D. Casa, J. Choi, S. Agrestini, K. Zhou, M. Garcia-Fernandez, and Y.-J. Kim, Physical Review B **108**, 155122 (2023).

[451] R. Birss, Proceedings of the Physical Society **79**, 946 (1962).

[452] R. Matsumoto, R. Shindou, and S. Murakami, Physical Review B **89**, 054420 (2014).

[453] H. Kondo, Y. Akagi, and H. Katsura, Progress of Theoretical and Experimental Physics **2020**, 12A104 (2020).

[454] L. Yadav, R. Bag, R. Dhakal, S. M. Winter, J. G. Rau, S. E. Dissanayake, A. I. Kolesnikov, A. A. Podlesnyak, C. M. Brown, N. P. Butch, *et al.*, Physical Review Materials **8**, 123401 (2024).

[455] B. Shen, E. Insuasti Pazmino, R. Dhakal, F. Freund, P. Gegenwart, S. M. Winter, and A. A. Tsirlin, npj Quantum Materials **10**, 9 (2025).

Curriculum Vitae

Ramesh Dhakal

Department of Physics, Wake Forest University, Olin Physical Laboratory, 2090 Eure Drive, Winston-Salem, NC 27109
(336) 938-938-9 | dhakr21@wfu.edu

RESEARCH INTERESTS

Modeling of Quantum Materials, Strongly Correlated System, Electronic Structure Theory, Spin-Phonon Interaction

EDUCATION

Wake Forest University, Department of Physics **2021 – PRESENT**
Winston-Salem, NC
PhD Student, Physics
Research Advisor: Dr. Stephen M. Winter

Tribhuvan University, Central Department of Physics **2018**
Kathmandu, Nepal
M.Sc., Physics
Research Advisor: Dr. Gopi Chandra Kaphle

RESEARCH EXPERIENCE

Graduate Research Assistant **2021 – PRESENT**
Wake Forest University, Winston-Salem, NC
Department of Physics
Projects:

- Developed a generic computational approach to treat spin-phonon couplings in quantum magnets
- Modeled Magneto-optical Spectra and Inelastic Neutron scattering spectra of Heisenberg-Kitaev quantum material to analyze magnetic excitations
- Computed and analyzed magnetic exchange interactions and phonons for wide range of magnetic materials

Graduate Research Assistant **2017 – 2018**
Tribhuvan University, Kathmandu, Nepal
Central Department of Physics
Projects:

- Developed an ab-initio method to identify experimentally feasible Heusler compounds for potential spintronics application
- Investigated the effect of doping and lattice distortions on the magnetic properties of Heusler compounds

TECHNICAL SKILLS

-Programming Python, Julia
-Computational Tools. Quantum Espresso, VASP, FPLO, Sunny, Phonopy, Phono3py, Perturbo, Wannier90
-HPC and Simulations MPI, Parallel Computing

Invited Talk

TOPIC - Effective Hamiltonians and Thermal Hall Effect in Quantum Magnets
Marco Bernardi Research Group **May-6, 2025**
Caltech

TOPIC – Spin-Phonon interactions in Quantum Magnets
Condensed Matter Seminar **Dec-9, 2025**
West Virginia University

SELECTED PUBLICATIONS

□ R. Dhakal, D. A. S. Kaib, K. Choi, S. Biswas, R. Valenti, S. M. Winter, Theory of Intrinsic Phonon Thermal Hall Effect in α-$RuCl_3$
https://arxiv.org/pdf/2407.00660

□ R. Dhakal, S. Griffith, K. Choi, S. M. Winter, Spin-Phonon Coupling in Transition Metal Insulators: General Computational Approach and Application to $MnPSe_3$
https://arxiv.org/pdf/2407.00659

□ R. Dhakal, S. Griffith, S. M. Winter, Hybrid Spin-Orbit Exciton-Magnon Excitations in $FePS_3$, npj Quantum Materials **9** (2024), 64.
https://www.nature.com/articles/s41535-024-00675-x

□ L. Xiang, R. Dhakal, M. Ozerov, Y. Jiang, B. S. Mou, et al., Disorder-Enriched Magnetic Excitations in a Heisenberg-Kitaev Quantum Magnet $Na_2Co_2TeO_6$, Physical Review Letters **131** (2023), 076701.
https://doi.org/10.1103/PhysRevLett.131.076701

□ B. Shen, E. I. Pazmino, R. Dhakal, F. Freund, P. Gegenwart, S. M. Winter, A. A. Tsirlin, Pressure-dependent magnetism of the Kitaev candidate Li_2RhO_3, npj Quantum Materials **10** (2025), 9.
https://www.nature.com/articles/s41535-025-00730-1

□ L. Yadav, R. Bag, R. Dhakal, S. M. Winter, et al., Synthesis and characterization of the novel breathing pyrochlore compound $Ba_3Tm_2Zn_5O_{11}$, Physical Review Materials **8** (2024), 123401.
https://journals.aps.org/prmaterials/abstract/10.1103/PhysRevMaterials.8.123401

□ B. Yang, Y. M. Goh, S. H. Sung, G. Ye, S. Biswas, D. A. S. Kaib, R. Dhakal, et al., Magnetic anisotropy reversal driven by structural symmetry-breaking in monolayer α-$RuCl_3$, Nature Materials **22** (2023), 50.
https://doi.org/10.1038/s41563-022-01401-3

□ S. Nepal, R. Dhakal*, I. Galanakis, S.M. Winter, R. P. Adhikari and G. C. Kaphle, Ab initio study of stable 3d, 4d and 5d transition-metal-based Quaternary Heusler compounds, Physical Review Materials **6** (2022), 114407.
https://doi.org/10.1103/PhysRevMaterials.6.114407

□ R. Dhakal, S. Nepal, I.Galanakis, R. P. Adhikari and G. C. Kaphle, Prediction of half-metallicity and spin-gapless semiconducting behavior in the new series of Fe-based quaternary Heusler alloys: An Ab initio study, Journal of Alloys and Compounds **882** (2021), 160500.
https://doi.org/10.1016/j.jallcom.2021.160500

□ S. Nepal, R. Dhakal*, I. Galanakis, Ab initio study of the half-metallic full-Heusler compounds Co_2ZAl [Z = Sc, Ti, V, Cr, Mn, Fe]; the role of electronic correlations, Materials Today Communications **25** (2020), 101498.
https://doi.org/10.1016/j.mtcomm.2020.101498

 R. Dhakal, S. Nepal, R.B. Ray, R. Paudel and G. C. Kaphle, Effect of doping on SGS and weak half-metallic properties of inverse Heusler Alloys, Journal of Magnetism and Magnetic Materials **503** (2020), 0304. https://www.sciencedirect.com/science/article/pii/S0304885319330136

CONFERENCE PRESENTATIONS AND WORKSHOPS

 Progress toward computing phonon thermal transport in alpha-$RuCl_3$, APS Global Physics Summit (Contributed talk), Denver, Colorado (March 15-20), 2026

 HybriD3 Materials Theory Training Workshop, Duke University, NC (November 21- November 22) 2025

 Perturbo Code Hybrid Workshop 2025, Caltech, Pasadena (September 18- September 19), 2025

 Spin-phonon Coupling in Transition Metal Insulators with Strong Spin Orbital Moments, Quantum Materials Workshop and CNMS User Meeting, (Poster presentation) Oak Ridge National Lab, Tennessee, (August 12-August 15), 2024

 Generic First Principles Approach for Spin-Phonon Coupling, International Conference on Magnetism (Poster presentation) Bologna, Italy (June 30- July 5), 2024

 Ab Initio Approach to Spin-Phonon Coupling in Transition Metal Insulators, Electronic Structure Workshop-24 (Poster presentation) Boston University, Boston (June 2-5), 2024

 Disorder-enriched magnetic excitations in the Kitaev quantum spin liquid candidate Na2Co2TeO6, TopoMag23 Workshop (Poster presentation) Ohio State University, Ohio (May 15-20), 2023

 Magnetic excitations in the Kitaev quantum spin liquid candidate Na2Co2TeO6 – Part II: Theory, Bulletin of the American Physical Society (Contributed talk), Las Vegas, Nevada (March 5-10), 2023

TEACHING

Teaching Assistant |Wake Forest University| Department of Physics

- Intermediate Laboratory II (PHY 266) **Spring 2023**
  - Experiments on Mechanics, Electronics and Computer Simulations
- General Physics Lab (PHY 113). **Fall and Spring 2022**
  - Experiments on Mechanics, Wave Motions, Heat and Sound
- General Astronomy Lab (PHY 109) **Fall 2021**
  - Observation and study of planets, satellites and constellations using telescope
- Physics and Chemistry of Environment Lab (PHY 120) **Fall 2022**
  - Experiments on basic physical and chemical process in the earth's atmosphere
- Physics Tutor (PHY 110, 113, 114) **Spring 2022**
  - Assisted students with assignment problems in mechanics, electricity, magnetism, optics, thermodynamics, and modern physics, applying extensive calculus and trigonometry

LEAP Mentor | Wake Forest University| Department of Physics **Summer 2023**

- Designed curriculum for high school students to introduce fundamental concepts of programming

– Aided students to create a presentation to showcase the work done during their internship

Student Teaching | Shree Janata Higher Secondary School|Nepal **Spring 2019 - Summer 2021**

– Developed and implemented lesson plans into a high school physics and math classroom (topics covered include mechanics, electricity and magnetism, trigonometry, linear algebra, vectors, matrix algebra)
– Created engaging labs and tutorial sessions for each topic
– Developed and delivered assessments to evaluate student understanding and progress

Student Teaching | Mahendra Memorial Academy|Nepal **Spring 2018 - Spring 2019**

– Taught Physics covering topics such as mechanics, electromagnetism, optics and thermodynamics
– Designed lesson plan and conducted interactive experiments to reinforce concepts in kinematics, electricity and waves
– Tracked academic progress of each student and offered tailored guidance to improve learning outcomes

OUTREACH

Volunteer | Meadowlark Middle School |Spring 2024

– Introduced children to a variety of physics concept including inertia, angular momentum, and electricity and magnetism, through exciting demonstration
–

Volunteer | College Launch Volunteering |Spring 2025, Spring 2026

– Introduced high school juniors to exciting world of physics and engineering through hands-on projects
– Guided students on building telescopes by combing lenses based on their focal lengths
– Led practical demonstration on electromagnetism, assisting students in constructing simple motors using magnets and coils

Astro-Fest Nepal Organizer|Central Department of Physics|April 2018

– Organized and managed Astro-Fest Nepal 2018, a national level astronomy event featuring experts talk, webinars and exhibitions
– Coordinated with guest speakers, including professors and international researchers, ensuring seamless executions of the sessions

REFERENCES

Dr. Stephen M. Winter, PhD (Supervisor)
Assistant Professor
Department of Physics, E-mail: winters@wfu.edu
Wake Forest University, United States of America

Dr. Ajay Ram Srimath Kandada, PhD
Assistant Professor
Department of Physics,
Wake Forest University, United States of America E-mail: srimatar@wfu.edu

Dr. Dmitry Smirnov, PhD
Research Faculty III
Condensed Matter Science, DC Field CMS
National High Magnetic Field Laboratory, USA E-mail: smirnov@magnet.fsu.edu